

Cover Page



Universiteit Leiden



The handle <http://hdl.handle.net/1887/50090> holds various files of this Leiden University dissertation

**Author:** Carton, David

**Title:** Resolving gas-phase metallicity in galaxies

**Issue Date:** 2017-06-29

Resolving gas-phase metallicity in galaxies

*ISBN: 978-94-6233-654-4*

# Resolving gas-phase metallicity in galaxies

Proefschrift

ter verkrijging van  
de graad van Doctor aan de Universiteit Leiden,  
op gezag van Rector Magnificus prof. mr. C.J.J.M. Stolker,  
volgens besluit van het College voor Promoties  
te verdedigen op donderdag 29 juni 2017  
klokke 11.15 uur

door

David Carton

geboren te Winchester, Verenigd Koninkrijk  
in 1990

Promotiecommissie

Promotor: Prof. dr. Joop Schaye

Co-promotor: Dr. Jarle Brinchmann

Overige leden: Dr. Rychard Bouwens

Dr. Thierry Contini

(IRAP, Université de Toulouse)

Prof. dr. Marijn Franx

Dr. Jacqueline Hodge

Prof. dr. Huub Röttgering

Prof. dr. Christy Tremonti

(University of Wisconsin-Madison)

Prof. dr. Paul van der Werf

Front cover: Stylized tessellation of spiral galaxy M101 (*The Pinwheel Galaxy*).

Back cover: Planetary nebula NGC3132 (*The Eight-burst Nebula*). Image derived from MUSE pseudo-narrowband observations of the [O III], [O II] and [O I] emission lines.

*For those that believe in me  
even when I don't*



---

# Contents

---

<b>1</b>	<b>Introduction</b>	<b>1</b>
1	Inside-out galaxy growth . . . . .	1
1.1	Star formation regulation and gas supply . . . . .	1
2	Gas-phase metallicity . . . . .	2
2.1	Measuring gas-phase metallicity . . . . .	3
3	Integral field spectroscopy (IFS) . . . . .	5
4	This thesis . . . . .	5
4.1	Outlook . . . . .	7
<b>2</b>	<b>Gas-phase metallicity profiles of the Bluedisk galaxies: Is metallicity in a local star-formation regulated equilibrium?</b>	<b>9</b>
1	Introduction . . . . .	10
2	Data . . . . .	11
2.1	Bluedisk galaxy classification . . . . .	11
2.2	Bulge-Disc-Bar decomposition . . . . .	12
2.3	Stellar mass densities . . . . .	12
3	Observations . . . . .	13
3.1	Reduction . . . . .	13
4	Analysis . . . . .	14
4.1	Bluedisk SDSS properties . . . . .	17
4.2	Contamination from non-star-forming sources . . . . .	17
4.3	Inferring Metallicities . . . . .	17
4.4	Estimating gas mass densities . . . . .	20
5	Results . . . . .	20
5.1	The local mass-metallicity relation and radial mass profiles . . . . .	20
5.2	Metallicity profiles of the Bluedisk galaxies . . . . .	21
5.3	Summary of results . . . . .	31
6	Discussion . . . . .	31
6.1	Modelling resolved galaxies as local gas regulators . . . . .	34
6.2	Bluedisk galaxies as local gas regulators . . . . .	38
7	Conclusions . . . . .	43
	Appendices . . . . .	46
A	Comparison of metallicity indicators . . . . .	46
B	Gas surface density estimates . . . . .	47
C	Metallicity profiles equally weighed by galaxy . . . . .	50
<b>3</b>	<b>Inferring gas-phase metallicity gradients of galaxies at the seeing limit: A forward modelling approach</b>	<b>55</b>
1	Introduction . . . . .	56
2	Model Description . . . . .	57
2.1	Simulating Observations . . . . .	57
2.2	Star Formation Rate (SFR) Maps . . . . .	59
2.3	The Galaxy Model . . . . .	60
2.4	Model fitting . . . . .	63
2.5	PSF model . . . . .	65

3	Model Testing . . . . .	66
3.1	Accuracy and precision tests . . . . .	66
3.2	Model tests with realistic data . . . . .	70
3.3	Interpreting the observed metallicity gradient . . . . .	77
4	Application . . . . .	77
4.1	Data . . . . .	77
4.2	Analysis . . . . .	78
4.3	Results . . . . .	79
4.4	Discussion . . . . .	85
5	Conclusions . . . . .	86
	Appendices . . . . .	89
	A Model line ratios . . . . .	89
	B Model systematics . . . . .	90
	C Spaxel binning algorithm . . . . .	93
	D SFR Maps . . . . .	93
	E Additional figures . . . . .	94
<b>4</b>	<b>First gas-phase metallicity gradients of <math>0.1 \lesssim z \lesssim 0.8</math> galaxies with MUSE</b>	<b>97</b>
1	Introduction . . . . .	98
2	Data . . . . .	99
2.1	MUSE Observations . . . . .	100
2.2	Derived global properties . . . . .	102
2.3	Sample Description . . . . .	104
3	Analysis . . . . .	109
3.1	Emission line flux extraction . . . . .	109
3.2	Inferring metallicities . . . . .	110
3.3	Sensitivity analysis . . . . .	112
4	Results . . . . .	116
5	Discussion . . . . .	120
5.1	Literature comparison . . . . .	120
5.2	Interpretation . . . . .	122
6	Conclusions . . . . .	124
	Appendices . . . . .	127
	A Additional figures . . . . .	127
<b>5</b>	<b>A dependency between the mass-metallicity relation and the metallicity gradients of galaxies</b>	<b>135</b>
1	Introduction . . . . .	136
2	Data . . . . .	136
3	Results . . . . .	137
3.1	Analysing a $M_*-Z_0-\nabla_r(\log_{10} Z)$ relation . . . . .	138
4	Discussion . . . . .	142
4.1	Implications for a $M_*-Z$ -SFR relation . . . . .	142
5	Summary . . . . .	143
<b>6</b>	<b>Samenvatting</b>	<b>147</b>
1	Wat zijn metalen? . . . . .	147
2	Waarom zijn metalen interessant? . . . . .	147
3	Hoe meet men metalliciteit? . . . . .	147
3.1	De <i>Multi Unit Spectroscopic Explorer</i> (MUSE) . . . . .	148

4	Deze thesis . . . . .	148
<b>7</b>	<b>Summary</b>	<b>153</b>
1	What are metals? . . . . .	153
2	Why study them? . . . . .	153
3	How to measure metallicity? . . . . .	153
3.1	The Multi Unit Spectroscopic Explorer (MUSE) . . . . .	154
4	This thesis . . . . .	154
	<b>Publications</b>	<b>157</b>
	<b>Curriculum Vitae</b>	<b>159</b>
	<b>Acknowledgements</b>	<b>161</b>



## 1 Inside-out galaxy growth

In their most basic form galaxies are gravitationally bound environments where gas is converted into stars.

Star forming galaxies generally consist of two discs (gaseous and stellar), embedded in a dark matter halo. Over time, atomic and molecular gas in the gaseous disc will cool, coalesce and collapse under gravity to form stars. Because the stellar disc is built from the gas disc, the two discs are aligned with each other. Note, however, the discs are not the same sizes, with the gas disc usually being the larger of the two (e.g. [Broeils & Rhee 1997](#)).

The sizes of the stellar and gas discs are not necessarily static throughout a galaxy's lifetime. Indeed we observe that the centres of galaxies are older (more metal rich) than their younger (metal poor) outskirts (e.g. [Sánchez-Blázquez et al. 2014](#)). This implies that historically the star-formation in galaxies was centrally concentrated and has since progressed outwards. This scenario is commonly referred to as the “inside-out” growth of galaxies ([Larson 1976](#)) and is in good qualitative agreement with many observations (e.g. [Prantzos & Boissier 2000](#)).

However, it remains unclear exactly which mechanisms are responsible for the apparent inside-out growth. To understand this it is important to understand how much of the stellar disc was formed in-situ and how many of the stars were formed in other galaxies that have since merged into the disc. Focusing in particular on the in-situ formation, it is necessary to understand the connection between the stellar and gaseous discs. We must ask how exactly do galaxies acquire their gas and how it is redistributed within a galaxy. In addition, we must also understand what are the necessary conditions for star-formation and which processes might regulate it.

### 1.1 Star formation regulation and gas supply

Evidence has indicated that galaxies continue to acquire gas throughout their lives. For example, by measuring the gas contents and star-formation rates of  $1 \lesssim z \lesssim 4$  galaxies [Tacconi et al. \(2013\)](#) found that the average galaxy has enough gas to sustain  $\sim 0.7$  Gyr of star formation. While this is long time, it is still substantially shorter than the age of the Universe.

A second interesting result about star-forming galaxies arises if we compare the stellar mass of a galaxy with its star-formation rate (SFR). One observes a correlation between stellar mass and SFR, such that the more massive galaxies are forming stars faster ([Whitaker et al. 2012](#)). This mass–SFR correlation is often referred to as the galaxy “main-sequence” ([Noeske et al. 2007](#)). However, this term is somewhat erroneous because there is no tight track along which galaxies move, and there is a significant scatter of galaxies about the main sequence ([Guo et al. 2013](#)). It is therefore important to ask what drives the scatter in the main sequence, i.e. what determines a galaxy's SFR.

Firstly, the environment that surrounds a galaxy is likely to influence its SFR. Galaxies

that live in low density environments may not acquire as much gas, consequently this may cause these galaxies to fall below the main sequence. In denser environments, not only might galaxies receive more gas, but encounters with other galaxies may be more frequent. These interactions could also enhance the SFR of galaxies (Barton et al. 2000).

However, there are potential mechanisms that could dampen these effects. Indeed the act of forming stars may produce negative feedback that inhibits the further production of stars (Silk 1997). For example, supernovae may cause turbulence that prevents gas clouds from collapsing and forming stars (e.g. Dib et al. 2006). There is good evidence that star formation is quite inefficient and negative feedback processes are often thought to play an important part in regulating the star-formation in galaxies. Feedback may act as a damping or restorative force that governs the SFR of galaxies, thus ensuring they remain close to the main sequence (Davé et al. 2012).

As we have just discussed, the gas supply and regulation of star formation in galaxies are some of the key concepts in the field of galaxy evolution today. As such, there are a few overarching questions that motivate this thesis:

- How do galaxies acquire the gas? What roles might gas inflows and outflows play in achieving or inhibiting this?
- What factors govern the star-formation rates of galaxies? Is star-formation regulated on local scales within a galaxy or is it regulated by a galaxy's global properties?
- How much are the properties of a galaxy determined by itself (internal processes) and how much by environment in which it lives (external factors)?

Naturally complete answers to these questions are beyond any single thesis. This thesis focuses on what we can learn from the gas-phase metallicity of galaxies.

## 2 Gas-phase metallicity

To understand galaxies one should not only study the amount of gas in galaxies, but one should also study its metallicity.

Metallicity is a powerful diagnostic with which we can learn about the history of the gas. Gas that has resided in galaxies for a long period will be heavily polluted with metals (e.g. from supernova ejecta), whereas gas that has been recently acquired from outside the galaxy should be relatively pristine. Simply stated, we can use gas-phase metallicity<sup>1</sup> to infer inflows of gas into galaxies.

However, inflows are not the only mechanism that can lower the metallicity of a galaxy. In fact outflowing gas will also produce a similar signature (Tremonti et al. 2004). It is this degeneracy between inflows and outflows that makes interpreting the metallicity of galaxies challenging.

Clearly gas-phase metallicity is not a panacea for understanding galaxy evolution. But, there are a few ways in which we can break this degeneracy. First and foremost metallicity should be studied in conjunction with other galaxy properties (e.g. stellar mass, star-formation rate). Chemical evolution models of galaxies suggest that metallicity exists in a dynamic equilibrium with these properties (Lilly et al. 2013), where it is essentially the balance of inflows and outflows that governs this equilibrium. Such models provide leverage for interpreting the roles of inflows and outflows. However, such models by themselves cannot address all the questions

---

<sup>1</sup>Unless otherwise stated, herein we will use (gas-phase) metallicity to refer to the oxygen abundance of the interstellar medium.

on the nature of such processes. Therefore we also need to spatially resolve the metallicity in galaxies to understand the physical scales on which these mechanisms exist.

## 2.1 Measuring gas-phase metallicity

So we have yet to explain how one measures the gas-phase metallicity of galaxies. Here we will briefly outline how metallicity (oxygen abundance) can be measured from rest-frame optical spectra of H II regions<sup>2</sup>.

The temperature and the emitted emission-lines of H II regions are dependent on the elemental abundances of the interstellar gas. As a result these luminous star-forming regions can be used to probe the metallicity of the interstellar medium in nearby and distant galaxies.

If we are able to measure the physical properties of the gas (e.g. temperature and density) then we can calculate the intrinsic emissivity of different ionic species. Under some simplifying assumptions, knowing the both observed emission-line ratios and the intrinsic emissivity ratios one can compute the abundance of the ionic species and, by extension, the metallicity.

### 2.1.1 The link between metallicity and temperature

Perhaps the most important physical property that metallicity affects is the temperature of gas. The reason for this is as follows. H II regions exist in a temperature equilibrium where heating is balanced by the cooling. The heating is provided by the photons emitted by the central star which ionizes the gas, ejecting electrons with some characteristic temperature. These electrons can subsequently recombine and, in theory, allow the gas to cool.

However, the recombination photons have a high probability to be reabsorbed and are unlikely to escape the H II regions. Recombination is inefficient at allowing the gas to cool. In contrast, forbidden emission-line photons have a low probability of being reabsorbed, providing an efficient cooling mechanism. The upper levels of forbidden emission-line transitions can be populated by collisional excitation between metal ions and electrons.

So in theory the more metals in the gas, the greater the cooling efficiency. However, since the heating and cooling rates must balance, the increased cooling efficiency is compensated by a reduced electron temperature. This is because a reduction in the temperature reduces the collisional excitation rate, and thus reduces the forbidden emission-line flux. For this reason metallicity and temperature are closely related properties of H II regions, the higher the metallicity the lower the temperature (e.g. [Wiersma et al. 2009](#))

### 2.1.2 The Direct method ( $T_e$ method)

If we wish to measure ionic abundances we need to know the intrinsic emissivities of the ions. To calculate the emissivity we must measure both the electron temperature and the electron density of the gas.

Electron densities can be inferred from density sensitive emission-line ratios, e.g.  $[\text{O II}]_{3729}/[\text{O II}]_{3726}$  and  $[\text{S II}]_{6731}/[\text{S II}]_{6717}$ . These emission-lines are typically bright and can be easily observed if they fall within the wavelength range of the spectrum. Typically one assumes that the electron density is constant throughout the H II region.

In contrast, measuring the electron temperature is more difficult (there is no single electron temperature for the whole H II region). Because different ionic species are found at different radii, different species have different characteristic electron temperatures.

For example, the zone containing  $\text{O}^{2+}$  (which is close to the star) is typically hotter than the  $\text{O}^+$  zone ([Izotov et al. 2006](#)). To calculate the emissivities of these  $\text{O}^{2+}$  and  $\text{O}^+$  zones, we

<sup>2</sup>Regions of ionized gas that surrounding young, hot O and B type stars

must measure the temperatures in both. In the case of  $O^{2+}$  we can use emission-line ratios such as  $[O\ III]_{4363}/[O\ III]_{5007}$ , and in the case of  $O^+$  states we can use  $[O\ II]_{3727}/[O\ III]_{7320,7330}$ . In most H II regions there is a negligible amount of  $O^{3+}$  (and no neutral oxygen), so the oxygen abundance can be derived by adding up the abundances of  $O^{2+}$  and  $O^+$ .

While it is ideal to measure the oxygen abundance (metallicity) in this way, the  $[O\ III]_{4363}$  and  $[O\ III]_{7320,7330}$  lines are relatively faint. So this “direct” method can only be applied to H II regions within the Milky Way and other nearby galaxies. For distant galaxies we must use another technique that uses only the bright (strong) emission-lines.

### 2.1.3 Strong-line methods

In distant galaxies we are often limited to using only the brightest emission lines to derive metallicity (e.g.  $[O\ II]_{3726,3729}$ ,  $H\beta$ ,  $[O\ III]_{5007}$ ,  $H\alpha$ ,  $[N\ II]_{6584}$  and  $[S\ II]_{6717,6731}$ ). While these lines do not provide useful diagnostics to *directly* infer the electron temperatures, they do nonetheless encode information on the metallicity.

There are a variety of methods that fall under the category of strong-line methods, exploiting different combinations of emission-lines to derive the metallicity (each with its own benefits and disadvantage). However, in general strong-line methods can be divided into two types. Those that are empirically calibrated to observed H II regions, and those that use theoretical photoionization models to calculate the metallicity. We shall now briefly discuss the relative merits of both the empirical and the theoretical approaches.

Empirical methods use nearby H II regions where metallicities have been derived using the direct method. With these observations the strong emission-lines can then be calibrated as a function of metallicity. The advantage of this approach is that one need not understand the underlying physics of H II regions to derive metallicities from the strong lines. However, there are two main issues with the empirical approach. Firstly, there are very few high-metallicity H II regions with reliable metallicity determinations. This is because at super-solar metallicities (low temperatures) the  $[O\ III]_{4363}$  emission-line is very faint. It is therefore questionable how reliable empirical calibrations are at high-metallicities. The second issue is that fundamentally we must assume that the H II regions in distant galaxies are similar to H II regions in the Universe today. Indeed there is good evidence that the conditions have changed, for example it is understood that the density of the interstellar medium was previously higher (Shirazi et al. 2014).

By deriving metallicity from theoretical photoionization models we can avoid both of these limitations/assumptions. Theoretical models do not suffer from the observational biases and they can explore a large portion of the potential parameter space. However, a theoretical approach does have its own limitations. Firstly, by permitting a large unconstrained parameter space there can be degenerate solutions for the metallicity. The empirical methods mitigate against this by encoding natural correlations between parameters, effectively reducing the dimensionality of the parameter space. That is not to say that theoretical methods cannot also encode such information, indeed some methods do (e.g. Pérez-Montero (2014) and that presented in Chapter 3 herein). There is a second concern over using theoretical methods that ultimately the accuracy of the theoretical methods is limited by the accuracy of our photoionization models.

In this thesis we will be studying distant galaxies and as such we must rely upon strong-line methods to derive the metallicities. In particular we will use those based on theoretical photoionization models.

### 3 Integral field spectroscopy (IFS)

Technical improvements in astronomical instrumentation have played a crucial role in advancing our knowledge of galaxies. Notably the past few decades has seen the development of integral-field spectrographs, taking spectroscopy to the next dimension. Integral-field spectroscopy (IFS) simultaneously obtains spectra over a 2D field of view (FoV), providing hyperspectral imaging of extended astronomical objects. IFS offers obvious advantages over traditional long-slit spectrographs that only provide a 1D view of the Universe.

Early integral-field spectrographs had significant drawbacks, suffering from a combination of having: a small FoV, poor spatial resolution, limited wavelength coverage, and/or low spectral resolution. However, over time with improvements in instrument design and manufacturing techniques, integral-field spectrographs now offer spectral resolutions and wavelength coverages comparable to traditional long-slit spectrographs. Furthermore some of the latest integral-field spectrographs also provide an image quality (spatial resolution) competitive with imagers.

A large portion of this thesis is based upon work with one instrument in particular: the Multi Unit Spectroscopic Explorer (MUSE; Bacon et al. (2010, and in prep.)). MUSE is a second generation for the Very Large Telescope (VLT) mounted on the Nasmyth focus of the Yepun telescope (UT4). MUSE is an optical integral-field spectrograph which, in Wide Field Mode, offers a  $1' \times 1'$  FoV with a  $0.2''$  sampling (the resolution is effectively seeing limited). In the spectral dimension MUSE provides a wavelength coverage over  $4750\text{\AA} - 9300\text{\AA}$ , with  $2.3\text{\AA}$  resolution.

On paper MUSE only offers modest technical gains and improvements of existing integral-field spectrographs. This, however, rather belies the true step-change that MUSE affords. Up to now spectrograph have been largely limited to a follow-up capacity. The large FoV and good sensitivity that MUSE affords is sufficient to perform “blind” spectroscopy. This avoids the need for preselection that would otherwise biased us against observing faint and unusual objects.

In this thesis we will use a combination of long-slit (Chapter 2) and IFS techniques (Chapters 3–5) to spatially resolve the gas-phase metallicity of low redshift ( $z \sim 0.025$ ) and intermediate redshift galaxies ( $0.1 \lesssim z \lesssim 1$ ), respectively.

## 4 This thesis

**Chapter 2** Using long-slit spectra we study the metallicity profiles of 50 galaxies ( $z \sim 0.025$ ). These galaxies were selected to have similar stellar masses ( $10.2 \lesssim \log_{10}(M_*/M_\odot) \lesssim 11.0$ ), but span a range of gas masses. This allows us to compare H I-rich galaxies to a control sample of H I-“normal” galaxies.

In previous work by Moran et al. (2012) it was found that in H I-rich galaxies the gas-phase metallicity profile steepens at large radii. They suggested this as evidence for the gas-rich galaxies having recently acquired excess gas that resides at the outermost radii. Our results, however, do not support their conclusions. While we do find galaxies with metallicity profiles steeper in the outer disc than the inner disc, we do not find the same dependency with H I-mass fraction ( $M(\text{H I})/M_*$ ). Outer metallicity drops occur in both H I-rich and H I-normal galaxies. However, even though we do not find these metallicity drops to be correlated with the global (total) gas fraction of the galaxy, we suggest that presence of the metallicity drops are consistent with the local (resolved) gas fraction. Using a simple analytical chemical evolution model we are able to account for the variety of metallicity profiles we observe. This provides a simple interpretation that the metallicity drops occur where the galaxy transitions from a stellar

dominated inner disc, to a gas dominated outer disc. As an important distinction from the work of Moran et al. (2012), this does not necessarily require the gas in the outer disc to have been recently deposited.

Intriguingly the success of the analytical model implies that the metallicity in these galaxies is in dynamic equilibrium with the local conditions. And by extension star-formation is regulated at the local level.

**Chapter 3** While in Chapter 2 we studied relatively nearby galaxies that could be well resolved, in the later Chapters we will study more distant, poorly resolved galaxies.

Resolution loss, which is primarily due to atmospheric seeing, can cause one to observe galaxy metallicity gradients that are much flatter than in reality (Yuan et al. 2013). In order to measure the true metallicity gradients in distant galaxies, it is critical to correct for seeing and other resolution loss effects. This chapter is devoted to developing and testing a method for deriving the intrinsic metallicity profiles from poorly resolved integral-field spectrographic observations. The method we present offers some benefits over existing approaches. These previous methods measure the raw metallicity gradient from the data, and then apply a seeing-dependent correction factor to obtain the true metallicity gradient. In contrast we forward model the effects of seeing and fit our model to the observed emission-line fluxes. By doing so we are not dependent on using a specific set of emission-lines. And as a result our method is independent of both the galaxy's redshift, and the wavelength coverage of spectrograph used.

We validate our approach using a series of mock observations. The most critical tests are performed using downgraded observations of real galaxies. We find one galaxy where our method fails to derive the correct metallicity profile. This galaxy does not have a well defined metallicity gradient, containing bright low-metallicity clumps. A key model assumption of ours is that there exists a single metallicity gradient that describes the galaxy. But if galaxies do not conform to this our model can fail and we may derive spurious metallicity gradients. We caution that the underlying reason for this failure is not specific to our model and could influence any comparison of metallicity gradients between low and high redshift observations.

**Chapter 4** We apply the method developed in Chapter 3 to MUSE observations of 94 intermediate redshift galaxies ( $0.08 < z < 0.84$ ). We identify a range of metallicity gradients in these galaxies. Most galaxies have negative metallicity gradients, but a few galaxies have positive metallicity gradients (with the metallicity in the centre of the galaxy lower than in the outskirts).

It had been suggested by previous studies that the metallicity gradient of a galaxy correlates with its mass and star-formation rate (Stott et al. 2014; Wuyts et al. 2016). However, our results do not support this.

Instead we suggest a dependency between the metallicity gradient and the size of the galaxy. We note that the large galaxies ( $r_d > 3$  kpc) typically present negative metallicity gradients, with minimal scatter. Whereas the small galaxies ( $r_d < 3$  kpc) span a large range of metallicity gradients (both negative and positive). Galaxies in the Universe today are generally found to have a common negative metallicity gradient. Because of their similarity to low-redshift galaxies, we suggest that the large galaxies in our sample are an emergent population of well-evolved galaxies, where inside-out growth dominates their metallicity profile.

**Chapter 5** Using a subsample of the galaxies presented in Chapter 4 we study the relationship between stellar mass, central metallicity and metallicity gradient.

At low redshift ( $z \lesssim 0.1$ ) it has been established that there exists a correlation between a galaxy's mass and its central metallicity (Tremonti et al. 2004; Foster et al. 2012). We observe a similar trend with our intermediate redshift galaxies, but there appears to be more scatter in our data. However, we note that this scatter can be explained by the metallicity gradient. We find at fixed mass the central metallicity is anti-correlated with the metallicity gradient.

This result is consistent with the idea that centrally concentrated inflow and outflow events may lower the central metallicity of a galaxy, flattening/inverting the metallicity gradient. Because inflows and outflows may have different effects on the outer discs of galaxies, we suggest that by studying the mass, central metallicity and metallicity gradients of galaxies all in conjunction one may be able to break the degeneracy between inflows and outflows.

## 4.1 Outlook

In astronomy today there is a drive towards obtaining larger samples and more complex datasets. With Chapter 2 we demonstrate that one does not need large samples or the latest instrumentation to produce valuable science. That said, in the coming years integral-field spectroscopy will play an ever increasing role in the study of galaxy evolution. As a particular example, metallicity studies today primarily discuss the radial metallicity profiles of galaxies entirely ignoring any azimuthal dependence. With integral-field spectroscopy it is now possible to study the latter.

However, in general with bigger data comes greater responsibility. We will need to develop more sophisticated analysis techniques to fully exploit potential of the data. Take for example, the method we present in Chapter 3, which can fail for galaxies with irregular metallicity profiles. The robustness of the method could be improved with a partially or fully non-parametric model. We consider the model presented in Chapter 3 to be a first step for the forward-modelling of metallicity gradients in galaxies, but certainly not the last word.

## Bibliography

- Bacon R., et al., 2010, in *Ground-based and Airborne Instrumentation for Astronomy III*. p. 773508, doi:10.1117/12.856027
- Barton E. J., Geller M. J., Kenyon S. J., 2000, *ApJ*, 530, 660
- Broeils A. H., Rhee M.-H., 1997, *A&A*, 324, 877
- Davé R., Finlator K., Oppenheimer B. D., 2012, *MNRAS*, 421, 98
- Dib S., Bell E., Burkert A., 2006, *ApJ*, 638, 797
- Foster C., et al., 2012, *A&A*, 547, A79
- Guo K., Zheng X. Z., Fu H., 2013, *ApJ*, 778, 23
- Izotov Y. I., Stasińska G., Meynet G., Guseva N. G., Thuan T. X., 2006, *A&A*, 448, 955
- Larson R. B., 1976, *MNRAS*, 176, 31
- Lilly S. J., Carollo C. M., Pipino A., Renzini A., Peng Y., 2013, *ApJ*, 772, 119
- Moran S. M., et al., 2012, *ApJ*, 745, 66
- Noeske K. G., et al., 2007, *ApJ*, 660, L43
- Pérez-Montero E., 2014, *MNRAS*, 441, 2663
- Prantzos N., Boissier S., 2000, *MNRAS*, 313, 338
- Sánchez-Blázquez P., et al., 2014, *A&A*, 570, A6
- Shirazi M., Brinchmann J., Rahmati A., 2014, *ApJ*, 787, 120
- Silk J., 1997, *ApJ*, 481, 703
- Stott J. P., et al., 2014, *MNRAS*, 443, 2695
- Tacconi L. J., et al., 2013, *ApJ*, 768, 74
- Tremonti C. A., et al., 2004, *ApJ*, 613, 898
- Whitaker K. E., van Dokkum P. G., Brammer G., Franx M., 2012, *ApJ*, 754, L29
- Wiersma R. P. C., Schaye J., Smith B. D., 2009, *MNRAS*, 393, 99
- Wuyts E., et al., 2016, *ApJ*, 827, 74
- Yuan T.-T., Kewley L. J., Rich J., 2013, *ApJ*, 767, 106



# 2

---

## *Gas-phase metallicity profiles of the Bluedisk galaxies: Is metallicity in a local star-formation regulated equilibrium?*

---

As part of the Bluedisk survey we analyse the radial gas-phase metallicity profiles of 50 late-type galaxies. We compare the metallicity profiles of a sample of H I-rich galaxies against a control sample of H I-‘normal’ galaxies. We find the metallicity gradient of a galaxy to be strongly correlated with its H I mass fraction ( $M(\text{H I})/M_*$ ). We note that some galaxies exhibit a steeper metallicity profile in the outer disc than in the inner disc. These galaxies are found in both the H I-rich and control samples. This contradicts a previous indication that these outer drops are exclusive to H I-rich galaxies. These effects are not driven by bars, although we do find some indication that barred galaxies have flatter metallicity profiles. By applying a simple analytical model we are able to account for the variety of metallicity profiles that the two samples present. The success of this model implies that the metallicity in these isolated galaxies may be in a local equilibrium, regulated by star formation. This insight could provide an explanation of the observed local mass-metallicity relation.

David Carton, Jarle Brinchmann, Jing Wang, Frank Bigiel, Diane Cormier, Thijs van der Hulst,  
Gyula I. G. Józsa, Paolo Serra, Marc A. W. Verheijen

2015, *MNRAS*, 451, 210

# 1 Introduction

Galaxy formation has been much studied over the past decades, but despite significant successes in this endeavour, it remains unclear exactly how disc galaxies evolve at late times. A particular stumbling block has been determining exactly through which processes a galaxy acquires its cold gas. One of the current leading scenarios is the accretion of gas into the galaxy halo. This halo gas subsequently cools to form a gas disc, from which stars will form (White & Rees 1978; Fall & Efstathiou 1980; Mo et al. 1998). It is predicted that the angular momentum of the accreting gas will grow over time. The angular momentum of the gas disc will therefore also increase, and thus gas cooling from this will settle at increasing radii. This paradigm is commonly referred to as “inside-out” growth (Pichon et al. 2011; Stewart et al. 2013).

The study of the formation and evolution of disc galaxies is complicated by the complex nature of star formation and the cycle of gas within the interstellar medium of galaxies. Nevertheless, with three fundamental observables, namely stellar mass, gas-phase metallicity<sup>1</sup> and the star-formation rate (SFR), we can begin to unravel the life of galaxies. The gas-phase metallicity, herein simply referred to as metallicity, is of particular interest since it is not simply a result of star formation integrated through time, but it is also strongly affected by gas flows into and out from the galaxy. With the advent of large spectroscopic fibre surveys, such as the Sloan Digital Sky Survey (SDSS) (York et al. 2000) and Galaxy And Mass Assembly project (GAMA) (Driver et al. 2011), a host of studies have explored the relationships between these three aforementioned parameters. Of particular interest is the mass-metallicity relation (Tremonti et al. 2004; Foster et al. 2012), which shows the most massive galaxies to be also the most metal rich. This correlation is commonly attributed to either a downsizing scenario, whereby the most massive galaxies are more efficiently forming stars, or alternatively that galactic-scale winds are more effective at expelling metals from lower mass galaxies. For a more in depth discussion of these and other mechanisms we refer the reader to Ellison et al. (2008).

More recently studies have reported a secondary correlation of the mass-metallicity relation with the SFR, forming the so-called fundamental metallicity relation (FMR) (Mannucci et al. 2010). The FMR presents an anti-correlation of metallicity with the SFR, which has been attributed to either inflows that dilute metallicity and/or outflows that remove metals. We hasten to point out, however, that the FMR is not without contest, with some debate over its origin or existence (Wuyts et al. 2014; Sánchez et al. 2013).

While we may have copious measurements for the central metallicities of galaxies, comparatively less well studied are radial trends of metallicity in galaxies. Early on the picture emerged that at late times ( $z \lesssim 0.1$ ) disc galaxies all show negative (declining radially outwards) metallicity gradients, and when expressed in terms of optical scale radii they showed remarkably similar gradients (Vila-Costas & Edmunds 1992; Zaritsky et al. 1994). Recently Ho et al. (2015) have shown that this common metallicity gradient can be explained by the coevolution of gas, metals and stars.

The common metallicity gradient, however, only applies to isolated galaxies. In a study of interacting systems, Rich et al. (2012) showed a clear tendency towards flatter metallicity gradients, which for the early stages of interaction is consistent with simulations (Rupke et al. 2010; Torrey et al. 2012).

Despite this work it is only recently that metallicity gradients have been systematically determined for large samples of galaxies (Moran et al. 2012; Sánchez et al. 2013). With the good statistics these studies provided, these authors have shown the existence of a correlation between stellar-mass density and metallicity. This correlation is commonly referred to the local

---

<sup>1</sup>By gas-phase metallicity we refer to the oxygen abundance ( $12 + \log_{10}(\text{O}/\text{H})$ ) of the interstellar medium (ISM).

mass-metallicity relation and, as with its global counterpart, its origin is unclear.

In the work of [Moran et al. \(2012\)](#), whose galaxies formed part of the GALEX Arecibo SDSS Survey (GASS) ([Catinella et al. 2010](#)), they attempt to connect metallicity to the atomic gas (H I) content of galaxies. They show tentative hints that the most H I-rich galaxies exhibit sudden drops in metallicity in their outer discs. It is these hints that provided impetus for the work we present here.

In this paper we present resolved metallicity profiles for all 50 low redshift ( $z \sim 0.025$ ) galaxies that form the Bluedisk survey ([Wang et al. 2013](#), herein W13). The resolved H I maps are the cornerstone of Bluedisk project, providing both the structure and kinematics of the atomic gas disc. The goal of the Bluedisk project is to study in detail two classes of galaxies: an ‘‘H I-rich’’ sample, consisting of those galaxies with stellar masses above  $10^{10} M_{\odot}$  and with excess atomic gas, and for comparison a ‘‘control’’ sample consisting of galaxies of similar stellar mass, whose H I content is normal or mildly poor.

We structure this paper as follows: in Section 2 we outline the existing data of the Bluedisk galaxies. In Section 3 we describe our observations and discuss our data-reduction process. In Section 4 we detail our spectral fitting procedures, discuss the global properties of our galaxy population. We also explain our method for determination of metallicity, among other quantities. In Section 5 we present our results, focusing on the resolved metallicity of the Bluedisk galaxies. We use Section 6 to develop and apply a simple a model to explain the radial metallicity profiles in terms of their gas and stellar mass contents. Finally, we provide our concluding remarks in 7. Throughout this paper we assume a cosmology with  $H_0 = 70 \text{ km s}^{-1} \text{ Mpc}^{-1}$ ,  $\Omega_m = 0.3$  and  $\Omega_{\Lambda} = 0.7$ .

## 2 Data

Measurements of the H I content of the Bluedisk galaxies have been obtained using the Westerbork Synthesis Radio Telescope (WSRT) with observations for 49 out of the sample of 50 galaxies, including one non-detection. SDSS images have been analysed to provide optical properties of the galaxies. A full description of the analysis is available in [W13](#). We will make use of this data in the context of our new optical spectroscopic data.

### 2.1 Bluedisk galaxy classification

A key aspect of the Bluedisk strategy is the classification of galaxies into two well-matched H I-rich and control samples. As uncovered by [Catinella et al. \(2010\)](#) there exists a scaling relation between the H I mass fraction ( $f_{\text{HI}} = M_{\text{HI}}/M_*$ ), the stellar mass surface density and the observed NUV –  $r$  color. Using the difference between the observed and expected H I mass fractions, we can bisect the Bluedisk population into H I-rich and control samples. We require the samples to contain only isolated galaxies, thus an additional category of non-isolated galaxies has been formed, namely the ‘‘excluded’’ sample. All three samples are described at length in [W13](#). We make, however, one minor modification to the classifications listed therein, such that in this paper we consider that BD 39, formerly part of the control sample, to now be a member of the excluded sample. Our motivation for this being that we have identified potentially a small neighbouring galaxy at the same redshift. As a result, this leaves 23 H I-rich galaxies and 18 control galaxies, which we will focus our attention on.

## 2.2 Bulge-Disc-Bar decomposition

We determine the inclination of the stellar disc using SDSS  $r$  band images. With these images we also perform a bulge-disc-bar decomposition, enabling use to measure a bulge-to-total ratio for each galaxy.

Our procedure for bulge-disc-bar decomposition mostly follows that of [Weinzirl et al. \(2009\)](#). The steps are as follows:

- (i) We use the SExtractor software ([Bertin & Arnouts 1996](#)) to measure the position, ellipticity ( $e$ ) and position angle (PA) for each galaxy. We also make mask images that flag all neighbouring sources using the segmentation map produced by SExtractor. These masks are used in all the following isophote and model fitting steps.
- (ii) Using the photometric measurements as an initial guess, we perform isophote ellipse fitting on the images, and obtain surface density, PA and  $e$  profiles for the galaxies. With the surface density profile, we accurately measure the background surface density of the images. The shape (size, PA and  $e$ ) of the outermost isophote is viewed as the shape of the galactic disc. See [Wang et al. \(2012\)](#) for further details of this step.
- (iii) We use the GALFIT package ([Peng et al. 2002](#)) to fit models of the bulge, disc and bar to the galaxies. We use exponential models to represent the discs, and use Sérsic models to represent bulges and bars. The Sérsic index is allowed to vary within 1.2 to 6 for bulge models and vary within 0.3 to 0.9 for bar models. These are typical values reported in [Gadotti & Kauffmann \(2009\)](#). We first fit a single bulge model, followed by a bulge+disc model and finally bulge+disc+bar model. The model obtained from each fitting step is used as initial guess for the following fitting step. When fitting discs and bars, the size, PA and  $e$  measurements from step 1 are used as initial guess. During the fitting, the PA of bars and discs and are allowed to vary in a very small range ( $\pm 20^\circ$ ). The  $e$  of the disc is fixed, and the  $e$  of bar is required to be smaller than the  $e$  of disc. So in the end, we have 3 types of models (bulge, bulge+disc and bulge+disc+bar) for each galaxy. We choose the model with the minimum value of reduced  $\chi^2$  calculated from the residual map as the best model.

## 2.3 Stellar mass densities

To derive spatial resolved maps of the stellar mass density,  $\Sigma_*$ , we use SDSS  $ugriz$  photometry.

We fit the five-band SDSS photometry using the composite stellar population synthesis (SPS) models of BC03, applying the procedure described in [Kauffmann et al. \(2003a\)](#) and [Gallazzi et al. \(2005\)](#). The SPS models combine an underlying exponentially declining star formation history with random bursts of star formation superposed on this. The modelling includes a dust component. The flux from young stars ( $< 10$  Myr) is attenuated following a dust attenuation curve of the form  $\tau(\lambda) \propto \lambda^{-1.3}$ . Whereas, the flux from long-lived stars ( $> 10$  Myr) is attenuated by a  $\tau(\lambda) \propto \lambda^{-0.7}$  power law. The library is described in more detail in [Gallazzi et al. \(2005\)](#). From the results of this SPS fitting we obtain a posterior distribution on  $\Sigma_*$ .

To perform this SPS modelling we require a good S/N across the images. We achieve this by using the weighted Voronoi tessellation method of [Diehl & Statler \(2006\)](#), a generalization of the algorithm by [Cappellari & Copin \(2003\)](#). We define our measure of S/N from that of the  $u - z$  colour maps (the  $u - z$  combination typically offering the poorest S/N). Adopting a threshold  $S/N = 5$  we therefore ensure a good S/N in all colour maps. As the SDSS images contain foreground objects we mask these objects manually, along with any other spurious features.

### 3 Observations

Optical long-slit spectroscopic observations of all 50 Bluedisk galaxies were performed in January and May 2013 using the Intermediate dispersion Spectrograph and Imaging System (ISIS) on the 4.2 m William Herschel Telescope (WHT), in a variety of seeing conditions (0.7–1.7 arcsec FWHM). The ISIS spectrograph was operated in a dual arm mode using the standard 5300 Å dichroic, with the GG495 blocking filter in the red arm. Employing the R600B and R600R gratings in the blue and red arms respectively, a discontinuous spectral coverage of 3700–5300, 5750–7200 Å was provided, with a spectral resolution of  $\sim 1.7$  Å FWHM constant across all wavelengths. Each target was observed with a minimum of  $3 \times 1200$  s exposures. A slit width of 3 arcsec was used for all observations presented here, optimizing emission line signal-to-noise (S/N) at the expense of spectral resolution.

Each spectroscopic slit was positioned to coincide with the centre of the galaxy, as defined by the SDSS photometric catalogue. The orientation of the spectroscopic slit was aligned to the kinematic major axis determined from the WSRT velocity moment maps. Where this angle was close to that of a clear natural axis of the galaxy, the slit was more precisely aligned with this optical feature. A final design requirement was to ensure a region observed by a 3 arcsec fibre in the SDSS spectroscopic catalogue was included in the slit, which for all but one target (BD 31), was at the galaxy centre. Overall, the general result was such that the slits were aligned with the optical major axis.

Standard bias frames were obtained for each night, in addition to lamp flat and twilight sky flat exposures. After each target pointing, additional spectroscopic calibration images were obtained, which comprised Cu-Ar+Cu-Ne arc-lamp exposures, as well as an observation of a standard star. The standard stars were selected from the ING spectrophotometric catalogue<sup>2</sup> and were observed at a similar airmass to the targeted galaxy. Finally, for characterization of the charge-coupled devices (CCDs), a set of dark frames were also gathered.

#### 3.1 Reduction

Standard PYRAF tasks were used to calculate the CCD bias offsets, pixel gain variations and telescope vignetting effects. With the IMCOMBINE task cosmic-ray rejection was performed using a mean image combine and a  $+3\sigma$  rejection. Bad-pixel masks were constructed manually, based upon the dark and lamp-flat frames. Wavelength calibration was performed using a custom routine, which fitted the arc-lamp spectra at multiple points along the spatial axis. With the use a 2D-spline interpolation, the corresponding wavelength of every pixel was identified. Subsequent sky subtraction was carried out using blank regions in slit.

The dispersion axis of the spectrograph was not perfectly aligned with the CCD axes, this rotation, while small, induced a small ( $\lesssim 4$  arcsec) shift in spatial position in the spatial CCD coordinates between the wavelength extrema. To remove this effect the centre of the target was traced by binning the spectrum in numerous wavelength bins, and fitting a symmetric profile to the spatial intensity distribution in each bin. Sérsic and Gaussian profiles were assumed for galaxy and standard star targets, respectively. A linear fit to this produced a mapping of wavelength to object centre, from which a rectified 2D spectrum was created.

Flux calibration was performed in a two-step procedure. Firstly an absolute flux calibration by comparing the response of the standard star against the reference spectrum. This was refined by extracting a spectrum from a 3 arcsec square effective aperture matched to the equivalent position of the SDSS fibre spectrum (3 arcsec diameter). We additionally applied

<sup>2</sup><http://catsserver.ing.iac.es/landscape/tn065-100/workflux.php>

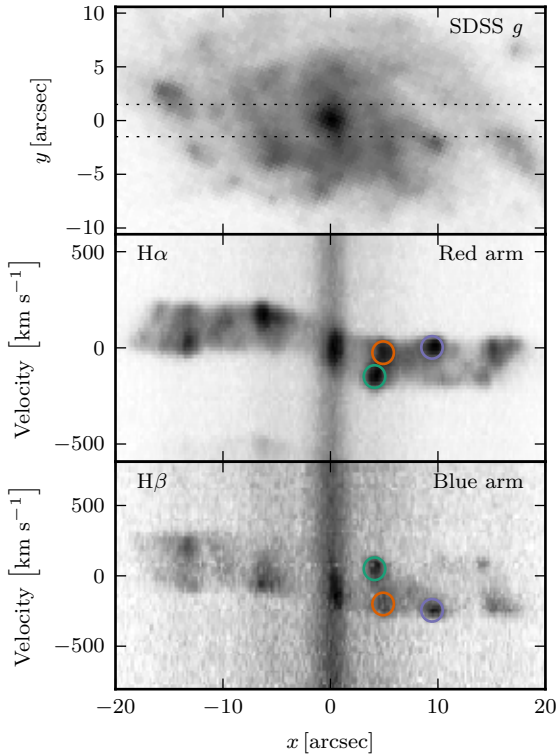


Figure 2.1: Illustration the “contrary offset” effect of the ISIS instrument, due to the opposite alignment of the dispersion axes of the red and blue spectral arms. (Top) SDSS  $g$  band image of BD 20 with 3 arcsec wide slit indicated by the dotted horizontal lines. (Centre Bottom) Corresponding 2D spectra centred about the  $H\alpha$  and  $H\beta$  emission line features of the red and blue arms. While the overall velocity curve is preserved, the vertical position in the slit, i.e. in the  $y$ -direction, of emitting region is convolved with the velocity information. The coloured circles highlight emission line clumps where this contrary spatial convolution effect is clearly seen.

a telluric correction by measuring the transmission of the standard star, adopting a linear pseudo-continuum across the affected spectral regions.

On inspection of the data, spectral information was significantly convolved with the spatial profile of the slit, this is an expected consequence of using a spectroscopic slit wider than the seeing disc. For clumpy emission-line regions, asymmetric line profiles will be produced and as a result, erroneous velocities will be inferred. Worthy of note is the optical design of the ISIS instrument, which has the dispersion axes in opposite directions for the red and blue arms. This results in “contrary offsets” in the two arms, as shown in Fig. 2.1. We must properly account for these in our analysis.

## 4 Analysis

A standard approach to emission line modelling is to assume the lines can each be approximated by a single Gaussian function all with the same velocity offset and dispersion. We preform this spectral fitting using the SDSS PLATEFIT spectral fitting routine (Tremonti et al. 2004; Brinchmann et al. 2004), which first fits a continuum to the spectrum with the emission-line features masked, before fitting a sum of Gaussian functions to the residual spectrum. The velocity offsets of the continuum and emission-line components are not tied together. The velocity of the emission-line component may vary up to  $\pm 500 \text{ km s}^{-1}$  from that of the continuum component. The initial continuum fitting was performed using stellar population synthesis templates from Bruzual & Charlot (2003, hererin BC03), with a fixed velocity offset given by the SDSS redshift. We therefore update with the velocity determined from the emission line

fitting, and again recompute both continuum and line fitting steps. Due to the discontinuous wavelength coverage and the relatively low spectral resolution, the velocity dispersion of the stellar continuum is difficult to determine, we therefore adopt the velocity dispersion calculated from the SDSS fibre spectrum. Typical values being twice that of the effect the spectral resolution at 5500 Å. We assume that the stellar velocity dispersion is constant across the whole galaxy, whilst this is not ideal we note that it produces a visibly acceptable result, see Fig. 2.2. Errors on measured line fluxes are determined by the Levenberg-Marquardt least-squares fitting, however, these formal errors are often an underestimate of the real errors of the line fluxes. Following a procedure derived from SDSS duplicate observations, as discussed by Brinchmann et al. (2013, herein B13), we can translate our formal uncertainties to more representative values. As a result of the aforementioned contrary offsets in the red and blue arms we modify the standard Gaussian fitting by tying the velocity offsets of the blue and red instrument arms separately.

Spatially binning the 2D spectrum is necessary to optimally extract emission line fluxes. In order to avoid the line broadening effects caused by co-adding spectra with different velocity offsets, we adopt a similar approach to Moran et al. (2010), whereby a two-stage binning strategy is applied. Firstly we adopt a simple binning process, working from the centre of the galaxy outwards, accreting spectra until a minimum continuum S/N of  $6 \text{ \AA}^{-1}$  is reached. If a bin spans more than 10 arcsec before this threshold is reached, then the binning is terminated. Using the spectral fitting routine, we extract the velocity of the emission lines in the red-arm, where H $\alpha$  is dominant. To this velocity we fit the rotation curve using the following parametrization of Böhm et al. (2004)

$$V(r) = V_{\max} \frac{r}{(r^a + r_0^a)^{1/a}} + V_0, \quad (2.1)$$

where  $r$  is the radius,  $V_{\max}$  is the maximum velocity at  $r \gg r_0$ ,  $V_0$  is a constant offset velocity,  $a$  and  $r_0$  control the shape of the profile. By using a model we can interpolate the rotation velocity at any position along the spectroscopic slit in a numerically stable fashion. Weighting the velocity measurements by H $\alpha$  S/N, this model provides a reasonable approximation to the true rotation curve, within the limitations imposed by clumpy emission smaller than the slit. Using this velocity fit, the 2D spectrum was shifted to a common rest frame.

Since we are interested in the emission line properties it is ideal to bin spectra on emission line criteria, as opposed to the stellar continuum criteria used previously. Therefore the best-fit model continuum is first subtracted from the rest-frame shifted spectra, before we apply a custom binning algorithm. Due to the clumpy nature of the emission, any binning algorithm must account for this. With this in mind, we apply a moving boxcar bin to the unbinned spectra, working from the galaxy centre outwards. On each subsequent pass the boxcar is incrementally increased in size. The S/N of each each boxcar bin is determined from a least-squares fit of a Gaussian function to the H $\alpha$  line, where a successful bin is when S/N in H $\alpha$  exceeds 6. After the boxcar binning is completed, any remaining unbinned spectra are accreted into the nearest bins, provided their contribution boosts the S/N. To reduce the statistical dependency between neighbouring bins we impose a minimum bin size of  $\sim 1.6$  arcsec, roughly equal to that of the worst FWHM seeing of our observations. The bin centre is defined by the H $\alpha$ -weighted contribution of each 1D spectrum to its respective bin. As the spectroscopic slits were not necessarily aligned with the measured semi-major axes of the galaxies, we additionally deproject these radii, assuming a thin disc and adopting the inclinations and position angles of the galaxies, as derived in Section 2.2.

With the new binning, we apply again our full spectral fitting procedure to the rest-frame shifted spectra. All results in the following are derived from the resulting outputs.

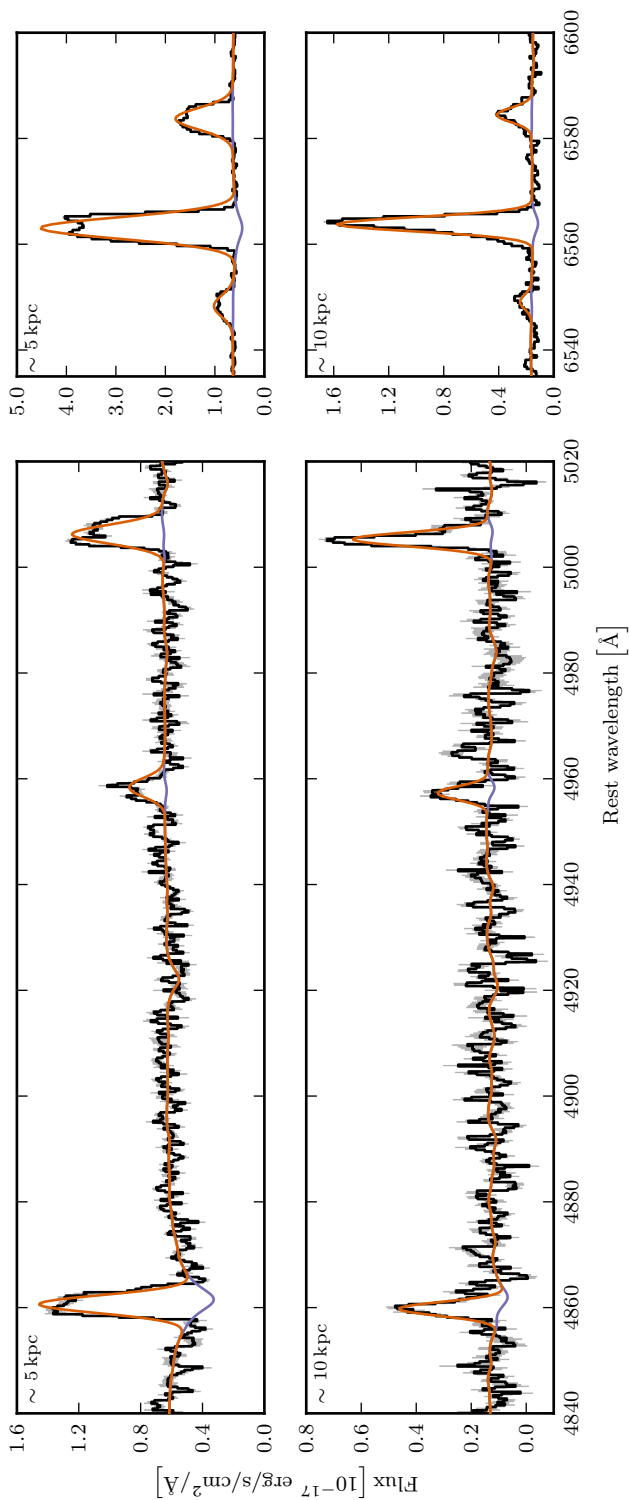


Figure 2.2: Example of PLATEFIT spectral fitting to emission lines for galaxy BD 5, shown at two radii,  $\sim 5$  kpc (top) and  $\sim 10$  kpc (bottom). Observed spectrum and its error indicated by black line and shaded area, respectively. The best-fitting model solution is shown in orange, the continuum component is shown in blue. (Left) Spectra from blue arm covering region containing  $H\beta$ ,  $[O\ III]4959$  and  $[O\ III]5007$  lines. (Right) Spectra from red arm covering region containing  $[N\ II]6548$ ,  $H\alpha$  and  $[N\ II]6584$  lines.

## 4.1 Bluedisk SDSS properties

In Fig. 2.3 we compare the central metallicities, central SFRs and total stellar masses of the Bluedisk sample to other galaxies drawn from the 7<sup>th</sup> data release (DR7) of the SDSS. We discuss the estimation of metallicity in Section 4.3 below, here it suffices to say that the same estimator has been used for SDSS and the Bluedisk spectra. The Bluedisk sample lies on the same mass-metallicity relation and mass-SFR relation of the DR7 population at a similar redshift. The galaxies have noticeably elevated metallicities with respect to their counterparts of similar SFRs, however, this is to be expected since they are amongst the most massive  $\sim 10\%$  of galaxies at their epoch. When observed as a function of SFR, a clear split is observed between the H I-rich and control populations, with H I-rich galaxies more actively forming stars at their centres. While not an explicit selection criteria of the survey, the two populations do not differ significantly in central metallicity.

## 4.2 Contamination from non-star-forming sources

To avoid deriving erroneous metallicities, we must take care to exclude spectra contaminated by significant line emission from active galactic nuclei (AGN) or low-ionization nuclear emission-line regions (LINERs).

Following the prescription of Brinchmann et al. (2004) we classify the spectra into five categories. Namely star-forming (SF), AGN/LINER, “composite” SF + AGN/LINER, low S/N AGN/LINER and low S/N SF. For this we use the diagnostic criteria of Kauffmann et al. (2003b) and Kewley et al. (2001), applied to the  $([\text{O III}]\lambda 5007/\text{H}\beta)$ , and  $([\text{N II}]\lambda 6584/\text{H}\alpha)$  emission-line ratios. However, we find the Kauffmann et al. (2003b) division between SF and composite emission is too aggressive, resulting in the rejection of data points at large radii. Following Moran et al. (2012), we therefore loosen our criteria by offsetting this diagnostic line diagnostic  $+0.1$  dex in both  $[\text{O III}]/\text{H}\beta$  and  $[\text{N II}]/\text{H}\alpha$  line ratios. Fig. 2.4 shows the Baldwin, Phillips & Terlevich (1981) (BPT) diagnostic diagram for the co-added spectra. From this we can see that almost all excluded data points are found in the inner regions of the galaxies where we could expect contamination by AGN and shock heated gas.

We ultimately apply an  $\text{H}\alpha$  S/N  $\geq 10$  cut to our data. Although we do not apply a equivalent width (EW) cut, we note that 96% of our spectral bins have  $\text{EW}(\text{H}\alpha) > 3$ . This EW limit was recommended by Cid Fernandes et al. (2011) to identify pure star-forming galaxies, where  $\text{H}\alpha$  emission is associated with H II regions rather than post-asymptotic giant branch stars.

## 4.3 Inferring Metallicities

We derive gas-phase metallicities using the method developed by B13. This method applies a Bayesian framework to a grid of photoionization models. We shall pair the B13 methodology with the photoionization models of Charlot & Longhetti (2001, herein CL01). To correct for dust, the B13 procedure uses a two-component dust-absorption model of Charlot & Fall (2000), with a wavelength dependant attenuation curve of the form  $\tau(\lambda) \propto \lambda^{-1.3}$ . For a set of emission-line fluxes<sup>3</sup>, we obtain a posterior probability distribution on the metallicity. However, to test our CL01 derived metallicities we will now outline a series of other metallicity determination methods.

A common set of methods for inferring metallicities is to use line-ratio diagnostics that have directly calibrated to oxygen abundances of H II regions (either theoretical or observed). We use two such methods, one using the theoretically derived relations of Kobulnicky & Kewley

<sup>3</sup>The B13 analysis was performed using emission lines:  $[\text{O II}]\lambda 3727$ ,  $\text{H}\delta$ ,  $\text{H}\gamma$ ,  $\text{H}\beta$ ,  $[\text{O III}]\lambda 4959$ ,  $[\text{O III}]\lambda 5007$ ,  $\text{H}\alpha$ ,  $[\text{N II}]\lambda 6584$ ,  $[\text{S II}]\lambda 6716$  and  $[\text{S II}]\lambda 6731$ .

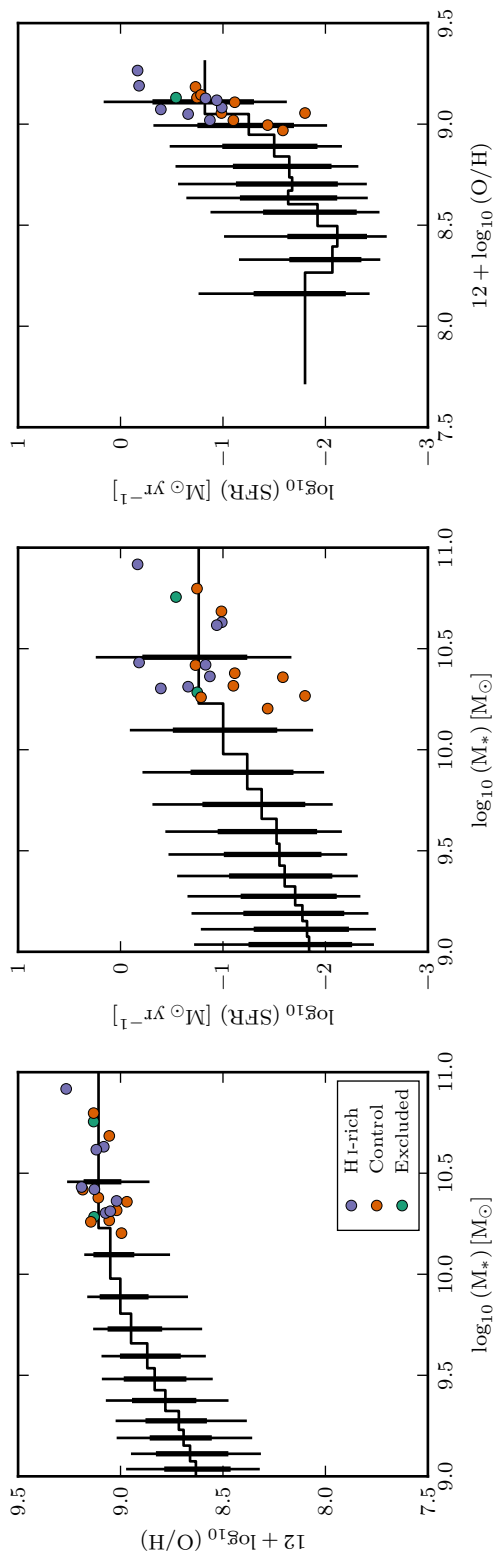


Figure 2.3: Comparison of Bluedisk galaxy properties with the whole SDSS DR7 population that has all three quantities determined (total galaxy stellar mass, fibre SFR, and gas-phase metallicity). The SDSS DR7 sample is selected to span a similar redshift range as the Bluedisk sample ( $0.02 \leq z \leq 0.03$ ). In each plot, crosses indicate SDSS measurements of the Bluedisk H I-rich, control and excluded samples. In each plot a stepped-curve represents the median ordinate value of given abscissal bin. (Left & Middle) Sample divided by mass into vigintile bins and (Right) Sample divided by SFR into decile bins. Thick and thin vertical lines represent the 68% ( $1\sigma$ ) and 95% ( $2\sigma$ ) ranges respectively.

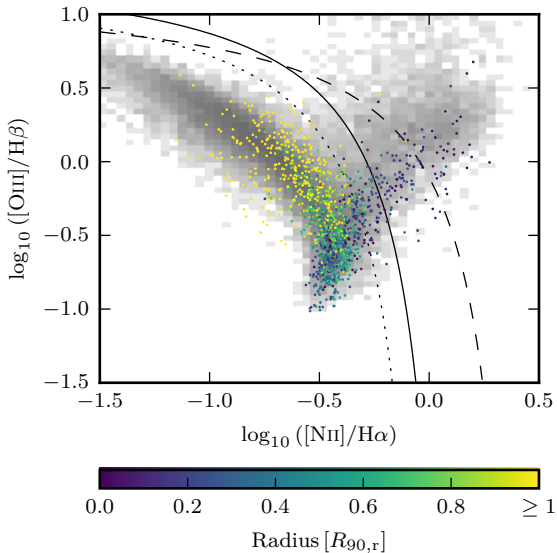


Figure 2.4: The BPT diagnostic diagram for all binned galaxy data points with  $H\alpha$   $S/N \geq 10$  and  $S/N \geq 3$  in the other three emission lines. Colours indicate radius from galaxy centre in units of  $R_{90,r}$ , the radius containing 90% of the SDSS  $r$  band luminosity. Shaded underlay shows BPT histogram of SDSS DR7 fibres in the same redshift range ( $0.02 \leq z \leq 0.03$ ). The dashed line indicates the division between pure AGN and “composite” galaxies (Kewley et al. 2001). The dotted line represents the nominal Kauffmann et al. (2003b) SF diagnostic line, but for our classification we use a modified form of this offset +0.1 dex in both axes (solid line).

(2004, herein KK04), and another method using the empirically derived relations of Pilyugin & Mattsson (2011) known as the NS calibrator. In addition we check the sensitivity of our CL01 metallicities to the choice of photoionization models, by applying the models of Dopita et al. (2013, herein D13) within the B13 framework. It should be noted that the B13 method is similar in principle to others such as IZI (Blanc et al. 2015) and HII-CHI-MISTRY (Pérez-Montero 2014).

Dust attenuation affects line ratios, therefore we must correct for dust before we apply the KK04 and NS calibrators. We adopt the same  $\tau(\lambda) \propto \lambda^{-1.3}$  attenuation curve and calculate its normalization by assuming an intrinsic  $H\alpha/H\beta$  Case-B ratio of 2.85 (temperature,  $T = 10^4$  K, and electron number density,  $n_e = 10^4 \text{ cm}^{-3}$ ) (Osterbrock & Ferland 2006, p. 78). We note, however, that by assuming such physical properties of the H II regions we must a priori assume a metallicity. With the B13 approach we avoid this assumption by simultaneously correcting for dust attenuation when inferring metallicity. Nevertheless, for spectra with high  $S/N$ , both the B13 and empirical Case-B approaches yield similar results for the strength of the attenuation.

Uncertainties on the metallicity determinations for the KK04 and NS methods are determined using Monte Carlo simulations. We assume the true line fluxes to be normally distributed about the measured line flux, with a standard deviation equal to the error in the measured value. Of these many realisations, we take the median as the metallicity value, and the symmetrized  $\pm 1 \sigma$  quantiles to be its associated error. For the CL01 and D13 models, we can extract the median and its error directly from the cumulative posterior probability of the metallicity parameter. Due to the finite sampling of the metallicity parameter in these models, we impose an additional minimum uncertainty of  $\pm 0.05$  dex (Brinchmann et al. 2004). We additionally apply the same minimum error to the KK04 and NS methods.

In Appendix A we compare the different metallicity methods. We show that the CL01 method produces results consistent with the other three methods. We adopt CL01 as our default method for metallicity determination. Herein for simplicity when we refer to metallicity, we are referring to that which is derived from the CL01 models.

Note that in contrast to some studies of abundance gradients our spatial bins include line emission from both H II regions and diffuse emission. Since previous studies have found

that the diffuse emission is powered by radiation escaping from H II regions (e.g. Hoopes & Walterbos 2003; Kim et al. 2013), we can approximately treat the combined line emission as coming from an H II region with larger volume and hence a lower ionization parameter. The CL01 models are well suited for this as they cover a range in ionization parameters. In addition, note that while the CL01 models are not specifically optimised for spatially resolved regions in galaxies, tests in B13 showed that the CL01 models perform well in this case.

#### 4.4 Estimating gas mass densities

To determine gas surface mass density at the same resolution as our metallicities, we estimate the gas surface mass densities directly from our spectra. In B13 it was shown that when most of the strong lines in the optical spectrum are available it is possible to use photoionization models with a flexible treatment of metal depletion to place constraints on the gas surface mass density of galaxies. The application shown in B13 used the CL01 models which we also use here. By jointly fitting the strong optical lines B13 showed that the total gas surface mass densities can be estimated through

$$\Sigma_{\text{gas}} = 0.2 \frac{\tau_V}{\xi Z} M_{\odot} \text{pc}^{-2}, \quad (2.2)$$

where  $\tau_V$  is the optical depth in the V-band,  $\xi$  the dust-to-metal ratio of the ionised gas, and  $Z$  the metallicity.

They compare the result of applying this relation to spectra from the SDSS to total mass densities measured from H I and H<sub>2</sub> mass maps from the THINGS (Walter et al. 2008) and HERACLES (Leroy et al. 2009) surveys. This point-by-point comparison showed that the spectroscopic method is in excellent agreement with the H I+H<sub>2</sub> mass maps, except at the very highest gas surface densities,  $\Sigma_{\text{gas}} > 75 M_{\odot} \text{pc}^{-2}$ .

For the present paper we note that we use the same set of emission lines used by B13 in their study with comparable signal-to-noise, so we expect this result to carry over to our study. This means that our spectroscopic gas densities are likely to be underestimated in the central regions of the galaxies. We expand on this and discuss this method more in Appendix B.

## 5 Results

### 5.1 The local mass-metallicity relation and radial mass profiles

From basic analytical arguments one expects the metallicity of a system to depend on the stellar and gas mass budgets (Pagel 1997). Indeed, recent works have uncovered a correlation between stellar-mass surface density and metallicity, known as the local mass-metallicity relation (Moran et al. 2012; Rosales-Ortega et al. 2012; Sánchez et al. 2013). However, it is worth noting Pilyugin et al. (2014) find that although local surface brightness and metallicity are correlated, there is no unique relation between the two that holds at all radii in galaxies. Nevertheless, we will now test whether the local mass-metallicity relation holds for the Bluedisk galaxies.

In Fig. 2.5 we present radial profiles of our spectroscopic dust-to-gas estimates of gas-mass surface densities,  $\Sigma_{\text{gas}}$ , as well as our stellar-mass surface densities,  $\Sigma_{*}$ , which are matched in aperture. The median trends for  $\Sigma_{*}$  exhibit clear differences between the H I-rich and control samples, with H I-rich being consistently less massive at a given scale radius. By contrast,  $\Sigma_{\text{gas}}$  shows no significant distinction between the samples. We caution that although there appears to be a slight upward trend in  $\Sigma_{\text{gas}}$  with radius, which may be artificial (see Section 4.4).

In Fig. 2.5 we also show the radial profiles of the gas-to-stellar mass ratio,  $r_{\text{gas}} = \Sigma_{\text{gas}}/\Sigma_*$ . Here we find that the H I-rich galaxies exhibit enhanced  $r_{\text{gas}}$  ratios at all but the very centre the stellar disk. We note that this is primarily driven by radial differences in  $\Sigma_*$  rather than  $\Sigma_{\text{gas}}$ . In other words, at a fixed  $\Sigma_*$  the H I-rich and control samples are indistinguishable in terms of  $r_{\text{gas}}$ .

In Fig. 2.6 we show the local mass-metallicity relation for the Bluedisk galaxies. We also plot the correlation between  $r_{\text{gas}}$  and metallicity. Crucially, neither of these correlations show any strong offsets between the H I-rich and control samples, implying that the processes that govern these parameters are similar in both classes of galaxies. We observe that the correlation of metallicity with  $r_{\text{gas}}$  is not visibly tighter than that with  $\Sigma_*$ . But, as exemplified in Fig. 2.6(c) we note that at the lowest stellar mass densities ( $\log_{10}(\Sigma_*) \lesssim 1.5 \text{ M}_{\odot} \text{ pc}^{-2}$ ) a significant portion of the metallicity variation can be explained by changes in  $\Sigma_{\text{gas}}$ . We must caution, however, that metallicity and  $\Sigma_{\text{gas}}$  are not independently derived. The nature of the modelling will introduce a small intrinsic correlation between these two parameters. The magnitude of this effect is not easily quantified.

Having shown that both H I-rich and control samples form a consistent local mass-metallicity relation, we shall explore the radial metallicity profiles of the Bluedisk galaxies.

## 5.2 Metallicity profiles of the Bluedisk galaxies

We present the metallicity profiles of the Bluedisk galaxies in Figs 2.7.<sup>4</sup> By visual inspection alone there is no clear distinction between H I-rich and control samples in terms of the profile shapes. The control sample does appear to be more radially truncated, however, this is to be expected. It has been shown by Wang et al. (2011) that H I mass fraction is correlated with the  $g - i$  colour gradient in galaxies. This implies that the H I-rich galaxies have higher rates of star formation in their outer discs. Therefore we expect the control sample to have less extended star formation, ultimately limiting the radius out to which we can robustly detect emission lines. For a more quantitative analysis we must study the measured gradients of the linear model.

As is common in the literature we approximate the metallicity profiles with a symmetric linear best fit. In most cases this simple functional form encapsulates the overall change in metallicity from the centre to the outskirts of the galaxy. In Fig. 2.8 we show the dependence of the metallicity gradient on both stellar mass and the H I mass fraction. There exists a significant correlation between H I mass fraction and metallicity gradient. Galaxies with larger H I mass fractions typically have steeper metallicity gradients. Whereas we find no significant correlation between stellar mass and metallicity gradient. However, this is unsurprising given the narrow range that we span ( $10.2 \lesssim \log_{10}(M_*/M_{\odot}) \lesssim 11.0$ ). We note these results remain unchanged when we adopt a different scale radius,  $R_{25g}$  (the radius at which the SDSS  $g$  band surface brightness reaches  $25 \text{ mag/arcsec}^2$ ). We highlight two galaxies with especially steep metallicity gradients. Firstly, BD 34 which shows very large errors in its measured metallicity gradient. This gradient is measured from only four valid data points and is poorly constrained. Secondly, BD 45 whose metallicity profile shows some hints of asymmetry, but otherwise offers no explanation for the excessively steep inferred metallicity gradient. Regardless, we retain both these outlying galaxies in our analysis.

From visual inspection, describing some of these galaxies with a straight-line model appears to poorly reflect the true metallicity profile. In a number of galaxies the metallicity gradient appears to be increasing with radius. As such, a gradient measured from the outer disc would be much steeper than one measured from the inner disc. With long-slit spectra we only measure metallicity along one dimension of the galaxy. So if significant azimuthal metallicity variations

<sup>4</sup>Larger versions of the metallicity profiles in conjunction their SDSS  $gri$  composite images are available online (<https://doi.org/10.5281/zenodo.581221>).

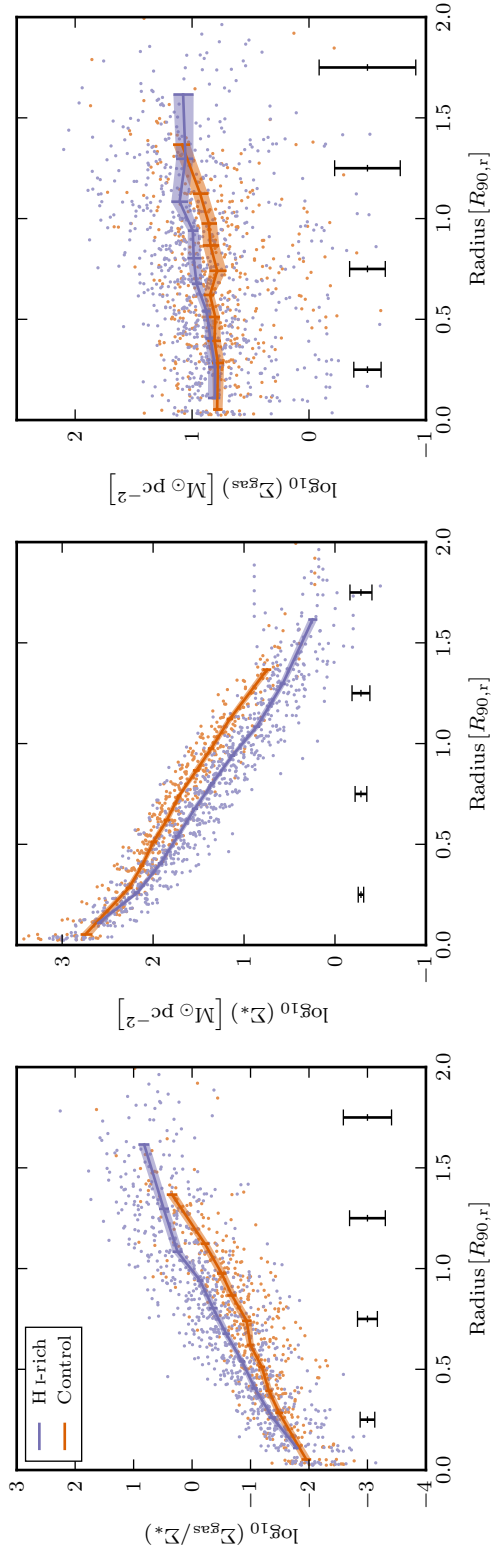


Figure 2.5: Radial profiles of gas-to-stellar mass ratio,  $r_{\text{gas}} = \Sigma_{\text{gas}}/\Sigma^*$ , stellar mass density,  $\Sigma^*$ , and gas mass density,  $\Sigma_{\text{gas}}$ , are shown from left to right. Data is shown for both Bluedisk HI-rich and control samples, coloured blue and orange respectively. We plot the individual data points, as well as the binned median trends in each plot. Shaded regions indicate  $\pm 1 \sigma$  errors on the trends, as determined by bootstrapped Monte-Carlo realisations. Radius is in scale units of  $R_{90,r}$ , the radius containing 90% of the SDSS  $r$  band luminosity. Black vertical bars indicate median error in each  $0.5 R_{90,r}$  division.

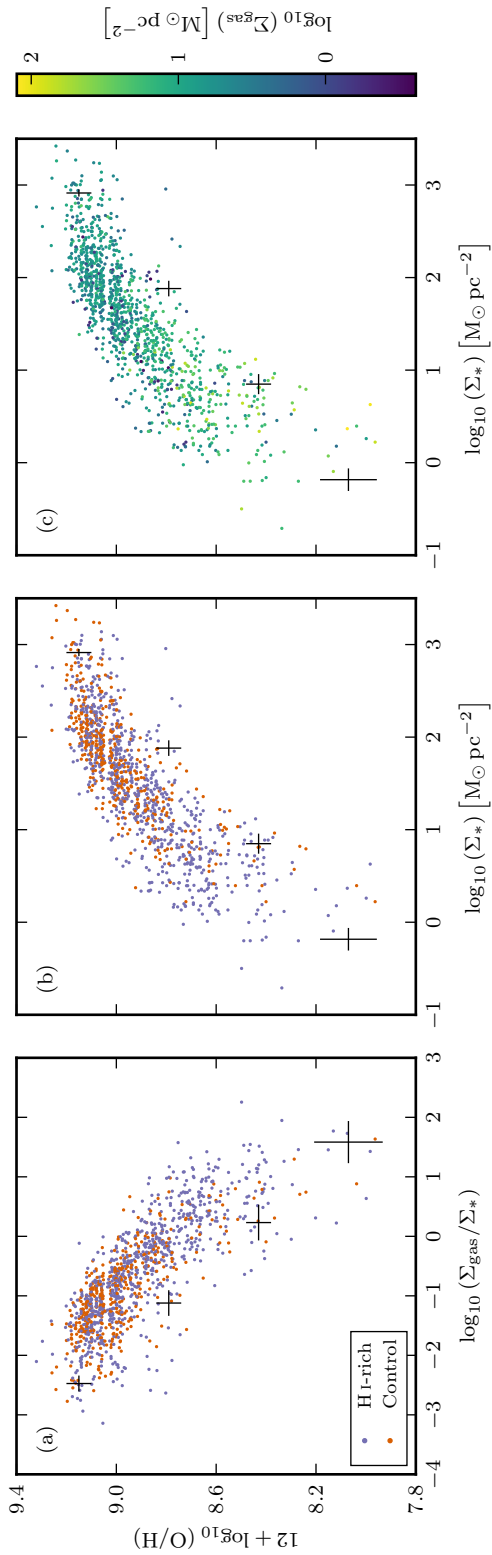


Figure 2.6: Correlations between metallicity and surface mass densities. (a) Metallicity against gas-to-stellar mass ratio. (b & c) Show metallicity against stellar surface mass density  $\Sigma_*$  i.e. the local mass-metallicity relation, but are colour-coded in differently. In (a) and (b) we colour according to Bluedisk sample, HI-rich and control samples, distinguished by blue and orange data points respectively. In (c) we colour the local mass-metallicity relation by gas surface mass density,  $\Sigma_{\text{gas}}$ . Black crosses indicate median error within equally spaced bins.

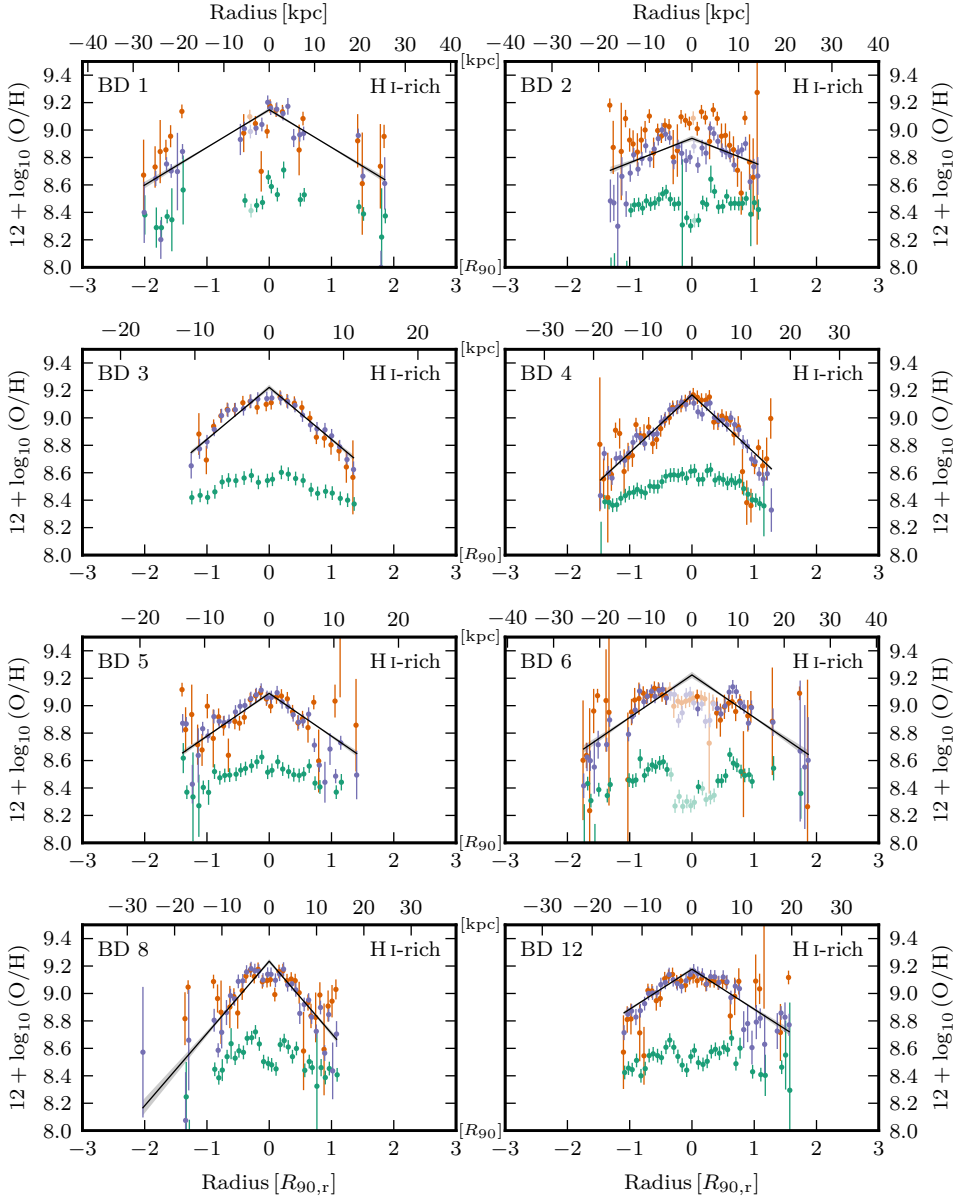


Figure 2.7: Individual metallicity profiles of the Bluedisk galaxies (grouped by their sample classification: H I-rich, control and excluded). The metallicity is inferred using the CL01, KK04 and NS methods, plotted as blue, orange and green respectively. For the CL01 metallicities we show the best-fitting straight-line model (black), where the shaded area indicates its associated  $\pm 1\sigma$  error in gradient. We also show in pale colours data points masked from the fitting due to their non-SF emission characteristics. All plotted data has an minimum  $H\alpha$   $S/N \geq 10$ . On the bottom axis of each plot radius is plotted in units of scale radius ( $R_{90,r}$ ). Where as on the top axis the radius is given in physical size units (kpc).

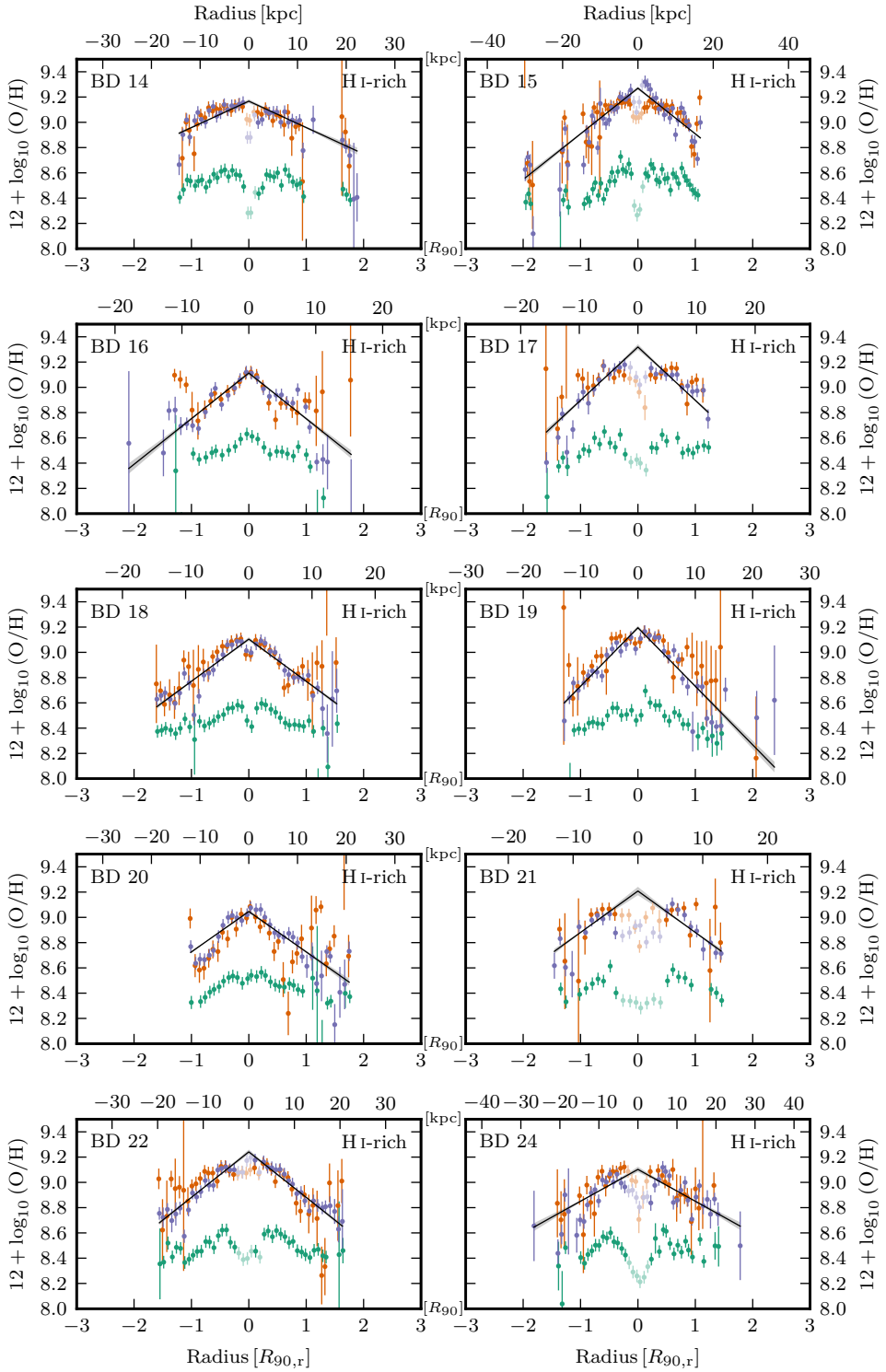


Figure 2.7 (cont.)

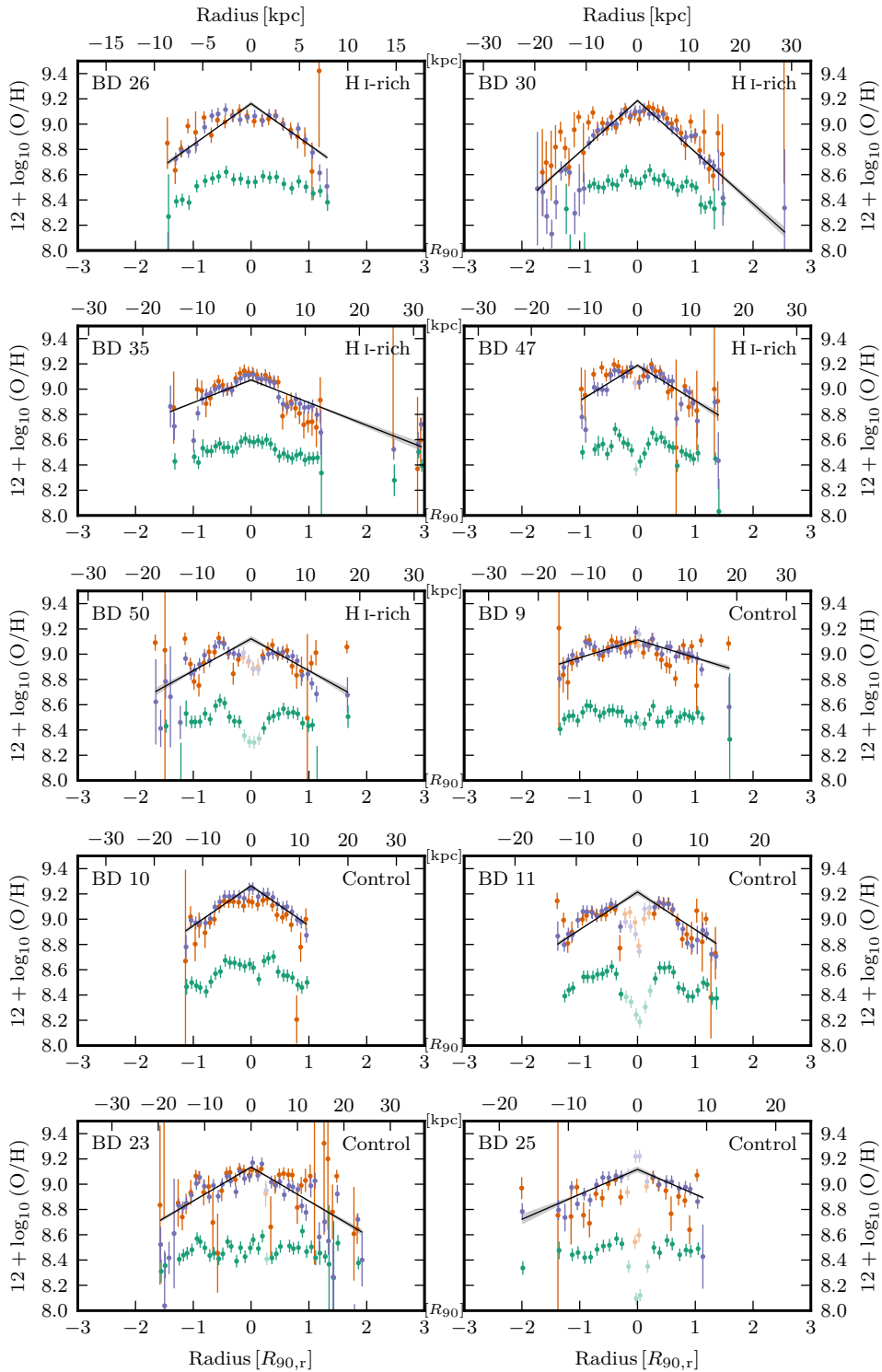


Figure 2.7 (cont.)

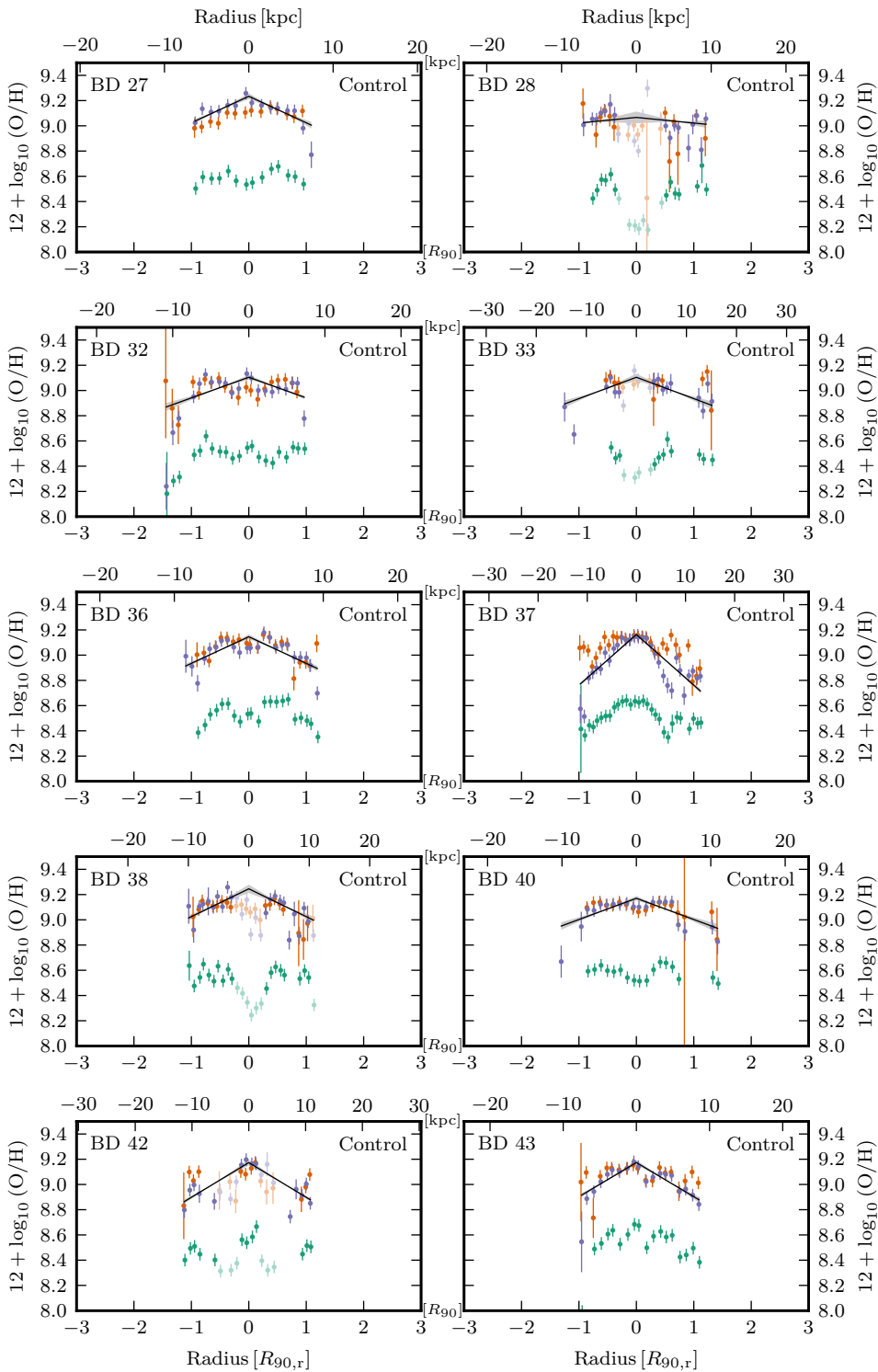


Figure 2.7 (cont.)

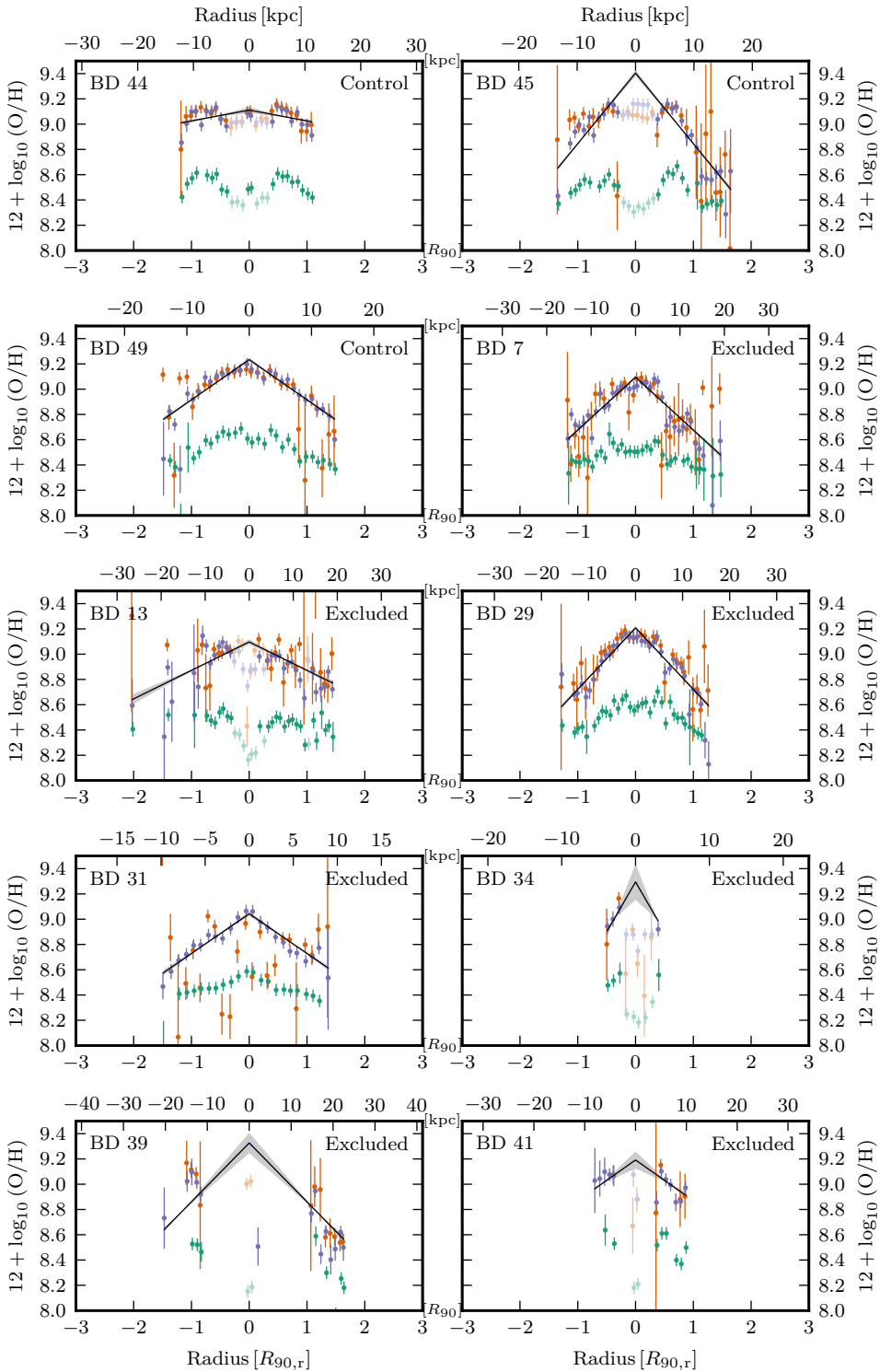


Figure 2.7 (cont.)

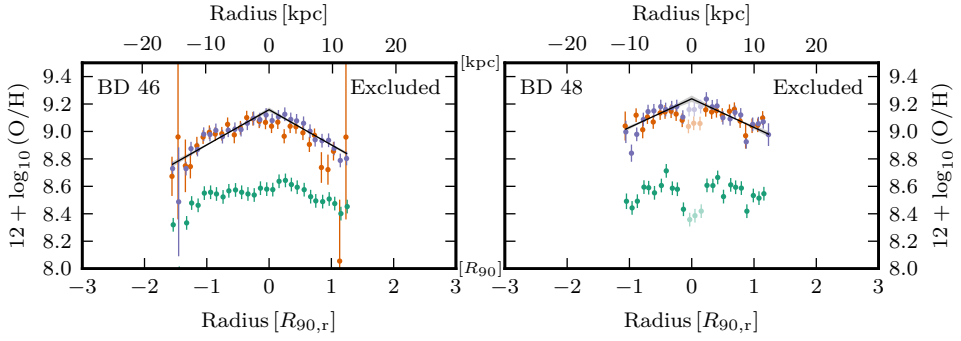


Figure 2.7 (cont.)

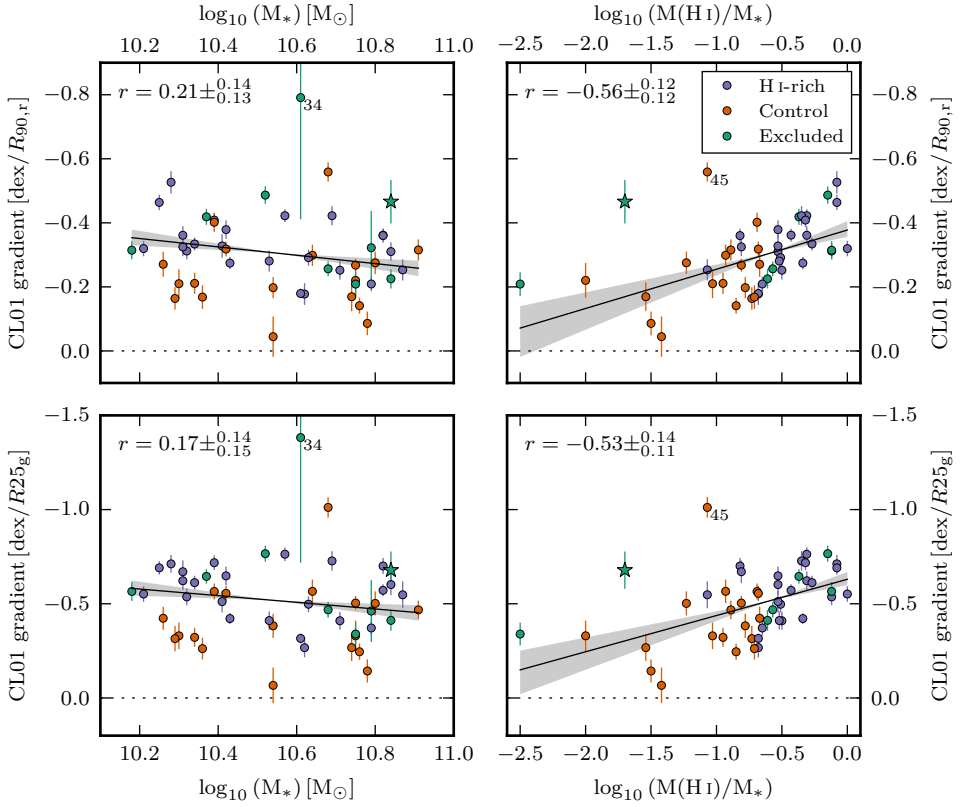


Figure 2.8: **CL01** metallicity gradients as a function of total stellar mass (left) and H I mass fraction (right). We report gradients using two different scale radii,  $R_{90,r}$  (top) and  $R_{25,g}$  (bottom). Colours indicate Bluedisk sample classification H I-rich (blue), control (orange) and excluded (green). Best linear fit and its error in slope are indicated by the solid lines and the shaded regions respectively. The Spearman's rank correlation coefficient is given in the top-left corner of each figure. A star indicates BD 39, which is excluded from the regression and the  $r$ -statistic computation. Numbers label individual galaxies with especially steep metallicity gradients that we reference in the text. For reference,  $r = 0.29$  is the two-tailed Spearman's  $r$ -value at a  $\alpha = 0.05$  significance level.

are present, our metallicity measurements may not be indicative the whole galaxy at a given radius. Simulations of [Petit et al. \(2015\)](#) indicate, however, that azimuthal variations decay are expected to decay on timescales shorter than the orbital period of the galaxy. Indeed, observationally there is little support for strong azimuthal variations, with [Sánchez et al. \(2015\)](#) reporting only modest ( $< 0.05$  dex) azimuthal variations.

In the following, by stacking the metallicity profiles we shall attempt to produce average metallicity profiles.

### 5.2.1 Stacked average metallicity profiles

To study the metallicity profiles for the Bluedisk galaxies further, we stack the individual metallicity data points into equal mass decile radial bins. Tracing the median metallicity of the bins we construct the average metallicity profiles, which are shown in [Fig. 2.9](#). We caution that since the metallicity data points are equally weighted, the outermost bin of each stack might be considered unreliable (see [Appendix C](#)).

In [Fig. 2.9\(b\)](#) we show the stacked profiles of the H I-rich and control samples. We also bisect each sample by total stellar mass. We observe that all galaxies have similar central metallicities, but different profile shapes. We note that the outermost bin of the high-mass control profile has a spuriously low metallicity and should be ignored (see [Appendix C](#)). Putting this aside, the stacked profiles appear to indicate a shallower inner gradient and a steeper outer gradient. It is difficult to define the characteristic radius at which this transition happens. However, by eye it seems that the transition occurs at a smaller radius in the H I-rich galaxies than in the control galaxies. Overall we note that the transitions in the stacked profiles do not appear as abrupt as they do in the unstacked profiles. This would imply that using  $R_{90,r}$  as a radial coordinate is not ideal for expressing this turnover. Indeed, since we observe a local mass-metallicity relation, a scale radius based on stellar mass density would perhaps be more appropriate.

Beyond H I characteristics there are other aspects which may affect metallicity profiles. Using semi-analytical models [Fu et al. \(2013\)](#) predict metallicity gradients should be correlated with bulge-to-total (B/T) ratio. In these models galaxies with more prominent bulges are expected to have shallower gas phase metallicity gradients as the gas distribution in these galaxies is set by later infall of gas. We show the stacked profiles of the galaxy samples bisected by B/T light ratio in [Fig. 2.9\(c\)](#). We observe no apparent connection between metallicity profiles and bulge prominence, however, given the low bisecting threshold ( $B/T=0.15$ ) we find our results to only be in mild tension with these predictions. These observations are consistent with [Sánchez et al. \(2014\)](#) who observe no correlation between metallicity gradient and morphological galaxy type.

It may be possible that the differences we observe between our H I-rich and control populations are driven by the effects of bars. It has been established that there exists an anticorrelation between H I mass fraction and the bar occurrence fraction ([Davoust & Contini 2004](#); [Masters et al. 2012](#)). Numerical simulations have also shown that the presence of galaxy bars can drive enhance gas mixing, flattening the metallicity profile ([Friedli et al. 1994](#); [Minchev et al. 2011](#)). These effects of bars on metallicity been borne out by observations (e.g [Martin & Roy 1994](#); [Dutil & Roy 1999](#)). However, it has also been shown that when metallicity gradients are expressed units of effective disk radius, rather than physical distance, bars show no significant impact on the metallicity gradient ([Sánchez et al. 2014](#)). Even so, it is prudent when comparing the metallicity profiles of the H I-rich and control populations that we take care to exclude the potential impact of bars.

By visual inspection we classify 30% of the Bluedisk galaxies to be strongly barred (with four galaxies indeterminate due to high inclination). This rate is consistent with galaxies of the

same stellar mass (Skibba et al. 2012). In Fig. 2.9(d) we show stacked metallicity profiles of the unbarred galaxies. The distinction between H I-rich and control samples clearly remains after excluding barred galaxies. In Fig. 2.9(f) we show the effects of bars on the whole sample, and in Fig. 2.9(g) the effects of bars exclusively on the control sample. From both of these figures we notice some flattening of the metallicity profile in galaxies with bars. We caution the reader that our sample of H I-rich galaxies with bars is very small.

We have repeated the stacking analyses for the other metallicity calibrators. We see similar effects when using the KK04 method, but we do not observe the outer metallicity drops when using the NS method. It should be noted, however, that the NS method does not allow for variations in the ionization parameter. Methods that do not include this extra dimensionality may not be best suited for the study we present here.

Finally, we note in Fig. 2.9(a) there appears to be a significant amount of scatter in the inner regions of the galaxies. We identify galaxies that harbour AGN using the (O III/H $\beta$ ) and (N II/H $\alpha$ ) emission-line ratios from the centre of each galaxy. We adopt the criterion of Kauffmann et al. (2003b) and identify galaxies with central non-SF emission. We find that galaxies with central non-SF emission exhibit a two-fold increase in the scatter of the metallicities in the inner region ( $r < 0.3 R_{90,r}$ ). This might be an indication of AGN interacting with the central environment. However, it is equally plausible that we are not sufficiently excluding non-SF contaminated data points, producing erroneous metallicity estimates. Our long-slit spectroscopic observations are not ideal for such study of metallicity scatter, integral field spectroscopy with good spatial resolution may provide sufficient data to study both the radial and azimuthal metallicity scatter in the inner regions of galaxies.

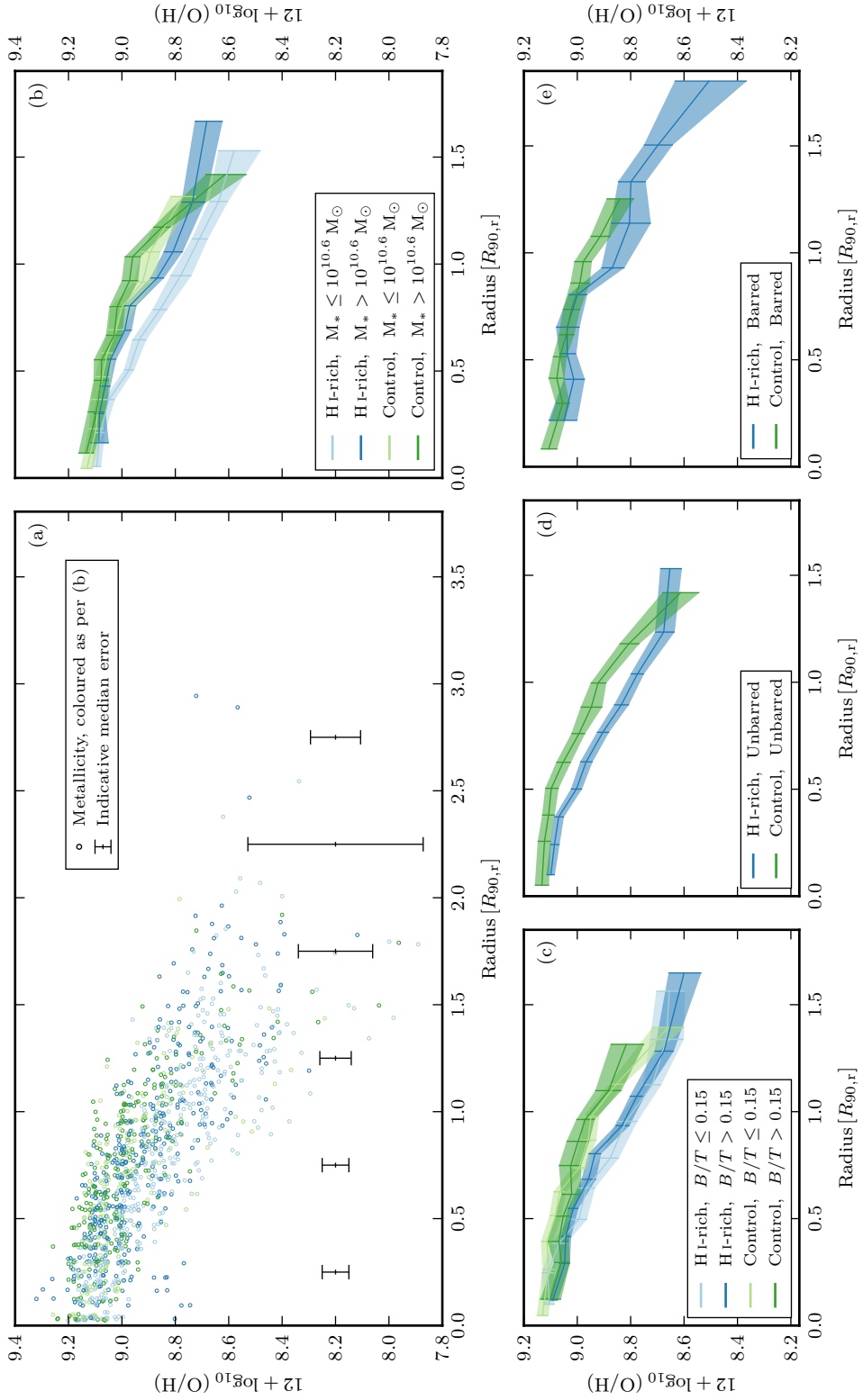
### 5.3 Summary of results

In the next section we shall construct a simple analytical model to explain the metallicity profiles we have observed. But first we shall briefly summarize our results:

- We reproduce the recently reported local mass-metallicity relation. However, we highlight that at low stellar-mass densities there appears to be a residual correlation of metallicity with gas-mass density.
- The metallicity gradients of a galaxy is strongly correlated with its H I mass fraction.
- We stack the metallicity of the galaxies and derive average profile shapes. We find different average profiles for the H I-rich and control galaxy samples.
- We find galaxies in both samples that exhibit transitions from shallower inner metallicity gradients to steeper outer metallicity gradients.
- Barred galaxies appear to have flatter metallicity profiles, but this effect does not drive the difference observed between the Bluedisk samples.

## 6 Discussion

Up to this point we have mainly concerned ourselves with the similarities and differences between our Bluedisk samples. We have, however, not yet suitably tackled the complex issue regarding the origin of the metallicity profile itself. Exploring quantitatively the interplay of the many potential mechanisms is challenging. However recent years have seen the emergence of a class of simple “reservoir” models (Bouché et al. 2010) in which stars form from a gas reservoir regulated by the star formation and gas flows in and out of the system. While simple,



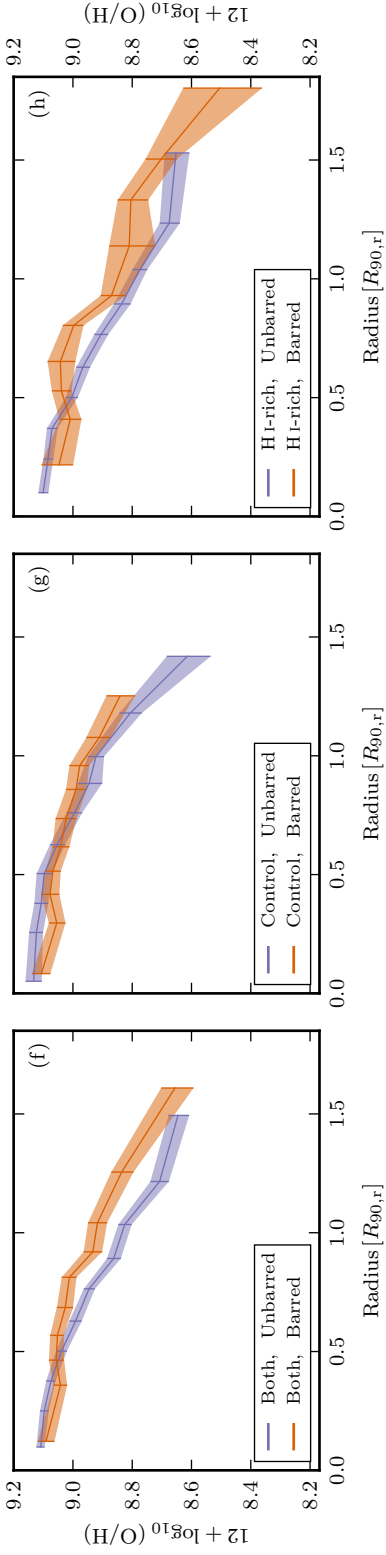


Figure 2.9: Results from stacking metallicity profiles. (a),(b) Metallicity of the Bluedisk galaxies, colour distinguishing H I-rich and control sample, as well as low and high stellar mass. (a) The individual metallicity data points. Vertical bars indicate median error in each  $0.5 R_{90,r}$  division. (b) Median value of galaxies stacked in decile radial bins. Shaded regions indicate  $\pm 1\sigma$  errors determined by bootstrapping Monte-Carlo realisations. (c) Similarly stacked profiles, however, split by  $B/T$  ratio instead of stellar mass. Dividing the H I-rich and control galaxies into barred and unbarred samples we generate the panels (d)-(h).

these models are able to provide simple descriptions of the (central) metal content of galaxies at low redshift (Finlator & Davé 2008; Davé et al. 2012; Lilly et al. 2013). The models are also naturally interpreted as a result of galaxies being generally close to equilibrium between star formation, outflows and inflows (Davé et al. 2012).

## 6.1 Modelling resolved galaxies as local gas regulators

The reservoir models generally consider the galaxies to be spatially unresolved. Here we therefore will develop a simple extension of these models to a resolved galaxy. In particular we will extend the “gas regulator” model (Lilly et al. 2013, herein L13) which has been shown to successfully fit the central metallicities of star forming galaxies in the SDSS. Our approach will be to minimally extend this model to 2D to see whether such a simple extension is sufficient to describe the metallicity profiles of our galaxies.

To do this we envisage our disc galaxy divided into a set of radial zones. We then assume that the mean properties of each radial zone can be described by individual gas reservoir models. Alternatively one might take this to mean that we assume that each radial zone individually is in an equilibrium between inflow, outflow and star formation – a detailed balance principle which is not required by the reservoir models in general. Note that we do not assume that such an equilibrium holds at each point but rather in an average sense across a radial bin.

Generally there might be radial mass transfer between these zones, but in the following we will make the simplifying assumption that radial mass transfer can be ignored. Since, semi-analytic models of Fu et al. (2013) have argued that gas flows are of minor importance. It should be noted, however, that the simulations of Minchev et al. (2011) have shown that in the presence of bars, gas can be efficiently transported resulting in flattened metallicity gradients.

In addition to gas flows, long-lived stars are expected to migrate from their original radius, particularly in the presence of bars (Roškar et al. 2008; Di Matteo et al. 2013). However, in the model we will assume that the mass of stars observed at a given radius represents the total mass of stars formed that given radius. Or rather, we assume the stars remain associated to the gas from which they form.

We now outline how we adapt and apply the gas regulator model to our data. We refer the reader to L13 for a full treatment and derivation of the model.

### 6.1.1 Transport of gas

The underlying equation describing the rate of change of the reservoir gas mass (in each radial bin) is

$$\dot{m}_{\text{gas}} = \dot{m}_{\text{in}} - \dot{m}_{\text{out}} - \dot{m}_{*} + \dot{m}_{\text{return}} + \dot{m}_{\text{radial}}. \quad (2.3)$$

The components are as follows:

- $\dot{m}_{\text{in}}$  is the rate of metal-poor gas inflowing from the halo to the reservoir. We do not explicitly parametrize  $\dot{m}_{\text{in}}$  and it shall be eliminated in due course.
- $\dot{m}_{\text{out}}$  is the rate at which gas flows out from the reservoir and into the halo or beyond. Since we are mostly concerned with the star forming disk, this is assumed to be driven by winds from massive stars, and we therefore consider  $\dot{m}_{\text{out}}$  to be linearly proportional linearly proportional SFR, i.e.  $\dot{m}_{\text{out}} = \lambda \cdot \text{SFR}$ , where  $\lambda$  is the mass-loading factor. In Section 6.1.3 we attempt to estimate this mass-loading factor.
- $\dot{m}_{*}$  is the rate at which gas is converted into stars. In other words  $\dot{m}_{*} = \text{SFR}$ . The SFR is itself assumed to be linearly proportional to the current mass of the reservoir,

$\text{SFR} = \epsilon \cdot m_{\text{gas}}$ , where  $\epsilon$  is the star-formation efficiency. This link between  $m_{\text{gas}}$  a SFR provides the regulatory aspect of the model.

- $\dot{m}_{\text{return}}$  is the rate at which enriched gas is returned from short-lived high-mass stars. A fraction  $R$  of the mass converted into stars is assumed to be instantaneously recycled back into the reservoir ( $\dot{m}_{\text{return}} = R \cdot \text{SFR}$ ).

Following L13 we adopt a fixed value of the return fraction  $R = 0.4$ . As shown by BC03 this is the mid-range value over a variety of initial mass functions (IMF), for a 10 Gyr stellar population. Provided there are no strong age gradients across the galaxies it is reasonable to adopt a radially constant return fraction. The exact value of the return fraction will depend on the choice of IMF. We note, however, that our conclusions are not sensitive the exact value we adopt for  $R$ . This insensitivity results from the degeneracy of  $R$  with parameters that we shall fit (see Section 6.1.4).

- $\dot{m}_{\text{radial}}$  is the rate at which radial flows within the disc change the gas content of the reservoir. For simplicity we assume  $\dot{m}_{\text{radial}} = 0$ , neglecting the effects of radial flows.

With these principle assumptions, equation 2.3 can be written as

$$\dot{m}_{\text{gas}} = \dot{m}_{\text{in}} - (1 - R + \lambda)\text{SFR}. \quad (2.4)$$

Furthermore L13 show that by introducing the variable  $r_{\text{gas}} = m_{\text{gas}}/m_*$ , the ratio of gas-to-stellar mass, equation 2.4 can be conveniently rewritten as

$$\dot{m}_{\text{in}} = \left( (1 - R)(1 + r_{\text{gas}}) + \lambda + \epsilon^{-1} \frac{d \ln(r_{\text{gas}})}{dt} \right) \cdot \text{SFR}, \quad (2.5)$$

which makes the regulatory link between the star formation rate and gas inflow explicit. We will assume that this holds in the mean in each radial bin.

### 6.1.2 Transport of metals

We now consider the flow of metals into and out from the reservoir. In the absence of radial flows, analogously to equation 2.3 we can write the rate of change of metals in the reservoir as

$$\dot{m}_{\text{Z,gas}} = \dot{m}_{\text{Z,in}} - \dot{m}_{\text{Z,out}} - \dot{m}_{\text{Z,*}} + \dot{m}_{\text{Z,return}}. \quad (2.6)$$

This contains two source terms and two sink terms. The components are as follows:

- $\dot{m}_{\text{Z,in}}$  represents the metals introduced from the metal-poor halo. We define this gas to have a typical metallicity  $Z_0$ .
- $\dot{m}_{\text{Z,out}}$  is the metal mass entrained in wind driven outflows. The metallicity of this gas is that of the reservoir,  $Z$ .
- $\dot{m}_{\text{Z,*}}$  represents the mass locked into long-lived stars, removing gas with metallicity  $Z$ .
- $\dot{m}_{\text{Z,return}}$  is the metal enrichment resulting from star formation. The characteristic yield,  $y$ , is defined as the metal mass returned per unit mass in long-lived stars.

With these principle assumptions, equation 2.6 can be expressed as

$$\dot{m}_{\text{Z,gas}} = Z_0 \dot{m}_{\text{in}} - Z(1 - R + \lambda)\text{SFR} + y(1 - R)\text{SFR}. \quad (2.7)$$

The rate of change of reservoir metallicity can be written

$$\dot{Z} = \dot{m}_{\text{Z,gas}} / m_{\text{gas}} - Z \dot{m}_{\text{gas}} / m_{\text{gas}}. \quad (2.8)$$

L13 find that the metallicity of such a system will approach equilibrium on a timescale shorter than the depletion timescale (i.e.  $\leq t_{\text{dep}} = \epsilon^{-1}$ ). In which case they show the equilibrium metallicity to be

$$Z_{\text{eq}} = Z_0 + \frac{y}{1 + r_{\text{gas}} + (1 - R)^{-1} \left( \lambda + \epsilon^{-1} \frac{d \ln(r_{\text{gas}})}{dt} \right)}. \quad (2.9)$$

We now have an expression for the equilibrium metallicity of the system as a function of  $r_{\text{gas}}$ , a quantity we have already obtained (see Section 5.1). We highlight that there are other conceptually interesting ways of interpreting  $r_{\text{gas}}$ , which can be alternatively be written as

$$r_{\text{gas}} = \frac{m_{\text{gas}}}{m_*} = \frac{\epsilon^{-1} \text{SFR}}{m_*} = \epsilon^{-1} \text{sSFR}, \quad (2.10)$$

where sSFR is the specific star formation rate.

By fitting their model to star forming galaxies from the SDSS, L13 estimate  $\epsilon^{-1} \frac{d \ln(r_{\text{gas}})}{dt} \approx -0.25$ , and we shall adopt this value. We note, however, that the model is not strongly sensitive to this factor, owing to the degeneracies arising from fitting the  $y$  and  $Z_0$  parameters (Section 6.1.4).

### 6.1.3 Estimating the mass-loading factor, $\lambda$

We have parametrized wind-driven outflows via  $\dot{m}_{\text{out}} = \lambda \cdot \text{SFR}$ , where  $\lambda$  is a mass-loading factor. We shall consider two scenarios, one with winds and the other without. We note here that this choice is not important, for we will show in Section 6.2 that these two scenarios are highly degenerate with  $y$  and  $Z_0$  parameters, which we shall fit.

In the simple windless scenario we will set  $\lambda = 0$  everywhere.

For our more complex windy model, we consider outflows that are powered by momentum-driven winds from supernovae (SNe). We follow the prescription described in Dutton & van den Bosch (2009) to define the mass-loading factor

$$\lambda = \frac{p_{\text{SN}} \eta_{\text{SN}}}{V_{\text{esc}}(\vec{r})}, \quad (2.11)$$

where  $p_{\text{SN}} = 3 \times 10^4 M_{\odot} \text{ km s}^{-1}$  is the momentum per SN,  $\eta_{\text{SN}} = 8.3 \times 10^{-3}$  is the number of SNe per solar mass of stars formed, and  $V_{\text{esc}}(\vec{r})$  is the escape velocity at a given point,  $\vec{r}$ , in the disc. The escape velocity itself is defined in terms of the gravitational potential

$$V_{\text{esc}}(\vec{r}) = \sqrt{2 |\Phi_{\text{tot}}(\vec{r})|}, \quad (2.12)$$

where the gravitational potential,  $\Phi_{\text{tot}}$ , is the sum of contributions from stars, gas and dark matter

$$\Phi_{\text{tot}}(\vec{r}) = \Phi_*(\vec{r}) + \Phi_{\text{gas}}(\vec{r}) + \Phi_{\text{DM}}(\vec{r}). \quad (2.13)$$

We must calculate the gravitational potential at the position in the galaxy where each reservoir/zone is situated. To achieve this we model the three potentials separately. We shall use thin discs to represent both the stellar and gaseous components. The dark matter component we assume to be distributed in a spherically symmetric halo.

We determine the stellar contribution using the stellar mass maps (Section 2.3). Assuming that the stars lie in a thin plane, we assign a point mass to every map pixel. The potential at any point in the galaxy is then calculated as a sum of the individual point mass potentials, i.e.

$$\Phi_*(\vec{r}) = - \sum_i \frac{G\Delta m_i}{|\vec{r}_i - \vec{r}|}, \quad (2.14)$$

where  $G$  is the gravitational constant,  $\Delta m_i$  is the mass of a pixel, and  $|\vec{r}_i - \vec{r}|$  is the distance in the plane of the galaxy to the centre of the mass pixel.

To estimate the gravitational potential arising from the gas, we adopt the following characteristic surface density profile from [Bigiel & Blitz \(2012\)](#)

$$\frac{\Sigma_{\text{gas}}}{14 M_{\odot} \text{pc}^{-2}} = 2.1 \exp(-1.65r/r_{25}), \quad (2.15)$$

where  $r_{25}$  is the optical radius where the surface brightness becomes 25 mag arcsec<sup>-2</sup>. We use equation 2.164a from [Binney & Tremaine \(2008\)](#) to calculate the gas contribution to the potential. It was shown in [Wang et al. \(2014\)](#) that the characteristic surface density profile provides a good description of the H I-rich galaxies in our sample. Admittedly the profile does not provide as good an approximation to the control sample. However, since the contribution of the gas to the total potential is small ( $\leq 10\%$ ) this will not affect our conclusions.

The dark matter halo provides the dominant contribution to the halo, making up 50–80% of the total potential, but it is also the most uncertain as we do not have direct constraints on its properties. In view of this we follow common practice to parametrise the dark matter halo mass distribution with the spherically symmetric NFW profile ([Navarro et al. 1997](#)). In order to do so we the halo mass and concentration. We get the former from halo mass-stellar relation derived by [Guo et al. \(2010, their equation 3\)](#) and the halo concentration from [Macciò et al. \(2007, their fig. 3\)](#) with the virial radius of the halo using equation 3 from [Dutton & van den Bosch \(2009\)](#). With this best guess dark matter potential, combined with the potentials of the stellar and gas discs, we are now able to estimate the mass-loading factor  $\lambda$ .

#### 6.1.4 Fitting $y$ and $Z_0$

Two components in the model remain unconstrained, namely the yield and the metallicity of the infalling gas.

The stellar yield,  $y$ , represents the metallicity of the gas returned by short-lived stars. If we assume there is a universal initial mass function, then we expect  $y$  to be constant between galaxies and independent of location within a specific galaxy. The stellar yield can in principle be calculated from stellar evolution models. However, the large and poorly understood systematic offsets between the various gas-phase metallicity indicators (see Appendix A) mean that we are unable to determine absolute abundances for our galaxies so we have decided to assume that  $y$  is the same for all galaxies, but unknown so we fit it as a global constant.

The metallicity of gas infalling from the halo,  $Z_0$ , is a poorly known quantity. For simplicity we therefore assume that the infalling gas has the same metallicity at all radii for each galaxy and that the halos of all the Bluedisk galaxies have the same metallicity. This may not be a bad assumption since all the galaxies are of similar total stellar mass, and therefore may possess similar mass halos. As with the stellar yield, our prediction of  $Z_0$  also suffers from effects of systematic offsets due to the choice in metallicity indicators. Thus we also make  $Z_0$  a global constant that is to be fit.

In summary given the stellar mass maps and gas mass distributions, the resulting model, equation 2.9, has two free parameters,  $y$  and  $Z_0$ . These global parameters, namely the stellar

yield and the halo metallicity, are fit for all radial bins, across all galaxies, simultaneously. Due to the systematic offsets between metallicity indicators, we caution that inferences should not be made on the fitted values themselves.

## 6.2 Bluedisk galaxies as local gas regulators

Having outlined the local gas regulator model, we demonstrate the results for all 50 Bluedisk galaxies in Fig. 2.10. Surprisingly this simplistic equilibrium model appears to match well for many, but by no means all, of the galaxies. It is strikingly clear that with only two globally-set free parameters we can reproduce a large variety of observed metallicity profile shapes that these galaxies exhibit. The model also reproduces the observed outer metallicity drops, which is attributed to the transition from a stellar-dominated inner disc to a more gas-dominated outer disc.

The centres of the galaxies appear to be most problematic for the local gas regulator model to reproduce. One of our key model assumptions is that we assume independence between radial zones. But the presence of bars and bulges at the centres of galaxies might invalidate this assumption. For example, a bar could be expected to drive strong radial flows inwards, which if this were the case, we could expect steepened metallicity gradients (Goetz & Koeppen 1992). However, we see no obvious connection between deviations from the local gas regulator model and the presence of a strong bars or a prominent bulges.

Alternatively the failure of the model may indicate that some of these deviant central regions are contaminated by emission whose origin is not photoionization, such as shocks and LINERs, which our selection criteria have failed to exclude. Emission from non-photoionizing origins can impact different metallicity determination methods in different ways. Although as shown in Appendix A different metallicity indicators yield different absolute and relative abundances, we should expect there to exist a monotonic mapping between the methods. For example, in Fig. 2.7 we can see the inner regions of BDs 2,15 that they show contradictory behaviour of the metallicity of the CL01 and KK04 indicators. This primarily indicates contamination from non-photoionizing origins, thus it is not surprising the local gas regulator model appears to fail in these regions.

We find no difference in the quality of fit of the local gas regulator model between the H I-rich and control galaxies. Overall both our H I-rich, control galaxies fitting equally well. However, our local gas regulator model should not be expected to succeed for galaxies that are interacting, since interactions could also drive strong gas flows. Indeed our excluded (non-isolated) sample of galaxies exhibit some of the most discrepant fits, e.g. BD 31, which has a very different metallicity profile from the one predicted by the model.

We construct the local gas regulator model with momentum-driven winds and windless cases, both of which appear to represent the data more or less equally well. This is not because winds have no effect, indeed they do impact strongly on the metallicity, but the effects of the wind is largely degenerate with our fitted parameters:  $\gamma$ , and  $Z_0$ . The wind model we employ modifies the metallicity changing the peak metallicity and inner slope (where  $r_{\text{gas}} \sim 0$ ). The loss of metals due to winds can be compensated by increasing the values of  $\gamma$  and/or  $Z_0$ . Since we are forbidden from interpreting the values of  $\gamma$  and  $Z_0$ , we are unable to conclude anything either for or against the existence of enriched wind-driven outflows.

We note that our results here are compatible with the recent work of Ho et al. (2015). Using a analytical formalism similar to the L13 gas regulator they are able to reproduce the distribution of metallicity gradients observed. Therein the metallicity profile is also determined by the current ratio of gas-to-stellar mass.

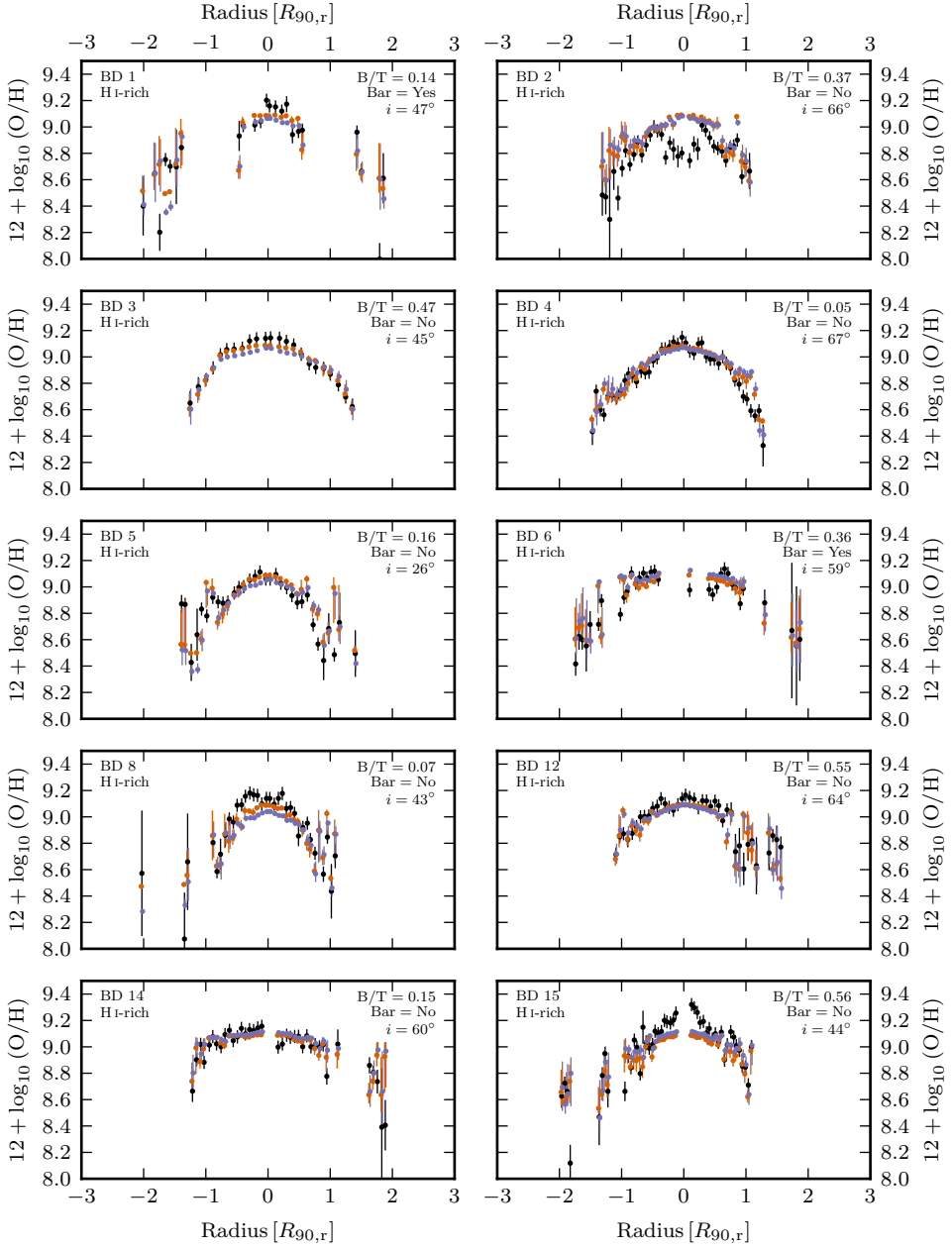


Figure 2.10: The local gas regulator model compared to the metallicity profiles of the Bluedisk galaxies. The observed CL01 metallicity is shown in black. Windless and windy models are shown in orange and blue, respectively. Error bars on the models are not the true full error, but rather they indicate the effects of  $\pm 1\sigma$  deviations in the gas-to-stellar mass ratio,  $r_{\text{gas}}$ . In the top right of each plot we label the bulge-to-total light ratio, B/T. We also denote whether a bar is present. In highly inclined systems where we that would not be able to determine the presence of a bar, we denote this with a “?” symbol. Since our modelling may be problematic at high inclinations, we also include the measured inclination  $i$ . The globally fitted parameter values are  $y = 1.27 \times 10^{-3}$ ,  $Z_0 = 1.91 \times 10^{-4}$  and  $y = 0.55 \times 10^{-3}$ ,  $Z_0 = 2.97 \times 10^{-4}$  in the windy and windless cases, respectively.

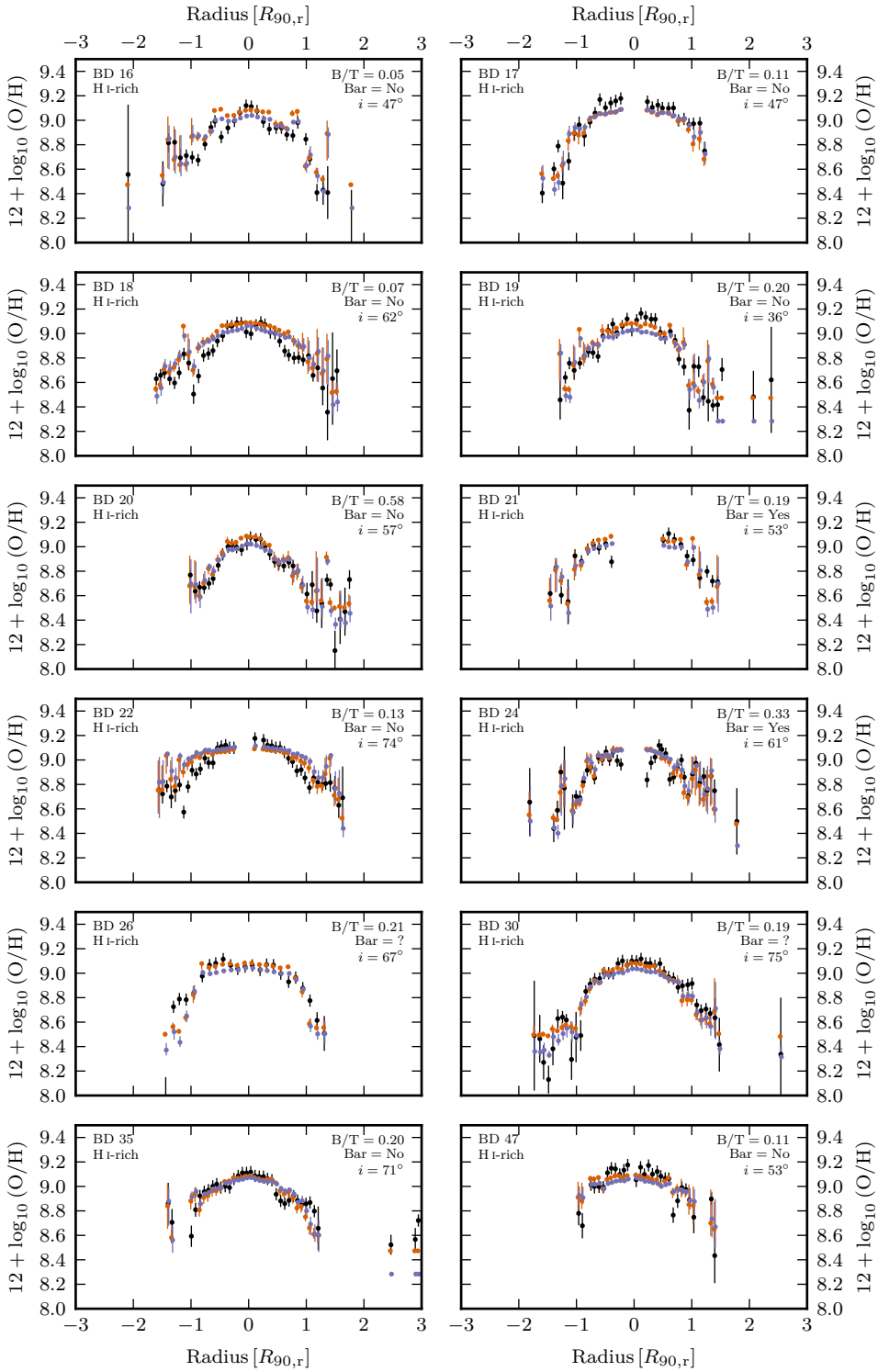


Figure 2.10 (cont.)

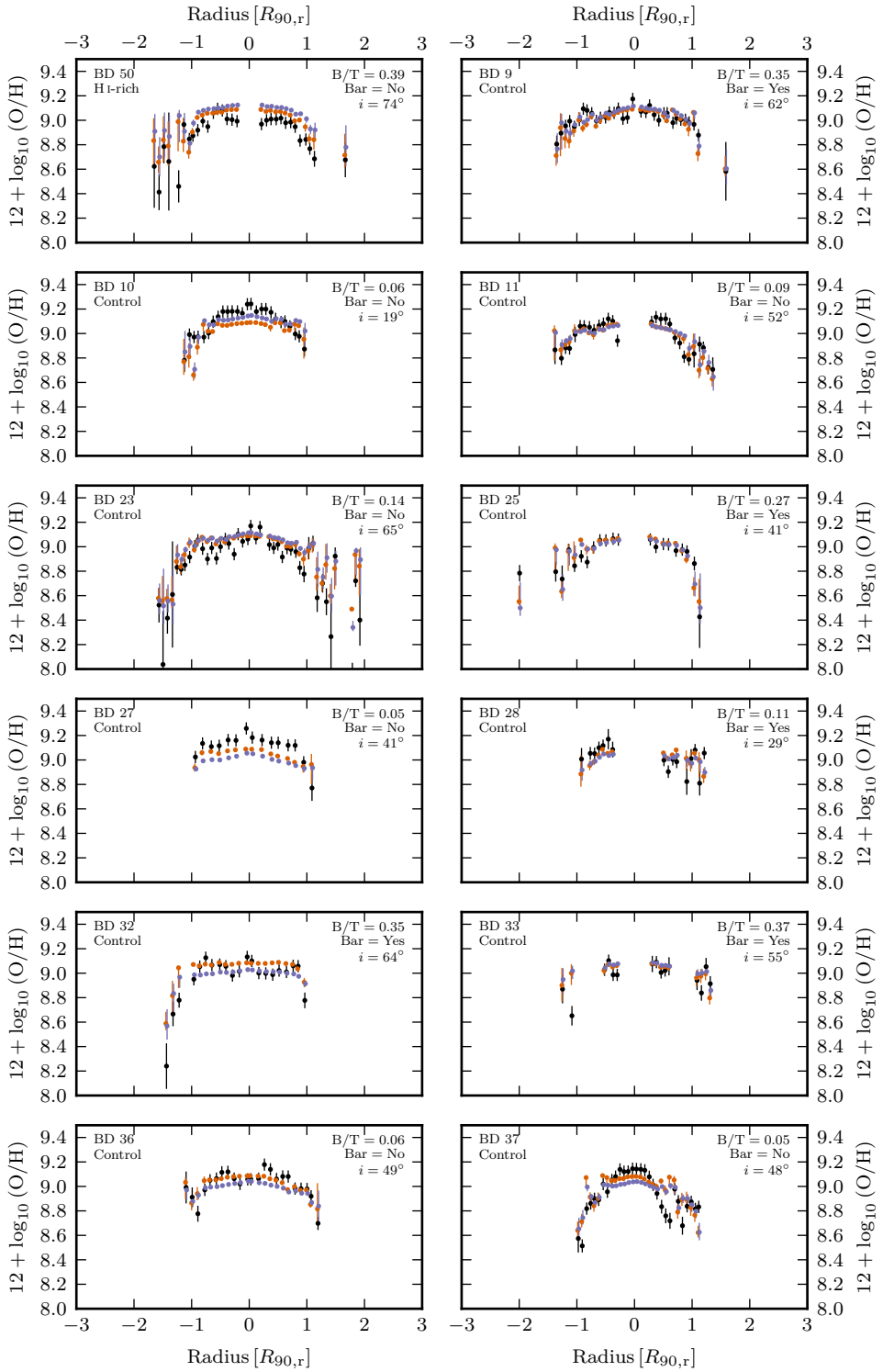


Figure 2.10 (cont.)

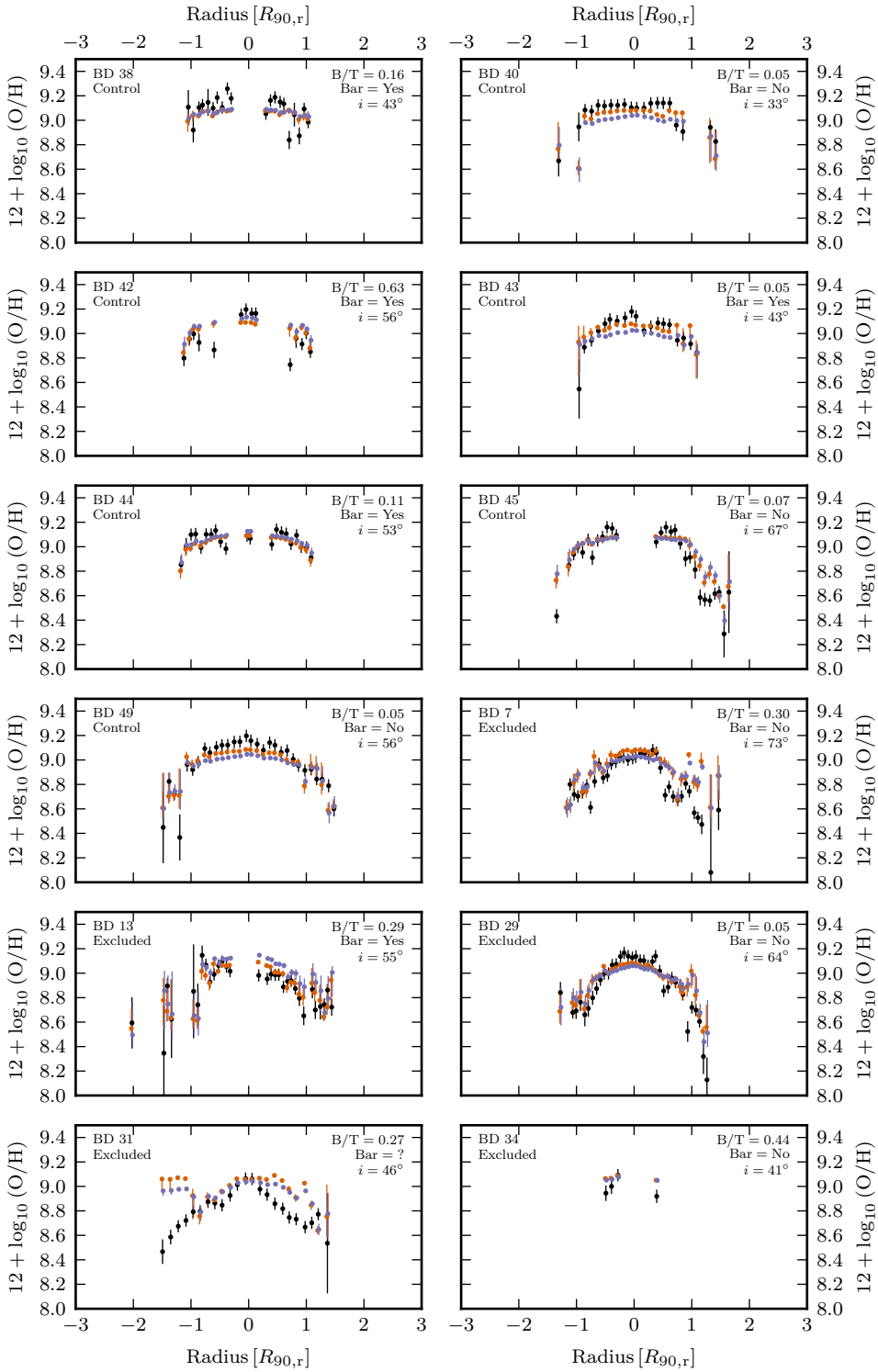


Figure 2.10 (cont.)

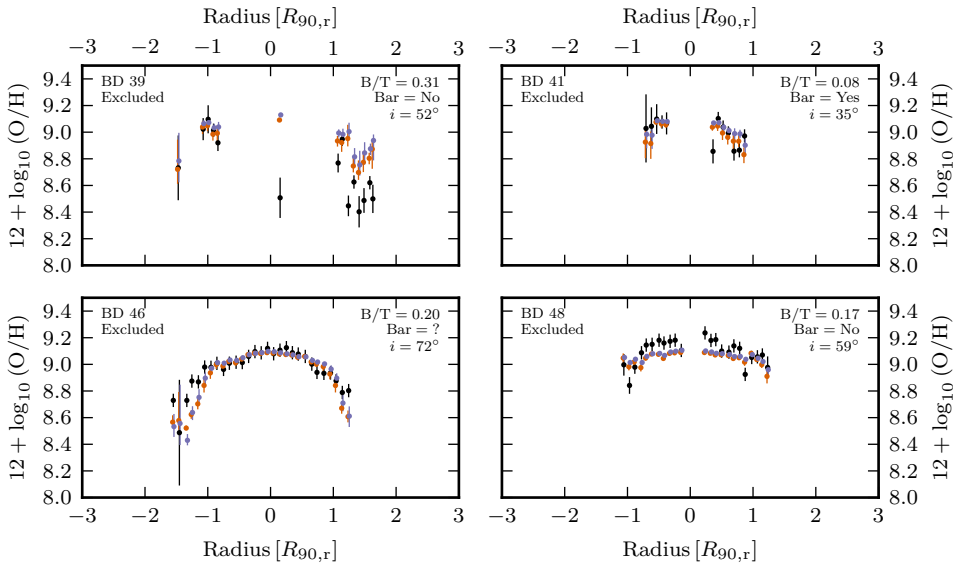


Figure 2.10 (cont.)

## 7 Conclusions

We present radial gas-phase metallicity profiles of 50 late-type galaxies that form the Bluedisk survey. We explore how the H I content of these galaxies affects their metallicity profiles. Although we find a correlation between H I mass fraction and the metallicity gradient, we observe that the metallicity profiles of our H I-rich and control samples show remarkable similarity. Furthermore we find that using a simple equilibrium model we are able to approximate the metallicity profiles of both samples with equal success. We summarize our main results as follows:

- (i) We confirm the local mass-metallicity relation for the Bluedisk galaxies. Although we note that at low stellar mass density there appears to be a residual anti-correlation of metallicity with gas mass density.
- (ii) The metallicity gradient of the galaxies is strongly correlated with their H I mass fraction. Galaxies with higher H I mass fractions have steeper metallicity gradients..
- (iii) We find that in some galaxies the outer disc exhibits steeper metallicity gradients than in the inner disc. However, unlike previous work that has shown this, we find these galaxies to be ubiquitous in both the H I-rich and control samples.
- (iv) The barred galaxies in our sample bars tend to have flatter metallicity profiles. This is not sufficient, however, to explain observed differences between the metallicity profiles of the H I-rich and control samples.
- (v) By applying a simple equilibrium analytical model, we find that we are able to approximate the metallicity profile shapes with the ratio of gas-to-stellar mass,  $r_{\text{gas}} = \Sigma_{\text{gas}}/\Sigma_{\text{*}}$ . In the outer disc where  $\Sigma_{\text{*}}$  is low, a transition to  $r_{\text{gas}} > 1$  occurs. This naturally gives rise to the steeper outer metallicity gradients which are observed.

If metallicity is truly in equilibrium, this would naturally explain the local mass-metallicity relation. Also, since the dynamic range of the stellar mass density is much greater than the gas mass density, the overall metallicity profile represents the integrated build up of metals.

## Acknowledgements

We would like thank the referee for their detailed comments, which have helped to improve this paper. We also thank Rob Crain and Simon Lilly who provided useful and stimulating discussions for this work.

This work is based on observations performed at the William Herschel Telescope under the programmes W12BN010 and W13AN010. The William Herschel Telescope is operated on the island of La Palma by the Isaac Newton Group in the Spanish Observatorio del Roque de los Muchachos of the Instituto de Astrofísica de Canarias.

FB acknowledges support from DFG grant BI 1546/1-1. JMvdH acknowledges support from the European Research Council under the European Union's Seventh Framework Programme (FP/2007-2013) / ERC Grant Agreement nr. 291531.

Funding for the SDSS and SDSS-II has been provided by the Alfred P. Sloan Foundation, the Participating Institutions, the National Science Foundation, the U.S. Department of Energy, the National Aeronautics and Space Administration, the Japanese Monbukagakusho, the Max Planck Society, and the Higher Education Funding Council for England. The SDSS Web Site is <http://www.sdss.org/>.

The SDSS is managed by the Astrophysical Research Consortium for the Participating Institutions. The Participating Institutions are the American Museum of Natural History, Astrophysical Institute Potsdam, University of Basel, University of Cambridge, Case Western Reserve University, University of Chicago, Drexel University, Fermilab, the Institute for Advanced Study, the Japan Participation Group, Johns Hopkins University, the Joint Institute for Nuclear Astrophysics, the Kavli Institute for Particle Astrophysics and Cosmology, the Korean Scientist Group, the Chinese Academy of Sciences (LAMOST), Los Alamos National Laboratory, the Max-Planck-Institute for Astronomy (MPIA), the Max-Planck-Institute for Astrophysics (MPA), New Mexico State University, Ohio State University, University of Pittsburgh, University of Portsmouth, Princeton University, the United States Naval Observatory, and the University of Washington.

We wish to also acknowledge the PYTHON programming language and the Interactive Data Language (IDL) which were both used throughout this project.

## Bibliography

- Baldwin J. A., Phillips M. M., Terlevich R., 1981, *PASP*, **93**, 5  
 Bertin E., Arnouts S., 1996, *A&AS*, **117**, 393  
 Bigiel F., Blitz L., 2012, *ApJ*, **756**, 183  
 Binney J., Tremaine S., 2008, *Galactic Dynamics: Second Edition*. Princeton University Press  
 Blanc G. A., Kewley L., Vogt F. P. A., Dopita M. A., 2015, *ApJ*, **798**, 99  
 Böhm A., et al., 2004, *A&A*, **420**, 97  
 Bouché N., et al., 2010, *ApJ*, **718**, 1001  
 Brinchmann J., Charlot S., White S. D. M., Tremonti C., Kauffmann G., Heckman T., Brinkmann J., 2004, *MNRAS*, **351**, 1151  
 Brinchmann J., Charlot S., Kauffmann G., Heckman T., White S. D. M., Tremonti C., 2013, *MNRAS*, **432**, 2112

- Bruzual G., Charlot S., 2003, *MNRAS*, 344, 1000
- Cappellari M., Copin Y., 2003, *MNRAS*, 342, 345
- Catinella B., et al., 2010, *MNRAS*, 403, 683
- Charlot S., Fall S. M., 2000, *ApJ*, 539, 718
- Charlot S., Longhetti M., 2001, *MNRAS*, 323, 887
- Cid Fernandes R., Stasińska G., Mateus A., Vale Asari N., 2011, *MNRAS*, 413, 1687
- Davé R., Finlator K., Oppenheimer B. D., 2012, *MNRAS*, 421, 98
- Davoust E., Contini T., 2004, *A&A*, 416, 515
- Di Matteo P., Haywood M., Combes F., Semelin B., Snaith O. N., 2013, *A&A*, 553, A102
- Diehl S., Statler T. S., 2006, *MNRAS*, 368, 497
- Dopita M. A., Sutherland R. S., Nicholls D. C., Kewley L. J., Vogt F. P. A., 2013, *ApJS*, 208, 10
- Driver S. P., et al., 2011, *MNRAS*, 413, 971
- Dutil Y., Roy J.-R., 1999, *ApJ*, 516, 62
- Dutton A. A., van den Bosch F. C., 2009, *MNRAS*, 396, 141
- Ellison S. L., Patton D. R., Simard L., McConnachie A. W., 2008, *ApJ*, 672, L107
- Fall S. M., Efstathiou G., 1980, *MNRAS*, 193, 189
- Finlator K., Davé R., 2008, *MNRAS*, 385, 2181
- Foster C., et al., 2012, *A&A*, 547, A79
- Friedli D., Benz W., Kennicutt R., 1994, *ApJ*, 430, L105
- Fu J., et al., 2013, *MNRAS*, 434, 1531
- Gadotti D. A., Kauffmann G., 2009, *MNRAS*, 399, 621
- Gallazzi A., Charlot S., Brinchmann J., White S. D. M., Tremonti C. A., 2005, *MNRAS*, 362, 41
- Goetz M., Koepfen J., 1992, *A&A*, 262, 455
- Guo Q., White S., Li C., Boylan-Kolchin M., 2010, *MNRAS*, 404, 1111
- Ho I.-T., Kudritzki R.-P., Kewley L. J., Zahid H. J., Dopita M. A., Bresolin F., Rupke D. S. N., 2015, *MNRAS*, 448, 2030
- Hoopes C. G., Waltherbos R. A. M., 2003, *ApJ*, 586, 902
- Hoopes C. G., Waltherbos R. A. M., Bothun G. D., 2001, *ApJ*, 559, 878
- Kauffmann G., et al., 2003a, *MNRAS*, 341, 33
- Kauffmann G., et al., 2003b, *MNRAS*, 346, 1055
- Kennicutt Jr. R. C., 1998, *ARA&A*, 36, 189
- Kewley L. J., Ellison S. L., 2008, *ApJ*, 681, 1183
- Kewley L. J., Dopita M. A., Sutherland R. S., Heisler C. A., Trevena J., 2001, *ApJ*, 556, 121
- Kim J.-h., Krumholz M. R., Wise J. H., Turk M. J., Goldbaum N. J., Abel T., 2013, *ApJ*, 775, 109
- Kobulnicky H. A., Kewley L. J., 2004, *ApJ*, 617, 240
- Leroy A. K., et al., 2009, *AJ*, 137, 4670
- Lilly S. J., Carollo C. M., Pipino A., Renzini A., Peng Y., 2013, *ApJ*, 772, 119
- Macciò A. V., Dutton A. A., van den Bosch F. C., Moore B., Potter D., Stadel J., 2007, *MNRAS*, 378, 55
- Mannucci F., Cresci G., Maiolino R., Marconi A., Gnerucci A., 2010, *MNRAS*, 408, 2115
- Martin P., Roy J.-R., 1994, *ApJ*, 424, 599
- Masters K. L., et al., 2012, *MNRAS*, 424, 2180
- Minchev I., Famaey B., Combes F., Di Matteo P., Mouhcine M., Wozniak H., 2011, *A&A*, 527, A147
- Mo H. J., Mao S., White S. D. M., 1998, *MNRAS*, 295, 319
- Moran S. M., et al., 2010, *ApJ*, 720, 1126

- Moran S. M., et al., 2012, *ApJ*, 745, 66
- Moustakas J., Kennicutt Jr. R. C., Tremonti C. A., Dale D. A., Smith J.-D. T., Calzetti D., 2010, *ApJS*, 190, 233
- Navarro J. F., Frenk C. S., White S. D. M., 1997, *ApJ*, 490, 493
- Osterbrock D. E., Ferland G. J., 2006, *Astrophysics of gaseous nebulae and active galactic nuclei*
- Pagel B. E. J., 1997, *Nucleosynthesis and Chemical Evolution of Galaxies*
- Peng C. Y., Ho L. C., Impey C. D., Rix H.-W., 2002, *AJ*, 124, 266
- Pérez-Montero E., 2014, *MNRAS*, 441, 2663
- Petit A. C., Krumholz M. R., Goldbaum N. J., Forbes J. C., 2015, *MNRAS*, 449, 2588
- Pichon C., Pogosyan D., Kimm T., Slyz A., Devriendt J., Dubois Y., 2011, *MNRAS*, 418, 2493
- Pilyugin L. S., Mattsson L., 2011, *MNRAS*, 412, 1145
- Pilyugin L. S., Grebel E. K., Zinchenko I. A., Kniazev A. Y., 2014, *AJ*, 148, 134
- Rich J. A., Torrey P., Kewley L. J., Dopita M. A., Rupke D. S. N., 2012, *ApJ*, 753, 5
- Rosales-Ortega F. F., Sánchez S. F., Iglesias-Páramo J., Díaz A. I., Vílchez J. M., Bland-Hawthorn J., Husemann B., Mast D., 2012, *ApJ*, 756, L31
- Roškar R., Debattista V. P., Quinn T. R., Stinson G. S., Wadsley J., 2008, *ApJ*, 684, L79
- Rupke D. S. N., Kewley L. J., Barnes J. E., 2010, *ApJ*, 710, L156
- Sánchez S. F., et al., 2013, *A&A*, 554, A58
- Sánchez S. F., et al., 2014, *A&A*, 563, A49
- Sánchez S. F., et al., 2015, *A&A*, 573, A105
- Skibba R. A., et al., 2012, *MNRAS*, 423, 1485
- Stewart K. R., Brooks A. M., Bullock J. S., Maller A. H., Diemand J., Wadsley J., Moustakas L. A., 2013, *ApJ*, 769, 74
- Torrey P., Cox T. J., Kewley L., Hernquist L., 2012, *ApJ*, 746, 108
- Tremonti C. A., et al., 2004, *ApJ*, 613, 898
- Vila-Costas M. B., Edmunds M. G., 1992, *MNRAS*, 259, 121
- Walter F., Brinks E., de Blok W. J. G., Bigiel F., Kennicutt Jr. R. C., Thornley M. D., Leroy A., 2008, *AJ*, 136, 2563
- Wang J., et al., 2011, *MNRAS*, 412, 1081
- Wang J., et al., 2012, *MNRAS*, 423, 3486
- Wang J., et al., 2013, *MNRAS*, 433, 270
- Wang J., et al., 2014, *MNRAS*, 441, 2159
- Weinzirl T., Jogee S., Khochfar S., Burkert A., Kormendy J., 2009, *ApJ*, 696, 411
- White S. D. M., Rees M. J., 1978, *MNRAS*, 183, 341
- Wuyts E., et al., 2014, *ApJ*, 789, L40
- York D. G., et al., 2000, *AJ*, 120, 1579
- Zaritsky D., Kennicutt Jr. R. C., Huchra J. P., 1994, *ApJ*, 420, 87

## Appendices

### A Comparison of metallicity indicators

In Section 4.3 we discuss a variety of methods for determining metallicity. We shall now discuss the similarities and differences between these methods and justify the use of our primary method that uses the CL01 models.

In Fig. 2.7 we present metallicities derived from the CL01, KK04 and NS methods. It should be immediately apparent that large (0.6 dex) systematic offsets in metallicity exist between these methods. The CL01 and KK04 methods, both derived from theory, produce

largely consistent metallicities. However, they report much higher metallicities than those from the NS method, which is derived empirically. It is also noticeable that the NS method produces shallower profiles than the CL01 models. Of course disparities between metallicity indicators are not unique to this work and they have been well documented by Kewley & Ellison (2008) and Moustakas et al. (2010).

Although it is not desirable to have absolute and relative differences between metallicity methods, we assert that this is of no major significance provided the metallicity indicators are consistent. In other words, a galaxy with a steeper profile in one method should yield a steeper profile in all methods. We test this assumption by fitting simple straight-line models to metallicity profiles derived from different methods, and compare the inferred gradients. In Fig. 2.11 we show the gradients inferred from the CL01 method versus KK04, NS and D13 methods. We note the strongest correlation exists between the CL01 and D13 models, indicating our results are not strongly dependant on the photoionization models employed. However, particularly remarkable is the similarity between CL01 and NS gradients, since the NS method is empirically calibrated. We note that the KK04 method often produces shallower gradients than CL01. Indeed it appears that the KK04 methods can produce much higher metallicities than CL01 in the outskirts of the galaxies (e.g. BD 50). This is often associated with significant differences in inferred dust attenuation strengths, with the standard Case B method, producing erratic results between adjacent bins. Nevertheless we derive comfort in using our CL01 metallicities as our default method for metallicity determination.

## B Gas surface density estimates

In Section 4.4 we use a technique developed by B13 to estimate gas surface mass densities from optical lines. It was shown there that when most of the lines in the optical spectrum are available it is possible to use photoionization models with a flexible treatment of metal depletion to place constraints on the gas surface mass density of galaxies.

This works because emission line ratios are sensitive to temperature and since metals are very important coolants, changing their depletion factor at fixed metallicity,  $Z$ , changes the temperature in the gas noticeably. Exploiting this fact, B13 showed that it is possible to place constraints on the dust-to-metal ratio,  $\xi$ , of ionised gas using only optical emission lines. When combined with an estimate of metallicity and the dust optical depth, primarily from Balmer lines, and a simple model for the interstellar medium of a galaxy they show that total gas surface mass densities can be estimated through

$$\Sigma_{\text{gas}} = 0.2 \frac{\tau_V}{\xi Z} M_{\odot} \text{pc}^{-2}. \quad (2.16)$$

We have calculated this quantity for each spatial bin in the spectra discussed in this paper.

We shall now provide an additional check of these spectroscopic  $\Sigma_{\text{gas}}$  estimates. In Wang et al. (2014), herein referred to as W14, azimuthally averaged  $\Sigma_{\text{gas}}$  were calculated. These were computed by combining the observed H I surface density with an estimated contribution from H<sub>2</sub>. The H<sub>2</sub> component was estimated using a SF scaling relation applied to the observed SFRs. In Fig. 2.12 we show a few select examples of our spectroscopic gas profile against those from W14. These galaxies were selected to span a range from very poor to very good agreement. Overall the match between the two estimators is reasonable given the differences in analysis and that the profiles from W14 are azimuthally averaged while the spectrally determined gas surface densities originate from long-slit spectra.

Nevertheless, it is noticeable that the spectroscopically determined gas surface densities do not show a strong drop in the outer regions of the galaxies. This is possibly due to a characteristic of the B13 method that is not discussed in detail by B13 (but see their fig. 15),

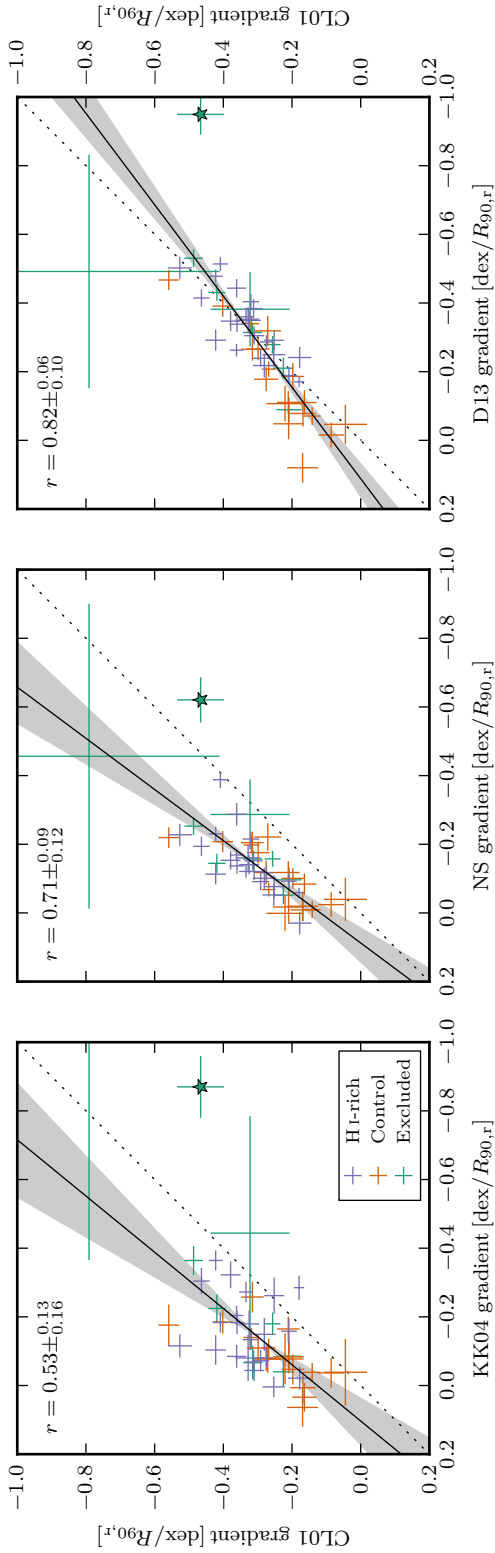


Figure 2.11: Comparison of straight-line gradients derived for CL01 against three difference metallicity indicators (KK04, NS and D13), for all 50 Bluedisk galaxies, HI-rich (blue), control (orange) and excluded (green). Linear fit, using orthogonal-distance regression, is shown (solid line) and the shaded region indicates the associated error in the slope. The dotted line indicates equal  $x=y$  mapping. The Spearman's rank correlation coefficient is given in the top-left corner of each figure. A star indicates BD 39, which is excluded from the regression and  $r$ -statistic computation, due to its companion galaxy. Median values and  $\pm 1\sigma$  errors on statistics and gradients are computed by bootstrapping Monte-Carlo-scattered resampled data. For reference,  $r = 0.34$  is the one-tailed Spearman's  $r$ -value at a  $\alpha = 0.01$  significance level.

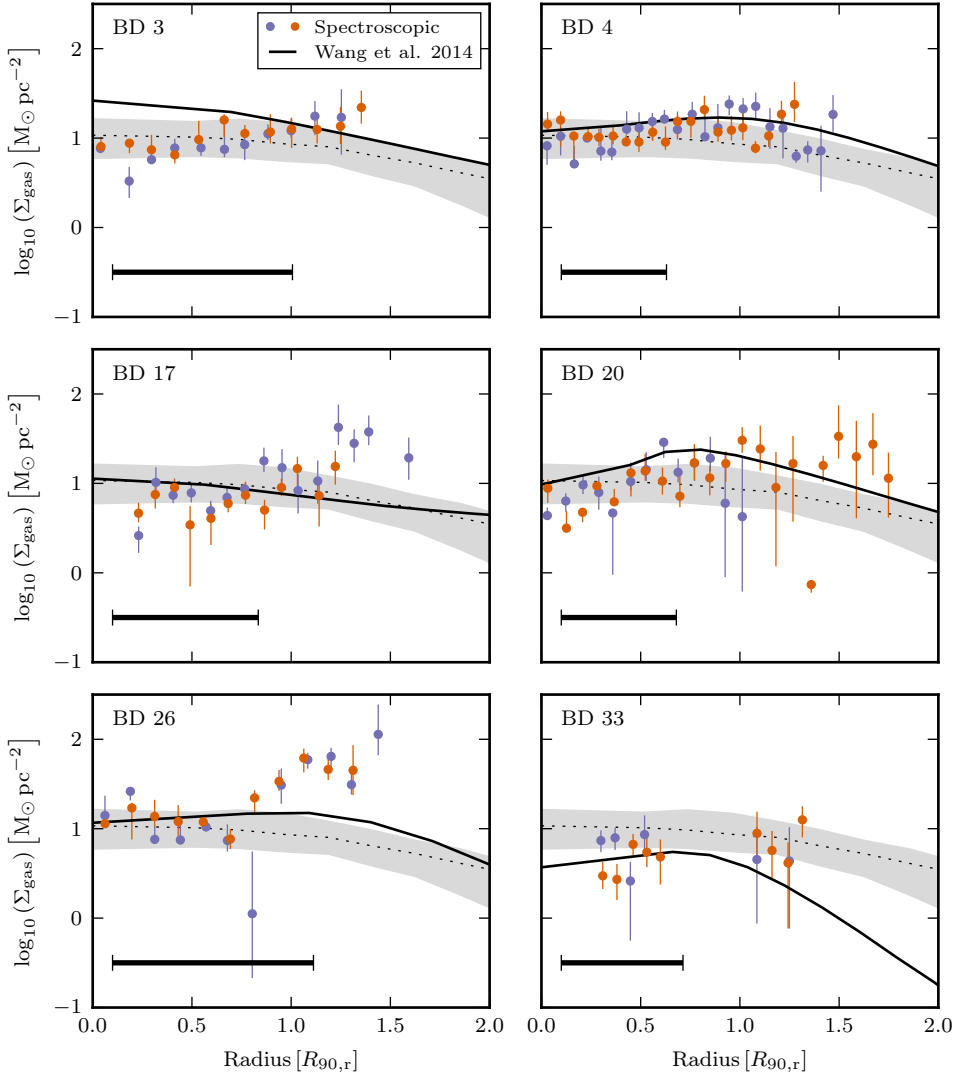


Figure 2.12: Comparison of gas density profiles of six galaxies using two different estimators. The spectroscopic  $\Sigma_{\text{gas}}$  estimates are represented by blue and orange data points, with the two colours distinguishing either side of the spectroscopic slit. The azimuthally averaged  $\Sigma_{\text{gas}}$  estimates from W14 are shown as a solid black line. We also show the  $\Sigma_{\text{gas}}$  profile averaged over all galaxies presented in W14. These are plotted as a dotted black line and a grey shaded area indicating the median and  $\pm 1\sigma$  quantile range, respectively. In the bottom-left corner of each plot, a thick black bar indicates the scale of 13 arcsec which roughly approximates the resolution limit of the W14 estimates.

namely that it might give a biased estimate of the *average* gas surface density in the outer regions of galaxies. The reason for this is that the method only works reliably when there is a clear emission line source, in practice an H II region in the spectral aperture. In the outskirts of galaxies these regions are fewer and tend to coincide with peaks in the local gas density. But these peaks provide biased estimates of the azimuthally averaged gas surface density at those radii so the spectroscopic method will also provide biased estimates.

To illustrate this fact, Fig. 2.13 shows the azimuthally averaged H I gas profiles for two large nearby spiral galaxies, NGC 628 and M 101 as black solid lines. The H I maps were taken from Walter et al. (2008). To illustrate the effect of probing the gas density at the location of H II regions in the outer disks we overplot the H $\alpha$  weighted H I profiles as orange symbols on top. The open symbols are for annuli where the mean SFR is  $< 10^{-3} M_{\odot} \text{yr}^{-1} \text{kpc}^{-2}$ , assuming a Salpeter initial mass function and the L(H $\alpha$ ) to SFR conversion factor of (Kennicutt 1998). We took the H $\alpha$  maps from Hoopes et al. (2001).

What is noticeable is that the two galaxies are rather different with the H $\alpha$  weighted profile in NGC 628 being very close to the straight mean profile. In contrast the H $\alpha$ -weighted profile in M101 is noticeably higher than the mean profile and it is also clear that star formation at large radii is connected to relatively high gas densities.

Nevertheless, the differences between two estimators of  $\Sigma_{\text{gas}}$  do not strongly impact on our analysis using the local gas regulator model (Section 6.2). This is demonstrated in Fig. 2.14, which highlights the relatively minor effect of the choice of gas-density estimator on our conclusions. The reason for the lack of significant difference is that the local gas regulator models depends on the ratio of gas-to-stellar mass. Across a galaxy the dynamic range of the stellar-mass density is much greater than that of the gas-mass density. Therefore the overall shape of the metallicity profile is primarily set by the stellar-mass density profile.

## C Metallicity profiles equally weighed by galaxy

In Section 5.2.1 we produce stacked metallicity profiles. As each data point receives an equal weight within a bin. Galaxies with many data points may, however, dominate a bin. If these galaxies have atypical metallicity profiles, this would be mimicked in the stacked profile. Such problems are only likely to arise in the outermost radial bin of a stack. To qualify and counteract this effect we also produce stacked profiles we use a weighted median, where data points are each weighted inversely to the number of data points from the same galaxy per bin.

In Fig. 2.15 we reproduce Fig. 2.9 with this new weighting. The only appreciable difference occurs in the for some control sample stacks, where the outermost metallicity is never lower than the metallicity of the H I-rich galaxies. Since these bins are dominated by a few galaxies, they may not be representative of the whole sample.

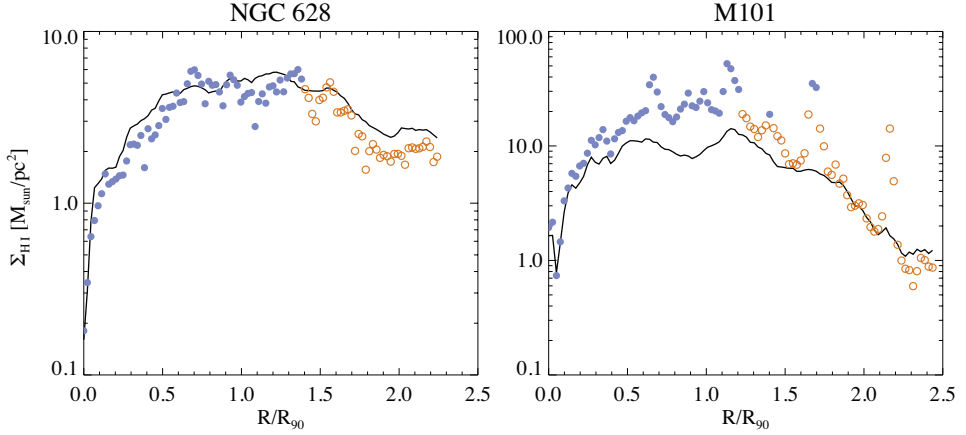


Figure 2.13: The azimuthally averaged H I gas density in galaxy disks (solid black line), compared to the H $\alpha$  flux weighted density (blue filled circles). The left panel shows the results for NGC 628 with the right-hand panel that of M 101. The orange open circles indicate annuli where the average SFR is  $< 10^{-3} M_{\odot} \text{yr}^{-1} \text{kpc}^{-2}$ .

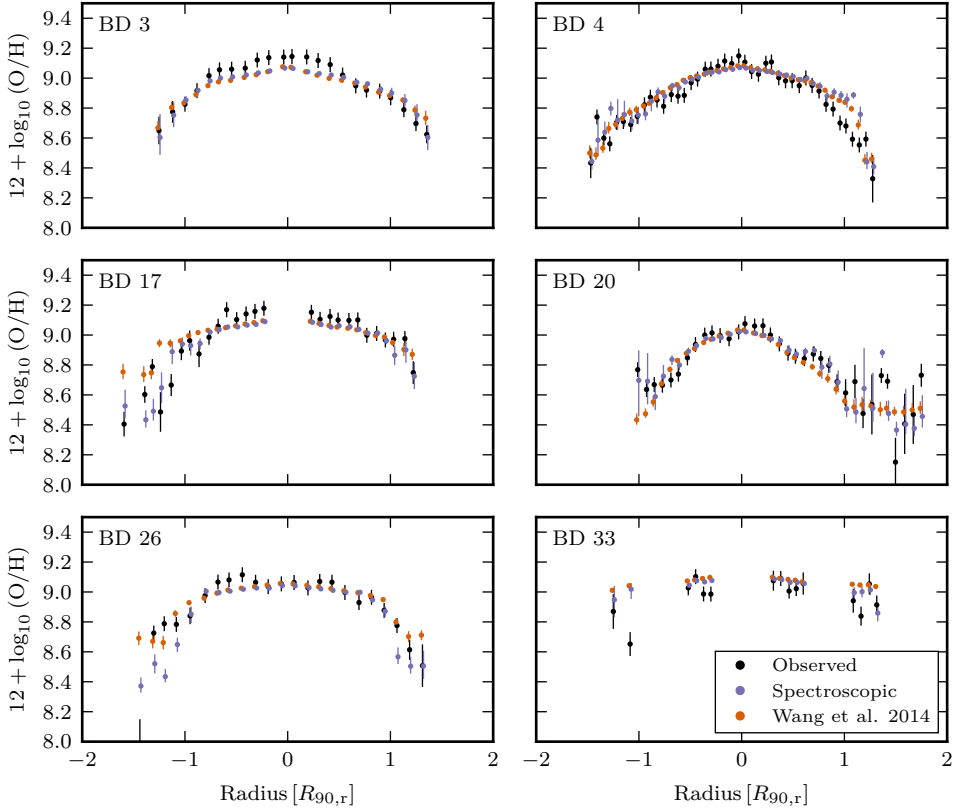
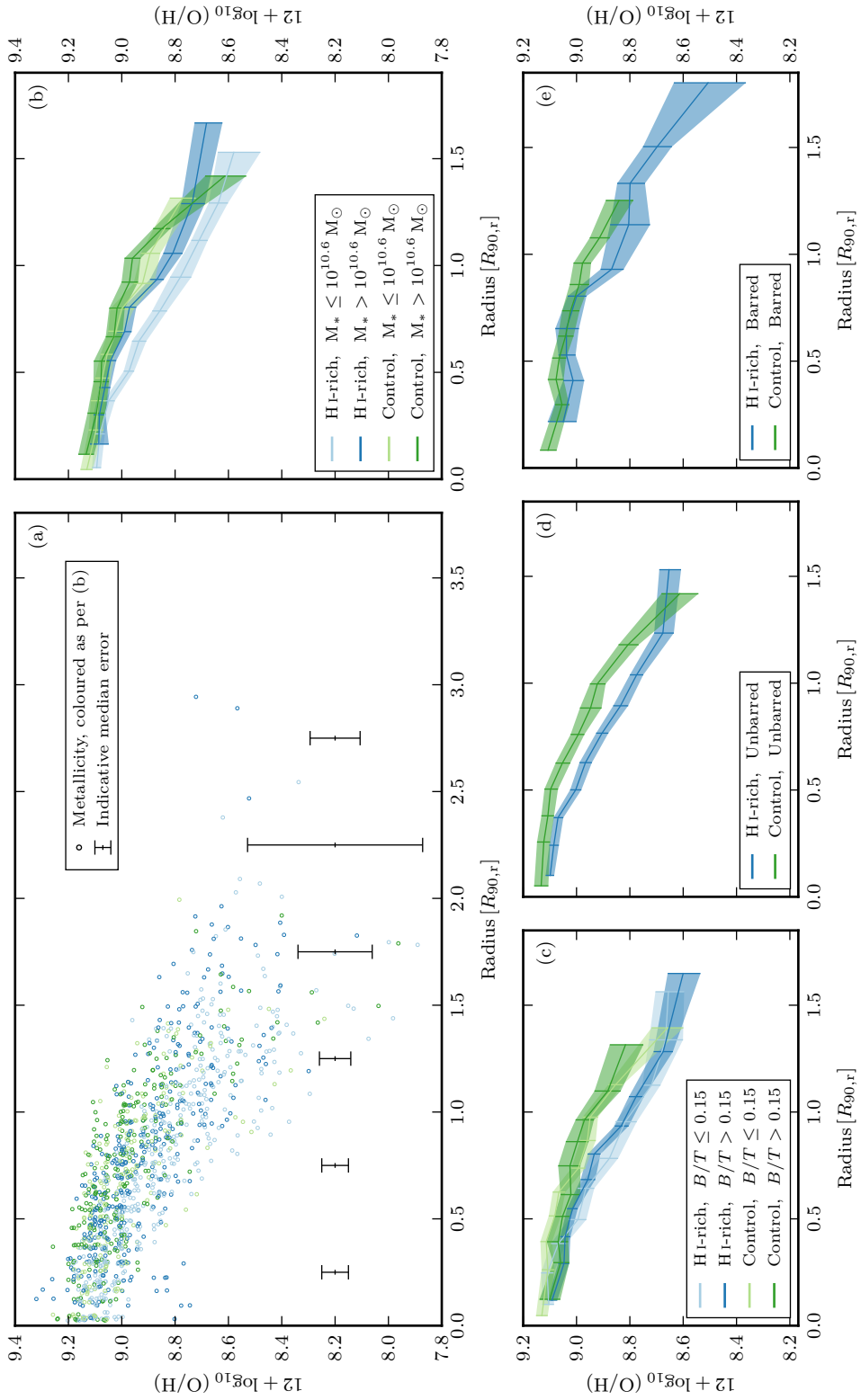


Figure 2.14: Comparing the effects of two gas density estimators on the local gas regulator model. The observed CL01 metallicity is shown in black. The model using spectroscopic  $\Sigma_{\text{gas}}$  estimates is shown in blue. The equivalent model using W14  $\Sigma_{\text{gas}}$  estimates is shown in orange. Both models assume the modelling scenario with winds.



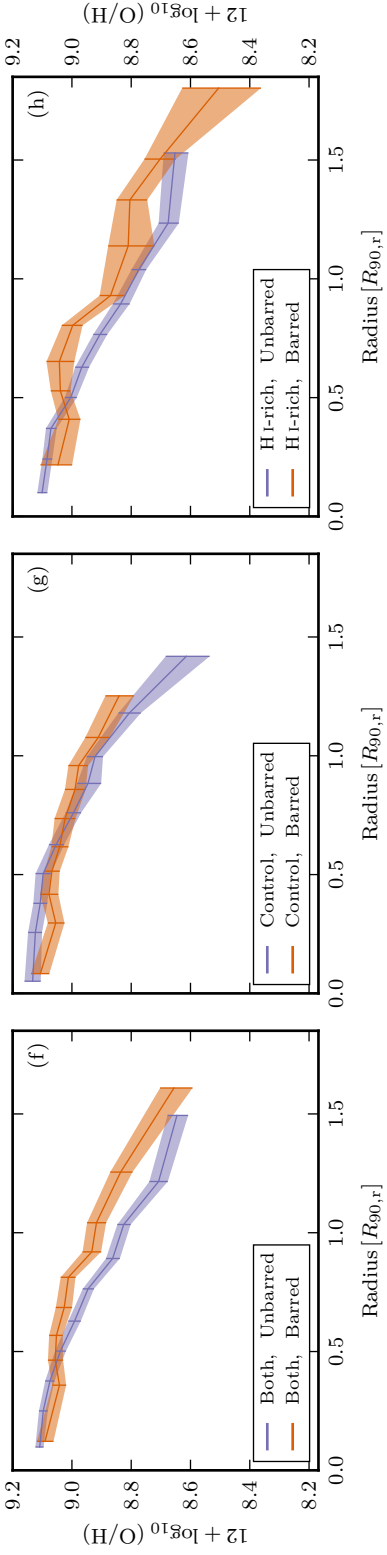


Figure 2.15: Equivalent of Fig. 2.9 but weighted such that each galaxy receives equal weight per bin. See Fig. 2.9 for description.



# 3

---

## *Inferring gas-phase metallicity gradients of galaxies at the seeing limit: A forward modelling approach*

---

We present a method to recover the gas-phase metallicity gradients from integral field spectroscopic (IFS) observations of barely resolved galaxies. We take a forward modelling approach and compare our models to the observed spatial distribution of emission line fluxes, accounting for the degrading effects of seeing and spatial binning. The method is flexible and is not limited to particular emission lines or instruments. We test the model through comparison to synthetic observations and use downgraded observations of nearby galaxies to validate this work. As a proof of concept we also apply the model to real IFS observations of high-redshift galaxies. From our testing we show that the inferred metallicity gradients and central metallicities are fairly insensitive to the assumptions made in the model and that they are reliably recovered for galaxies with sizes approximately equal to the half width at half maximum of the point-spread function. However, we also find that the presence of star forming clumps can significantly complicate the interpretation of metallicity gradients in moderately resolved high-redshift galaxies. Therefore we emphasize that care should be taken when comparing nearby well-resolved observations to high-redshift observations of partially resolved galaxies.

David Carton, Jarle Brinchmann, Maryam Shirazi, Thierry Contini, Benoît Epinat,  
Santiago Erroz-Ferrer, Raffaella A. Marino, Thomas P. K. Martinsson, Johan Richard,  
Vera Patrício

2017, *MNRAS*, 468, 2140

# 1 Introduction

It is well known that star forming galaxies present a moderately tight relation between their stellar masses and their star formation rates (e.g. Brinchmann et al. 2004; Noeske et al. 2007; Whitaker et al. 2014). Further it has been well established that the star formation rates of these galaxies is correlated with their gas content (e.g. Kennicutt 1998b; Bigiel et al. 2008; Genzel et al. 2010), but that these gas reservoirs are insufficient to sustain star formation periods  $> 0.7$  Gyr (Tacconi et al. 2013). It has been suggested that galaxies grow in a regulated fashion which maintains an equilibrium between these quantities, where the star formation rate is limited by the supply and removal of gas (inflows/outflows) (Bouché et al. 2010; Davé et al. 2012; Lilly et al. 2013). Therefore to understand how galaxies form and evolve we should study gas flowing into and out from galaxies.

Gas-phase metallicity<sup>1</sup> provides an indirect tracer of gas flows in galaxies. While gas-phase metallicity does not directly track the volume of gas in a galaxy, it does, however, indicate the origin of the gas. To understand this it is often helpful to consider metallicity in the context of two other fundamental observables: the star-formation rate, and the stellar mass. Both gas-phase metallicity and stellar mass track a similar quantity, the time-integrated star-formation history. However, the presence of gas flows will cause the metallicity and stellar mass to diverge from a simple one-to-one relation.

Inflows and outflows can both have similar effects, both lowering the observed metallicity, one introduces metal-poor gas into the system, whilst the other preferentially expels metals entrained in winds (see Veilleux et al. 2005). Studying the interplay of the star formation rate, stellar mass, and gas-phase metallicity is imperative to understanding the relation to the regulated growth of galaxies (e.g. Lilly et al. 2013; Ma et al. 2016).

By examining the metallicity gradients of massive ( $\gtrsim 10^8 M_{\odot}$ ) low-redshift galaxies it has been found that the centres of galaxies are more typically metal-rich than their outskirts (Vila-Costas & Edmunds 1992; Zaritsky et al. 1994). Furthermore it is often claimed that when normalized for disc scale-length, the same (common) metallicity gradient is found in all isolated galaxies (Sánchez et al. 2014; Ho et al. 2015). This is not, however, the case for interacting or non-isolated galaxies, for which the metallicity profiles are typically shallower (Rich et al. 2012). In these cases Rupke et al. (2010) have suggested that galaxy-galaxy interactions have triggered strong radial flows of gas towards the galaxy centre which act to temporarily erase the common metallicity gradient.

There are numerous reports of high redshift ( $z \gtrsim 1$ ) galaxies having inverted (positive) metallicity gradients (e.g. Queyrel et al. 2012; Jones et al. 2013; Leethochawalit et al. 2016). However, this phenomenon for galaxies to have central regions more metal poor than their outskirts is not normally observed in low redshift galaxies. It has been suggested that anomalously metal-poor centres may be a result of low-metallicity gas being deposited in the inner regions of galaxies: either via cold flow accretion (e.g. Cresci et al. 2010; Mott et al. 2013; Troncoso et al. 2014) or the transport of gas from the outer disc (Queyrel et al. 2012). Support for these ideas comes with the indication that the metallicity gradient is correlated with the specific star-formation rate, with the trend for aggressively star-forming (starbursting) galaxies to possess flatter (less negative) or even positive metallicity gradients (Stott et al. 2014). This could be consistent with low redshift results that interacting galaxies exhibit flatter metallicity gradients, since interacting galaxies often show elevated star formation activity.

Measuring the metallicity gradients of high-redshift galaxies is not straightforward as one has to contend with the effects of seeing (e.g. Mast et al. 2014). Observing strongly lensed

---

<sup>1</sup>Throughout this work we use metallicity, gas-phase metallicity and oxygen abundance,  $12 + \log_{10}(\text{O}/\text{H})$ , interchangeably.

galaxies has proven to be a successful approach for overcoming the loss of resolution (e.g. Yuan et al. 2013). However, with lensing alone it is hard to survey the larger galaxy population, and in particular assess environment effects. Therefore, as a complement, we should attempt to derive the metallicity gradients of barely resolved galaxies, correcting for the effects of seeing. In recent surveys Stott et al. (2014) and Wuyts et al. (2016) use integral field spectroscopy (IFS) to provide metallicity gradients for a large sample of  $0.6 < z < 2.6$  galaxies. After measuring the seeing corrupted metallicity gradients they applied a correction factor to infer the true uncorrupted metallicity gradient. Here we will present a similar, but inverse approach for deriving the true metallicity gradient in galaxies from IFS observations. Instead of applying an a posteriori correction we propose a forward modelling approach in which we directly fit a model to the emission-line flux data. From this model we can derive both the true metallicity gradient and its associated uncertainty. Unlike previous methods, our approach is flexible and is not limited to a particular set of emission lines. Our method can therefore be applied to galaxies observed over a variety of redshifts and/or with different instruments.

This paper is dedicated to outlining and testing a model which we shall apply in future work using the Multi Unit Spectroscopic Explorer (MUSE) (Bacon et al. 2010, and in prep.).

We structure the paper as follows. Section 2 provides a detailed description of our method. Afterwards we perform a comprehensive series of tests to analyse our model (Section 3). In Section 4 we apply our method to real data and discuss some characteristics of the model. Finally we summarize our results in Section 5. Throughout the paper we assume a  $\Lambda$ CDM cosmology with  $H_0 = 70 \text{ km s}^{-1} \text{ Mpc}^{-1}$ ,  $\Omega_m = 0.3$  and  $\Omega_\Lambda = 0.7$ .

## 2 Model Description

We are interested in measuring the metallicity gradients of distant galaxies. However, our observations are often limited by the resolution of the telescope. The point spread function (PSF) can have two effects on the metallicity gradient. Firstly we expect that the larger the PSF, the flatter the observed metallicity gradient will be. However, the PSF is also wavelength dependent and will alter the emission-line ratios and ultimately the derived metallicity in a complex manner. Applying an a posteriori correction to infer the true metallicity gradient would be non-trivial. Here we present the opposite approach whereby we construct a model galaxy with a given metallicity profile and predict the 2D flux distribution. We can fit the predicted fluxes to the observed fluxes and thereby find the best-fit metallicity gradient. In this section we will describe this model and fitting procedure.

### 2.1 Simulating Observations

We shall now outline the workflow that we use to simulate observations, i.e. how we project the model from the source plane to the observed flux. At this point we will not concern ourselves with the physical properties (metallicity etc.) of the galaxy model itself.

To address the problem outlined above, our simulated observations must propagate the effects of seeing. In addition, however, we must also mimic the aggregation (or “binning”) of spaxels<sup>2</sup>. The binning of spaxels is often required to increase the signal-to-noise ratio (S/N) of the data, but at the cost of further spatial resolution loss.

We shall now describe our model. To accompany this text we show a schematic outline of the model in Fig. 3.1. Our methodology is as follows:

---

<sup>2</sup>spatial pixel

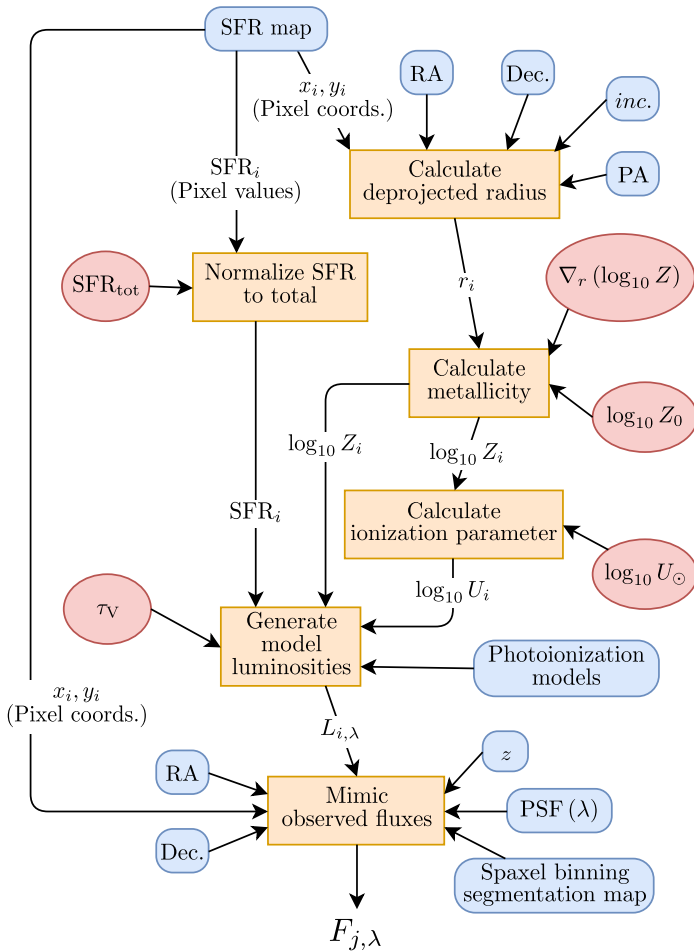


Figure 3.1: Directed acyclic graph outlining the model workflow for generating model fluxes  $F_{j,\lambda}$ . Fixed model inputs are represented as blue rectangles with rounded corners. The five free parameters to the model are shown as red ellipses. Computation steps within the model are drawn as yellow rectangles.  $i^{\text{th}}$  subscripts denote values assigned for each pixel in the input SFR map.

- (i) The galaxy is initialized from a star formation rate (SFR) map. This map is a 2D Cartesian grid which lies in the plane of the sky. For simplicity we treat each pixel to be represented by a point source situated at the centre of the pixel, and with a star formation rate (SFR) equal to that of the whole pixel. In practice, to ensure the model is well-sampled, we will oversample our SFR maps by a factor two or three.
- (ii) We use the galaxy model to associate a set of emission line luminosities to each point source. We project each point source through the galaxy model (the galaxy lies in a plane inclined with respect to the observer). Given the projected galaxy-plane coordinates and the SFR, the galaxy model generates a list of emission line fluxes as a function of position in the galaxy. (The details of the galaxy model will be given in Section 2.3).
- (iii) We now simulate image pixelization and PSF effects. An output image pixel grid is constructed with same geometry as that of the observed image. We calculate the distance from each point source to the centre of each pixel. By evaluating the PSF at these distances we can approximate how much flux is diffused from each point source into each output pixel.
- (iv) To mimic the effects of aggregating spaxels together to increase the S/N, we also coadd the model pixels to match the exact binning that was applied to the data.

In step (ii) we project source coordinates into the galaxy model plane. This requires four morphological parameters: the Right Ascension (RA) and Declination (Dec.) of the galaxy centre, the inclination (inc.) of the galaxy, and the position angle (PA) of the major axis on the sky. Partly for reasons of computational efficiency these morphological parameters are fixed a-priori. The galaxy morphology can, for example, be determined from either high-resolution imaging or the kinematics of the ionized gas. When fitting the model we will need to repeat steps (ii)–(iv) many times. We can, however, vastly reduce the computation time if we cache the mapping operations (steps (iii) & (iv)) as a single sparse<sup>3</sup> matrix.

So far we have only outlined how we simulate observations. We have not yet touched upon how the emission-line luminosities are generated. Our methodology divides this into two separate components: an SFR map and the galaxy model (i.e. steps (i) & (ii), respectively). Essentially, the former describes the 2D spatial emission-line intensity distribution, and the latter the 2D line-ratio distribution. In the following sections we will describe both these components.

## 2.2 Star Formation Rate (SFR) Maps

Nebular emission lines are associated with the H II regions that surround young massive stars. We therefore need to model the spatial SFR distribution. The simplest approach would be to assume that the star formation rate density declines exponentially with radius, but while this might be an acceptable approximation, it is difficult for any parametric model to accurately describe the SFR distribution of a galaxy. We shall later show that the clumpy nature of the SFR can have important consequences for the metallicity profile that we infer (see §3.2). If a realistic (and reliable) empirical map of the SFR can be obtained then we should input this into the modelling. In Appendix D we describe how these maps can be obtained in practice. It is important to note that the map should have higher resolution than the data we are modelling.

The SFR map is not, however, entirely fixed a priori; to allow some flexibility in the model fit we shall allow one free parameter in the SFR. We introduce a normalization constant, the

<sup>3</sup>The matrix is sparse as we only actually evaluate the PSF in step (iii) for the closest pairs of point sources and output pixels. The maximum evaluation distance is chosen to enclose 99.5% of the PSF.

total star formation rate ( $\text{SFR}_{\text{tot}}$ ) which is used to rescale the SFR map, and thereby it also rescales the emission-line luminosities without altering the line ratios in any way.

## 2.3 The Galaxy Model

In our model we describe a galaxy as a series of H II regions, each with a SFR set by the input SFR map. We assume the galaxy is infinitesimally thin, lying in an inclined plane. Apart from the SFR distribution, the galaxy model is axisymmetric. I.e. the emission line ratios only depend on one coordinate,  $r$ , the galactocentric radius.

There are three H II region properties in our model which set the observed line-ratios: metallicity, ionization parameter, and attenuation due to dust. We shall now describe the radial parametrizations of these components.

### 2.3.1 Metallicity and Ionization Parameter

The physical properties of H II regions determine the observed emission-line intensities. Varying elemental abundances alters the cooling rate of an H II region and thereby impacts upon the thermal balance of the H II region. Temperature sensitive emission line ratios have long been used to infer the abundances of an H II region (Aller & Liller 1959). However, metallicity does not single-handedly control the emission-line intensities of H II regions. Indeed the line-ratios will be affected by variations in the electron density and changes due to the ionizing continuum spectrum (Kewley et al. 2013). Theoretical photoionization models partly encapsulate these effects in the dimensionless ionization-parameter,  $U$ , which is in effect the ratio of the number density of ionizing photons to the number density of hydrogen atoms. At fixed metallicity the largest variation in line ratios with physical properties is function of the ionization parameter (Dopita et al. 2000). So, similarly for our galaxy model we will assume that the emission line luminosities at each spatial position in the galaxy are prescribed by these two parameters: metallicity and ionization parameter. We therefore need to parametrize both metallicity and ionization parameter spatially throughout the galaxy disc.

It has long been established that the metallicity in the inner disc of low redshift galaxies is well described by simple exponential function (e.g. Moustakas et al. 2010). With this precedent, and in accordance with others (e.g. Queyrel et al. 2012), we shall adopt the same functional form

$$\log_{10} Z(r) = \nabla_r (\log_{10} Z) r + \log_{10} Z_0, \quad (3.1)$$

where  $r$  is the radius,  $\nabla_r (\log_{10} Z)$  is the metallicity gradient, and  $\log_{10} Z_0$  is the metallicity at the galaxy centre.

In contrast, the ionization parameter may depend on the local environmental conditions of the H II region, and therefore is not necessarily a simple function of galactocentric radius. It would be very computationally challenging to non-parametrically incorporate the ionization parameter into the model. We wish to have a simple one parameter description for the ionization parameter as a function of radius, but we do not wish to assume the ionization parameter to be constant throughout the galaxy. Instead we exploit a natural anti-correlation between ionization parameter and metallicity (Dopita & Evans 1986). The origin of this anti-correlation has been discussed fully in Dopita et al. (2006). But to summarize, fewer ionizing photons escape from higher metallicity stars because at higher abundances stellar winds are more opaque and the photospheres scatter more photons. These effects combined predict an anti-correlation between ionization parameter and metallicity with dependence  $U \propto Z^{-0.8}$ . In Fig. 3.2 we show the dependence of ionization parameter on metallicity for the Sloan Digital Sky Survey (SDSS; York et al. (2000)) Data Release 7 (DR7; Abazajian et al. (2009)). It is clear that the SDSS

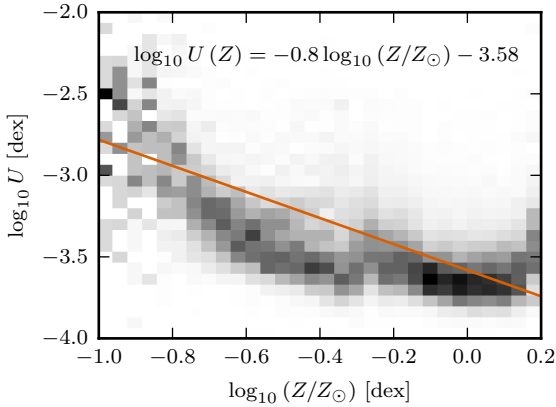


Figure 3.2: Anti-correlation in the SDSS DR7 sample between ionization parameter,  $\log_{10} U$ , and central metallicity,  $\log_{10} Z$ . SDSS galaxies show as a grey histogram. The histogram is normalized per each metallicity bin (i.e. column). The orange line indicates the best fit solution for the theoretical  $U \propto Z^{-0.8}$  dependence. To exclude active galactic nuclei (AGN) contamination we use the star-forming classification of Brinchmann et al. (2004) (with a cut on emission-line S/N > 10). To further exclude weak AGN we require that the stellar surface-mass density within the fibre is  $< 10^{8.3} M_{\odot}/\text{kpc}^2$ . Note that because of the AGN removal our sample does not extend to very high metallicities.

sample broadly follows the  $U \propto Z^{-0.8}$ , although at low metallicities ( $\lesssim -0.5$  dex) the data implies a steeper dependence and is better described with a second-order polynomial.

In our galaxy model we shall couple the ionization parameter to the metallicity using

$$\log_{10} U(Z) = -0.8 \log_{10} (Z/Z_{\odot}) + \log_{10} U_{\odot}, \quad (3.2)$$

where  $Z_{\odot}$  is solar abundance and  $\log_{10} U_{\odot}$  is the ionization parameter at solar abundance. We consider  $\log_{10} U_{\odot}$  to be constant throughout the galaxy. It has been suggested that higher redshift galaxies exhibit elevated ionization-parameters (Shirazi et al. 2014; Kewley et al. 2015), therefore we will allow the constant offset,  $\log_{10} U_{\odot}$ , to be a free parameter.

There is a second, but equally important reason for coupling the ionization-parameter to the metallicity. In a typical use case of the model, we will have a galaxy with only a limited set of emission lines observed (e.g. [O II] $_{3727,3729}$ , H $\beta$ , [O III] $_{5007}$ ). With these three emission lines the infamous R $_{23}$  degeneracy arises. See for instance McGaugh (1991) and Kewley & Dopita (2002) who provide informative discussions of this degeneracy. In this case, solving for metallicity produces two solutions, one low metallicity and the other high. Without additional information it is impossible to constrain which is the true solution. However, consider the scenario in which we simultaneously measure a high O $_{32}$  = ([O III] $_{5007}$ /[O II] $_{3727,3729}$ ) ratio, from this we would infer a high ionization-parameter. By assuming metallicity and ionization-parameter are anti-correlated we could conclude the low-metallicity (high ionization-parameter) solution to be the correct one. Our modelled galaxies therefore possess both metallicity and ionization parameter gradients, the slopes of which are anti-correlated with one another.

In this paper we adopt the photoionization models of Dopita et al. (2013, herein D13). In addition to metallicity and ionization parameter, these models introduce a third parameter,  $\kappa$ , that allows non-equilibrium electron energy distributions (Nicholls et al. 2012). We will, however, limit ourselves to the traditional Maxwell-Boltzmann case ( $\kappa = \infty$ ). These photoionization models have been computed on a grid spanning  $0.05 Z_{\odot} \leq Z \leq 5 Z_{\odot}$ <sup>4</sup> and  $-3.98 \lesssim \log_{10} U \lesssim -1.98$ . However, our above parametrization of  $Z(r)$  and  $\log_{10} U(r)$  is not explicitly bound to this region. And since we do not wish to extrapolate the photoionization

<sup>4</sup>The undepleted solar abundance of these photoionization models is  $12 + \log_{10} (\text{O}/\text{H}) = 8.69$  (Grevesse et al. 2010).

model grids, we “clip”  $Z(r)$  and  $\log_{10} U(r)$  so that they do not depart from the grid region. I.e. where  $Z(r) < 0.05 Z_{\odot}$  we set  $Z(r) = 0.05 Z_{\odot}$  and likewise where  $Z(r) > 5 Z_{\odot}$  we set  $Z(r) = 5 Z_{\odot}$ . In Appendix A we show the D13 photoionization model grids for a few standard line-ratios.

The D13 models adopt an electron density  $n_e \sim 10 \text{ cm}^{-3}$ . This is thought to be appropriate for low redshift galaxies, but this is not necessarily the case for high redshift ( $z \gtrsim 1$ ) galaxies (e.g. Shirazi et al. 2014; Sanders et al. 2016). We caution the reader that if our model is to be applied to high redshift galaxies, different photoionization models would likely be needed. Indeed, the model could easily be extended to include the electron density of the galaxy as an additional free parameter. However, since we will be applying this model to  $z \lesssim 1$  galaxies, we simply choose to fix the electron density at  $n_e \sim 10 \text{ cm}^{-3}$ .

It is also worth noting that D13 models assume that the underlying stellar population has a continuous star formation history (as opposed to a instantaneous burst). But, since we are applying our model to poorly resolved data, we are in effect averaging over many individual H II regions. Therefore, while an instantaneous burst might be most appropriate for modelling individual H II regions, we consider the continuous star-formation assumption to be more valid for our purposes.

The line fluxes are scaled to luminosities based on the SFR map, with the following scaling relation between H $\alpha$  luminosity and SFR as taken from Kennicutt (1998a)

$$\frac{L(\text{H}\alpha)}{\text{erg s}^{-1}} = \frac{1}{7.9 \times 10^{-42} \text{ M}_{\odot} \text{ yr}^{-1}} \text{ SFR}. \quad (3.3)$$

This assumes a Salpeter (1955) initial mass function, consistent with the D13 photoionization modelling.

The emission-line luminosities are computed as follows:

- (i) Evaluate the metallicity for each radial coordinate using equation 3.1 (for given values of  $\log_{10} Z_0$  and  $\nabla_r(\log_{10} Z)$ ).
- (ii) Clip  $\log_{10} Z(r)$  to the metallicity range of the photoionization model grid.
- (iii) Calculate the associated ionization parameter using equation 3.2 (for a given value of  $\log_{10} U_{\odot}$ ).
- (iv) Clip  $\log_{10} U(r)$  to the ionization parameter range of the photoionization models.
- (v) Infer the relative emission line luminosities by interpolating the photoionization grid at  $(\log_{10} Z(r), \log_{10} U(r))$ .
- (vi) Scale the emission-line luminosities appropriate for the SFR using equation 3.3.

### 2.3.2 Dust attenuation

There remains one hitherto undiscussed ingredient in the model, the attenuation due to dust. Since dust attenuation is wavelength dependent it will alter the emission-line ratios.

We adopt the dust absorption curve appropriate for H II regions as proposed by Charlot & Fall (2000)

$$L_{\text{ext}}(\lambda) = L(\lambda)e^{-\tau(\lambda)} \quad (3.4)$$

with

$$\tau(\lambda) = \tau_V \left( \frac{\lambda}{5500 \text{ \AA}} \right)^{-1.3}, \quad (3.5)$$

where  $L_{\text{ext}}(\lambda)$  and  $L(\lambda)$  are the attenuated and unattenuated luminosities respectively,  $\lambda$  is the rest-frame wavelength of the emission line, and  $\tau_V$  is the V-band (5500Å) optical depth. Thus the absorption curve is described by only one parameter,  $\tau_V$ .

The radial variation of the dust content of galaxies is not well known. For simplicity we shall therefore assume the optical depth to be constant across the whole galaxy. We discuss the appropriateness of this assumption in Section 4.3.1.

It should be noted that, even aside from the lack of radial variation, this dust model is relatively basic. We have assumed the galaxy to be infinitesimally thin, and we do not include any radiative transfer effects along the line-of-sight. Approximating the galaxy in this way as a thin disc becomes highly questionable for highly-inclined ( $\gtrsim 70^\circ$ ) galaxies and we do not claim that our model works for such edge-on systems.

### 2.3.3 Summary

We have now outlined how we assign the emission-line luminosities. All told there are five free parameters: the total star formation rate of the galaxy,  $\text{SFR}_{\text{tot}}$ , the central metallicity,  $\log_{10} Z_0$ , the metallicity gradient,  $\nabla_r(\log_{10} Z)$ , the ionization parameter at solar abundance,  $\log_{10} U_\odot$ , and the V-band optical depth,  $\tau_V$ . In the next section we discuss the fitting of our model, and the bounds we place on these parameters.

As a final cautionary note we highlight that the model only describes the nebular emission from star-forming regions. In the centres of galaxies, however, active galactic nuclei (AGN) and low-ionization nuclear emission-line regions (LINERs) can contribute significantly to the emission-line flux. Therefore this model should not be applied to galaxies that present signs of significant AGN/LINER contamination.

## 2.4 Model fitting

In the preceding sections we have described our model which we will use to derive the metallicity of barely resolved galaxies. Of the modelled parameters the most scientifically interesting are the central metallicity,  $\log_{10} Z_0$ , and the metallicity gradient,  $\nabla_r(\log_{10} Z)$ . We would like to derive meaningful errors, accounting for the degeneracies among the parameters. Such a problem naturally lends itself to a Markov chain Monte Carlo (MCMC) approach. Here we use the MULTINEST algorithm (Feroz et al. 2009; Feroz & Hobson 2008; Feroz et al. 2013) accessed through a PYTHON wrapper (Buchner et al. 2014). In light of the known degeneracies between metallicity and ionization-parameter we anticipate that the likelihood surface may be similarly degenerate. For this reason we have adopted the MULTINEST algorithm, which is efficient at sampling multimodal and/or degenerate posterior distributions.

### 2.4.1 Prior probability distributions (Priors)

For the Bayesian computation we place an initial probability distribution (prior) on each parameter. We set the priors to be all independent of one another, described as follows:

- $\text{SFR}_{\text{tot}}$ : The total SFR of the galaxy provides the overall flux normalization of the model, we place a flat prior on the interval  $[0, 100] M_\odot \text{yr}^{-1}$ . This sufficiently covers the expected range of galaxies we could observe.

It may seem more logical to adopt a logarithmic prior for this normalization constant. Adopting such a prior caused our model to converge to local minima in our highest S/N tests (§3.1.1). Real data, which has much lower S/N, will not suffer the same convergence

issues as the likelihood surface will be smoother. For consistency we adopt a uniform prior throughout this paper. This does not affect our conclusions.

- $\log_{10} Z_0$ : We place a flat prior on the central metallicity,  $\log_{10} Z_0$ , (logarithmic over  $Z_0$ ). The interval is chosen to match the full metallicity range allowed by the photoionization-model grid ( $\sim[-1.30, 0.70]$  dex).
- $\nabla_r(\log_{10} Z)$ : We set a flat prior on the metallicity gradient of galaxies spanning the range  $[-0.5, 0.5]$  dex/kpc. Current evidence suggests galaxies at high redshifts ( $z \gtrsim 1$ ) may exhibit metallicity gradients steeper than those found in lower redshift galaxies. Typically high redshift galaxies have metallicity gradients between  $-0.1$  and  $0.1$  dex/kpc, and at most  $-0.3$  dex/kpc (Leethochawalit et al. 2016). Our prior is therefore sufficiently broad to incorporate even the steepest gradients.

It should be noted that a flat prior on a metallicity gradient is not an uninformative prior. A uniform prior in gradient is *not* uniform in angle, but is biased towards steeper profiles (see VanderPlas 2014). Furthermore, a minimally informative prior would yield equal probability to find any metallicity at all radii,  $r$ . I.e. the 2D  $(r, \log_{10} Z_0)$  space should be evenly sampled. Since we clip our metallicities to a finite grid of photoionization models this is difficult to achieve perfectly. Therefore, for the simplicity of this paper we adopt a uniform prior on the metallicity gradient. The choice of this prior will have to be revisited in future work. We further discuss the effect of this prior in Appendix B.

- $\log_{10} U_{\odot}$ : The photoionization-model grid already sets bounds on the allowed values of  $\log_{10} U$ . We set a flat prior on  $\log_{10} U_{\odot}$  such that  $\log_{10} U$  can span this full range, at any metallicity. For this paper this range is  $\sim[-5.02, -1.42]$  dex. Remember that ultimately  $\log_{10} U(r)$  will be clipped to remain within the photoionization-model grid.
- $\tau_V$ : We place a flat prior on the V-band optical depth on the interval  $[0, 4]$ . This should be sufficient to include all galaxies we are interested in, which have relatively strong emission-lines.

## 2.4.2 Likelihood function

The likelihood function assigns the probability that, for a given model, we would have measured the observed emission-line fluxes.

We will have a set of observed fluxes,  $F_{\text{obs},i}$ , for each observed emission-line and for each spatial bin. Correspondingly we have a set of errors,  $\sigma_{\text{obs},i}$ , estimated from the data. Our model predicts a complementary set of fluxes,  $F_{\text{model},i}$ . Following Brinchmann et al. (2004), we additionally assign a constant 4% theoretical error,  $\sigma_{\text{model},i} = 0.04 F_{\text{model},i}$ .

We assume that the observed fluxes,  $F_{\text{obs},i}$ , are related to the true fluxes,  $F_{\text{true},i}$ , through

$$F_{\text{obs},i} = F_{\text{true},i} + \epsilon_i, \quad (3.6)$$

where the noise,  $\epsilon_i$ , is drawn from a Student's t-distribution. Our likelihood function is therefore

$$\mathcal{L}(x_1, \dots, x_n \mid \nu, \sigma_1, \dots, \sigma_n) = \prod_{i=1}^n \mathcal{L}(x_i \mid \nu, \sigma_i) \quad (3.7)$$

with

$$\mathcal{L}(x_i \mid \nu, \sigma_i) = \frac{\Gamma\left(\frac{\nu+1}{2}\right)}{\Gamma\left(\frac{\nu}{2}\right) \sqrt{\pi\nu}\sigma_i} \left(1 + \frac{1}{\nu} \left(\frac{x_i}{\sigma_i}\right)^2\right)^{-\frac{\nu+1}{2}}, \quad (3.8)$$

Table 3.1: Moffat parameters of the adopted PSF model, indicating knots of a piecewise-linear interpolation. Each wavelength has an associated full-width half-maximum size (FWHM) and a Moffat- $\beta$  parameter.

Wavelength [Å]	FWHM [arcsec]	$\beta$
4750	0.76	2.6
7000	0.66	2.6
9300	0.61	2.6

where we define the residual as

$$x_i = F_{\text{obs},i} - F_{\text{model},i}, \quad (3.9)$$

and the square of the scale parameter as

$$\sigma_i^2 = \frac{\nu - 2}{\nu} (\sigma_{\text{obs},i}^2 + \sigma_{\text{model},i}^2). \quad (3.10)$$

In this paper we assume  $\nu = 3$  degrees of freedom.

There are two motivations for adopting Student's t-distribution over the more traditional normal distribution. The first and highly practical reason is to add robustness to our fitting. Student's t-distribution is more heavily tailed than the normal distribution. Therefore outliers with large residuals will be penalized less by Student's t-distribution than by the normal distribution. Even if most of the data is well described by the normal distribution, one errant data point can have disastrous consequences on the inference. Essentially by adopting a more robust likelihood function we are trading an increase in accuracy for a decrease in precision.

The second reason for adopting Student's t-distribution is that in fact our data may indeed be better described by Student's t-distribution than the normal distribution. The emission-line fluxes are typically measured from spectra where the resolution is such that the emission line is covered only by a few wavelength elements. In this case the associated errors are calculated only from a few independent pieces of information, and hence the Student's t-distribution is more appropriate. Precisely calculating the degrees of freedom of each emission-line is difficult, although in theory can be estimated from repeat observations. For simplicity we assume the number of degrees of freedom is small, and hence we choose a constant  $\nu = 3$  degrees of freedom.

## 2.5 PSF model

There is one further aspect of the model that we have not yet discussed. The galaxy model fluxes are distributed assuming a PSF. To derive meaningful results from the best fit model it is important to input a PSF that closely matches the true seeing of the observations. The adopted PSF should therefore be driven by the data itself.

In this paper we will use MUSE observations of the Hubble Deep Field South (Bacon et al. 2015). The authors use a moderately bright star also within the MUSE field of view (FoV) to derive the PSF. The best-fit Moffat profile for this star has the parameters as given in Table 3.1. For consistency, unless otherwise specified, we will adopt this empirical model throughout this paper as our fiducial PSF.

### 3 Model Testing

In the previous section we presented our method for modelling the emission lines of distant galaxies. Before moving to the modeling of distant galaxies in the following section, we here assess the reliability of our model. Of all the modelled quantities, we are most interested in the metallicity profile, hence we will only focus on validating two of the model's parameters: the central metallicity, and the metallicity gradient. In essence we consider  $\text{SFR}_{\text{tot}}$ ,  $\log_{10} U_{\odot}$  and  $\tau_V$  all to be nuisance parameters.

Here we present two categories of tests. In the first set of tests (§3.1) we fit the model to mock data constructed using noisy realizations of the model itself. This will allow us to observe intrinsic systematics and uncover inherent limitations of our method. However, these tests cannot assess whether our model is actually a good description of a real galaxy. So, to answer this we present a second set of tests (§3.2) using mock data from downgraded observations of low redshift galaxies. With these we can study how the model performs for realistic galaxies with complex structure, violating our idealized model assumptions.

#### 3.1 Accuracy and precision tests

In order to validate our method we must minimally show that the model can recover itself. With the inclusion of noise it is not obvious that this should be the case. A combination of low S/N and resolution loss may yield highly degenerate model solutions.

In the following tests we use our model to construct simulated mock observations for a galaxy at a redshift of  $z = 0.5$ , using the PSF given in Table 3.1. We assume the star forming disc of the galaxy to have an exponentially declining star-formation rate density

$$\Sigma_{\text{SFR}} \propto e^{-r/r_d} \quad (3.11)$$

where  $r_d$  is the exponential scale-length of the disc. With our model we generate four noise-free emission-line images<sup>5</sup>. To this data we add normally distributed noise, with the standard deviation depending on the pixel flux  $F_i$  as follows

$$\sigma_i = \alpha \sqrt{F_i}, \quad (3.12)$$

where  $\alpha$  is a scaling factor. This scaling factor is the same for all emission lines. By adjusting the scaling factor we can achieve different S/N observations. We define the S/N as that of the brightest pixel in the unbinned H $\beta$  map.

We must treat the fake data as we would for real data, therefore we bin spaxels together to reach a minimum S/N = 5 in all emission lines. This binning algorithm is outlined in Appendix C.

##### 3.1.1 Varying S/N

Our solution should converge to the true solution at high S/N, but might be biased or show incorrect uncertainty estimates at lower S/N. In the following we therefore explore a range of S/N levels (S/N = 3, 6, 9, 50).

For the test we construct 50 realisations of mock data, at a given S/N ratio. For each realisation we fit the model and retrieve marginal posterior probability distributions of the two parameters of interest (the central metallicity,  $\log_{10} Z_0$ , and metallicity gradient,  $\nabla_r(\log_{10} Z)$ ). We take the median of each marginal posterior to be the best-fit solution.

<sup>5</sup>[O II]3726,3729, H $\gamma$ , H $\beta$ , and [O III]5007

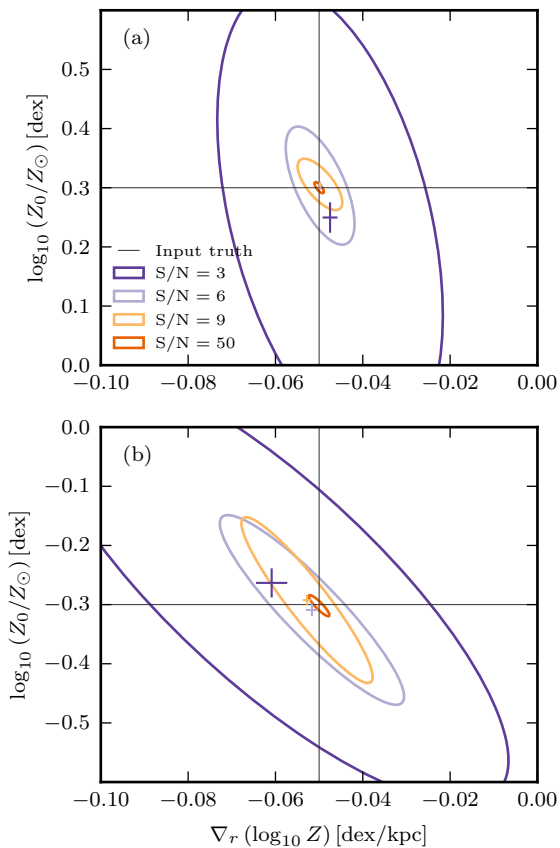


Figure 3.3: The effects of S/N on accuracy and precision of the inferred central metallicity,  $\log_{10} Z_0$ , and metallicity gradient,  $\nabla_r(\log_{10} Z)$ . Plot showing error ellipses for varying S/N, drawn such that they enclose 90% of the scatter (assuming the data to be distributed normally). Coloured error crosses indicated the means (and standard error on the mean) at each S/N level. The two different panels show this experiment for two different sets of original model inputs. In panel (a) Model inputs were  $\log_{10}(Z_0/Z_\odot) = 0.3$  dex,  $\nabla_r(\log_{10} Z) = -0.05$  dex/kpc,  $\text{SFR}_{\text{tot}} = 1 M_\odot \text{ yr}^{-1}$ ,  $r_d = 0.4''$ ,  $\log_{10} U_\odot = -3$  dex,  $\tau_V = 0.7$ . In panel (b) Model inputs identical to (a) except for  $\log_{10}(Z_0/Z_\odot) = -0.3$  dex.

In Fig. 3.3 we show the mean and scatter of these best-fit values over the 50 realizations. We provide this for a range in S/N levels, and for two slightly different input models (Panels a & b). From this we can assess that at all but the lowest S/N level there is little systematic offset of the mean from true value. For  $S/N \geq 6$  we find that bias on the central metallicity is  $< 0.01$  dex and on the metallicity gradient  $< 0.003$  dex/kpc. At  $S/N = 3$  there is some noticeable offset, but the realization-to-realization scatter is much larger. We discuss biases in more detail in Appendix B. Therein we explore a larger portion of the parameter space where strong systematic offsets can arise.

The tests here also show that there is considerable scatter in the poor  $S/N=3$  data. This is of course unsurprising, however, even the good  $S/N=9$  results in Fig. 3.3(b) show moderate scatter. Since we are performing an MCMC fit, we retrieve the full posterior probability distribution (or *posterior* for short). We can use the 50 repeat realizations to infer whether the posterior is a good estimate of this error. For each realisation we define the z-score to be the difference between the true value and the estimated mean in units of the predicted uncertainty. If the uncertainty estimates are accurate, these z-scores should be distributed as a standard normal distribution (zero mean and unit variance). In Tables 3.2 & 3.3 we summarize these z-scores for the model shown in Fig. 3.3(b). We see that the tabulated percentages are slightly smaller than would be expected. This indicates that our posteriors typically underestimate the true error. However, this is only a relatively small difference so, although not perfect, we conclude these error estimates to be acceptable. For reference we also present Q-Q plots in the appendix

Table 3.2: Percentage of 50 repeat realizations with  $\log_{10}(Z_0)$  z-scores within a given range. Associated Q-Q plot are found in the appendix (Fig. 3.15). Results here are for the model shown in Fig. 3.3(b).

S/N	$-1 \leq z < 0$	$0 \leq z < 1$	$-1 \leq z < -1$	$-2 \leq z < 2$
3	(22 ± 3)%	(46 ± 4)%	(68 ± 3)%	(98 ± 1)%
6	(28 ± 3)%	(30 ± 3)%	(58 ± 3)%	(84 ± 3)%
9	(28 ± 3)%	(26 ± 3)%	(54 ± 4)%	(88 ± 2)%
50	(30 ± 3)%	(34 ± 3)%	(64 ± 3)%	(90 ± 2)%
Expected	34%	34%	68%	95%

Table 3.3: Percentage of 50 repeat realizations with  $\nabla_r(\log_{10} Z)$  z-scores within a given range. Associated Q-Q plot are found in the appendix (Fig. 3.15). Results here are for the model shown in Fig. 3.3(b).

S/N	$-1 \leq z < 0$	$0 \leq z < 1$	$-1 \leq z < -1$	$-2 \leq z < 2$
3	(40 ± 3)%	(10 ± 2)%	(50 ± 4)%	(84 ± 3)%
6	(26 ± 3)%	(32 ± 3)%	(58 ± 3)%	(86 ± 2)%
9	(22 ± 3)%	(32 ± 3)%	(54 ± 4)%	(90 ± 2)%
50	(26 ± 3)%	(28 ± 3)%	(54 ± 4)%	(90 ± 2)%
Expected	34%	34%	68%	95%

(Fig. 3.15), comparing the z-scores to a theoretical normal distribution.

### 3.1.2 Varying PSF

The preceding section showed that at moderate to high S/N, our model is unbiased when fitting itself. These tests were performed with decent spatial resolution ( $r_d \gtrsim 0.5 \times \text{FWHM}$ ), so we will now explore the effect of degrading the PSF. To do this, we create a series of mock data with fixing the physical model parameters, but with different PSFs.

We model changes in the seeing simply through changes in the FWHM of the PSF. The wavelength dependence of the seeing is retained, and we modulate the FWHM amplitude by a multiplicative factor. The Moffat  $\beta$  parameter remains fixed. We remind the reader that our S/N is defined on the peak (unbinned) flux of the H $\beta$  emission line (§3.1), so by changing the PSF we inadvertently alter the S/N. To isolate the effects of resolution from those of S/N, we shall keep  $\alpha$  (the noise scaling factor in equation 3.12) fixed to that used for the fiducial PSF. The total flux from the galaxy remains unchanged.

In Fig. 3.4 we show the mean and scatter of 50 realizations for four different PSFs. This shows that even with significantly poorer seeing our model is still able to recover the true values with little systematic offset. However, poorer seeing will introduce information loss and the precision to which we can determine the metallicity gradient is much reduced. We caution the reader that this statement can not readily be converted into an absolute FWHM of the PSF since what is of real importance here is the relative size of the PSF to the size of the galaxy. But as a guide for the reader, the percentages in Fig. 3.4 correspond to PSFs between  $\sim 0.4$ – $1.5''$  FWHM, which should be compared to a galaxy that has a  $r_d = 0.4''$  disc scale-length (which would be typical for  $3 \times 10^{10} M_\odot$  disc galaxies at  $z = 0.75$  (e.g. van der Wel et al. 2014)).

It should be noted that the direction of the systematic offset in the poor (PSF = 200%) seeing data is actually towards a steeper metallicity gradient, rather than towards the flat gradient that one might naïvely expect. Since seeing is wavelength dependent its effects can be complicated, and therefore worse seeing may not automatically lead to a flatter inferred gradient. However, it is perhaps more likely a reflection of systematics intrinsic to the modelling and/or introduced

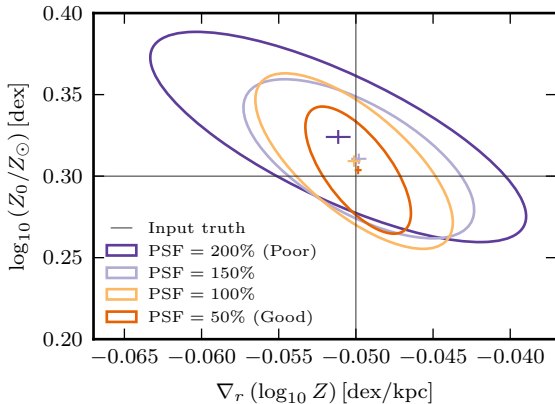


Figure 3.4: Effects of changing the PSF on the inferred central metallicity and metallicity gradient. We show error ellipses for a series of improving PSFs (see Fig. 3.3 for plot description). Here a 200% PSF indicates observations with a FWHM double that of the fiducial (100%) model. The noise scaling factor ( $\alpha$  in equation 3.12) is fixed such that the 100% model has a peak S/N = 9. We adopt the same model inputs as used Fig. 3.3(a). The disc scale-length is  $r_d = 0.4''$ .

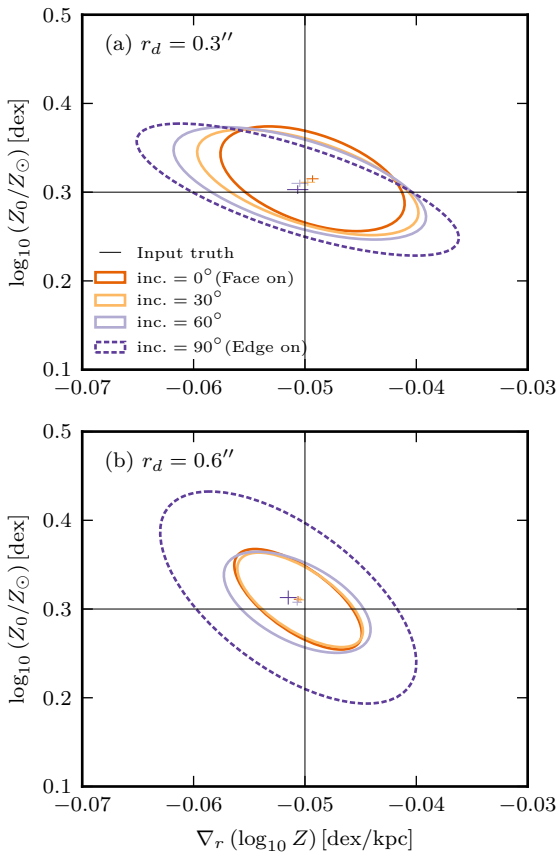


Figure 3.5: The impact of inclination on the accuracy and precision to which we can derive the central metallicity and metallicity gradient. We show error ellipses for a set of progressively more inclined models (see Fig. 3.3 for plot description). The noise scaling factor ( $\alpha$  in equation 3.12) is fixed such that the  $\text{inc.} = 0^\circ$  model has a peak S/N = 9.

by the model priors (see Appendix B).

### 3.1.3 Varying inclination

Altering the PSF is not the only way to reduce spatial information. Highly inclined (edge-on) galaxies lose considerable resolution along the minor axis. We should check that our method is able to recover the same metallicity profile for a galaxy independent of its inclination.

Again we construct a series of mock observations where the only variation is in the inclination of the galaxy. As before, in order to remove the effects of changing S/N, we fix  $\alpha$  (the noise scaling factor in equation 3.12) to that used for the fiducial inc. =  $0^\circ$  model.

In Fig. 3.5 we show the mean and scatter of 50 realizations for four different inclinations. We perform this exercise for two galaxies of different sizes ( $r_d = 0.3''$  and  $r_d = 0.6''$ ), where the smaller galaxy should be more sensitive to inclination effects. It can be seen that even in the edge-on case we are able to well recover the metallicity profile, although admittedly to a lower precision than for the face-on galaxy.

It should be stressed, however, that even though the method works for the extreme edge-on cases there are significant limitations in the galaxy model at high inclinations. Because we assume the galaxy to be infinitesimally thin, two issues arise. Firstly, at high inclinations the centres of dusty galaxies may be obscured, but since we do not include any radiative transfer effects along the line-sight the model does not reproduce this. Secondly, when a galaxy is nearly edge-on it becomes almost impossible to distinguish metallicity that varies with radius from metallicity that varies with vertical disc height. Even with high-spatial resolution observations these problems would remain. For these reasons we caution the reader that the results for highly inclined galaxies are unlikely to be relevant for real galaxies and we will limit our studies to galaxies with inclinations less than  $\sim 70^\circ$ .

The tests presented so far are not sufficient to validate our model, and indeed further tests are required. In the following section we use mock observations constructed from real observations of low redshift galaxies. This will enable us to compare our model against data that more closely resembles real, rather than idealized, galaxies.

## 3.2 Model tests with realistic data

So far we have ascertained that our method is able to recover the true metallicity profile. Although adverse conditions (low S/N and poor seeing) reduce the precision of the method, they do not significantly impact upon the accuracy. This does not, however, verify that the model is a good description of real galaxies. To address this we will fit the model to mock data generated from observations of low redshift galaxies, downgraded in both S/N and resolution.

The mock data is constructed from IFS observations of three low redshift galaxies (UGC463, NGC628, NGC4980). These galaxy were not selected especially to be representative of higher redshift galaxies (although their SFRs are comparable to those we will study). Instead these galaxies were chosen primarily owing to the availability of high quality IFS data, and because they are not highly inclined galaxies. Two of these galaxies were observed with MUSE (UGC463 and NGC4980) and the other (NGC628) was observed as part of the PPAK IFS Nearby Galaxies Survey (Sánchez et al. 2011). We construct emission-line maps<sup>6</sup> of  $H\beta$ ,  $[O III]5007$ ,  $H\alpha$ ,  $[N II]6584$  and  $[S II]6717,6731$  from these observations and convolve these maps with the seeing and bin them to the appropriate pixel scale to produce mock images. Finally noise is added and the data binned as described above (Section 3.1). In the following we define the size of the galaxies using the disc scale-length of dust-corrected  $H\alpha$  flux profile. Note that

<sup>6</sup>The exact details of how these maps are obtained are not crucial to our analysis. For a self-consistent analysis we simply require realistic mock inputs, ideally with high S/N and good spatial resolution.

the galaxy centres are defined using the stellar light *not* the nebular emission (which can be clumpy and asymmetric).

In addition to the emission-line images, our method requires a SFR map for each galaxy. Typically these SFR maps will be created from high-resolution observations. So, we generate SFR maps using the dust-corrected  $H\alpha$  maps of the low redshift galaxies. These maps are then degraded to a resolution comparable to that of the Hubble Space Telescope (HST), i.e. a Gaussian PSF with  $\text{FWHM} = 0.1''$  and pixel scale  $0.05''$ . We do not add any additional noise to the SFR maps.

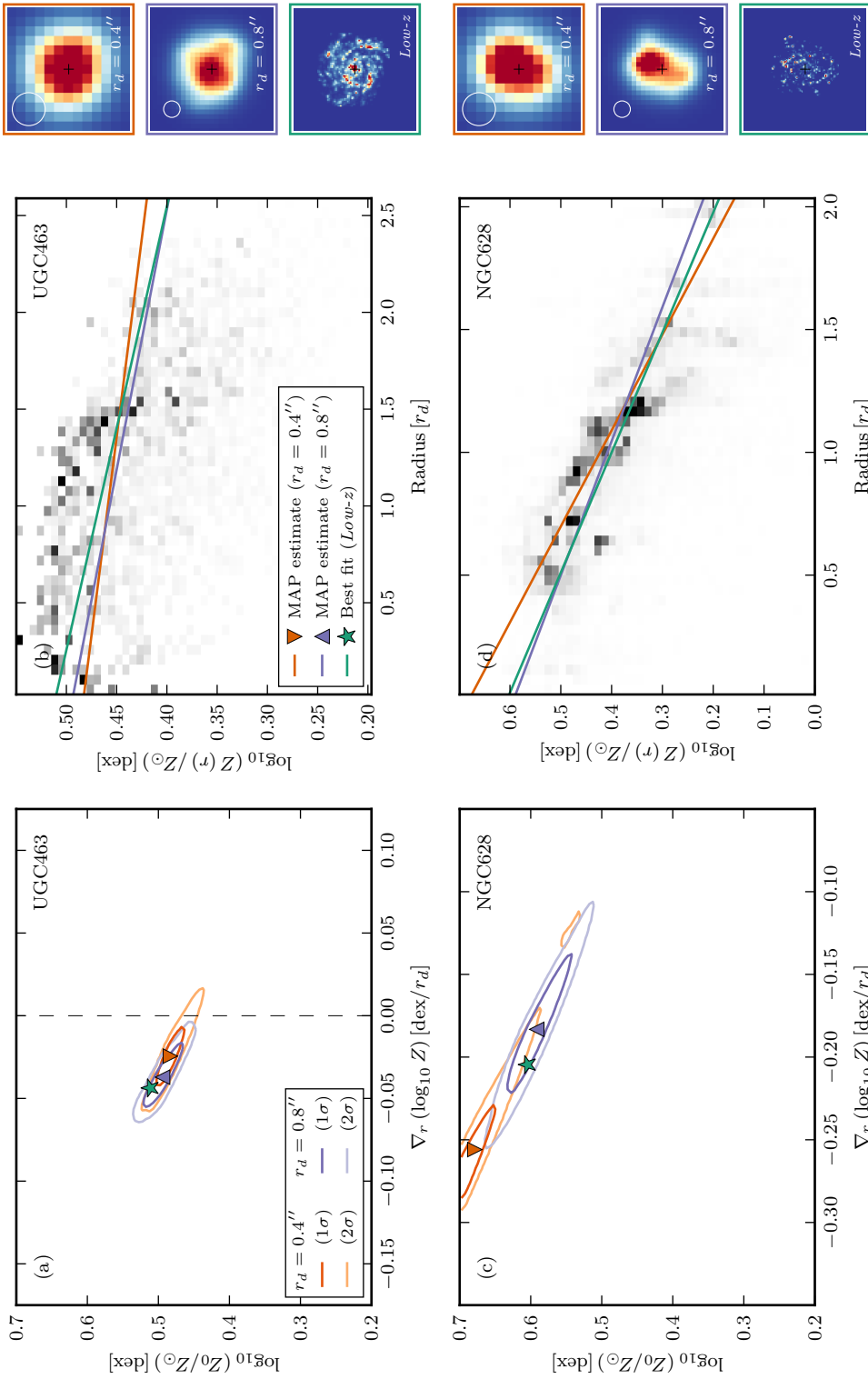
To test our ability to measure the metallicity profile of these mock observations, we run our full model fitting procedure on galaxies of two different sizes ( $r_d = 0.4''$  and  $r_d = 0.8''$ ), simulated with  $S/N = 9$ , at a redshift  $z = 0.255^7$ , and with the PSF given in Table 3.1. At this redshift  $H\beta$ , the most blueward emission line, is the most affected by seeing and has a  $\text{FWHM} = 0.7''$ . These results are then compared to the metallicity derived from the high-resolution (non-degraded) data. We compute the latter using the IZI procedure developed by Blanc et al. (2015), which solves for metallicity, marginalized over the ionization parameter. For consistency with our galaxy model we use the same D13 ( $\kappa = \infty$ ) photoionization model grid. We fit a simple exponential model for the metallicity as a function of radius (i.e. equation 3.1), where each data point is weighted proportional to its  $H\alpha$  flux. We weight by flux because unless one can resolve H II regions individually, one is unavoidably weighted towards the emission-line ratios of the brightest H II regions. Thus, for comparison to our low-resolution mock data, it is appropriate to weight our fit by the  $H\alpha$  flux. We caution the reader that the high-resolution metallicity profiles presented here should not be considered definitive. The analysis that follows is nonetheless self-consistent.

In Fig. 3.6 we present a comparison of the inferred and true metallicity profiles. For each mock dataset we create 50 realizations and calculate the marginalized 2D probability on the central metallicity,  $\log_{10} Z_0$ , and metallicity gradient,  $\nabla_r(\log_{10} Z)$ . The left-hand panels show this marginalized probability, after stacking all 50 realizations. A triangle indicates the maximum a posteriori (MAP) estimate of this stacked marginalized probability. In the central panels we present the true metallicity profile, with the best-fit exponential model and MAP estimate models overplotted. As can be seen, our model performs well for UGC463 and NGC628, but derives an entirely different solution for NGC4980. We shall now discuss each galaxy in turn.

**UGC463** This is a SAB(rs)c galaxy (de Vaucouleurs et al. 1991, herein V91) and has a stellar mass  $\log_{10}(M_*/M_\odot) = 10.6$  (Martinsson et al. 2013). This galaxy was observed during MUSE commissioning (Martinsson et al. in prep.). Before we downgrade them, the physical resolution of the observations is  $\sim 240$  pc. The convolved images indicate that the galaxy is roughly axisymmetric, with the brightest flux consistent with the centre of the galaxy. From panel (a) we note that both the inferred model solutions are in agreement with the best fit to the high-resolution data. Despite the  $r_d = 0.4''$  MAP metallicity gradient estimate being a factor two shallower than the best fit, panel (b) shows this solution is still consistent with the data. In fact it could be argued that no solution is an exceptionally good description of the data. The data indicates the galaxy has a downturn in metallicity beyond  $r \gtrsim 1.3 r_d$  and therefore does not support any simple exponential metallicity profile.

We actually find it quite unexpected that the model succeeds in recovering the metallicity profile. This is because the galaxy demonstrably breaks our assumption that the ionization parameter is anti-correlated to the metallicity (equation 3.2). In this galaxy the ionization parameter and metallicity are in fact positively correlated (see Fig. 3.14). Nevertheless the model is perfectly

<sup>7</sup>At this redshift all five emission lines are within the MUSE wavelength coverage. More typically, however, we will apply this model to higher redshift galaxies where [O II] $\lambda$ 3726,3729 is available, but  $H\alpha$ , [N II] and [S II] are not.



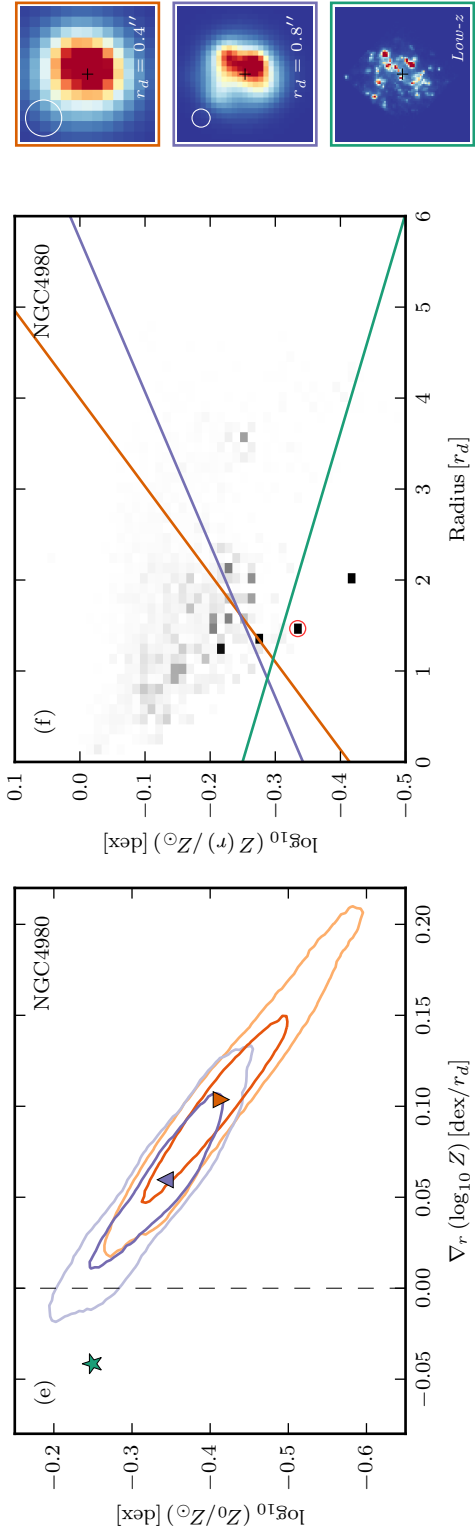


Figure 3.6: Comparison between the true and model derived metallicity profiles for three galaxies: UGC463, NGC628 and NGC4980, shown in descending order. (Left) We show the marginalized 2D probability contours for the central metallicity,  $\log_{10} Z_0$ , and metallicity gradient,  $\nabla_r(\log_{10} Z)$  (after stacking 50 mock realizations). Results are shown for two mock galaxies of different sizes:  $r_d = 0.4''$  (orange) and  $r_d = 0.8''$  (blue). In addition to the 1 $\sigma$  & 2 $\sigma$  contours, we plot the MAP estimates as triangles. N.B. panels (a,c,e) are all scaled to span the same axis ranges. (Centre) Using the full resolution data we construct a 2D histogram of metallicity versus radius. We weight the histogram by the H $\alpha$  flux of each data point. Overplotted are the MAP solutions for the  $r_d = 0.4''$  and  $r_d = 0.8''$  models (orange and blue respectively). Additionally we also show the exponential best-fit to the full resolution data (green). The locations of the the best-fit parameters for the full resolution data are indicated on the left as a green star. Histograms are plotted on a linear scale, clipped between the 1<sup>st</sup> and 99<sup>th</sup> percentiles. In panel (f) we indicate one bin with a red circle. This single bin contains 10% of the total H $\alpha$  flux. (Right) We show aligned images of the H $\beta$  emission line for the two mocks and the full resolution data. The images are shown without noise, and are plotted on a linear scale, clipped between the 1<sup>st</sup> and 99<sup>th</sup> percentiles. The white circle indicates a 0.7'' FWHM PSF in the mock images.

able to recover the truth, although since this is a single case it is not possible generalise about the robustness of our model. We can, however, infer that our derived metallicity gradients are not entirely driven by ionization parameter gradients in galaxies.

**NGC628** This galaxy, like the previous, appears to be a SA(s)c galaxy (V91) with stellar mass  $\log_{10}(M_*/M_\odot) = 10.3$  (Querejeta et al. 2015). Before we downgrade it, the galaxy physical resolution of the data is  $\sim 120$  pc. Dissimilarly, however, NGC628 has a dearth of star forming regions in its centre. This is accentuated by the  $r_d = 0.8''$  image the galaxy, which is visibly lopsided and features a strong star forming complex to the upper-right of the centre. Panel (c) indicates that in the  $r_d = 0.8''$  case our model is able to recover the same result as the best fit. Whereas for the smaller  $r_d = 0.4''$  case the model appears to perform less well, and is mildly inconsistent with the best fit solution. Notably the solution for the  $r_d = 0.4''$  case favours a steeper metallicity profile than  $r_d = 0.8$  solution. It is interesting to note that in this case, with significant emission line flux outside the central region, worse seeing does not lead automatically to a shallower metallicity gradient, which one might naïvely expect.

On examination of panel (d), however, it becomes clear that the  $r_d = 0.4''$  MAP estimate is not actually a bad description of the data and arguably provides a better characterization of the data than either the  $r_d = 0.8''$  MAP estimate or high-resolution best fit. A plausible explanation is that with worsening resolution, we become increasingly weighted towards the metallicity of the brightest H II regions. In the high-resolution case it appears that the metallicity trend deviates from linear in this galaxy, and the small scale structure of the metallicity profile plays a central role. When the relative importance of the PSF is larger (i.e. in the  $r_d = 0.4''$  case) these features are smeared out and the fit is no longer affected by these structures. It should be noted that even supplying a very high resolution SFR map does not resolve this issue. A combination of the seeing and finite S/N produces an irreversible loss of information.

We direct the interested reader towards a similar study by Mast et al. (2014) who also study resolution effects on the metallicity gradient with NGC628 amongst other galaxies.

**NGC4980** This galaxy was observed as part of the MUSE Atlas of Disks (MAD) (Carollo et al. in prep.). It is a SAB(rs)a pec? galaxy (V91) and has a stellar mass  $\log_{10}(M_*/M_\odot) = 9.2$  (Querejeta et al. 2015). Before we downgrading, the physical resolution of the data is  $\sim 80$  pc. Spiral structure is not readily evident in the H $\beta$  images, instead the emission-line flux is dominated by a few H II regions. NGC4980 is extremely clumpy, for example  $\sim 10\%$  of the total H $\alpha$  flux is contained within one spaxel. As shown in panel (e), both the  $r_d = 0.4''$  and  $r_d = 0.8''$  MAP solutions are consistent with one another. However, they are both inconsistent with the best fit solution to the extent that they even have the opposite sign for the metallicity gradient.

Panel (f) shows the true metallicity profile of the galaxy. The lower surface brightness emission supports a flat or slightly negative metallicity gradient. But the flux is dominated by a few bright H II regions which have metallicities significantly lower than fainter H II regions at the same radius. As a result, none of the solutions (including the low-z best fit) provide a good depiction of the data. It should be stressed that the model parameter uncertainties estimate the impact of the random data errors, however, by definition they do not account for the systematic errors caused by applying the wrong model.

It is challenging to define a meaningful metallicity gradient in galaxies like NGC4980. At low redshift one could potentially treat the bright low-metallicity H II regions as outliers from the true metallicity profile. Whereas as at higher redshifts one would treat the brightest emission as representative of the metallicity profile.

Testing our model against these three galaxies has shown that our method does indeed have the power to recover the metallicity profile even at the marginally resolved limit. However,

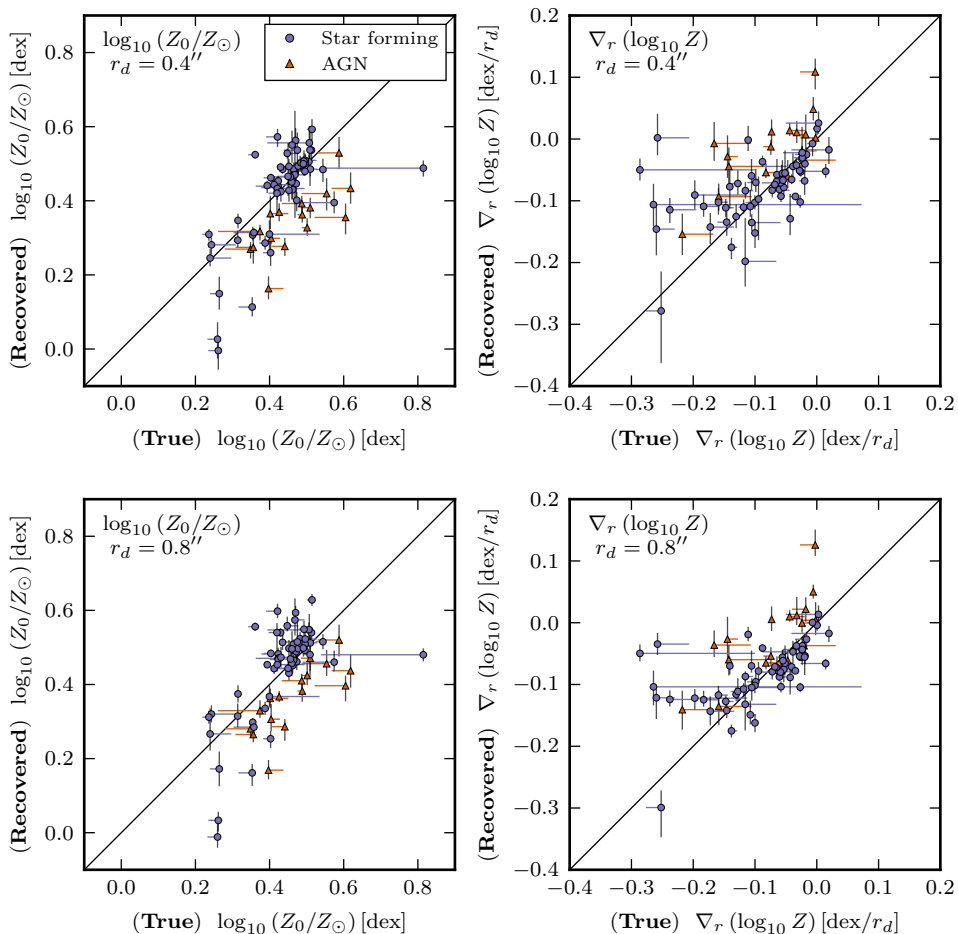


Figure 3.7: Assessment of the models ability to recover the “true” metallicity profile for a sample of 76 CALIFA galaxies. On the vertical axes we plot the MAP estimates of the model, and on the horizontal axes we plot the best fit value to the low- $z$  data. As before, we simulate mock versions of each galaxy at 2 different sizes,  $r_d = 0.4''$  (top) and  $r_d = 0.8''$  (bottom). (Left) We plot the model derived value for the central metallicity vs the true value derived from the undegraded data. (Right) Similarly, we compare the model derived metallicity gradient. In each panel galaxies are represented by blue circles or orange triangles, the former indicating regular star-forming galaxies and the latter indicating galaxies with AGN. The vertical errorbars indicated the  $1\sigma$  errors reported by the model fit. The horizontal “errorbars” do *not* indicate the statistical error in the true gradient, but rather they indicate by how much the result would change if the true profile was instead determined from azimuthally averaged data, see text for details. We indicate the 1:1 relation with a black line. If our model is good at recovering the true metallicity profile we would expect most galaxies should lie along this line.

for one of the galaxies our model fails catastrophically. Clearly a larger sample is required to assess whether such cases are common.

We repeat the previous exercise, downgrading IFS observations with a larger sample of nearby galaxies selected from the 3<sup>rd</sup> CALIFA Data Release (Sánchez et al. 2016, 2012; Walcher et al. 2014). From this we select a sub-sample that has morphological information (RA, Dec., inc., PA) provided by HyperLEDA (Makarov et al. 2014). We exclude galaxies that are either highly-inclined ( $\geq 70^\circ$ ), have low H $\alpha$  SFR ( $< 1 M_\odot \text{ yr}^{-1}$ ), or are very small ( $r_d < 7''$ ). After pruning the sample, 76 CALIFA galaxies remain. For each of these galaxies we downgrade images of their emission lines<sup>8</sup> and use our model to recover the metallicity profile.

In Fig. 3.7 we compare the model recovered values of the central metallicity ( $\log_{10} Z_0$ ) and the metallicity gradient ( $\nabla_r(\log_{10} Z)$ ) against those derived from the full-resolution data. For this we employ two methods of determining the true metallicity profile in the full-resolution data. Our primary method is the same as before, where we perform a H $\alpha$  flux weighted linear-fit to the metallicity derived in the individual CALIFA spaxels. The metallicity is computed using IZI in the spaxels that have all emission lines ([O II]3726,3729, H $\beta$ , [O III]5007, H $\alpha$ , [N II]6584 and [S II]6717,6731) with S/N > 3. We exclude spaxels that do not have [O III]/H $\beta$  and [N II]/H $\alpha$  line-ratios consistent with emission from star-formation. Unfortunately individual spaxels may not have sufficient S/N which could bias our metallicity profile towards that of the brightest H II regions. Therefore to assess the impact this might have we employ a second method for determining the true metallicity profile. Instead of using individual spaxels, we first integrate the flux into elliptical annuli (with major width 4'') before deriving the metallicity in each. This avoids excluding low-luminosity H II regions that, while faint, could be numerous enough have a non-negligible contribution to the total flux. This second method is somewhat limited, however, and might be skewed by the emission of diffuse ionized gas particularly in the outskirts of the galaxies. With this caution in mind, we indicate both results in Fig. 3.7, where the data points represent the fit to individual spaxels, and the end of the horizontal ‘‘errorbar’’ is situated at the location of the fit to the annularly binned data. It can clearly be seen that for most galaxies there is little difference between the binned and unbinned methods. However, a few galaxies do show large differences, indicating that a ‘‘true’’ metallicity profile for these galaxies is perhaps poorly defined.

In the figure we observe that there is a good agreement between the results recovered by the model and the low-z best fit, with most galaxies lying close to the 1:1 line. Many of the galaxies that lie off the 1:1 line possess AGN (shown as triangles in the plot). We define galaxies as possessing an AGN if the innermost annular bin has [O III]/H $\beta$  and [N II]/H $\alpha$  line-ratios typical of AGN (Kewley et al. 2001). Unsurprisingly our model is unable to infer the metallicity profiles of galaxies with AGN. So we reiterate that when applying our method we must be careful to exclude such galaxies.

We conclude that, in general, our model is able to recover central metallicities and metallicity gradients from realistic galaxies. However, while most galaxies lie close to the 1:1 line, a few of the galaxies with the steepest true metallicity gradients do not. Several of these exhibit large differences between our two methods for defining the true metallicity gradient, clearly indicating that a metallicity gradient is poorly defined in these galaxies. Nevertheless, there are a few galaxies for which our model significantly underestimates the metallicity gradient. These, alongside NGC4980, could be considered as cases where our model fails catastrophically.

<sup>8</sup>H $\beta$ , [O III]5007, H $\alpha$ , [N II]6584 and [S II]6717

### 3.3 Interpreting the observed metallicity gradient

Our analysis has highlighted some intrinsic limitations when working with low-resolution data. Namely the effect that clumpy emission will have on the inferred gradient, particularly if the clumps have uncharacteristically low/high metallicities. This will become an important consideration if one is to compare the metallicity gradients of galaxies between the low and high redshift universes.

As mentioned in the introduction, there have been many reports of inverted (positive) metallicity gradients in high-redshift galaxies. This is often interpreted as either evidence of possible accretion of metal poor gas to the centres of galaxies, or evidence for centrally concentrated winds which entrain metals in the outflow. Therefore it is intriguing that a galaxy like NGC4980 that has a normal (negative) metallicity gradient can appear to have an inverted (positive) one when analysed using the methodology normally applied to distant galaxies. It would be inappropriate for us to claim that clumpy emission explains any or all of the observed positive metallicity gradients. However, we suggest that when interpreting these results, it is important to consider the implication that the positive gradients can be caused by low-metallicity strongly star-forming clumps, whose metallicity is not indicative of the overall metallicity profile.

In this section we have shown that our model performs satisfactorily well in both ideal and realistic scenarios. Our model is able to recover the metallicity gradients of barely resolved galaxies, but we have identified that there are important considerations to be made with regards to the interpretation. In the following section we will apply our method to real observations as a proof on concept.

## 4 Application

In the previous section we successfully tested our model against mock data. We shall now demonstrate the model applied to real IFS observations of high-redshift galaxies. This will allow us to assess how well the model can constrain the metallicity profile of distant galaxies.

### 4.1 Data

We will use MUSE observations of the Hubble Deep Field South (HDFS) which were taken during the last commissioning phase of MUSE (June–August 2014). MUSE is an integral field spectrograph providing continuous spatial coverage over a  $1' \times 1'$  FoV, across the wavelength range  $4750\text{\AA} - 9300\text{\AA}$ , with a spectral resolution of  $2.3\text{\AA}$  FWHM.

The data and its reduction (version 1.0)<sup>9</sup> are described at length by [Bacon et al. \(2015\)](#). With the 54 exposures (27h) it is possible to obtain a  $1\sigma$  emission-line surface-brightness limit of  $1 \times 10^{-19} \text{ erg s}^{-1} \text{ cm}^{-2} \text{ arcsec}^{-2}$ . Here we use a more recent reduction (version 1.24) that incorporates some minor improvements in the uniformity and sky subtraction of the data. However, for the sources that we concern ourselves with here these modifications are not important. The PSF in these observations is characterized by a Moffat profile with parameters as given in [Table 3.1](#). The final data cube is sampled with equally sized voxels<sup>10</sup> ( $0.2'' \times 0.2'' \times 1.25\text{\AA}$ ).

Our model requires a set of predetermined morphological parameters: the location of the centre of the galaxy, its inclination and the position angle of the major axis (PA). The details of the measurement of these quantities are given in [Contini et al. \(2016\)](#), but briefly they were

<sup>9</sup>Public data products and catalogues are available at <http://muse-vlt.eu/science/>

<sup>10</sup>volumetric pixels

determined by running GALFIT (Peng et al. 2002) on the F814W HST images (Williams et al. 1996), using a disc+bulge model.

We adopt the redshifts of the galaxies as those tabulated by Bacon et al. (2015). We will also use the same object ID numbers.

## 4.2 Analysis

To separate the nebular emission from the underlying stellar component we do full-spectral fitting using the PLATEFIT code described in Tremonti et al. (2004) and Brinchmann et al. (2004). We process a spectrum as follows:

**Redshift determination** Although we already know the redshift of each galaxy, the galaxy's own rotation will result in small velocity offsets from this value. We determine the redshift of the spectrum using the AUTOZ code described by Baldry et al. (2014), which determines redshifts using cross-correlations with template spectra. If there is a strong correlation peak within  $\pm 500 \text{ km s}^{-1}$  of the galaxy's redshift, then we accept this peak as the redshift of the spectrum. If no significant correlation peak is found within this range, we assume the spectrum's redshift to be the same as the galaxy as a whole.

**Stellar velocity dispersion** The stellar velocity dispersion is determined using VDISPFIT<sup>11</sup>. This uses a set of eigenspectra, convolved for different velocity dispersions. From this the best fit velocity dispersion is determined. This value includes the instrumental velocity dispersion. If the best fit velocity dispersion lies outside the range  $[10 - 300] \text{ km s}^{-1}$  we assume the fit has failed and adopt a default value of  $80 \text{ km s}^{-1}$ . Such failures are typical when the stellar continuum is faint or non-existent.

**Continuum fitting** For the spectral fitting we use the PLATEFIT spectral-fitting routine (Tremonti et al. 2004; Brinchmann et al. 2004). PLATEFIT, which was developed for the SDSS, fits the stellar continuum and emission lines separately. In this continuum fitting stage, regions around possible emission-lines are masked out. The stellar continuum is fit with a collection of Bruzual & Charlot (2003) stellar population synthesis model templates. The template fit is performed using the previously derived redshift and velocity dispersion. If the continuum fitting fails, i.e. because the continuum has very low S/N, then we construct the continuum from a running-median filter with a  $150 \text{ \AA}$  width.

**Emission-line fitting** The second PLATEFIT emission-line fitting stage is now performed on the residual spectrum (after continuum subtraction). The emission lines are each modelled with a single Gaussian component. Doublets such as  $[\text{O II}]_{3726,3729}$  are fit with two Gaussian components. All emission lines share a common velocity offset and a common velocity dispersion. The velocity offset and velocity dispersion are not fixed, but are instead free parameters in the fit. The amplitudes and associated errors are determined as part of a Levenberg-Marquardt least-squares minimization. However, analysis of duplicate SDSS observations has shown that these formal errors typically underestimate the true uncertainties. Corrections for this can, however, be derived from the duplicate observations (e.g. Brinchmann et al. 2013). We use these corrections to rescale our formal uncertainties to more representative values.

For this paper we make it a requirement that all our emission-line flux measurements have  $S/N \geq 5$ . Near the bright centres of galaxies individual spaxels will satisfy this criterion. However, at larger radii we need to coadd spaxels to reach the required S/N. To combat the effects of seeing we will need as much radial information as possible, and therefore it is necessary to bin (aggregate) spaxels together. There is, however, no perfect binning algorithm.

<sup>11</sup>[http://spectro.princeton.edu/idlspec2d\\_install.html](http://spectro.princeton.edu/idlspec2d_install.html)

Table 3.4: Galaxy properties: disc scale-length, stellar mass and star-formation rate. These results were reported in [Contini et al. \(2016\)](#), but we reproduce them here for convenience.

Galaxy	$r_d$ [arcsec]	$\log_{10}(M_*)$ [ $M_\odot$ ]	$\log_{10}(\text{SFR})$ [ $M_\odot \text{ yr}^{-1}$ ]
HDFS-0003	$0.660 \pm 0.007$	$9.66 \pm 0.14$	$0.24 \pm 0.37$
HDFS-0016	$0.40 \pm 0.01$	$8.74 \pm 0.21$	$-0.65 \pm 0.55$

We present our adopted procedure in Appendix C. The method bins the galaxy into annular sectors, and attempts to avoid binning spaxels at very different radii, although this last point is far from guaranteed. This should help minimize addition radial resolution loss as a result of the binning. It should be noted that these bins are not contiguous, i.e. non-adjacent spaxels will be combined. In many cases the bins will be smaller than the PSF, and therefore the derived fluxes will not be statistically independent of one another.

### 4.3 Results

In this section we present the results of fitting our model to real data. Using this we will discuss characteristics of the method, outline certain limitations, and discuss future improvements that could be made.

As examples we will show results for two galaxies, one of which is well resolved (HDFS-0003), and another barely resolved galaxy (HDFS-0016). These galaxies were selected to represent these two extremes. Of the two, HDFS-0003 is the larger, more massive, and more strongly star forming (see Table 3.4). Both galaxies have similar redshifts ( $z = 0.5637$  and  $z = 0.4647$ , respectively), which means that the intrinsic physical resolution of both observations is approximately 4 kpc FWHM. In our analysis we use the same set of emission lines for both galaxies.

In Figs. 3.8 & 3.9 we present a comparison between the observed emission-line fluxes and the model fit for the two galaxies. The model reproduces the observed emission-line fluxes in both. However, while the model is able to capture the overall radial flux profile, it does not (by construction) have the flexibility to match the observed azimuthal metallicity variations. This is especially evident in HDFS-0016 where the emission line fluxes are not single-valued at all radii. In this galaxy it appears that the radial run of emission line fluxes could be described by two branches, with the brightest branch originating from a star-forming clump offset to the West of the galaxy centre.

We discussed in the previous section that star-forming clumps can conceptually be divided into two categories: either clumps that are bright, but have the same metallicity as other gas at the same radius, and clumps which have uncharacteristically low/high metallicities. In the case of the former the line ratios (but not line fluxes) would be single valued as function of radius.<sup>12</sup> However, HDFS-0016 falls into the latter category as it is clear to the eye that the upper branch of fluxes has a consistently higher [O III]/[O II] ratio. For a range of radii in HDFS-0016 there is no single characteristic line-ratio.

The existence of multiple branches in the flux profiles can cause problems for the model fitting even if the line-ratios are unaltered. One can envisage a scenario where, for example, the model might have fit the upper branch in [O III], but the lower branch in [O II]. Obviously this would result in deriving an entirely incorrect best fit model. Indeed Fig. 3.9 shows slight hints of this problem. Notably the model fits the lower flux branch in all emission lines, except

<sup>12</sup>This is not entirely true since seeing has a wavelength dependence.

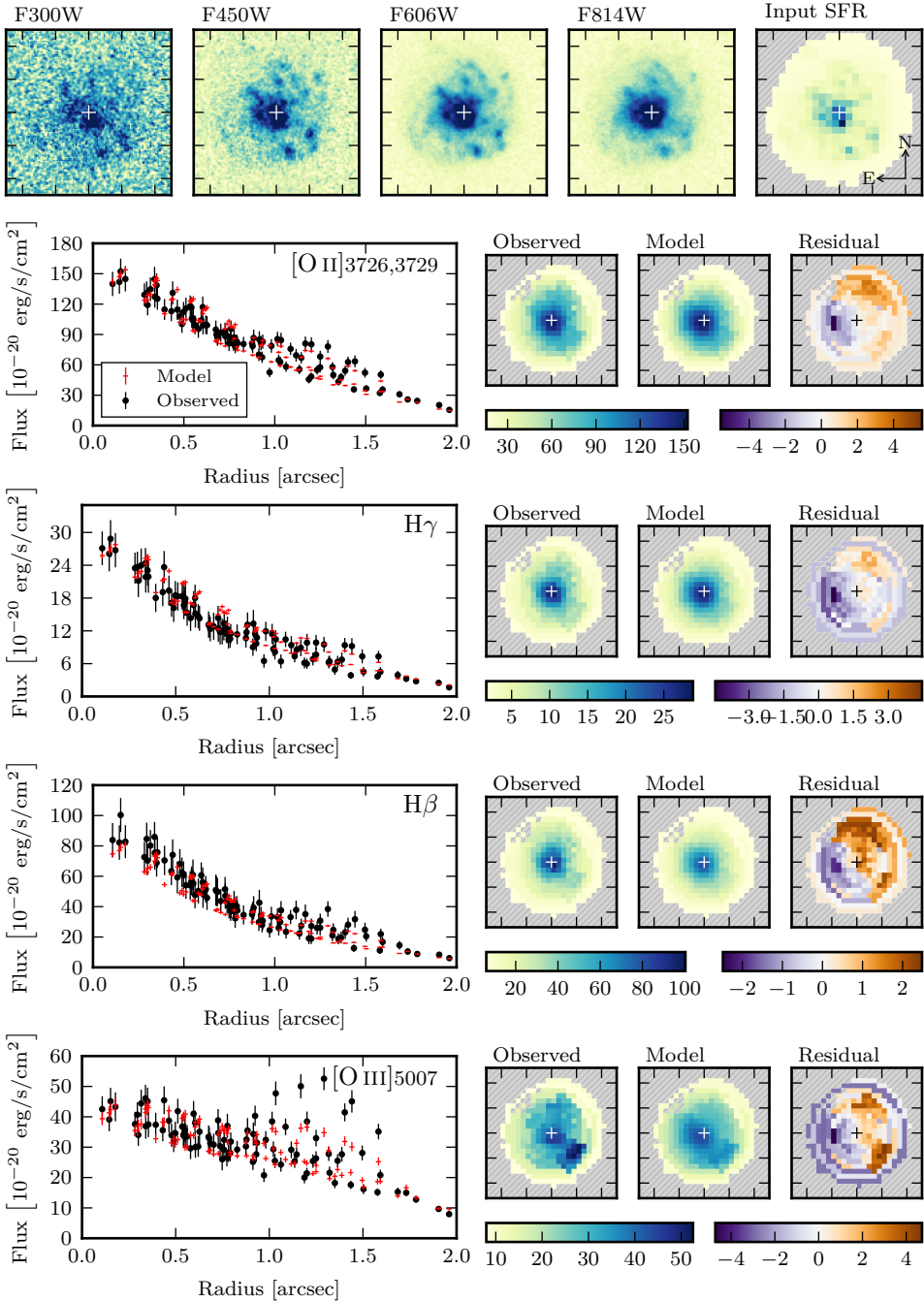


Figure 3.8: Summary of model fitting for visual quality assessment of galaxy HDFS-0003. (Top) We plot five images: four HST broadband images, and the derived SFR map which is used as an input to the model. (Left) We show the radial flux profiles for all four emission-lines ( $[O II]$ ,  $H\gamma$ ,  $H\beta$  and  $[O III]$ ). Black data points indicate observed fluxes and their  $\pm 1\sigma$  errors. The red crosses show the median model solution, the size of the vertical bar indicates a  $\pm 2\sigma$  range in fluxes. (Right) Three images respectively show 2D binned images of the observed fluxes, model fluxes, and scaled residuals  $((\text{Observed} - \text{Model})/\text{Error})$  for each emission line.

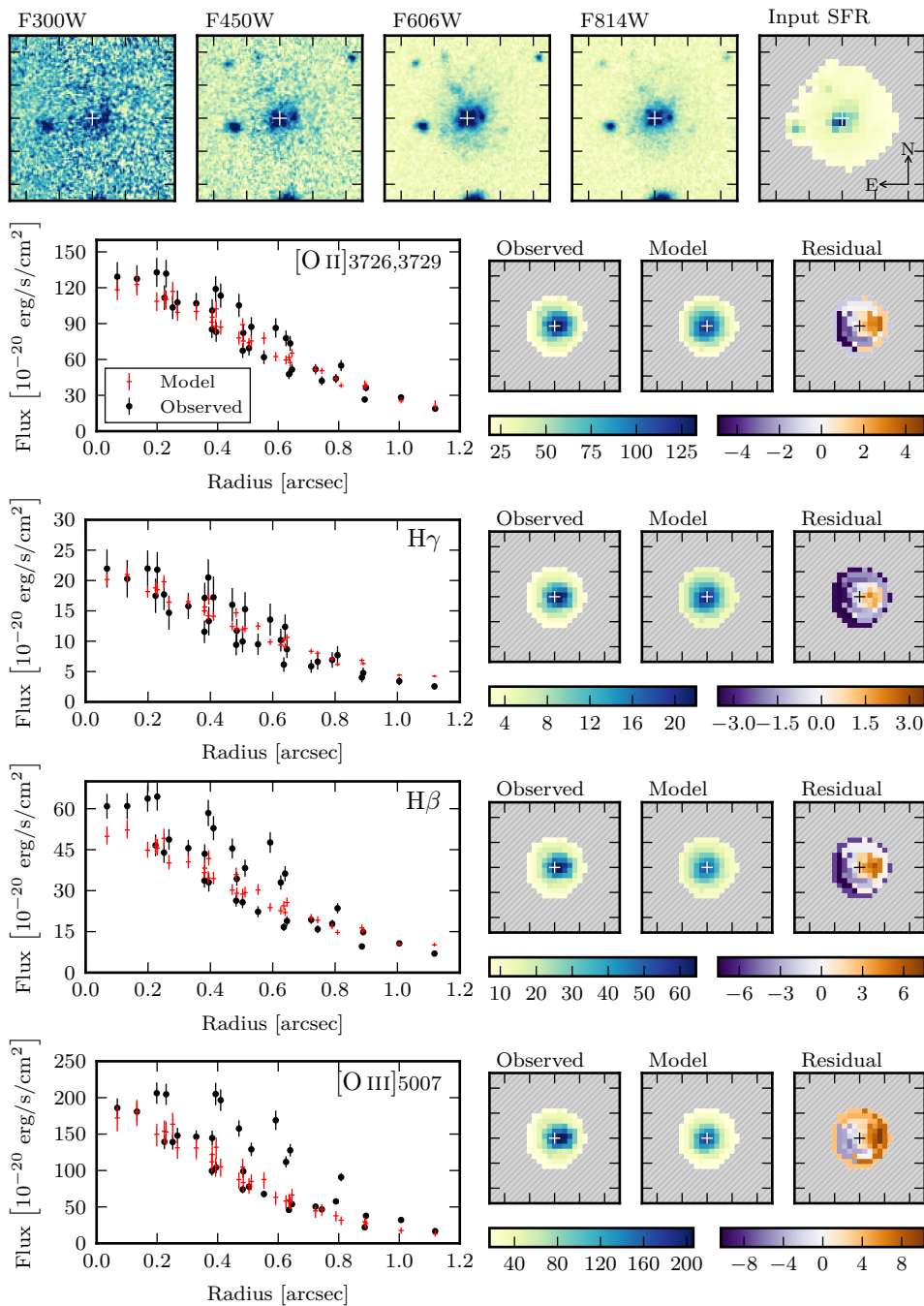


Figure 3.9: Summary of model fitting for visual quality assessment of galaxy HDFS-0016. See Fig. 3.8 for details.

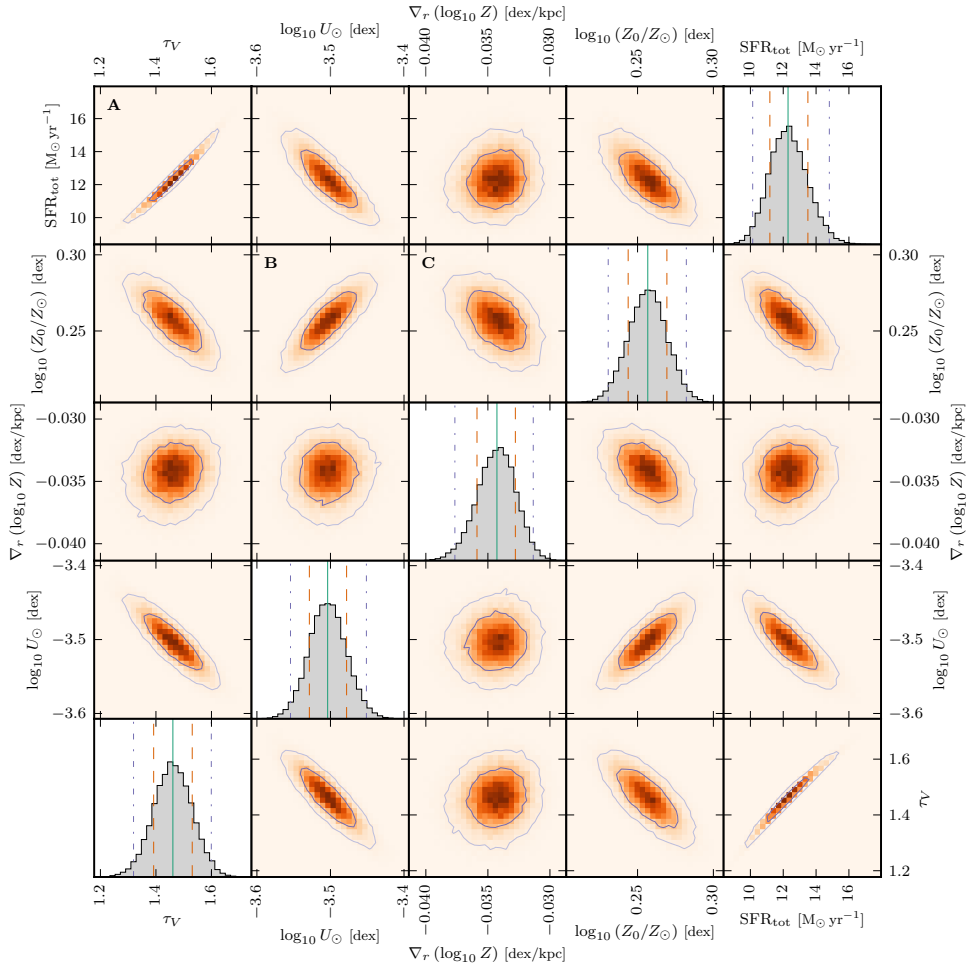


Figure 3.10: MCMC fitting results shown for galaxy HDFS-0003. We show both 1D and 2D marginalized histograms for all 5 parameters: the total star-formation rate,  $\text{SFR}_{\text{tot}}$ , central metallicity,  $\log_{10} Z_0$ , metallicity gradient,  $\nabla_r(\log_{10} Z)$ , ionization parameter at solar metallicity,  $\log_{10} U_{\odot}$ , and V-band optical depth,  $\tau_V$ . In each 1D histogram the vertical lines indicate the median (solid),  $\pm 1\sigma$  quantiles (dashed) and  $\pm 2\sigma$  quantiles (dash-dotted). In each 2D histogram we plot  $1\sigma$  and  $2\sigma$  contours. All axes span a  $[-4\sigma, 4\sigma]$  interval in their respective parameters. Letters label particular panels that we refer to in the text.

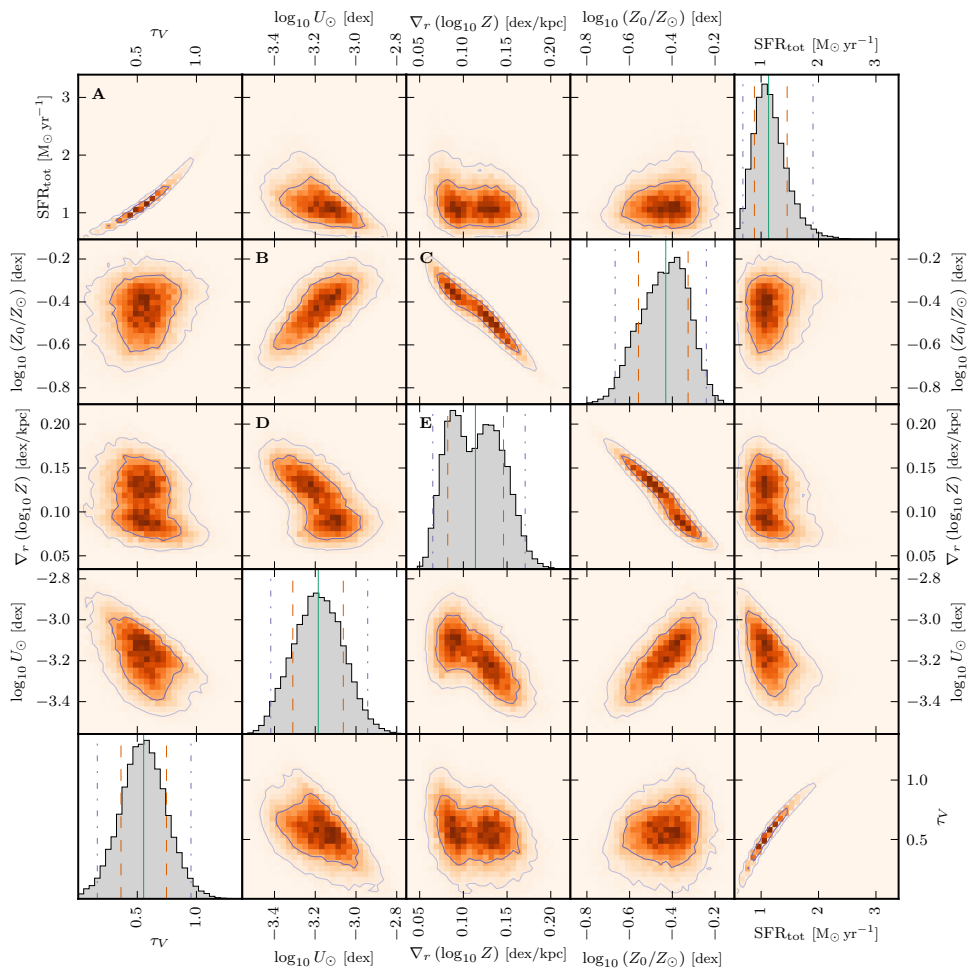


Figure 3.11: MCMC fitting results shown for galaxy HDFS-0016. See Fig. 3.10 for details.

for  $H\gamma$  where the model fits in between the lower and upper branches. Albeit relatively minor in this case, it is crucial to be aware of this possible problem and assess its severity.

### 4.3.1 Validity of constant dust approximation

For our model we assume there is a constant attenuation due to dust across the whole galaxy. Studying the  $H\beta$  and  $H\gamma$  profiles in both Figs. 3.8 & 3.9 one observes that the model slightly underpredicts the  $H\beta$  flux in the centre of the galaxies. This would imply that there is perhaps a mild dust gradient across the galaxy, with galaxy centres being slightly more dusty than their outskirts.

Using high spatial-resolution grism spectroscopy Nelson et al. (2016) identified radial dust variations in  $z=1.4$  galaxies. They found that the most massive galaxies presented the strongest variations, but less massive  $10^{9.2} M_{\odot}$  galaxies exhibited almost no variation and little dust attenuation overall.

We reperform our analysis of HDFS-0003 using a dust model with the same radial dependence as Nelson et al. (2016) propose for a  $10^{9.66} M_{\odot}$  galaxy. The normalization of this model is allowed as a free parameter. We find that dust model produces a significantly worse fit to the data than the constant dust model. Admittedly, since the Nelson et al. (2016) dust models are based on  $z=1.4$  galaxies they may not be appropriate for our galaxies.

Using the new dust model changes many of the derived best fit values. For example the inferred central metallicity is increased by  $\sim 0.14$  dex, however, the metallicity gradient is bizarrely unaffected and changes by  $< 0.001$  dex/kpc.

Choosing an appropriate dust model is clearly important for deriving the metallicity of galaxies. But, on the whole the data appears largely consistent with our assumption of a constant optical depth for the whole galaxy.

### 4.3.2 Parameter constraints

So far we have only discussed the quality of the model fits. We will now discuss how well the model can constrain the metallicity profile of these galaxies. In Figs. 3.10 & 3.11 we show 1D and 2D histograms of the derived model parameters for both HDFS-0003 and HDFS-0016. We note that most of the derived parameters are relatively well constrained. For example in HDFS-0016 the errors on central metallicity and metallicity gradient are  $\pm 0.1$  dex and  $\pm 0.03$  dex/kpc respectively. These errors are more than sufficient to establish HDFS-0016 as possessing a significantly sub-solar central metallicity and a positive metallicity gradient. The constraints on HDFS-0003 are tighter. Naturally the quality of the constraints will vary with the S/N of the data. It is therefore perhaps more interesting to discuss the correlations between the modelled parameters.

It is clear from Panel A that the model produces a very tight correlation between the total star-formation rate and the V-band optical depth. Dustier model solutions are fainter, so intrinsically higher SFRs are required to compensate.

The model also shows a strong anti-correlation between the metallicity gradient and central metallicity of a galaxy (Panel C). This degeneracy is of course not surprising given that data directly constrains the metallicity profile, not the metallicity gradient, which is dependent on the central metallicity. However, the situation may actually be more complicated than this. For example in HDFS-0016, as depicted by Panels B & D, the ionization parameter at solar metallicity,  $\log_{10} U_{\odot}$ , is (anti-)correlated with both the metallicity gradient and central metallicity. HDFS-0003 does not show this dependence between  $\log_{10} U_{\odot}$  and  $\nabla_r(\log_{10} Z)$ . However, HDFS-0003 does show an interdependency between  $\text{SFR}_{\text{tot}}$ ,  $\log_{10} Z_0$ ,  $\log_{10} U_{\odot}$  and  $\tau_V$ .

Table 3.5: Comparison of derived metallicity profile parameters from two methods. One method is a simple linear fit to the metallicity derived in a series of annular bins. The other is the full model fitting that accounts for seeing effects.

Galaxy	Parameter	Simple Annular	Full Modelling
HDFS-0003	$\log_{10}(Z_0/Z_\odot)$ [dex]	$+0.31 \pm 0.01$	$+0.26^{+0.01}_{-0.01}$
	$\nabla_r \log_{10}(Z)$ [dex/kpc]	$-0.026 \pm 0.002$	$-0.034^{+0.001}_{-0.002}$
HDFS-0016	$\log_{10}(Z_0/Z_\odot)$ [dex]	$-0.28 \pm 0.02$	$-0.43^{+0.10}_{-0.13}$
	$\nabla_r \log_{10}(Z)$ [dex/kpc]	$+0.016 \pm 0.004$	$+0.11^{+0.03}_{-0.03}$

Because we have assumed an intrinsic correlation between metallicity and ionization parameter, it is somewhat difficult to unravel these dependencies. In essence metallicity gradients and ionization-parameter gradients are one and the same. It is this which allows us to mitigate against the  $R_{23}$  degeneracy (the degeneracy between metallicity and ionization parameter that arises from the limited set of emission lines used here). However, as a consequence the ionization parameter at solar metallicity, central metallicity and metallicity gradient are now inadvertently coupled.

Interestingly, the metallicity gradient in HDFS-0016 is slightly bimodal (see Panel E). An effect which may in part be explained by the dual-valued nature of the  $R_{23}$  degeneracy, although this is hard to verify. Currently there is insufficient evidence to place an informative prior on  $\log_{10} U_\odot$ . If in the future this were possible one could in theory achieve a more precise measurement for central metallicity and the metallicity gradient.

It is important to note that in our model testing we have only verified the central metallicity and the metallicity gradient parameters. We have not applied the same testing scrutiny to the other parameters, so their values should not be considered validated and used only with great care.

## 4.4 Discussion

As we have seen, we can use the model to constrain the true metallicity gradient in galaxies. To emphasise the necessity for correcting for the effects of seeing, we have also derived the metallicity profiles of these galaxies without making any corrections for seeing.

We extract emission-line fluxes in a series of elliptical annular apertures (semi-major width  $0.35''$ ) with axis-ratios to match the galaxy. In each annulus we derive the metallicity following [Maiolino et al. \(2008, herein M08\)](#), except that our method differs slightly as we use the [Charlot & Fall \(2000\)](#) dust absorption model. We use the same set of emission lines as for the full modelling, but also include the [O III] $\lambda 4959$  required for the  $R_{23}$  index.

In Table 3.5 we summarize the derived central metallicities and gradients, and compare them to those derived from the full modelling. As a cautionary note it can be dangerous to compare metallicities derived from different methods and calibrations ([Kewley & Ellison \(2008\)](#) provide a good discussion of this). Nevertheless it is still interesting to compare the results, as they should be broadly consistent.

HDFS-0003 is a well resolved galaxy, therefore the effects of seeing will be limited. Indeed both methods produce shallow, negative metallicity gradients. Although the annular method is

slightly shallower, this is not likely to be seeing effect and is more probably due to differences between the methods for deriving metallicity and/or the fact that the annular method derives the dust in each annulus, allowing for possible radial dust variations.

In stark contrast, HDFS-0016 will be much more affected by seeing effects. The predominant effects of seeing will be to flatten the metallicity gradient. And this is exactly what is observed, the naïve annular method yields a significantly flatter (but still positive) metallicity gradient. This method also estimates a  $\sim 0.15$  dex higher central metallicity. While this could entirely be due to difference between the methods for deriving metallicity, there are other important factors to consider. If the galaxy truly has a steep positive metallicity gradient, then a significant fraction of the flux from the outer, higher metallicity material could be scattered into the central bin. Thus the uncorrected central metallicity may be much closer to the average metallicity of the galaxy (although given the non-linear nature of the connection between metallicity and emission-line flux this may not necessarily be the case in all galaxies).

As a final cautionary note, throughout this section we have made use of high-resolution SFR maps to provide a more realistic model for these galaxies. Whilst employing SFR maps may be theoretically optimal, in practice good SFR maps are challenging to obtain. The SFR maps contain systematic and random errors. For example in Fig. 3.9 we observe a star-forming clump to the West of the galaxy centre which is seen in the HST images. This clump is however not apparent in the derived SFR maps. Additionally the SFR maps can be contaminated by other galaxies in the (fore/back)ground. Both the systematic and random uncertainties, which are not factored into the modelling, may limit or even negate their effectiveness.

## 5 Conclusions

It is important to correct for the effects of seeing when determining metallicity gradients in galaxies. Here we have outlined an approach that allows us to directly model the emission-line fluxes. By fitting this model to the data we can infer the true metallicity profile of a galaxy in the absence of seeing. Unlike other existing approaches, our method is general can be applied to many IFS studies of distant galaxies.

We use theoretical photoionization models to predict the emission-line ratios as a function of metallicity and ionization parameter. As such the model can be applied to a flexible set of observed emission-lines, enabling a self-consistent analysis across a range of redshifts and a variety of instrument wavelength coverages. To alleviate degeneracies we enforce a correlation between metallicity and the ionization parameter. We, however, do permit global ionization-parameter variations, accommodating for both possible redshift and environmental evolution of the ionization parameter.

We have performed an extensive set of tests to validate the method and understand its limitations. In summary:

- (i) By creating noisy model realizations for a variety of S/N, inclination, and seeing conditions, we have established that the model is able to recover the metallicity profile even in adverse conditions. In addition the method produces appropriate error estimates.
- (ii) We have downgraded observations of nearby galaxies to test our method against realistic mock data. With limited resolution the metallicity profile will inevitably be weighted towards the metallicity of the brightest clumps.
- (iii) This effect is not wholly reversible, even if the underlying SFR distribution is known a priori. Providing a good map of the underlying SFR distribution is challenging, and proves to be the greatest limitation for our model.

- (iv) The ability for bright star-forming clumps to skew the measured metallicity gradient should be taken into account when interpreting metallicity gradient studies.

In future work we will apply this method to allow us derive the metallicity profiles of galaxies observed with MUSE.

## Acknowledgements

JB acknowledges support from FCT grant IF/01654/2014/CP1215/CT0003. TC acknowledges support from the ANR FOGHAR (ANR-13-BS05-0010-02), the OCEVU Labex (ANR-11-LABX-0060) and the A\*MIDEX project (ANR-11-IDEX-0001-02) funded by the “Investissements d’avenir” French government program managed by the ANR. BE acknowledges financial support from “Programme National de Cosmologie and Galaxie” (PNCG) of CNRS/INSU, France. TPKM acknowledges financial support from the Spanish Ministry of Economy and Competitiveness (MINECO) under grant number AYA2013-41243-P.

Funding for the SDSS and SDSS-II has been provided by the Alfred P. Sloan Foundation, the Participating Institutions, the National Science Foundation, the U.S. Department of Energy, the National Aeronautics and Space Administration, the Japanese Monbukagakusho, the Max Planck Society, and the Higher Education Funding Council for England. The SDSS Web Site is <http://www.sdss.org>.

The SDSS is managed by the Astrophysical Research Consortium for the Participating Institutions. The Participating Institutions are the American Museum of Natural History, Astrophysical Institute Potsdam, University of Basel, University of Cambridge, Case Western Reserve University, University of Chicago, Drexel University, Fermilab, the Institute for Advanced Study, the Japan Participation Group, Johns Hopkins University, the Joint Institute for Nuclear Astrophysics, the Kavli Institute for Particle Astrophysics and Cosmology, the Korean Scientist Group, the Chinese Academy of Sciences (LAMOST), Los Alamos National Laboratory, the Max-Planck-Institute for Astronomy (MPIA), the Max-Planck-Institute for Astrophysics (MPA), New Mexico State University, Ohio State University, University of Pittsburgh, University of Portsmouth, Princeton University, the United States Naval Observatory, and the University of Washington.

We acknowledge the usage of the HyperLeda database (<http://leda.univ-lyon1.fr>).

This study uses data provided by the Calar Alto Legacy Integral Field Area (CALIFA) survey (<http://califa.caha.es>). Based on observations collected at the Centro Astronómico Hispano Alemán (CAHA) at Calar Alto, operated jointly by the Max-Planck-Institut für Astronomie and the Instituto de Astrofísica de Andalucía (CSIC).

Additionally we wish to acknowledge both the PYTHON programming language and the Interactive Data Language (IDL) that were both used extensively throughout this work.

## Bibliography

- Abazajian K. N., et al., 2009, *ApJS*, 182, 543  
 Aller L. H., Liller W., 1959, *ApJ*, 130, 45  
 Bacon R., et al., 2010, in *Ground-based and Airborne Instrumentation for Astronomy III*. p. 773508, doi:10.1117/12.856027  
 Bacon R., et al., 2015, *A&A*, 575, A75  
 Baldry I. K., et al., 2014, *MNRAS*, 441, 2440  
 Bigiel F., Leroy A., Walter F., Brinks E., de Blok W. J. G., Madore B., Thornley M. D., 2008, *AJ*, 136, 2846

- Blanc G. A., Kewley L., Vogt F. P. A., Dopita M. A., 2015, *ApJ*, 798, 99
- Bouché N., et al., 2010, *ApJ*, 718, 1001
- Brinchmann J., Charlot S., White S. D. M., Tremonti C., Kauffmann G., Heckman T., Brinkmann J., 2004, *MNRAS*, 351, 1151
- Brinchmann J., Charlot S., Kauffmann G., Heckman T., White S. D. M., Tremonti C., 2013, *MNRAS*, 432, 2112
- Bruzual G., Charlot S., 2003, *MNRAS*, 344, 1000
- Buchner J., et al., 2014, *A&A*, 564, A125
- Cappellari M., Copin Y., 2003, *MNRAS*, 342, 345
- Charlot S., Fall S. M., 2000, *ApJ*, 539, 718
- Contini T., et al., 2016, *A&A*, 591, A49
- Cresci G., Mannucci F., Maiolino R., Marconi A., Gnerucci A., Magrini L., 2010, *Nature*, 467, 811
- Davé R., Finlator K., Oppenheimer B. D., 2012, *MNRAS*, 421, 98
- Diehl S., Statler T. S., 2006, *MNRAS*, 368, 497
- Dopita M. A., Evans I. N., 1986, *ApJ*, 307, 431
- Dopita M. A., Kewley L. J., Heisler C. A., Sutherland R. S., 2000, *ApJ*, 542, 224
- Dopita M. A., et al., 2006, *ApJ*, 647, 244
- Dopita M. A., Sutherland R. S., Nicholls D. C., Kewley L. J., Vogt F. P. A., 2013, *ApJS*, 208, 10
- Feroz F., Hobson M. P., 2008, *MNRAS*, 384, 449
- Feroz F., Hobson M. P., Bridges M., 2009, *MNRAS*, 398, 1601
- Feroz F., Hobson M. P., Cameron E., Pettitt A. N., 2013, preprint, ([arXiv:1306.2144](https://arxiv.org/abs/1306.2144))
- Gallazzi A., Charlot S., Brinchmann J., White S. D. M., Tremonti C. A., 2005, *MNRAS*, 362, 41
- Genzel R., et al., 2010, *MNRAS*, 407, 2091
- Grevesse N., Asplund M., Sauval A. J., Scott P., 2010, *Ap&SS*, 328, 179
- Ho I.-T., Kudritzki R.-P., Kewley L. J., Zahid H. J., Dopita M. A., Bresolin F., Rupke D. S. N., 2015, *MNRAS*, 448, 2030
- Jones T., Ellis R. S., Richard J., Jullo E., 2013, *ApJ*, 765, 48
- Kauffmann G., et al., 2003, *MNRAS*, 341, 33
- Kennicutt Jr. R. C., 1998a, *ARA&A*, 36, 189
- Kennicutt Jr. R. C., 1998b, *ApJ*, 498, 541
- Kewley L. J., Dopita M. A., 2002, *ApJS*, 142, 35
- Kewley L. J., Ellison S. L., 2008, *ApJ*, 681, 1183
- Kewley L. J., Dopita M. A., Sutherland R. S., Heisler C. A., Trevena J., 2001, *ApJ*, 556, 121
- Kewley L. J., Dopita M. A., Leitherer C., Davé R., Yuan T., Allen M., Groves B., Sutherland R., 2013, *ApJ*, 774, 100
- Kewley L. J., Zahid H. J., Geller M. J., Dopita M. A., Hwang H. S., Fabricant D., 2015, *ApJ*, 812, L20
- Leethochawalit N., Jones T. A., Ellis R. S., Stark D. P., Richard J., Zitrin A., Auger M., 2016, *ApJ*, 820, 84
- Lilly S. J., Carollo C. M., Pipino A., Renzini A., Peng Y., 2013, *ApJ*, 772, 119
- Ma X., Hopkins P. F., Faucher-Giguère C.-A., Zolman N., Muratov A. L., Kereš D., Quataert E., 2016, *MNRAS*, 456, 2140
- Maiolino R., et al., 2008, *A&A*, 488, 463
- Makarov D., Prugniel P., Terekhova N., Courtois H., Vauglin I., 2014, *A&A*, 570, A13
- Martinsson T. P. K., Verheijen M. A. W., Westfall K. B., Bershadsky M. A., Andersen D. R., Swaters R. A., 2013, *A&A*, 557, A131

- Mast D., et al., 2014, *A&A*, 561, A129
- McGaugh S. S., 1991, *ApJ*, 380, 140
- Mott A., Spitoni E., Matteucci F., 2013, *MNRAS*, 435, 2918
- Moustakas J., Kennicutt Jr. R. C., Tremonti C. A., Dale D. A., Smith J.-D. T., Calzetti D., 2010, *ApJS*, 190, 233
- Nelson E. J., et al., 2016, *ApJ*, 817, L9
- Nicholls D. C., Dopita M. A., Sutherland R. S., 2012, *ApJ*, 752, 148
- Noeske K. G., et al., 2007, *ApJ*, 660, L43
- Peng C. Y., Ho L. C., Impey C. D., Rix H.-W., 2002, *AJ*, 124, 266
- Querejeta M., et al., 2015, *ApJS*, 219, 5
- Queyrel J., et al., 2012, *A&A*, 539, A93
- Rich J. A., Torrey P., Kewley L. J., Dopita M. A., Rupke D. S. N., 2012, *ApJ*, 753, 5
- Rupke D. S. N., Kewley L. J., Barnes J. E., 2010, *ApJ*, 710, L156
- Salpeter E. E., 1955, *ApJ*, 121, 161
- Sánchez S. F., Rosales-Ortega F. F., Kennicutt R. C., Johnson B. D., Diaz A. I., Pasquali A., Hao C. N., 2011, *MNRAS*, 410, 313
- Sánchez S. F., et al., 2012, *A&A*, 538, A8
- Sánchez S. F., et al., 2014, *A&A*, 563, A49
- Sánchez S. F., et al., 2016, *A&A*, 594, A36
- Sanders R. L., et al., 2016, *ApJ*, 816, 23
- Shirazi M., Brinchmann J., Rahmati A., 2014, *ApJ*, 787, 120
- Stott J. P., et al., 2014, *MNRAS*, 443, 2695
- Tacconi L. J., et al., 2013, *ApJ*, 768, 74
- Tremonti C. A., et al., 2004, *ApJ*, 613, 898
- Troncoso P., et al., 2014, *A&A*, 563, A58
- VanderPlas J., 2014, preprint, ([arXiv:1411.5018](https://arxiv.org/abs/1411.5018))
- Veilleux S., Cecil G., Bland-Hawthorn J., 2005, *ARA&A*, 43, 769
- Vila-Costas M. B., Edmunds M. G., 1992, *MNRAS*, 259, 121
- Walcher C. J., et al., 2014, *A&A*, 569, A1
- Whitaker K. E., et al., 2014, *ApJ*, 795, 104
- Williams R. E., et al., 1996, *AJ*, 112, 1335
- Wuyts E., et al., 2016, *ApJ*, 827, 74
- York D. G., et al., 2000, *AJ*, 120, 1579
- Yuan T.-T., Kewley L. J., Rich J., 2013, *ApJ*, 767, 106
- Zaritsky D., Kennicutt Jr. R. C., Huchra J. P., 1994, *ApJ*, 420, 87
- de Vaucouleurs G., de Vaucouleurs A., Corwin Jr. H. G., Buta R. J., Paturel G., Fouqué P., 1991, Third Reference Catalogue of Bright Galaxies. Volume I: Explanations and references. Volume II: Data for galaxies between  $0^h$  and  $12^h$ . Volume III: Data for galaxies between  $12^h$  and  $24^h$ .
- van der Wel A., et al., 2014, *ApJ*, 788, 28

## Appendices

### A Model line ratios

In Fig. 3.12 we show the D13 model predictions for a set of standard line-ratios. We show two versions: one with tracks of constant ionization parameter,  $\log_{10} U$ , and the other with tracks of constant ionization parameter at solar metallicity,  $\log_{10} U_{\odot}$ . Both versions span the full model grid range. To enable this the  $\log_{10} U_{\odot}$  parameter must span a large range in values

$\sim (-5.0, -1.4)$ . As a result the grids are artificially clipped at extreme values of  $\log_{10} U_{\odot}$ . I.e. at high metallicities the low  $\log_{10} U_{\odot}$  model tracks pile-up and, vice versa, at low metallicities the high  $\log_{10} U_{\odot}$  tracks pile-up. This is most readily seen in  $O_{32}$  line-ratio. In fact there is only a very narrow safe range  $\sim (-3.4, -3.0)$  of  $\log_{10} U_{\odot}$  values for which there is no clipping at any metallicity. At first glance this may appear bad, however, no realistic galaxy would span both extremes in metallicity. The safe range will vary on a galaxy to galaxy basis. If clipping becomes a significant issue the inferred  $\log_{10} U_{\odot}$  parameter should become degenerate and unbounded. Visual inspection of plots, such as those shown in Fig. 3.8, would reveal if clipping has become an issue.

In Fig. 3.12 we also compare the model grid predictions with the parametrizations from M08. We note that there are some discrepancies, especially at low metallicities where the D13 models are unable to reproduce the highest  $O_{32}$  values.

It is interesting to also note that in  $O_{32}$ , which is mostly sensitive to ionization conditions, the M08 parametrization shows a similar dependence to the tracks of constant  $\log_{10} U_{\odot}$ . Much like our approach, M08 implicitly encodes some empirical dependence of ionization conditions as a function of metallicity.

## B Model systematics

In Section 3.1.1 we briefly discussed systematic offsets in the model. Here we expand upon this by exploring a larger variety of metallicity profiles (i.e. combinations of  $\log_{10}(Z_0/Z_{\odot})$  and  $\nabla_r(\log_{10} Z)$ ). This is shown in Fig. 3.13, where we fit the model to data generated by the model itself. The differences that arise indicate systematic offsets.

It can be clearly seen that portions of parameter show strong systematic offsets, typically towards steeper gradients. However, there is also a distinguishable safe region that runs diagonally from models with high metallicity and negative gradients to models with low metallicity and positive gradients (i.e. from top-left to bottom-right in Fig. 3.13). On the whole models with shallow inferred gradients ( $|\nabla_r(\log_{10} Z)| < 0.2 \text{ dex/kpc}$ ) are free from strong systematics. However, one cannot truly generalize this statement since this will depend upon, amongst other things, the size of the galaxy, the PSF of the seeing and the S/N of the observations.

There are two related effects that can explain the large systematics we observe. Firstly we notice that the models with large systematic offsets tend to pileup around  $\sim \pm 0.35 \text{ dex/kpc}$  with large errors. This is highly indicative of model degeneracy and is to be expected since, in the model we clip metallicities to the lower/upper bounds of the D13 model grid. As a direct result, models with low central metallicities and negative gradients become almost identical. The same is also true for models with high central metallicities and positive gradients.

The second reason is that we adopt a flat prior on the metallicity gradient, which, as previously noted in Section 2.4.1, is not the minimally informative prior. It is fundamentally harder to distinguish  $\nabla_r(\log_{10} Z) = 0.4$  &  $0.5 \text{ dex/kpc}$  models than it is to distinguish  $\nabla_r(\log_{10} Z) = 0.1$  &  $0.2 \text{ dex/kpc}$  models. This is true even in the absence of the aforementioned clipping issue, and this should be reflected in the prior by down-weighting steeper gradients. By choosing a broad, flat prior that includes unrealistic extreme metallicity gradients, we exacerbate the systematics.

A way to partially resolve the issue of systematic errors could be to adopt a joint prior on  $\log_{10} Z_0$  and  $\nabla_r(\log_{10} Z)$  which traces the safe region, effectively eliminating the problematic portions of the parameter space. This of course makes explicit assumptions about the nature of metallicity gradients, but it would formalize such assumptions in a tractable manner.

To summarize the origin of the systematic errors stem from the finite extent of the D13 model grids. When the model infers galaxies to have extreme metallicity gradients, these

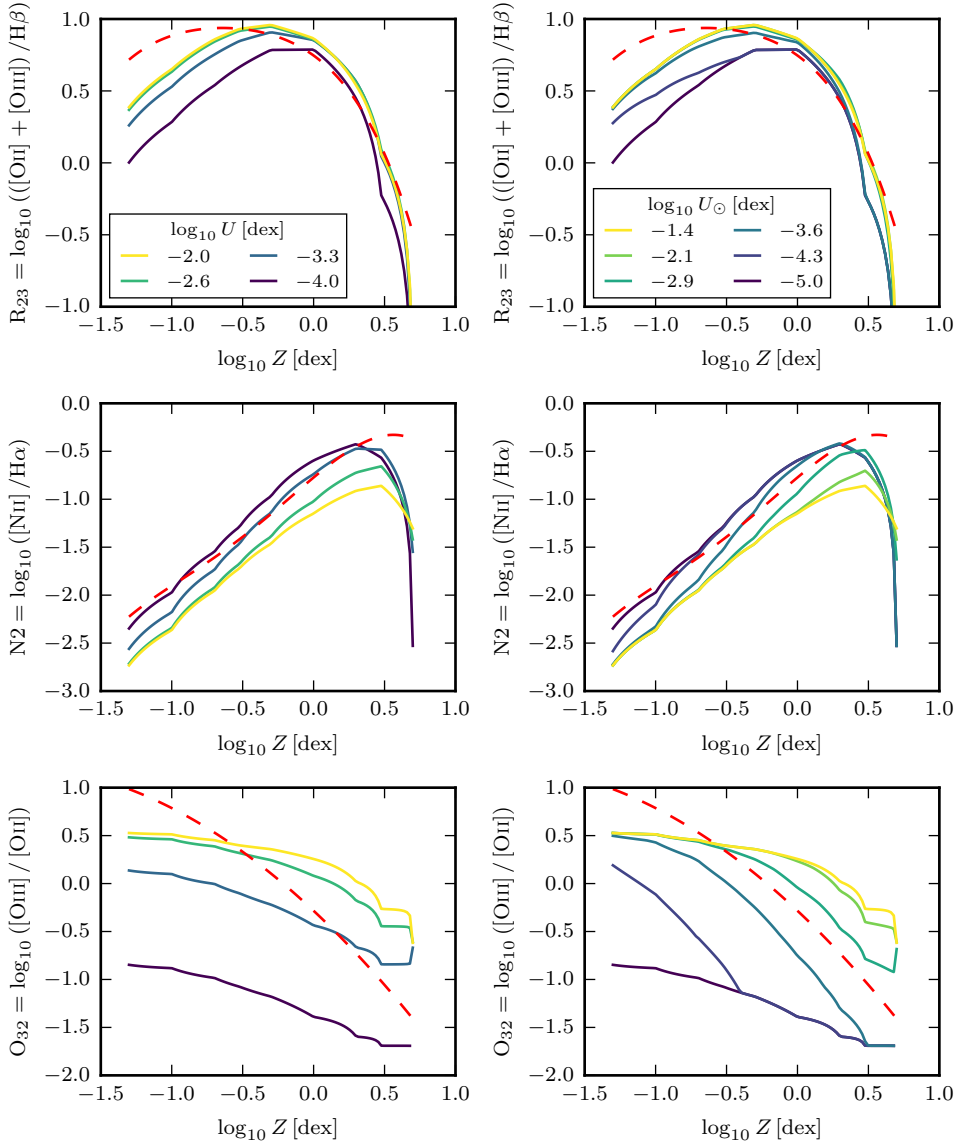


Figure 3.12: Theoretical model predictions for the  $R_{23}$ ,  $N2$  and  $O_{32}$  line ratios. (Left) We show the **D13** models grids with tracks of constant ionization parameter,  $\log_{10} U$ . (Right) We show the same model grids, but instead with tracks of constant ionization parameter at solar metallicity,  $\log_{10} U_{\odot}$ , assuming the coupling between metallicity and the ionization parameter (equation 3.2). All plots show the parametrizations of **M08** as a red dashed line.

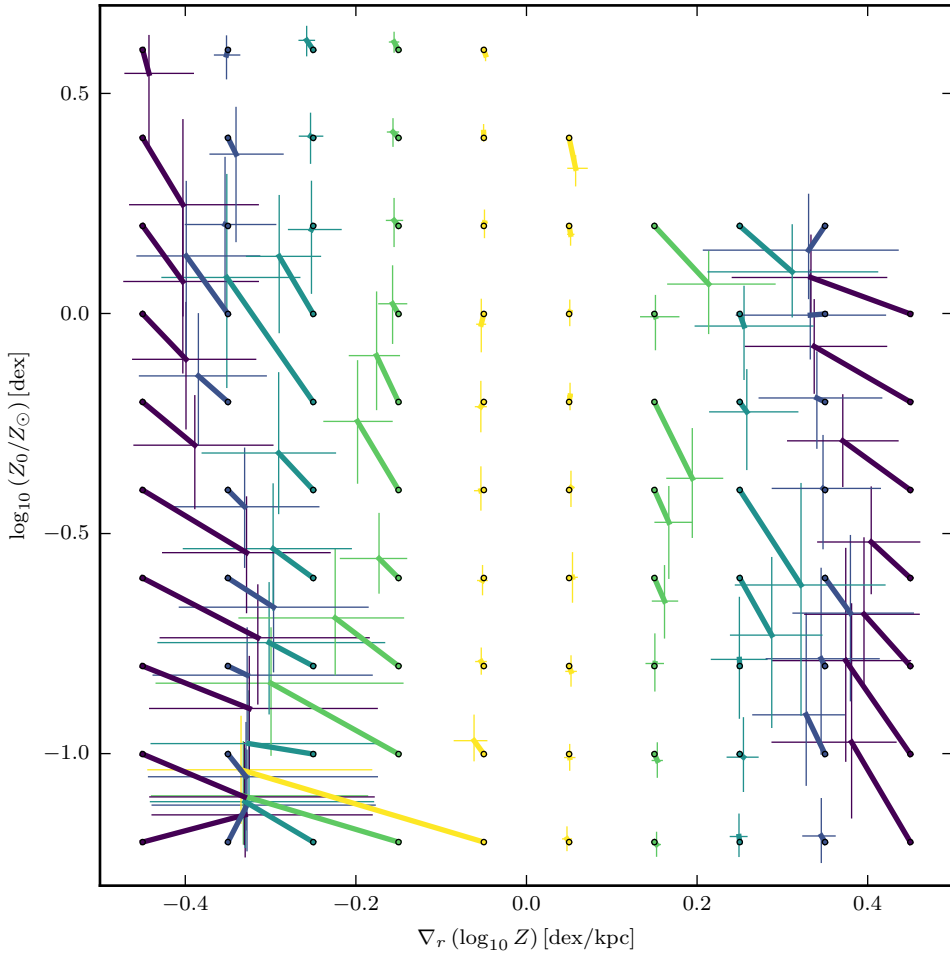


Figure 3.13: Model systematics spanning a wide range of  $\log_{10}(Z_0/Z_\odot)$  and  $\nabla_r(\log_{10} Z)$  combinations. The true input model parameters are indicated by circles. Crosses are plotted at the values inferred by the model. Size of the crosses indicate the  $\pm 1\sigma$  errors derived from the 1D marginalized posterior distributions on each parameter. Thick lines join the crosses to the true value, thereby indicating the systematic offset. Colours are added primarily to enhance clarity. Other models input parameters are the same in each model  $\text{SFR}_{\text{tot}} = 1 \text{ M}_\odot \text{ yr}^{-1}$ ,  $r_d = 0.4''$ ,  $\log_{10} U_\odot = -3 \text{ dex}$ ,  $\tau_V = 0.7$ , however, they remain free parameters in the fitting. We use a constant  $\text{S/N} = 6$  as defined on the peak flux of  $\text{H}\beta$  line. At high metallicity  $[\text{O II}]_{3726,3729}$  and  $[\text{O III}]_{5007}$  become faint and have insufficient S/N to fit the model. Therefore models with high central metallicities and steeply positive metallicity gradients (i.e. the upper-right corner) are missing from this plot. In fact this is in itself an unrelated (but nonetheless important) selection bias on the galaxies we can study.

should be treated with scepticism. Investigation of plots such as Fig. 3.8 will reveal if a the metallicity gradient is poorly constrained and unbounded. Overall, one must be acutely aware of the tendency of the model to be biased towards steeper gradients. However, a careful choice in priors may be able to mitigate against the systematics.

## C Spaxel binning algorithm

Here we outline our binning algorithm for aggregating spaxels such that the coadded spectrum meets certain acceptance criteria. In this work our S/N will be defined such that the set of emission-line fluxes are all above a minimum S/N threshold.

Any form of binning trades spatial information for an increased S/N. This algorithm is intended to reduce the impact of radial information loss, while extracting as many bins as possible, out to large radii. We therefore need to know what is the galactocentric radius of each spaxel. With all our data we have higher-resolution images that provides us with accurate estimates for the centre of the galaxy, inclination of the galaxy, and its position angle on the sky. This inclination is, however, not a good match to the lower-resolution data we are binning. We use GALFIT to fit a 2D Gaussian function to a narrow-band image of a Balmer-series emission line. We fix the galaxy centre and PA to that of the high-resolution imaging, and obtain the axis ratio of the narrow-band image. Using these four parameters, we assign radial,  $r_i$ , and azimuthal coordinates,  $\theta_i$ , to each spaxel.

The binning algorithm is as follows:

- (i) Loop over all spaxels individually. Perform spectral fitting on each. If the spaxel's S/N is above the set threshold, assign it a unique bin ID number remove spaxel from future binning.
- (ii) For each remaining unbinned spaxel, coadd the spaxel with other spaxels within  $\Delta r$  and  $\Delta\theta$  of the spaxel's coordinates. ( $\Delta r$  and  $\Delta\theta$  define some initial bin size in radial coordinates.) Perform spectral fitting on the coadded spectrum and record the S/N of the weakest emission line in this bin.
- (iii) Find the bin with the lowest S/N, but still above the S/N threshold. Assign these spaxels with a bin ID number, and remove them from future binning.
- (iv) Repeat steps (ii) & (iii) until there are no bins above threshold.
- (v) Increase  $\Delta r$  and/or  $\Delta\theta$  (i.e. increase bin size) and goto step (ii). These increases follow some predefined sequence. Once  $\Delta r$  and/or  $\Delta\theta$  reach a maximum size limit, continue to next step.
- (vi) For each remaining unbinned spaxel. Accrete the spaxel to the nearest bin at a greater radius than it. If the S/N of the new bin is greater than previous then record the new bin. Otherwise discard the spaxel and leave the bin unchanged.

## D SFR Maps

In order to fit our model to the emission-line data we require the SFR distribution as an input. We could simply fit our data with an exponentially declining SFR density (see equation 3.11), but, as discussed in section 3.2, clumpy star formation can affect the inferred metallicity profile. For this reason, we wish to input a best-guess SFR map.

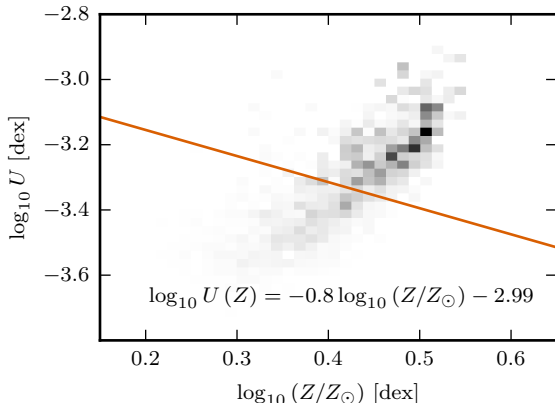


Figure 3.14: Correlation between ionization parameter and metallicity for UGC463. The individual spaxels are shown as a grey histogram, weighted by the  $H\alpha$  flux of each spaxel. The orange line indicates the best fit solution for the  $\log_{10} U_{\odot}$  assuming the fixed coupling between the ionization parameter and metallicity (i.e. equation 3.2).

To generate these high-resolution SFR maps we use a combination of multi-band<sup>13</sup> HST imaging and stellar population synthesis (SPS) modelling. Maps of the SFR and other derived quantities will be published by Shirazi et al. (in prep.). The modelling procedure is described in detail by Kauffmann et al. (2003) and Gallazzi et al. (2005). For the SPS models we adopt a star formation history which is a combination of an exponentially declining SFR and superimposed random bursts. The photometry is calculated using the Bruzual & Charlot (2003) stellar template library. Stellar fluxes are attenuated by dust, with the adopted attenuation curve depending on the stellar age. Young stars ( $< 10$  Myr) are attenuated by a  $\tau(\lambda) \propto \lambda^{-1.3}$  power-law, whilst older stars will be attenuated by a shallower  $\tau(\lambda) \propto \lambda^{-0.7}$  power-law. This dust model was proposed by Charlot & Fall (2000).

For a reliable SPS analysis we require a minimum  $S/N \geq 5$  in the (F450W – F606W) colour image. To reach this we bin the data using the weighted Voronoi tessellation by Diehl & Statler (2006), a generalization of the algorithm by Cappellari & Copin (2003). Using the SPS modelling we calculate the total SFR in each bin. However, we wish to partially restore the resolution lost by binning. We therefore redistribute the binned SFR into the individual pixels using the same proportions as the pixel F814W flux.

Following this procedure we can use high-resolution photometry to produce SFR maps. We will use these maps as inputs for our emission-line modelling.

## E Additional figures

In Fig. 3.14 we show the correlation between ionization parameter and metallicity in UGC463. This positive correlation shows a very different dependence from the typical anti-correlation that we assume.

In Fig. 3.15 we show Quantile-Quantile (Q-Q) for models shown in Tables 3.2 & 3.3. If there are no systematic offsets then the data should pass through the (0,0) coordinate (within error). If the model errors are normally distributed then they should match the black one-to-one line.

<sup>13</sup>F300W, F450W, F606W and F814W

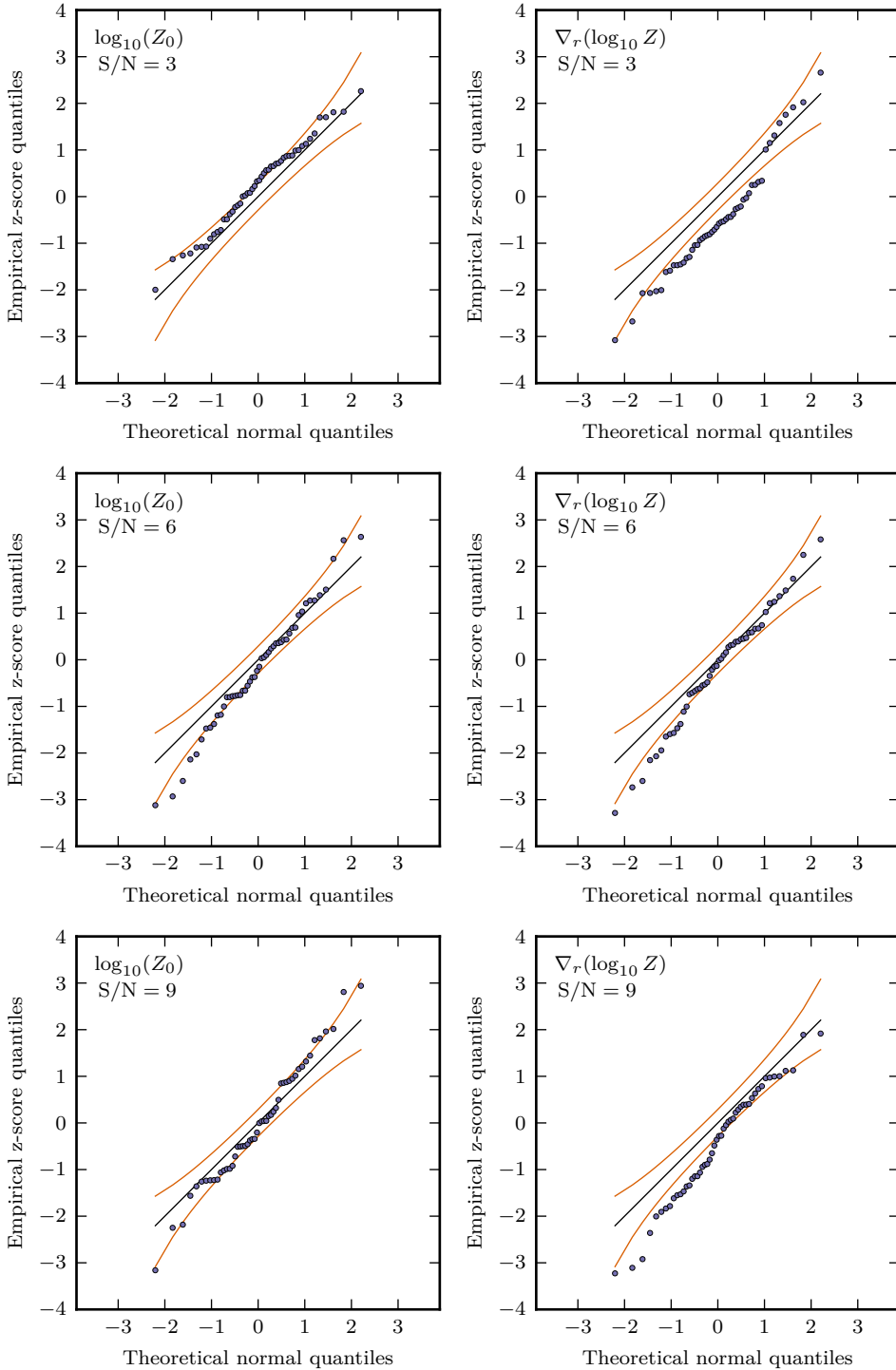


Figure 3.15: Quantile-Quantile plots showing the distribution of inferred model solutions relative to the true input value. The z-scores of the 50 realizations are plotted on the y-axis, whilst the x-axis shows the z-scores if they were normally distributed. The orange lines indicate a 90% confidence interval.



# 4

---

## *First gas-phase metallicity gradients of $0.1 \lesssim z \lesssim 0.8$ galaxies with MUSE*

---

We present gas-phase metallicity gradients for 94 star-forming galaxies between  $0.08 < z < 0.84$ . We find a negative median metallicity gradient of  $-0.043^{+0.009}_{-0.007}$  dex/kpc, i.e. on average we find the centres of these galaxies to be more metal-rich than their outskirts. However, there is significant scatter underlying this and we find that 10% (9) galaxies have significantly positive metallicity gradients, 39% (37) have significantly negative gradients, 28% (26) have gradients consistent with being flat, the remainder 23% (22) are considered to have unreliable gradient estimates. We find a slight trend for a more negative metallicity gradient with both increasing stellar mass and increasing star formation rate (SFR). However, given the potential redshift and size selection effects, we do not consider these trends to be significant. Indeed when we normalize the SFR of our galaxies relative to the main sequence, we do not observe any trend between the metallicity gradient and the normalized SFR. This finding is contrary to other recent studies of galaxies at similar and higher redshifts. We do, however, identify a novel trend between the metallicity gradient of a galaxy and its size. Small galaxies ( $r_d < 3$  kpc) present a large spread in observed metallicity gradients (both negative and positive gradients). In contrast, we find no large galaxies ( $r_d > 3$  kpc) with positive metallicity gradients, and overall there is less scatter in the metallicity gradient amongst the large galaxies. We suggest that these large (well-evolved) galaxies may be analogues of galaxies in the present-day Universe, which also present a common negative metallicity gradient.

David Carton, Jarle Brinchmann

# 1 Introduction

Gas is a key ingredient for star-formation in galaxies. Understanding how galaxies gain and lose gas is essential to explaining galaxy evolution. We know that now and in the past the gas reserves within galaxies are insufficient to sustain star-formation for long periods (Tacconi et al. 2013). Consequently we know that galaxies continue to acquire gas throughout their lives.

Metals provide a chemical tag that identifies the gas that has previously been associated with star-formation. Therefore by tracing the spatial distribution of gas-phase metallicity<sup>1</sup> throughout a galaxy we can learn how gas is recycled and redistributed within galaxies. Equally, we can also study how galaxies accrete and lose their gas.

In the classical inside-out picture of galaxy evolution, the inner regions of galaxies formed first from low angular momentum gas. And with the increase of angular momentum over time, radial scale-length of star-formation has progressed outwards in galaxies (Larson 1976). Inside-out growth can explain why the centre of the Milky Way is more metal-rich than its outskirts (Portinari & Chiosi 1999). Moreover it can also explain why exponentially-declining radial metallicity profiles are ubiquitous in isolated massive ( $\gtrsim 10^8 M_\odot$ ) galaxies (e.g. Vila-Costas & Edmunds 1992; Zaritsky et al. 1994, and references therein).

More interestingly, not only do all star-forming galaxies present negative metallicity gradients, they present the same slope. That is, however, only once the metallicity gradient is normalized to the size of the galaxy (e.g. Sánchez et al. 2014; Ho et al. 2015). There is some debate over whether this trend continues into the outer disc of the galaxy. Indeed some have suggested that at large galactocentric radii the metallicity profile flattens (e.g. Rosales-Ortega et al. 2011; Bresolin et al. 2012; Marino et al. 2016), although it has also been suggested that the profile might steepen in the outer disc (Carton et al. 2015). Nevertheless the ubiquitous existence of a common metallicity gradient in the *inner discs* of galaxies is highly indicative of secular processes that dominate the growth of galaxies at late times.

Juxtaposed against this uniformity are observations of higher-redshift galaxies ( $z \gtrsim 0.6$ ). Although on average metallicity gradients in these galaxies are flatter than today, there is a large amount of scatter (Stott et al. 2014; Wuyts et al. 2016). A common metallicity gradient does not exist in these galaxies. Strikingly, many high-redshift galaxies have positive (inverted) metallicity gradients (see e.g. Queyrel et al. 2012). Galaxies with centres more metal poor than their outskirts are rarely if ever observed in the present-day Universe.

The prevailing explanation for this phenomenon is that metal-poor gas is flowing (or has flowed) into the inner regions of these galaxies. The inflowing gas dilutes the metals, suppressing the metallicity. The acquisition of extra gas is subsequently expected to trigger intense star formation in the galaxy. In this regard Stott et al. (2014) identified a weak trend for elevated star-formation rates in the galaxies with flatter and inverted metallicity gradients.

There are two mechanisms that have been proposed to cause the inflow of metal-poor gas: galaxy–galaxy interactions and cold flows. Firstly, galaxy–galaxy interactions might trigger radial flows within a galaxy’s disc, transporting metal-poor gas from the outskirts to the inner regions. There is observational support for this idea at low-redshift. Indeed, while it is true that there is a common metallicity gradient in isolated galaxies, non-isolated (interacting) galaxies possess significantly flatter metallicity gradients (Rich et al. 2012). Furthermore, this mechanism by which mergers flatten metallicity gradients has been demonstrated in numerical simulations (Rupke et al. 2010; Torrey et al. 2012). It appears, however, that galaxy–galaxy interactions are merely capable of flattening the metallicity gradient of galaxies, but not inverting it.

---

<sup>1</sup>Unless otherwise stated gas-phase metallicity (or simply metallicity) refers to the oxygen abundance ( $12 + \log_{10}(\text{O}/\text{H})$ ).

On the other hand, cold flows, the other mechanism proposed for producing inverted gradients, may be more successful (Cresci et al. 2010). These flows are cold streams of gas which can penetrate through a galaxy's hot halo to reach the galaxy itself (Kereš et al. 2005; Dekel & Birnboim 2006). If this material follows the gravitational potential, it could dump metal-poor gas into the inner regions of galaxies. However, it has been suggested that instead these streams form an extended gas disc (Stewart et al. 2011; Danovich et al. 2015). The hypothesized cold-flows are expected to dominate the gas supply of a galaxy at early times ( $z \gtrsim 1.8$ ), but are rarer at later times (van de Voort et al. 2011; Woods et al. 2014, e.g.). So while cold flows may explain why at  $z \approx 3.4$  observed galaxies present inverted gradients (Troncoso et al. 2014), it is harder to invoke cold flows to explain the inverted gradients at  $z \approx 1$ .

To summarize briefly, there is disparity between metallicity gradients in the high-redshift and low-redshift Universe. While not necessarily contradictory, the high-redshift results point to stochastic processes dominating galaxy evolution, while the low-redshift results suggest a secular evolution of galaxies. There are few or no observations of metallicity gradients in galaxies between  $0.1 \lesssim z \lesssim 0.6$ . Clearly, bridging this gap is a necessary step towards understanding the disparity between high and low redshift results. Here, with the Multi Unit Spectroscopic Explorer (MUSE; Bacon et al. (2010, and in prep.)), we will provide for the first time a large sample of metallicity gradients in intermediate-redshift galaxies ( $0.08 < z < 0.84$ ).

Making these observations presents several challenges. The first challenge is to correct for the effects of seeing on our data. As demonstrated by Yuan et al. (2013), failing to correct for seeing effects will produce systemically flatter metallicity gradients. The challenge seeing poses is not unique to our work and other recent studies have used simulated observations to apply a-posteriori corrections to infer the true metallicity gradient. In Carton et al. (2017, herein Chapter 3) we presented an alternative forward-modelling approach. This method is better able to quantify the degeneracies that arise from seeing corrupted data, and therefore yields formal estimates for uncertainty in the recovered metallicity gradient.

A second challenge we face is that we derive metallicities from a combination of nebular emission-lines. Depending on a galaxy's redshift, different emission-lines fall within the wavelength range of a spectrograph. It is a well-documented issue that different metallicity calibrations (especially when using different emission-lines) produce different results (e.g. Kewley & Ellison 2008). With our forward-modelling approach we can overcome these limitations and thereby self-consistently infer metallicity gradients independently of redshift.

With our observations of intermediate redshift galaxies we will attempt to reconcile the high and low-redshift pictures of galaxy evolution, particularly with respect to the gas-supply in these systems. We structure the paper as follows. In Section 2 we describe our observations our outline our galaxy selection and sample. We detail our methodology in Section 3, where we also include a sensitivity analysis for our model. Section 4 is dedicated to presenting the results on the derived metallicity gradients. In Section 5 we provide a discussion of these results. Finally we conclude our findings in Section 6.

Throughout the paper we assume a  $\Lambda$ CDM cosmology with  $H_0 = 70 \text{ km s}^{-1} \text{ Mpc}^{-1}$ ,  $\Omega_m = 0.3$  and  $\Omega_\Lambda = 0.7$ .

## 2 Data

We wish to spatially resolve metallicity gradients in distant ( $0.1 \lesssim z \lesssim 0.8$ ) galaxies. Using integral-field spectroscopy (IFS) we can map the nebular emission-lines emitted by star forming regions in these galaxies, and therefore measure radial metallicity variations.

Here we will use observations taken with the MUSE situated at UT4 of the Very Large Telescope (VLT). We will construct our galaxy sample by combining data from both Guaranteed

Time Observations (GTO) programmes and commissioning activities. However, because of the differing observing strategies employed in these observing campaigns, our data is rather inhomogeneous. Galaxies were observed with a variety of integration times (between 1 – 30 h) and in a variety of seeing conditions. We will describe these datasets fully in Section 2.1.2.

## 2.1 MUSE Observations

### 2.1.1 Instrument Description

MUSE is an integral-field spectrograph that employs an image slicing technique at optical wavelengths. In normal wide-field mode MUSE provides spectra over a continuous  $1' \times 1'$  Field of View (FoV) with a continuous spectral coverage ( $4750\text{\AA} - 9300\text{\AA}$ ). The spectra have a wavelength resolution of  $2.3\text{\AA}$  full-width half-maximum (FWHM). The spatial sampling of the data is  $0.2'' \times 0.2''$ , but the spatial resolution of our data is seeing-limited.

### 2.1.2 Field Description

Given MUSE's large contiguous field, we do not target individual galaxies, rather we target collections of galaxies with limited pre-selection. While each field was chosen to optimize the scientific objectives of the different observing programmes, in general the galaxy selection is essentially blind. There is one exception where one field (CGR28) targets a galaxy group at  $z \approx 0.7$ .

While the parent galaxy sample selection is essentially blind, there are no straightforward criteria for selecting the galaxies where we can measure metallicity gradients. That said we would expect that we can measure metallicity gradients in the largest and brightest galaxies at a given redshift. Therefore we do not make a-priori selection criteria, and analyse all MUSE detected galaxies that have known redshifts, rejecting those with insufficient signal-to-noise (S/N). We describe this S/N cut in Section 2.3.1. We present a post-hoc description of the final sample in Section 2.3.

We will now outline the data used in our analysis as follows (a summary is displayed in Table 4.1):

**Hubble Deep Field South (HDFS)** As one of the commissioning activities MUSE acquired a single deep field in the HDFS at a 26.5h depth ( $53 \times 1800$  s). The average seeing conditions were good (FWHM =  $0.66''$  at  $7000\text{\AA}$ ). Bacon et al. (2015) present a full description of the data. Here we use a slightly improved data reduction to the one presented therein. This new reduction includes improvements to the sky subtraction and slice normalization (quasi flat-fielding).

**Hubble Ultra Deep Field (UDF)** The MUSE-Deep GTO survey has observed a 9 field mosaic that covers the UDF. This  $3' \times 3'$  field has been observed to a depth of  $\approx 10$  h (in exposures of 1500 s each). In addition, there is also an extra-deep  $1' \times 1'$  portion of the mosaic that reaches  $\approx 31$  h. During the observations the average seeing conditions were good resulting in a PSF with FWHM =  $0.61'' - 0.67''$  at  $7000\text{\AA}$ . This data will be appear in Bacon et al. (in prep.), the redshifts in Brinchmann et al. (in prep.) and the full catalogue with line fluxes etc. in Inami et al. (in prep.).

**Chandra Deep Field South (CDFS)** The MUSE-Wide GTO program is surveying a portion of the Chandra Deep Field South (amongst other fields). In the end this will produce a 60 tile mosaic of the CDFS at 1 h depth (using exposures of  $4 \times 900$  s). Here we will use only the first 24 fields that have been observed. These observations were performed in moderate and

Table 4.1: Summary of galaxy observations. The final sample of galaxies were obtained from a various targeted fields (with differing exposure depths and seeing conditions). We list the number of galaxies obtained from each field.

Field	Depth [h]	PSF FWHM [arcsec]	# of galaxies in final sample
HDFS	26.5	0.66	12
UDF-Medium	≈ 10	0.61 – 0.67	33
UDF-Deep	≈ 31	0.65	9
CDFS	1	0.7 – 1.1	35
CGR28	9.75	0.60	4
CGR28-Snapshot	1	0.60	1

poor seeing conditions, resulting in a FWHM =  $0.7'' - 1.1''$  at  $7000\text{\AA}$ ) This dataset will be described by Urrutia et al. (in prep.).

**COSMOS Group 28 (CGR28)** A third GTO program is surveying galaxies in group environments. In our analysis here we will use observations of one of these galaxy groups (namely Group 28 as identified in the zCOSMOS 20k Group Catalogue [Knobel et al. \(2012\)](#)). The deepest portion of the field is slightly less than the full  $1' \times 1'$  FoV and reaches a 9.75 h depth ( $39 \times 900$  s). However, due to none overlapping field pointings, a region at the field edge was only observed with 1 h depth. One galaxy (ID: 767296) in our final sample lies in this shallow region. The average seeing conditions were good (FWHM =  $0.60''$  at  $7000\text{\AA}$ ). This field will be presented in [Epinat et al. \(in prep.\)](#).

### 2.1.3 Data Reduction

Above we described fields from four different observing programmes and as is to be expected, there are differences in the specifics for each of the data reductions. However, in common all reductions use the standard data reduction pipeline ([Weilbacher, in prep.](#))<sup>2</sup> to produce calibrated datacubes. In all fields sky subtraction is performed using Zurich Atmospheric Purge (ZAP; [Soto et al. \(2016\)](#)) which employs a principal component analysis technique developed specifically for MUSE data.

The largest difference between the reductions are the implementations (or lack thereof) slice normalization. Slice<sup>3</sup> normalization improves the uniformity (flatness) of the field and are primarily required because the flat-field calibrations are not taken at the exact same time as the science exposures. Small changes in the instrument alignment due to thermal variations can alter the throughput to the slits. Slice normalization is essentially a secondary flat-fielding, that self-calibrates on the individual science exposures. Because multiple exposures are combined, these semi-random slice systematics contribute to the effective noise in the final datacube. The slice normalization is very important for faint galaxies, but will have little impact on the bright galaxies that we study here. Thus the fact that the various data reductions implement the normalization differently will not affect our results.

The final datacubes are constructed with equal sized voxels<sup>4</sup> ( $0.2'' \times 0.2'' \times 1.25\text{\AA}$ ), which mirrors the native pixel size at the charge-coupled device (CCD) level. With this voxel size, the typical seeing-limited point-spread function (PSF) is well sampled, whilst the  $2.3\text{\AA}$  line-spread function (LSF) is only just critically sampled.

<sup>2</sup>A short description of the pipeline can be found in [Weilbacher et al. \(2012\)](#)

<sup>3</sup>By slice we refer to the optical image slicers within MUSE, not the wavelength layers (channels).

<sup>4</sup>volumetric pixel

### 2.1.4 PSF Determination

A critical part of our analysis is to forward model the seeing effects on our data. It is therefore necessary to measure the final PSF directly from our datacubes. It is known that the MUSE PSF is relatively spatially invariant across the FoV, thus a PSF model fit to a bright star within the FoV can be applied across the whole field. Unfortunately, not all fields contain such bright stars, and therefore we use a variety of PSF determination techniques in the different fields:

**HDFS** This field contains a bright star to which [Bacon et al. \(2015\)](#) fit a Moffat function. The FWHM of the Moffat profile is allowed to vary as a function of wavelength, but the Moffat  $\beta$  parameter is not. We describe the FWHM as a piecewise linear function with three knots (at 4750, 7000, 9300Å).

**UDF** Some of the MUSE UDF pointings do not contain any bright stars. Thus the PSF must be inferred from non-point source objects (i.e. galaxies). Hubble Space Telescope (HST) images are convolved with the Moffat function and fit<sup>5</sup> to MUSE pseudo-broadband images. We obtain a best fit Moffat profile as a linear function of wavelength. The Moffat  $\beta$  parameter is assumed to be constant. The accuracy of this method has been verified by comparing the results in those fields that do contain bright stars.

**CDFS** As with the UDF, many of the CDFS fields are also devoid of bright stars. Here we use the brightest galaxies to measure the PSF. The shapes of these galaxies are measured using [SEXTRACTOR \(Bertin & Arnouts 1996\)](#). By modelling these sources as a 2D Gaussian, the best fit PSF for a series of MUSE pseudo-broadband images is found. This PSF is modelled as a Gaussian profile, where the FWHM varies linearly with wavelength. Fields that contain bright stars are also modelled with a direct fit to the star. These stellar fits are used if they indicate a FWHM that is a better match to the telescope autoguiding measurements.

**CGR28** This field contains four relatively faint stars. We perform a simultaneous fit to all stars using a Moffat PSF. The FWHM is assumed to have a 3<sup>rd</sup> order polynomial, whilst the Moffat  $\beta$  is assumed to only have a linear dependence.

To summarize, we model the PSF with an axisymmetric function (either a Moffat or Gaussian function). The FWHM is free to vary as function of wavelength, and is larger at bluer wavelengths. These wavelength-dependent PSF models are directly used in our forward-modelling of our observations.

## 2.2 Derived global properties

As part of our analysis we study metallicity gradients as a function of global galaxy properties, e.g. stellar mass, star formation rate, and disc size. We now outline how these quantities are derived.

### 2.2.1 Stellar Mass

There exists extensive broadband photometry for all of the fields that we study here. Stellar masses are estimated through stellar population synthesis (SPS) modelling. This yields a self-consistent mass estimate, despite the differing availability of filters in different fields. We use [FAST \(Kriek et al. 2009\)](#) to fit the photometry of each galaxy, using [Bruzual & Charlot \(2003\)](#) SPS models with a [Chabrier \(2003\)](#) initial mass function (IMF). We assume an exponentially declining star-formation history,  $\text{SFR} = \exp(-t/\tau)$ . The model grid is sampled in steps of 0.2 dex spanning  $\log_{10}(t/\text{yr}) = [8.0, 10.2]$ . The decay timescale is sampled in intervals

<sup>5</sup>The fit is performed in the Fourier space

of 0.5 dex covering  $\log_{10}(\tau/\text{yr}) = [8.5, 10.0]$ . We include models with a range of *stellar* metallicities  $Z = \{0.004, 0.008, 0.020, 0.050\}$ . A Calzetti et al. (2000) dust law is assumed with V-band attenuations varied between  $A_V = [0, 3]$  (in steps of 0.1 mag). We fix the redshift of the galaxy to that derived from the MUSE spectra.

Photometry used in each of the four fields is derived from various sources, all of which are approximations of the total magnitude:

**HDFS** For this field we use the four-band HST photometry {F300W, F450W, F606W, F814W} from Casertano et al. (2000).

**UDF** Extensive deep multi-band HST photometry is provided by Rafelski et al. (2015) in {F225W, F336W, F435W, F606W, F775W, F850LP, F105W, F125W, F140W, F160W}. Where possible, we use all filters.

**CDFS** Here we use the photometric catalogue of Guo et al. (2013) using exclusively the HST photometry {F606W, F775W, F814W, F850LP, F105W, F125W, F160W}, using all where available.

**CGR28** In this field we adopt the photometric catalogue of Capak et al. (2007) using {Subaru  $B_j V_j g^+ r^+ i^+ z^+$  NB816, SDSS  $u g r i z$ , CFHT  $u^* i^*$ , HST F814W, CTIO/KPNO  $K_s$ }.

### 2.2.2 Star Formation Rate (SFR)

We derive global star formation rates directly from the MUSE data, taking the spectrum integrated across the whole galaxy. On this we perform a full spectral-fitting using PLATEFIT (Tremonti et al. 2004; Brinchmann et al. 2004). We will describe the spectral fitting in Section 3.1.2. Here it simply suffices to say that we obtain the  $H\alpha$ ,  $H\beta$  and  $H\gamma$  emission-line fluxes, accounting for the underlying stellar absorption.

For low-redshift galaxies ( $z \lesssim 0.4$ ) we use  $H\alpha$  and  $H\beta$  to compute the SFR. At higher redshifts  $H\alpha$  is redshifted beyond the MUSE wavelength range, so we compute the SFR in these galaxies using  $H\beta$  and  $H\gamma$  instead.

To correct for dust we adopt the Charlot & Fall (2000) birth-cloud absorption curve

$$L_{\text{ext}}(\lambda) = L(\lambda)e^{-\tau(\lambda)}, \quad (4.1)$$

with

$$\tau(\lambda) = \tau_V \left( \frac{\lambda}{5500 \text{ \AA}} \right)^{-1.3}, \quad (4.2)$$

where  $\tau_V$  is the V-band optical depth. Depending on the redshift we use either the observed  $H\alpha/H\beta$  or  $H\gamma/H\beta$  ratios to calculate  $\tau_V$ . For this we assume intrinsic Case B Balmer recombination ratios of  $j_{H\alpha}/j_{H\beta} = 2.86$  and  $j_{H\gamma}/j_{H\beta} = 0.468$ . These values are appropriate for H II regions of temperatures,  $T_e = 10000$  K, and electron densities,  $n_e = 100 \text{ cm}^{-3}$  (Dopita & Sutherland 2003).

Finally, we convert dust corrected  $H\alpha$  luminosities to SFRs using a scaling relation between  $H\alpha$  and SFR

$$\log_{10} \left( \frac{\text{SFR}}{\text{M}_{\odot} \text{ yr}^{-1}} \right) = \log_{10} \left( \frac{L(H\alpha)}{\text{erg s}^{-1}} \right) - 41.27, \quad (4.3)$$

(Murphy et al. 2011; Hao et al. 2011; Kennicutt & Evans 2012).

### 2.2.3 Galaxy Morphology

In Chapter 3 we presented a method for modelling the metallicity gradients in our galaxies. As inputs, this method requires four basic morphological parameters describing: the galaxy centre (Right Ascension, RA, and Declination, Dec.), the inclination of the galaxy (inc.) and the position angle of the major axis on the sky (PA). For our discussion we also need galaxy size, which we shall express as the exponential disc scale-length,  $r_d$ .

All the fields we present here are well studied and have existing morphological catalogues.

**HDFS** For this field [Contini et al. \(2016\)](#) provide a detailed morphological analysis of the resolved galaxies. They perform a bulge-disc decomposition on the HST F814W imaging, which yields all the necessary morphology information.

**UDF + CDFS** For both these fields [van der Wel et al. \(2012\)](#) provide a catalogue of single Sérsic fits. While this catalogue provides most of the relevant information, it does not provide estimates for the galaxy inclinations. Instead it only provides the axis ratios of the galaxies. Since axis ratio is primarily a function of inclination, we can convert axis ratios into inclinations. However, axis ratios have a secondary dependence on the morphological type of the galaxy. Since the Sérsic index is a proxy for morphological type, we can reduce this secondary dependence by partitioning the catalogue into quintile bins of the Sérsic index. Within each of these bins we order the galaxies by decreasing axis-ratio. Since we view galaxies from orientations, we assume this order represents a linear sequence of increasing galaxy inclination between  $[0^\circ - 90^\circ]$ . We can use the rank order of the galaxy within the bin to estimate its inclination.

To estimate the galaxy sizes we use the half-light radii,  $r_e$ , reported in the catalogue. To convert these to disc scale-lengths we simply assume that the galaxy profile is a bulgeless exponential disc (i.e.  $r_d \approx 0.596 r_e$ ).

The catalogue provides the morphology derived from three HST bands (F105W, F125W and F160W). For any given galaxy we use the morphology of the band with the highest S/N.

**CGR28** For this field we use the morphological assessment provided by the COSMOS 2005 Morphology Catalogue, which uses MORPHEUS ([Abraham et al. 2007](#)) to measure the morphological parameters. As above, this catalogue also only reports a galaxy's axis ratio, not inclination. Again we apply the rank ordering method to convert to axis ratio into an inclination. To avoid mixing morphological types, we use the concentration index as a proxy for morphological type. We divide the catalogue into decile bins of the concentration index, and perform the rank ordering within each. This catalogue provides the half-light radii of the galaxies, which we convert to exponential disc scale-lengths as above.

The galaxy morphology from the different catalogues are measured in different photometric bands. This will systematically affect the measured galaxy sizes. Sizes of late-type galaxies measured at redder rest-frame wavelengths will appear systematically smaller. To correct for this we use the parametrization of [van der Wel et al. \(2014\)](#) (their equations 1 & 2). This correction depends only on the galaxy's redshift and stellar mass. In this work all galaxy sizes are quoted as if they were measured at a rest-frame wavelength of  $5000\text{\AA}$ .

## 2.3 Sample Description

As mentioned previously, we do not make an a-priori selection for our sample. Nevertheless, there are many galaxies for which we cannot meaningfully constrain the metallicity gradient. Naturally we would expect we can only measure metallicity gradients in the largest and brightest galaxies. However, it is non-trivial to map this to a clean cut on global properties

(e.g. stellar mass, size and SFR). Therefore we build our final sample based upon data-driven criteria (i.e. S/N).

### 2.3.1 Selection Criteria

We extract spatially resolved emission-line fluxes from our parent sample of 590 MUSE detected galaxies (with  $z < 0.85$ ). The procedure for this extraction is described in Section 3.1. In many galaxies we fail to detect any emission-line component.

To meaningfully constrain metallicity (and distinguish its effects from dust) we need two strong forbidden lines and two Balmer lines to be detected at  $S/N \geq 5$ . Exactly which emission lines are chosen depends on the galaxy. Using the globally integrated spectrum we choose the two forbidden lines with the highest S/N, and the two Balmer lines with the highest S/N. A typical emission-line choice for a low-redshift galaxy might be  $\{H\beta, [O\ III]5007, H\alpha, [S\ II]6717,6731\}$ . And a typical choice at high-redshift might be  $\{[O\ II]3726,3729, H\gamma, H\beta, [O\ III]5007\}$ .

Since we need to constrain the metallicity gradient of the galaxy, not just its metallicity, the line emission must be detected in multiple spatial bins. Explicitly we require that the four chosen emission-lines are all detected at  $S/N \geq 5$  in at least three spatial bins. (The spatial binning scheme is described in Section 3.1.1).

Overall these criteria amount to a minimum S/N cut. How this selection maps to galaxy properties depends on the field (because our observations have different depths and seeing conditions).

In addition to this main selection cut, we apply three further criteria:

- Rarely, but on occasion, the emission we detect may not be associated with the target of interest, i.e. the data is contaminated by a brighter neighbouring galaxy, at the same redshift. These cases can be identified through visual inspection. We manually excluded galaxies where contamination is apparent.
- When modelling the metallicity gradients in our galaxies we assume the galaxies infinitesimally thin disc. This approximation is acceptable for face-on galaxies, however, it becomes increasingly questionable for more inclined systems. We therefore exclude galaxies with an estimated inclination  $\text{inc.} > 70^\circ$ .
- Galaxies with bright active galactic nuclei (AGN) will produce bright line-emission. Such emission would alter the observed emission-line ratios, and thus alter the inferred metallicities. In the following section we explain how we exclude AGN.

### 2.3.2 AGN Exclusion

It is difficult to determine the metallicity of galaxies when they are contaminated by emission from AGN or low-ionization nuclear emission-line regions (LINERs). We could treat such galaxies in one of three ways. Firstly one could attempt to model the flux contribution from a compact central source. Secondly we could mask out the central regions of a galaxy, and derive the metallicity gradient from the outer regions of the galaxies. A third approach, and the one we adopt here, is to simply discard galaxies from our sample if they appear to have a significant AGN/LINER component. We classify our galaxies using standard emission-line ratios classifications, which we apply to a galaxy's globally integrated spectrum.

At low redshift ( $z \lesssim 0.4$ ) we use the both  $[N\ II]/H\alpha$  and  $[O\ III]/H\beta$  ratios to classify galaxies. We follow the classification scheme of Brinchmann et al. (2004) to divide galaxies into three categories: pure star forming, those with significant AGN, and those that fall in between (i.e.

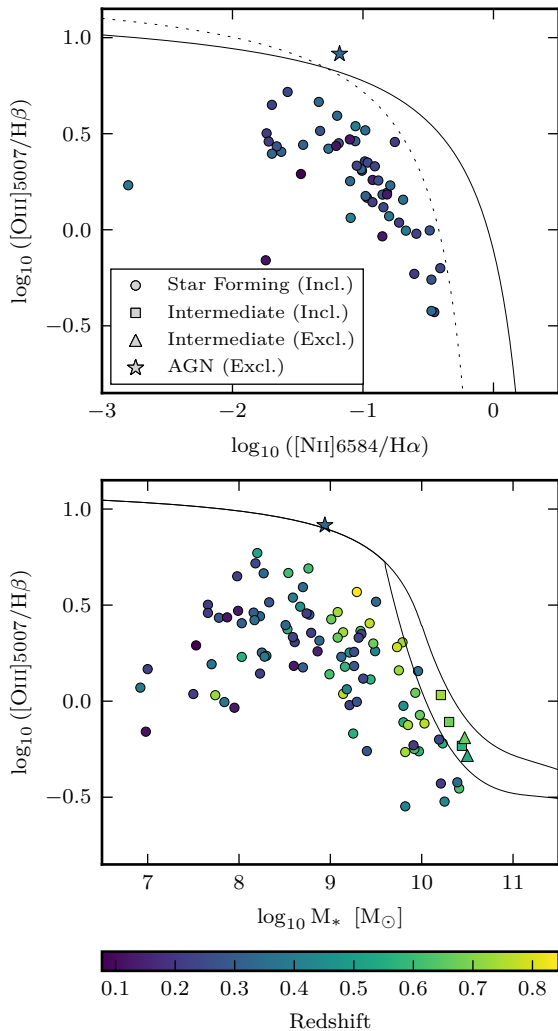


Figure 4.1: Diagnostic plots for AGN classification. Our final sample of star forming galaxies and included intermediate galaxies are plotted as circles and squares, respectively. Excluded intermediate and AGN/LINER galaxies are indicated by triangles and stars, respectively. Data points are colour coded by redshift. (Left) We plot  $[\text{N II}]/\text{H}\alpha$  versus  $[\text{O III}]/\text{H}\beta$  diagnostic (a BPT (Baldwin et al. 1981) diagram) for the low redshift ( $z \lesssim 0.4$ ) portion of our sample. As a solid line we indicate the Kewley et al. (2001) theoretical maximum limit for star formation alone. With a dashed line we show the Kauffmann et al. (2003) curve, the empirical division between emission from star formation and AGN/LINER emission. (Right) We show the Mass-Excitation (MEx) diagram for our sample, including also the Juneau et al. (2014) demarcations as solid black lines. Note that galaxies which appear on left (the BPT diagram) also appear the right (the MEx diagram).

intermediate). We exclude galaxies classified as AGN, but we do not automatically exclude the intermediate cases. These intermediate galaxies are inspected manually and we exclude those that possess broad emission-line velocity components, indicative of AGN.

At  $z \gtrsim 0.4$  the  $[\text{N II}]/\text{H}\alpha$  is redshifted out of MUSE’s wavelength range. Therefore we adopt the Mass-Excitation (MEx) diagnostic (Juneau et al. 2014) to classify the galaxies into the same three classifications (star forming, intermediate, AGN). As before intermediate cases are manually inspected.

In Fig. 4.1 we show where our galaxies lie with respect to the two diagnostics. Out of 97 galaxies we exclude one galaxy below  $z \approx 0.4$  and two galaxies above.

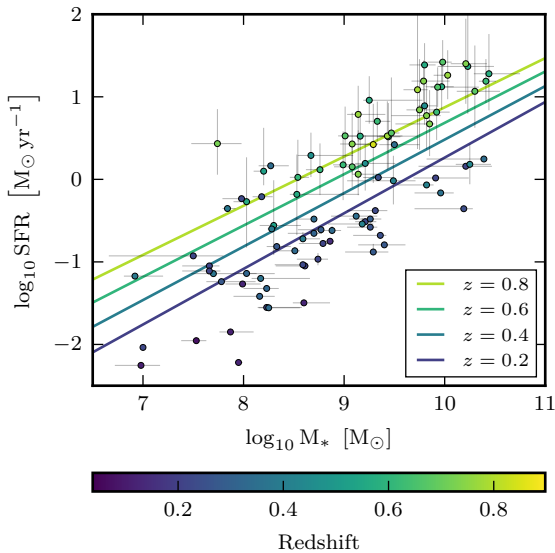


Figure 4.2: Mass versus SFR for our final sample plotted as coloured circles. For comparison, we display the main sequence at four different redshifts as solid lines, adopting the parametrization of Whitaker et al. (2012). Note that the SFR of the low redshift galaxies are derived from  $H\alpha$  and  $H\beta$  lines, whilst the high redshift galaxies are derived from  $H\beta$  and faint  $H\gamma$  lines. Consequently the SFR errors are much smaller for the low redshift galaxies.

### 2.3.3 Sample Properties

In Fig. 4.3 we present the global properties of our final sample. Therein we show the distributions of stellar mass, SFR, rest frame  $B-V$  colour and main-sequence offset ( $\Delta SFR$ )<sup>6</sup> In addition and for comparison we also plot the parent sample of MUSE galaxies. This includes all galaxies, even those that do not meet our selection criteria (Section 2.3.1).

It can clearly be seen that our final sample preferentially selects the more massive and more strongly star forming galaxies. There is also a clear redshift dependence such that in panel (a) the low-mass are almost exclusively low-redshift galaxies. Similar is true for the SFR (panel b), where the effect appears even stronger.

In contrast, both  $B-V$  colour and  $\Delta SFR$  show different trends. In panel (c) we see that below  $(B-V) \lesssim 0.6$  mag our final sample is fairly representative of the parent sample. We note that the galaxy redshifts are relatively evenly distributed between each bin.

Similar is true for the main-sequence offset parameter (panel d) where, above  $\Delta SFR \gtrsim 0$  dex, the final sample traces the same shape of the parent sample. Above the main-sequence ( $\Delta SFR > 0$  dex) the redshifts are also evenly distributed. We can display this another way; in Fig. 4.2 we show the mass–SFR correlation for our galaxies. At high-redshift our galaxies all lie above or on the main-sequence. And at low-redshift a large fraction of galaxies are found below the main-sequence.

To summarize, while at high redshift we are biased towards massive, strongly star-forming galaxies, at all epochs we are selecting blue galaxies that lie on the upper-half of the main sequence.

<sup>6</sup>We define  $\Delta SFR$  to be the difference in the observed SFR relative to what would be expected for a galaxy on the main-sequence, with the same stellar mass and at the same redshift. Here and throughout this paper we adopt the main sequence as that parametrized by Whitaker et al. (2012).

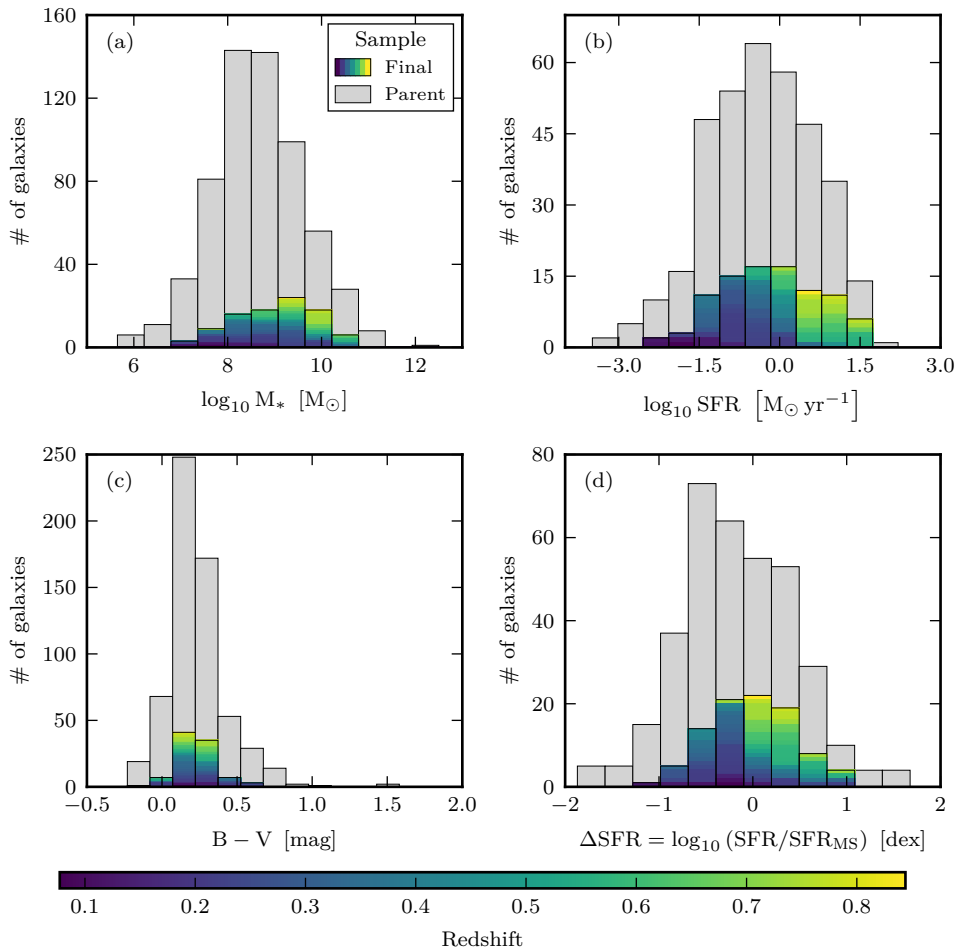


Figure 4.3: The distributions of various global galaxy properties of our final sample are shown as coloured histograms. The grey histograms show the distribution of galaxies from the parent sample. Galaxies in the final sample are coloured by their redshift. If the histogram bins were independent of redshift then each bin would be similarly coloured. We show four properties: (a) stellar mass, (b) star-formation rate, (c) rest frame Bessell B–V colour and (d) offset from the star-forming main sequence, accounting for redshift evolution. Rest frame colours are determined from the best-fit FAST spectrum to the photometry (see Section 2.2.1). While most galaxies in the parent sample have reliable photometry allowing us to derive masses and colours, fewer galaxies in the parent sample have detected line-emission. Consequently there are fewer galaxies in the parent sample in panels (b & d).

## 3 Analysis

Many of the galaxies are heavily corrupted by seeing. Additionally we further lose resolution when we aggregate (or “bin”) spaxels<sup>7</sup> together. Binning spaxels is essential for increasing the S/N in our data. So, to recover the intrinsic metallicity gradient in our galaxies, we must model both the effect of seeing and binning on our data.

In Chapter 3 we demonstrated such a method for inferring both the central metallicity,  $\log_{10} Z_0$ , and metallicity gradients,  $\nabla_r(\log_{10} Z)$  in distant galaxies. In this paper we now apply this method to a sample of galaxies observed with MUSE. We have made a few minor modifications to the method presented in Chapter 3. For brevity here we only describe the method in outline.

In the next section we will first explain how we extract the emission line fluxes (Section 3.1). We will then proceed to describe the fitting of our model to the data (Section 3.2). Finally we shall demonstrate how sensitive our recovered model parameters are to particular model inputs (Section 3.3).

### 3.1 Emission line flux extraction

When extracting emission-line fluxes there is a trade off between the number of spatial bins and the S/N of the data within each bin. One must choose a S/N threshold that is sufficiently high to minimize systematic errors in the emission-line measurements, whilst avoiding losing too much spatial information.

#### 3.1.1 Spatial Binning

In Chapter 3 (appendix C) we designed a binning algorithm that attempts to maximize the number of spatial bins above a S/N threshold. In essence this algorithm performs successive passes over the data where, on each iteration, the bin size is increased.

When calculating the S/N of a bin, we perform a full spectral fitting to the coadded spectrum. A successful bin must have all emission-lines with  $S/N \geq 5$ , where set of tested emission-lines is chosen on an object-by-object basis. This set typically consists of four lines, the two highest S/N Balmer lines and two highest S/N forbidden lines.

There are some oddities that arise from our binning strategy. To preserve radial information we define our spatial bins in polar coordinates (in a plane inclined to the observer). As a direct consequence of working in a non-Cartesian coordinate system, the pixels within a bin are not necessarily all close to each other in Cartesian space. An addition oddity is caused by the successive passes with increasing bin size. This can result with bins that are (partially or entirely) enclosed within another. While neither of these effects are ideal, we remind the reader that we mirror the exact binning in the model (the segmentation map, which is the same for all emission lines, is a model input).

Finally we note that, because we do not impose a minimum bin size, our spatial bins can be much smaller than the PSF. Consequently emission-line fluxes of adjacent bins are not strictly statistically-independent.

#### 3.1.2 Spectral Fitting

To extract the emission-line fluxes from the MUSE spectra we use the PLATEFIT spectral fitting code (Tremonti et al. 2004; Brinchmann et al. 2004). PLATEFIT applies a two-step process that first fits the stellar continuum (with emission-lines masked) before fitting the nebular

---

<sup>7</sup>spatial pixels

emission-line component (with the best-fit continuum subtracted). Note that the procedure we employ here is identical to that presented in Chapter 3 (section 4.2). Nevertheless we shall summarize it briefly here.

The continuum fitting step of PLATEFIT is not able to fit either the redshift or velocity dispersion of the spectrum. These two parameters must be provided in advance, and we do so as follows. The redshift of the spectrum is obtained using AUTOZ (Baldry et al. 2014). We wish this to be robust, so if value determined by AUTOZ deviates by more than  $\pm 500 \text{ km s}^{-1}$  from our initial redshift guess we default to that initial value. To estimate the velocity dispersion we use VDISPFIT<sup>8</sup>. At low S/N, however, VDISPFIT can yield outliers beyond the range  $[10 - 300] \text{ km s}^{-1}$ . If values outside this range are produced, we adopt a default value of  $80 \text{ km s}^{-1}$ .

With the values of the redshift and velocity dispersion predetermined, the stellar continuum is fit using a combination of Bruzual & Charlot (2003) SPS model templates. If the continuum fitting fails (because the stellar continuum is too faint or non-existent) we estimate the continuum using a running median filter (width  $150 \text{ \AA}$ ).

In the second PLATEFIT step the best fit continuum is subtracted from the observed spectrum. The emission lines are modelled as Gaussian functions. The velocity offset and velocity dispersions are the same for all emission lines. However, unlike the continuum fitting, these two velocity components are free parameters and need not be specified in advance.

The emission-line fluxes are determined from the spectral fitting, however, the formal emission-line flux errors are typically underestimated (see Brinchmann et al. 2013). We rescale these formal errors using a S/N dependent correction to obtain better estimates of the true flux error. The correction factors for this were determined from duplicate Sloan Digital Sky Survey (SDSS; York et al. (2000)) observations. Note that the SDSS spectra are of resolution comparable to MUSE.

### 3.2 Inferring metallicities

In Chapter 3 (section 2) we described our method for modelling the 2D emission-line flux distribution of galaxies and how this is fit to our observations. The galaxy is approximated as an infinitesimally thin disc, inclined to the observer. The disc is described by four fixed morphological parameters (RA, Dec, inc., PA). Our model contains five free parameters: total SFR of the galaxy,  $\text{SFR}_{\text{tot}}$ , central metallicity,  $\log_{10} Z_0$ , metallicity gradient  $\nabla_r (\log_{10} Z)$ , ionization parameter at solar metallicity,  $\log_{10} U_{\odot}$ , and the V-band optical depth,  $\tau_V$ .

The metallicity profile in the galaxy is axisymmetric and is described by an exponential function

$$\log_{10} Z(r) = \nabla_r (\log_{10} Z) r + \log_{10} Z_0, \quad (4.4)$$

where  $r$  is the radius.

We assume the ionization parameter is anti-correlated with metallicity following

$$\log_{10} U(Z) = -0.8 \log_{10} (Z/Z_{\odot}) + \log_{10} U_{\odot}, \quad (4.5)$$

where  $Z_{\odot}$  is solar abundance and  $\log_{10} U_{\odot}$  is the ionization parameter at solar abundance.

To predict the observed emission-line ratios we use the photoionization models of Dopita et al. (2013, herein D13). At each spatial position we interpolate the model grids with the appropriate values of metallicity and ionization parameter. The modelled emission-line ratios only depend on the radial coordinate; there is no azimuthal dependence.

We wish to include the  $\text{H}\delta$  and  $\text{H}\epsilon$  emission lines in our model fit. However, these Balmer lines are not provided by the D13 photoionization models. To include these lines

<sup>8</sup>[http://spectro.princeton.edu/idlspec2d\\_install.html](http://spectro.princeton.edu/idlspec2d_install.html)

we need to extend the D13 photoionization models. We do this by tabulating the Case B recombination ratios  $j_{H\delta}/j_{H\beta}$  and  $j_{H\epsilon}/j_{H\beta}$  as a function of  $j_{H\gamma}/j_{H\beta}$ . By interpolating these at the D13 photoionization model values of  $L_{H\gamma}/L_{H\beta}$ , we assign the appropriate  $L_{H\delta}$  and  $L_{H\epsilon}$  for each photoionization model. The Case B recombination ratios were determined with PYNEB (Luridiana et al. 2015) using atomic data from Storey & Hummer (1995).

### 3.2.1 SFR Maps

To model the emission-line *luminosities* we need to model the SFR distribution in the galaxy. For this one could adopt a parametric model, for example Wuyts et al. (2016) assume an exponential disc (SFR declines exponentially with increasing radius). However, since we have high-resolution HST imaging for all our galaxies, we prefer to relax this assumption and provide a 2D SFR map. Unlike the emission-line *ratios*, the modelled emission-line *luminosities* do have an azimuthal dependence.

Using the HST images we assume the distribution of stellar light provides a rough approximation for the relative SFR distribution. In the MUSE-Deep UDF fields we use the deep HST F775W imaging. In all other fields we use the F814W band which is close in wavelength. To ensure a consistent approach, we choose to use the F775W and F814W filters, which are similar in pivot-wavelength. These filters also have good S/N in all fields.

We construct SFR maps of our galaxies by cropping the HST images to only include flux within an ellipse of radius  $4 \times r_d$ . This ellipse has the same morphology (RA, Dec, inc., PA) as above. We inspect each image and alter the mask if necessary to ensure that we include all flux from the object and to remove other objects or defects. When necessary we interpolate over these rather than mask them. Negative flux values are set to zero. The final result is an SFR map that represents the *relative* spatial distribution of the SFR. The absolute SFR values are determined by normalizing the map to the total SFR,  $SFR_{\text{tot}}$ , which is a free parameter in the model.

### 3.2.2 Model Fitting

With this galaxy model we are able to mimic the resolution loss due to the seeing and spatial binning. Thus for every spatial bin we can generate a set of model fluxes that can be compared to those observed.

We fit emission lines that are observed at  $S/N \geq 5^9$ . For clarity, we emphasize that this is all emission-lines, not just the four chosen in Section 2.3.1. In other words, some emission-lines may only be detected in a few bins, but a critical subset (two Balmer, two forbidden) will be detected in all bins.

To fit our model to the data we use the MULTINEST multi-modal nested sampling algorithm (Feroz et al. 2009; Feroz & Hobson 2008; Feroz et al. 2013) that we access through a PYTHON wrapper (Buchner et al. 2014). With MULTINEST we can calculate the posterior probability distributions (posteriors) of our five model parameters.

The prior probability distributions (priors) that we place on our model parameters are outlined in Table 4.2. Except for two differences, these priors are mostly similar to the priors that were adopted in Chapter 3.

One difference is that we now adopt a logarithmic prior on  $SFR_{\text{tot}}$ , where previously (for technical reasons) we had adopted a linear prior between  $[0, 100] M_{\odot} \text{yr}^{-1}$ . For a normalization parameter we believe that a logarithmic prior is more appropriate. Changing this prior should

<sup>9</sup>We fit [O II]3726, [O II]3729, [O II]3726,3729, [Ne III]3869, H $\epsilon$ , H $\delta$ , H $\gamma$ , H $\beta$ , [O III]4959, [O III]5007, [N II]6548, H $\alpha$ , [N II]6584, [S II]6717, [S II]6731 and [S II]6717,6731. We exclude redundant lines, i.e. if [O II]3726,3729 is detected at  $S/N \geq 5$ , then we do not also fit [O II]3726 and [O II]3729.

Table 4.2: Priors on model parameters. For each parameter we detail the type of prior and the range of values covered.

Parameter	Prior type	Range
$\text{SFR}_{\text{tot}}$	Logarithmic	$[0.01, 100] \text{ M}_{\odot} \text{ yr}^{-1}$
$\log_{10} Z_0$	Linear	$\approx [-1.30, 0.70] \text{ dex}$
$\nabla_r (\log_{10} Z)$	Linear	$[-0.3, 0.3] \text{ dex/kpc}$
$\log_{10} U_{\odot}$	Linear	$\approx [-5.02, -1.42] \text{ dex}$
$\tau_V$	Linear	$[0, 4]$

have little effect on the derived metallicity profiles, provided that the dust attenuation,  $\tau_V$ , is well constrained by the data.

A second and more significant change is that we now adopt a narrower prior on the metallicity gradient,  $\nabla_r (\log_{10} Z)$  (previously we had adopted  $[-0.5, 0.5] \text{ dex/kpc}$ ). In Chapter 3 (appendix B) we identified that the inferred metallicity gradients could be sensitive to the choice of prior. We attributed this sensitivity to the finite range of metallicities spanned by the photoionization model grid. Metallicity profiles of galaxies with low central metallicities and a steep negative metallicity gradients will bottom-out at the lowest metallicity allowed by the photoionization model grid. As a direct result, negative metallicity gradients become somewhat degenerate in models with low central metallicities. Likewise, positive metallicity gradients become degenerate in models with high central metallicities.

In Chapter 3 we found that allowing an unnecessarily broad range of metallicity gradients could skew our inferences towards extreme values of the metallicity gradient. Hence we have now chosen to limit our metallicity gradient prior to the range  $[-0.3, 0.3] \text{ dex/kpc}$ . This spans the variety of currently measured metallicity gradients (e.g. [Marino et al. 2016](#); [Wuyts et al. 2016](#); [Leethochawalit et al. 2016](#)). In the following section we will assess the sensitivity of our results to various parameters, including the width of this prior.

### 3.3 Sensitivity analysis

With our model we perform fit with five free parameters. However, in our modelling we make particular choices, and fix certain parameters. We should attempt to assess the sensitivity of our results to these, considering both the magnitude of systematic errors we could expect, and the significance of unaccounted random uncertainties.

Here we will investigate four possible sources of additional errors: the width of the metallicity gradient prior, a misestimation of the PSF, a miscalculation the galaxy's inclination, and a misidentification of the galaxy centre. To estimate the size of these effects we re-analyse our galaxies, altering one of the parameters (e.g. increasing the FWHM of the PSF by 10%). By comparing the difference between this alternate model and the fiducial model, we can assess the impact of unaccounted systematics.

#### 3.3.1 Sensitivity to the width of metallicity gradient prior

First we wish to identify the galaxies that are sensitive to the choice in metallicity gradient prior. In Fig. 4.4(a) we compare the differences between two flat priors with different widths:  $[-0.3, 0.3]$  (our fiducial prior) and  $[-0.5, 0.5] \text{ dex/kpc}$  (the alternate prior). We see that most galaxies lie on the 1:1 line indicating that they are robust against the choice of prior. However, we note that some galaxies deviate significantly, showing a high degree of sensitivity to the prior. This sensitivity to the prior indicates an unreliable estimate of the metallicity gradient.

These galaxies should be treated with care in any analysis.

To assess this sensitivity we need a metric to quantify the difference between the fiducial and alternate models. For this we use the Jensen–Shannon distance applied to the metallicity gradient posteriors derived from the two models

$$\text{JS}_{\text{dist}} = \sqrt{\frac{1}{2} \sum_i P_i \ln \frac{P_i}{Q_i} + \frac{1}{2} \sum_i Q_i \ln \frac{Q_i}{P_i}}, \quad (4.6)$$

where  $P_i$  and  $Q_i$  are the discretized posteriors of the fiducial and alternate models, respectively. We place an arbitrary cut on galaxies with large Jensen–Shannon distances ( $\text{JS}_{\text{dist}} > 0.3$ ). From Fig. 4.4(a) this can be seen to be a good identifier of galaxies deviating from the 1:1 line. In the remainder of this work we consider the derived metallicity gradients for these galaxies to be suspect, and we will flag them as potentially unreliable. For transparency we do not discard them and, unless otherwise stated, we include them in our statistics.

### 3.3.2 Sensitivity to PSF errors

The assumed PSF is perhaps one of the greatest sources of unaccounted error in our analysis. In our model we assume to know the PSF perfectly, however, the true PSF is somewhat uncertain, particularly in the fields that do not contain bright stars. Uncertainties in the PSF lead to additional random errors in our result. But more severely, if we incorrectly parametrize the PSF, we could systematically bias our inferred metallicity gradients.

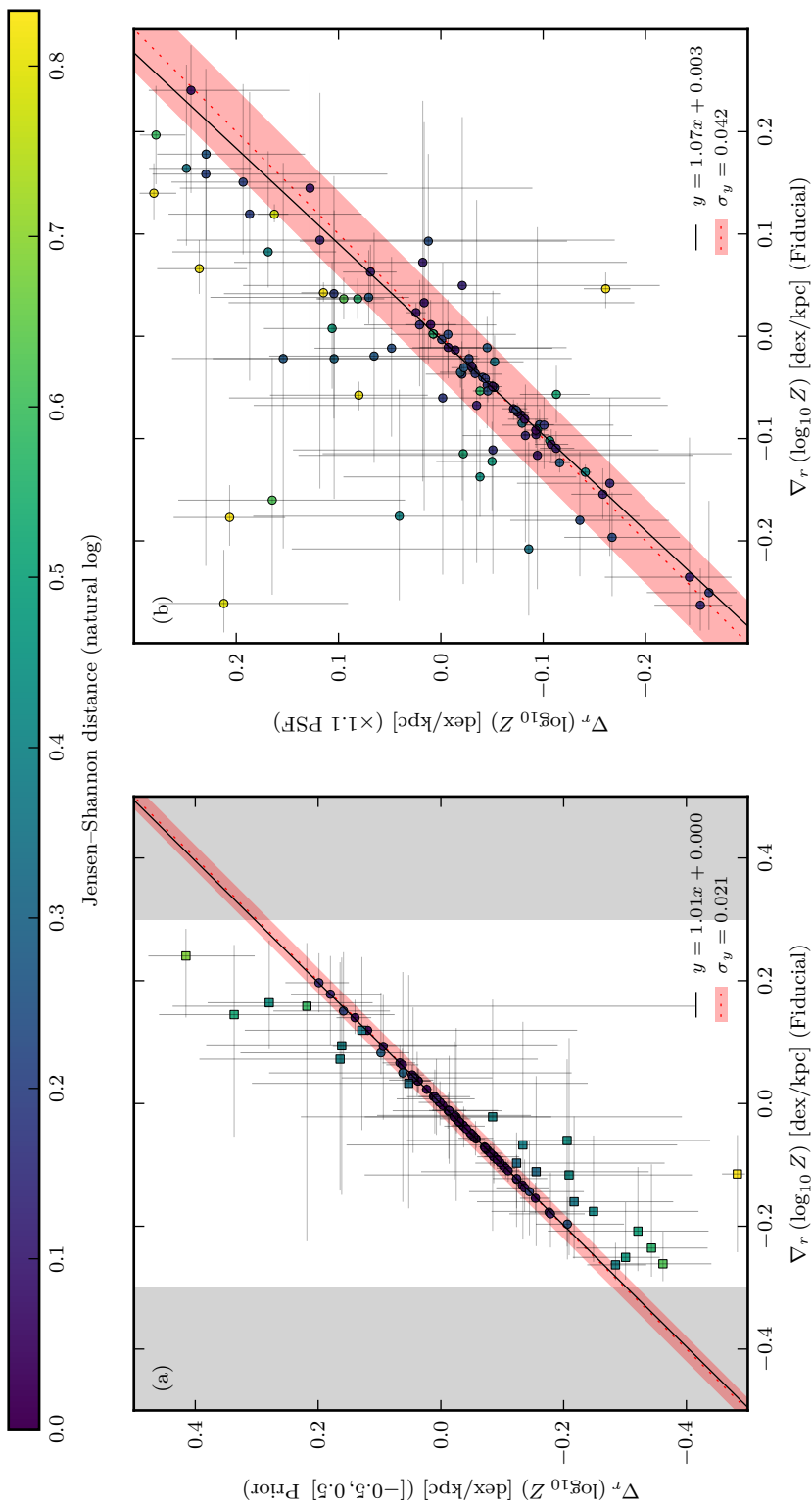
While it is challenging to truly characterize the effects of PSF errors, we can nevertheless attempt to estimate the magnitude of the problem. To do this we re-analyse our galaxies adopting two different PSF, one where the FWHM is systemically 10% smaller than the fiducial model, and another where it is 10% larger. We show the latter case in Fig. 4.4(b) and, as is to be expected, if we overestimate the PSF width then we will systematically overcorrect for seeing effects and infer systemically steeper metallicity gradients.

There is also noticeable scatter, a moderate uncertainty in the PSF will displace some galaxies significantly from the 1:1 line. In general, we find that the smaller galaxies are most sensitive. We can use the vertical displacement from the 1:1 line as indication of the expected additional uncertainty. We calculate the standard deviation (weighted by the inverse of the mean  $1\sigma$  error), and find the additional uncertainty to be  $\approx 0.03$  dex/kpc. This estimate is the mean uncertainty averaging the two alternative models where the PSF is 10% smaller and 10% larger. Naturally this value is only indicative and should not be treated as exact. Not least because it will vary from galaxy to galaxy.

### 3.3.3 Sensitivity to galaxy inclination errors

Another possible source of uncertainty is the inclination of the galaxy. Whilst it is not so likely that we systematically miscalculate the inclination, there is certainly some random error. In general inclination is most uncertain for face-on galaxies, however, this is counteracted by the fact that the metallicity gradient derived from face-on galaxies are probably the most robust against errors in the inclination.

As a rough guess we consider inclination uncertainties of the order  $\pm 10^\circ$  and construct two alternate models. We show one of these models in Fig. 4.4(c). This plot indicates that if we overestimate the inclination we will derive systemically smaller metallicity gradients. However, we note that most galaxies have small Jensen–Shannon distances and clearly lie on the 1:1 line (with minimal scatter). This would indicate that in general our model is robust against inclination uncertainties. As before, from the vertical scatter we estimate the additional uncertainty to be  $\approx 0.01$  dex/kpc.



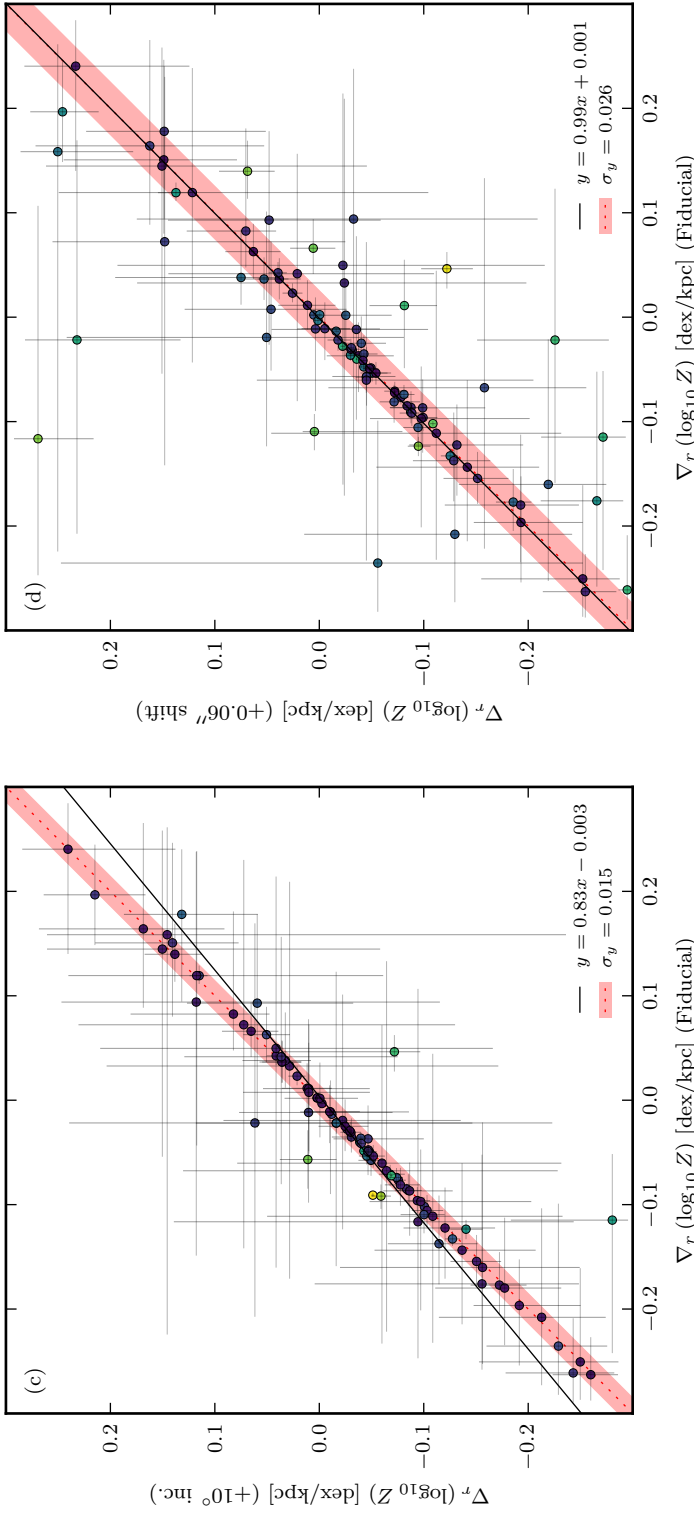


Figure 4.4: Sensitivity analysis of model inputs. On the horizontal axes we plot the metallicity gradients derived from our fiducial model. On the vertical axes we compare the metallicity gradients derived from the same data, but with the alternate model. The alternative models are identical to the fiducial except for one fixed parameter that has been adjusted slightly (see text for details). A different alternative model is plotted in each of the four panels, showing the effects of: (a) the width of metallicity gradient prior, (b) a miscalculation of the inclination and (d) misidentification of the galaxy centre. The errorbars show the  $\pm 1\sigma$  quantiles of the metallicity gradient posterior probability distribution. Note that the errors of the two models are not independent and are likely to be highly correlated, consequently the errors appear much larger than the scatter. Each data point is coloured by the Jensen–Shannon distance between the 1D marginal posteriors of the fiducial and alternate models. In each panel a solid black line shows the best fit to the data (weighted by the inverse of the formal data errors). We show the 1:1 relation as a red dotted line. A red shaded region indicates the (weighted) vertical scatter about this 1:1 relation. Equations for the best fit and scatter are given in the bottom-right corner of each panel. N.B. the errors between the fiducial and alternate models are likely to be highly correlated.

### 3.3.4 Sensitivity to galaxy centre misidentification

Finally, we address the impact of misidentifying the centre of the galaxy (the point about which the radial metallicity profile is defined). To explore this we re-analyse the data, but shift the galaxy centre  $0.06''$  along the direction of the galaxy's major axis. This distance is approximately one tenth the size of the MUSE's PSF. However, we remind the reader that the galaxy centre is actually defined from higher-resolution HST imaging. While an absolute  $0.06''$  shift will impact the smallest galaxies in our sample the most, it is arguable, however, that it is easier to define the centre of small compact galaxies than it is to define the centre of large irregular galaxy.

If galaxies have a radial metallicity profile, we might naïvely expect that shifting away from the true centre would result in a flatter metallicity gradient. However, in Fig. 4.4(d) we see no systematic trend towards flatter metallicity gradients. Misidentifying the galaxy centre appears to add no systematic bias, but it could add moderate scatter to the inferred metallicity gradients. We estimate this additional uncertainty to be  $\approx 0.04$  dex/kpc. We stress, as with the other results above, that these are only estimates of the additional uncertainty.

## 4 Results

In this section we study the metallicity gradients of our galaxies and search for trends with galaxy size, mass and SFR. Our main findings are as follows:

- We find that the average galaxy in our sample has a negative metallicity gradient. But, there is considerable scatter about this and a few galaxies have positive metallicity gradients.
- If we select the largest galaxies ( $r_d > 3$  kpc) in our sample we find this scatter reduces. In fact there are no large galaxies with inverted metallicity gradients.
- We do not find significant trends between a galaxy's metallicity gradient and either its mass or its SFR. The lack of correlation with SFR is in contrast with other studies.

From our MUSE observations we have constructed a sample of 94 galaxies between  $0.08 < z < 0.84$ . At a  $2\sigma$  significance level we identify 37 galaxies with negative metallicity gradients and 9 with positive gradients. We classify 26 galaxies having metallicity gradients that is consistent with zero gradient. Herein we shall term these galaxies as having flat metallicity gradients, a name which should not be over-interpreted; we do not claim galaxies with flat metallicity gradients to have no metallicity gradient, instead it is our analysis that may lack the statistical power to discriminate. A further 22 galaxies are flagged as unreliable for being sensitive to the metallicity gradient prior (Section 3.3.1). In Fig. 4.8 we provide an image atlas of the galaxies, wherein we indicate the metallicity gradient classification of each galaxies.

Our first result is that on average our galaxies have a negative metallicity gradient with a median of  $-0.043^{+0.009}_{-0.007}$  dex/kpc (using bootstrap and Monte Carlo resampling). We also apply a Wilcoxon signed-rank test and reject the null hypothesis that the average metallicity gradient is zero ( $p = 0.0013$ ). This contrasts with the findings of Wuyts et al. (2016) in their study of  $0.6 \lesssim z \lesssim 2.6$  galaxies they find an average metallicity gradient that is flat.

In Fig. 4.5 we present the metallicity gradients of galaxies against their size. Panels (a & b) show the metallicity gradient expressed in both scaled units (dex/ $r_d$ ) and physical units (dex/kpc), respectively. Throughout the remainder of this work we will present metallicity gradient in scaled units that normalize for the galaxy's size. At low redshift there is growing consensus that when expressed this way, isolated massive galaxies ( $\gtrsim 10^8 M_\odot$ ) share a common

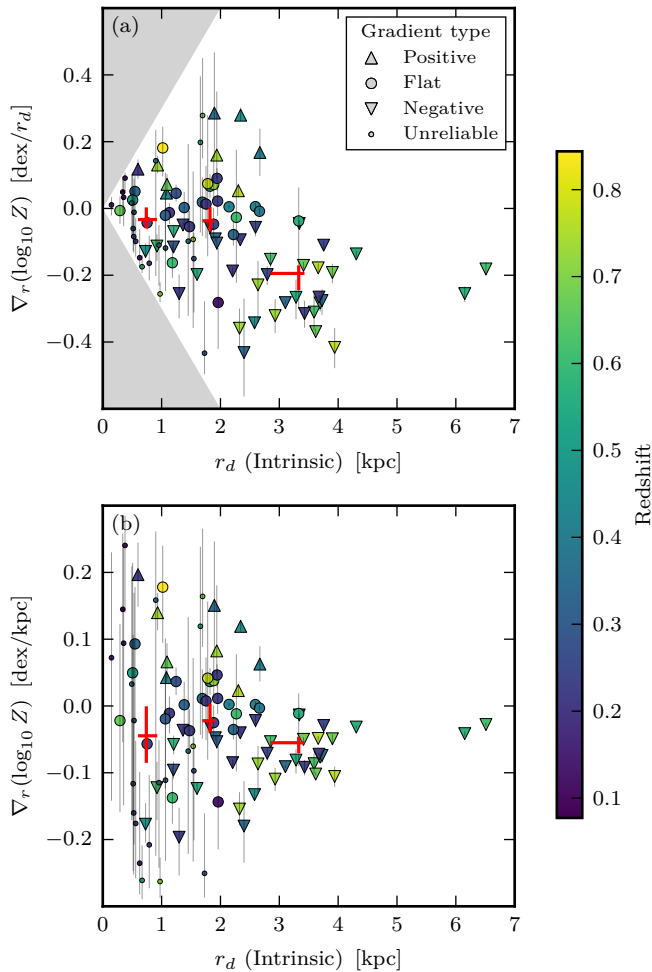


Figure 4.5: Metallicity gradients of galaxies as a function of their size. On the horizontal axes we plot the disc scale-length of the galaxies. On the vertical axes we show the metallicity gradient. In (a) we have normalized the metallicity gradient to the disc scale-length, while in (b) we display the same data but with the metallicity gradient expressed in physical units. Symbols indicate our metallicity gradient classification: triangles pointing up/down are galaxies with  $2\sigma$  positive/negative gradients, large circles represent galaxies that have metallicity gradients consistent flat, and small circles indicate galaxies flagged for their sensitivity to the prior (the squares in Fig. 4.4(a)). Data points are coloured according to the galaxy’s redshift. We overplot three red crosses, which indicate the median trend of the metallicity gradient with size. Errors on the median are determined by bootstrapping the sample, and Monte Carlo sampling of the errors (this includes unreliable galaxies). In (a) a portion of the plot is shaded grey, this denotes a region that is disallowed by our prior on the metallicity gradient.

Table 4.3: Analysis of unexplained (intrinsic) scatter in the metallicity gradients. We model the metallicity gradients as if they were normally distributed with mean,  $\mu$ , and standard deviation,  $\sigma_{\text{int}}$ . The galaxies are divided into two groups: those smaller, and those larger than  $r_d = 0.3$ . We show results for metallicity gradients expressed in both physical units (dex/kpc) and scaled units (dex/ $r_d$ ). The unreliable galaxies, which are sensitive to the prior, are not included in this analysis. Including them would not significantly alter the results.

Gradient units	Size	$\mu$	$\sigma_{\text{int}}$	# of galaxies
dex/kpc	$\leq 3$ kpc	$-0.023^{+0.012}_{-0.012}$	$0.080^{+0.011}_{-0.009}$	54
	$> 3$ kpc	$-0.062^{+0.008}_{-0.008}$	$0.031^{+0.008}_{-0.005}$	18
dex/ $r_d$	$\leq 3$ kpc	$-0.043^{+0.019}_{-0.020}$	$0.134^{+0.017}_{-0.015}$	54
	$> 3$ kpc	$-0.232^{+0.023}_{-0.025}$	$0.099^{+0.025}_{-0.018}$	18

value for the metallicity gradient (Sánchez et al. 2014; Ho et al. 2015). While this may not be true at higher redshift, we will nonetheless use scaled units.

From Fig. 4.5 it is clear that the average galaxy has a negative metallicity gradient. However, it is also clear that there is considerable scatter. There is a noticeable trend for the median metallicity gradient to become more negative with increasing galaxy size. We see that amongst the large galaxies ( $\gtrsim 3$  kpc) there are no galaxies with positive metallicity gradients. Indeed almost all large galaxies have negative metallicity gradients. Conversely, the small galaxies ( $\lesssim 3$  kpc) present a range of metallicity gradients, some negative and some positive.

The scatter in the metallicity gradient appears to sharply increase below  $\lesssim 3$  kpc. However, we see that the errorbars of the small galaxies also increase. It is therefore important to ask whether there is a true increase in the *intrinsic* scatter in the small galaxies. In Table 4.3 we present an analysis of the amount of intrinsic scatter in both the small and large galaxies. For this we model the metallicity gradients if they were normally distributed with mean,  $\mu$ , and standard deviation,  $\sigma_{\text{int}}$ . This analysis accounts for the full posterior distributions on the metallicity gradient. We see that there is indeed an increase in the intrinsic scatter in the small galaxies ( $\lesssim 3$  kpc) and that the mean is overall negative.

However, we caution that although we call this intrinsic scatter, it is perhaps more honest to call it unexplained scatter. It could simply be that our model is underestimating the true error in the metallicity gradient. Indeed it is somewhat suspicious that we see an increase in the scatter towards the smaller galaxies. We naïvely would expect that the small galaxies to be more sensitive to model specification errors, i.e. errors in the PSF or inclination (see Section 3.3). Nevertheless the sharpness of increase in scatter is certainly worthy of note.

Given that we see the galaxies with positive metallicity gradients are exclusively small, we also might expect they are also less massive. However, this does not appear to be the case in Fig. 4.6(a) where we compare the metallicity gradients against the total stellar mass of the galaxy. Galaxies with positive metallicity gradients span a similar mass range to those with negative gradients. That said, it does appear that on average metallicity gradient decreases with increasing mass. However, because of our galaxy selection, it is hard to interpret this. With a larger sample one might be disentangle the coupled selection effects on mass, size and redshift.

It is easier, however, to discuss the more massive portion of our sample. For example, at masses above  $\approx 10^9 M_{\odot}$  we notice there is a large range of metallicity gradients, with hints that the scatter is perhaps greater in the higher-redshift galaxies. This certainly is in direct contrast to the low-redshift result of a common metallicity gradient. This discrepancy might be resolved if many of these galaxies are not isolated, but are instead interacting with other

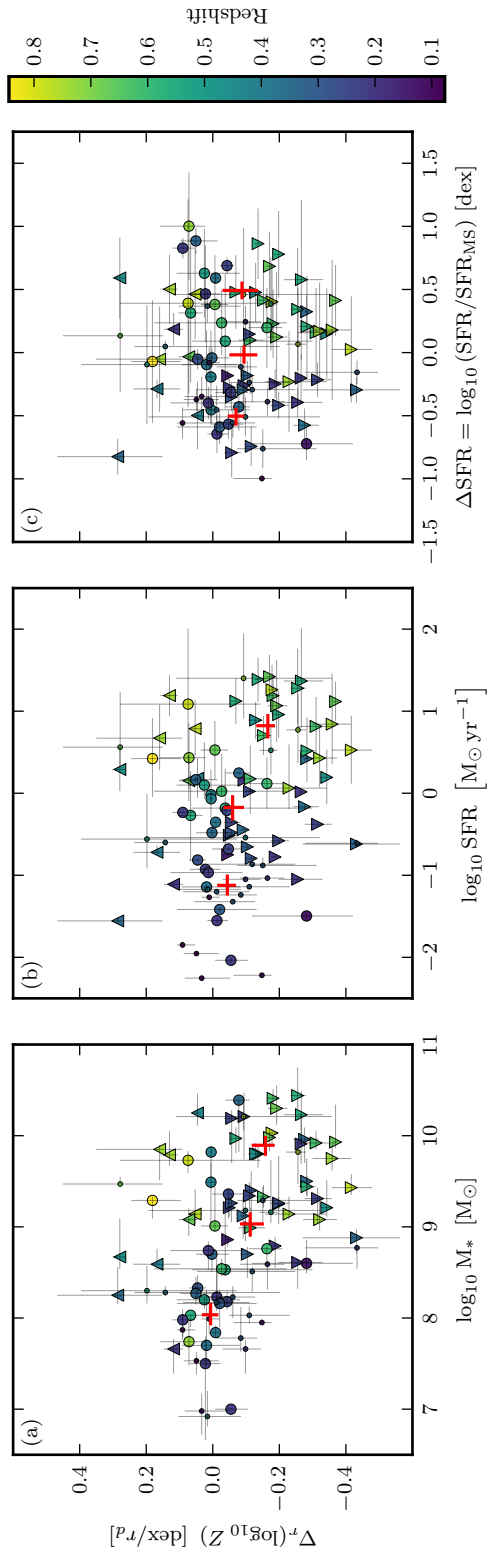


Figure 4.6: Metallicity gradients of galaxies as a function of their: stellar mass, star formation rate, and  $\Delta \text{SFR}$  (the SFR of a galaxy relative to what would be expected for a galaxy on the main-sequence with identical mass and redshift). These are shown in panels (a), (b) and (c) respectively. See Fig. 4.5 for a full description of plot (symbols, colours etc.). In panel (c) we have used the main-sequence parametrization of [Whitaker et al. \(2012\)](#).

galaxies. Because interacting galaxies typically have flatter metallicity gradients than would otherwise be expected (Rich et al. 2012).

Since interactions could trigger increased star-formation rates in interacting galaxies, Stott et al. (2014) suggested that the scatter in the observed metallicity gradients could be explained by the SFR. In Fig. 4.6(b) we compare the metallicity gradient to the SFR, however, we do not observe a trend towards more positive metallicity at high SFRs. Admittedly the association between interacting galaxies and higher SFR might be probably weak. However, in fact we see a slight trend in the opposite direction more negative gradients at high-SFRs. We caution that this trend could be a manifestation of our sample selection. Notably the SFR of a galaxy in our sample correlates with its redshift. This is in part because at higher redshifts we are biased towards the brighter, more strongly star-forming galaxies. But, it is also in part because the galaxy main-sequence has evolved, and the average SFR has decreased since  $z \approx 1$ .

So, to put galaxies on an even footing, we normalize the SFR relative to the main sequence. We define the main-sequence offset,  $\Delta\text{SFR}$ , as the difference between a galaxy's SFR and the SFR of a galaxy on the main sequence which has identical mass and redshift, where we take the parametrisation of the main sequence evolution from Whitaker et al. (2012). In Fig. 4.6(c) we show the metallicity gradients of our galaxies against  $\Delta\text{SFR}$ . We see that the trend towards negative gradients with increasing SFR now disappears. In fact in this projection, there appears to be no trends whatsoever. The average gradient is more or less constant, and there is large scatter irrespective of a galaxy's position relative to the main-sequence.

This is in contrast to the results of Stott et al. (2014) who find a positive correlation between specific star-formation rate (sSFR) and metallicity gradient. They find galaxies that are vigorously forming stars have flatter or even positive gradients. The authors suggest that an event causing infall of metal-poor gas would simultaneously trigger intense star-formation and reduce the central metallicity (thus flattening or inverting the metallicity profile). Our findings challenge such a simplistic explanation for the cause of inverted metallicity gradients. However, our results do not automatically preclude the mechanisms of galaxy–galaxy interactions and/or cold flows for triggering star-formation.

In the next section we shall discuss our results in more detail, placing them in context with other observations and theoretical work.

## 5 Discussion

### 5.1 Literature comparison

The work we present here is the first large systematic study of metallicity gradients in galaxies between  $0.1 \lesssim z \lesssim 0.8$ . However, there have been numerous studies of metallicity gradients in galaxies at lower and higher redshifts. In Fig. 4.7(a) we plot our results alongside several of these studies. Many of the high-redshift observations have used IFS techniques similar to ours, although some use observations of gravitationally lensed galaxies. Ideally these lensed observations will have sufficient resolution that seeing does not significantly affect the observed metallicity gradient. Therefore it is worth of note that both the lensed and non-lensed studies are consistent with one another, both having means centred around zero. And, apart from some lensed galaxies with very steep negative metallicity gradients, the scatter of the two are similar.

There is, however, a notable discontinuity between our observations and the other studies at  $0.8 \lesssim z \lesssim 2.6$ . This transition is most visible in the increased scatter of our observations. But there is also a shift in the average gradient to slightly negative gradients. While these effects could be attributed to the real evolution of metallicity gradients with cosmic time, the sharpness of the discontinuity would argue for a less-astrophysical causes.

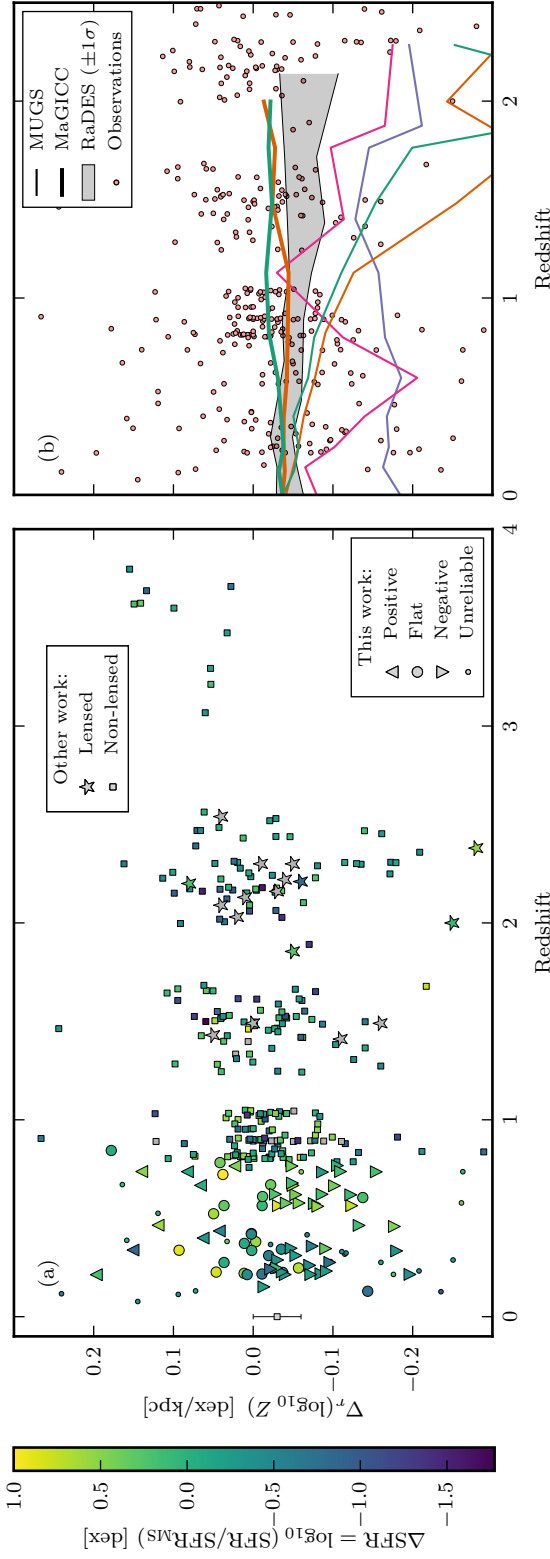


Figure 4.7: Comparison of our results with other literature, including both numerical simulation and observations. (Left) We show observational results (ours and others) compared with various numerical simulations that are overlotted. The grey shaded region indicated the  $\pm 1\sigma$  spread of metallicity gradients from 19 RaDES galaxies (Few et al. 2012). Thin coloured lines indicate MUGS galaxies (Stinson et al. 2010). Two of these galaxies (the orange and green lines) were re-simulated with the MaGICC simulations (Gibson et al. 2013) and are shown as thick orange/green lines. (Right) We compare our observational results against other studies. These metallicity gradients come from studies of galaxies that have been gravitationally lensed (star symbols), and non-lensed galaxies (squares). Where possible we colour data points to indicate the SFR relative to the main sequence ( $\Delta\text{SFR}$ ). The  $z \approx 0$  data point represents the mean and scatter in metallicity gradients reported in Sánchez et al. (2014). We compile lensing results from Yuan et al. (2011), Jones et al. (2013), Jones et al. (2015), Leethochawalit et al. (2016) and Wang et al. (2017). The non-lensed results are gathered from Queyrel et al. (2012), Stott et al. (2012), Swinbank et al. (2014), Troncoso et al. (2014) and Wuyts et al. (2016).

There are a few plausible explanations. Of which the most concerning for us is that this could highlight an issue with our method for determining metallicity gradients. A systematic overcompensation for seeing effects certainly could produce steeper gradients. It is harder, however, to conceive of systematic effects that would produce a shift away from a non-zero average gradient. In support of our results, a slightly negative average gradient is in fact consistent with observations in the low-redshift universe (e.g. [Sánchez et al. 2014](#)).

There is another reason that we might see this discontinuity between the observational studies. The vast majority the  $0.8 \lesssim z \lesssim 2.6$  galaxies have metallicity gradients determined using the N2 ratio ( $[\text{N II}]_{6584}/\text{H}\alpha$ ). Whereas we use a very different method for deriving metallicity. It is well known that there are large discrepancies between different metallicity determination methods ([Kewley & Ellison 2008](#)). The particular N2 calibration used in the other studies may produce metallicity gradients that are systematically flatter than our method.

An advantage of our method is that it produces a self-consistent metallicity gradient analysis, independent of the available emission-lines. With our MUSE observations we lose emission-lines redward of  $\text{H}\alpha$  at  $z \gtrsim 0.4$ . However, we do not observe a systematic shift in our measurements at  $z \approx 0.4$ , suggesting that our method is indeed self-consistent.

On a related note it is questionable whether any of these metallicity methods are valid at high redshift, since most metallicity calibrations and photoionization models are designed for low-redshift interstellar medium (ISM) conditions. For example, it is generally accepted that the electron density of the ISM was higher at earlier times ([Shirazi et al. 2014](#); [Sanders et al. 2016](#)), but the D13 photoionization models we use are computed only at low densities ( $\approx 10 \text{ cm}^{-3}$ ). Beyond changes in density, there lack of consensus whether other conditions have changed. At earlier times the ionization parameter, hardness of the ionizing spectrum, or nitrogen-to-oxygen abundance ratio may have been different, although there is little consensus (e.g. [Onodera et al. 2016](#); [Kashino et al. 2017](#); [Steidel et al. 2016](#), and references therein). Our method is certainly not immune to these issues, however, since our observations are all below  $z \approx 0.8$  it may not be so incredible to apply the same assumptions that we use at low-redshift. It is worth noting that, because we marginalize over galaxy wide variations in the ionization parameter, our method may partially mitigate against some of the variations in ISM conditions. Because, to first order the largest variations in nebular emission-line spectra are typically due to metallicity and ionization-parameter ([Dopita et al. 2000](#)).

## 5.2 Interpretation

In the work presented here we find on average galaxies between  $0.1 \lesssim z \lesssim 0.8$  have a negative metallicity gradient. However, there is considerable scatter about this, with some galaxies exhibiting a positive metallicity gradient. As reported by [Pilkington et al. \(2012\)](#), at any given redshift the numerical simulations predict that there is intrinsic scatter in the metallicity gradient. This can be seen in [Fig. 4.7\(b\)](#) when comparing the scatter *within* the MUGS galaxies ([Stinson et al. 2010](#)) and within the RaDES galaxies ([Few et al. 2012](#)). One should note that the difference *between* the MUGS and RaDES simulations are, however, attributable to differences in the numerical recipes for star-formation and feedback in the various simulations. Flatter metallicity gradients arise from the model prescriptions with more intense feedback. For example the MaGICC simulations ([Gibson et al. 2013](#)) re-simulate two of the MUGS galaxies using an enhanced feedback recipe. The increased feedback produces galaxies with metallicity gradients that are consistently flatter at all redshifts. [Gibson et al. \(2013\)](#) attribute this to central gas being lost in outflows that is later recycled back into the galaxy, but at larger radii.

The intrinsic diversity in metallicity gradients that we observe (also mirrored in the simulations) would indicate that at earlier times there is no common metallicity gradient. It is perhaps surprising that we observe a common abundance gradient in the universe today. That said, as

we shall later suggest, this contradiction is not necessary as acute as it would first appear. A common metallicity gradient may only exist in large galaxies.

Even though simulations can produce a large range of metallicity gradients, they typically do not reproduce the same inverted metallicity gradients that we and others observe. Simulations tend to produce galaxies with negative metallicity gradients (both steep and shallow). Some of these simulations have next to no redshift dependence, while others suggest the metallicity gradient was steeper at earlier times. Despite this variety, simulations never produce galaxies with positive metallicity gradients. Indeed, with the classical understanding of inside-out growth one expects negative metallicity gradients (Portinari & Chiosi 1999). Radial mixing of gas could flatten the metallicity gradient, but it is hard to conceive of secular processes that could produce positive metallicity gradients.

Consistent with other higher redshift studies we identify a small fraction of our galaxies that have significantly positive metallicity gradients. Contrast this with galaxies at much high-redshift ( $z \approx 3.4$ ) where all galaxies have galaxy centres are systematically more metal poor than their outskirts (Troncoso et al. 2014). In related work, Cresci et al. (2010) attribute this metallicity gradient inversion to cold flows (e.g. Dekel et al. 2009). Cold flows are streams of cold gas that penetrate the hot galaxy halo and fuel star formation in galaxies. It is argued that if this metal-poor cold gas can reach the innermost regions of a galaxy (the deepest part of the gravitational potential) then this would explain the metallicity gradient inversion.

It should be noted that cold flows are not the only way to transport metal-poor gas inner portions of a galaxy. As suggested by Rich et al. (2012) galaxy–galaxy interactions could cause radial inflow of gas though the galaxy’s disc. Metal-poor gas from the outskirts is therefore deposited in the galaxy centre. Simulations of Rupke et al. (2010) and Torrey et al. (2012) find that interacting galaxies have flat (but not positive) metallicity gradients. Is not clear whether galaxy interactions could truly invert the metallicity gradient.

In contrast to the inflow mechanisms above, outflows could also provide an alternative explanation for positive metallicity gradients. Intense centrally-concentrated star formation could produce significant outflows that entrain metal-rich gas. Using simple analytical chemical evolution arguments Cresci et al. (2010) disfavoured a wind scenario as it would require mass outflow rates far in excess of the observed SFR. That said, Troncoso et al. (2014) point out that if this metal-rich gas falls back preferentially onto the outer regions of the galaxy, it could raise the outer metallicity. This “fountain” could then enhance the ability of winds to produce positive metallicity gradients and hence reduce the required outflow rates down to more realistic levels.

Of course, the inflow and outflow scenarios need not be mutually exclusive. Gas accretion could trigger intense star formation that drives the winds. In either case (inflows and/or outflows) we should expect to observe elevated star-formation rates. In support of this Stott et al. (2014) and Wuyts et al. (2016) find weak correlations between the specific star-formation rate (sSFR) and metallicity gradient (galaxies with more intense star-formation have flatter or even positive metallicity gradients). In contrast, we do not find systematically different metallicity gradients in galaxies with elevated SFR (Fig. 4.6(c)). A difference in the sample selection might plausibly account for the difference between our results and previous studies. Alternatively one should also consider that, if the intense star-formation is confined to a galaxy’s centre, the *global* SFRs of a galaxy may not be a very sensitive indicator of inflow or outflow events.

There is perhaps another way to reconcile the lack of correlation between metallicity gradient and star-formation intensity. Contrary to our earlier assertion, it has been recently proposed by Schönrich & McMillan (2017) that inverted metallicity gradients can actually arise mostly within the framework of secular inside-out growth. This is achieved in conjunction

with outflows that recycle enriched gas from the galaxy centre, transporting to larger radii. Schönrich & McMillan (2017), however, show that these positive metallicity gradients do not persist throughout a galaxies life, and in fact are only expected to exist at early times in a galaxy's evolution. Unfortunately, given the large number of model uncertainties, they are unable to make rigorous predictions for how long this phase may last.

We find the results of Schönrich & McMillan (2017) intriguing as they may shed light on another curious result of our study. In the small galaxies ( $r_d < 3$  kpc) we observe a large scatter of the metallicity gradient, whilst larger galaxies present negative metallicity gradients with minimal scatter. If the smaller galaxies are comparatively less evolved systems, then this secular evolution (with metallicity gradient inversion at early times) may account for the diversity of metallicity gradients observed. Consequently the larger galaxies, with their negative metallicity gradients, would be emblematic of the more classical understanding of inside-out growth which produces a common metallicity gradient (e.g. Prantzos & Boissier 2000). This would reconcile our results with the low-redshift universe. And as such we could expect to find inverted metallicity gradients in small galaxies today.

## 6 Conclusions

Using MUSE GTO data we present metallicity gradients for a sample of 94 intermediate redshift galaxies ( $0.1 \lesssim z \lesssim 0.8$ ). By applying a forward-modelling technique we are able to infer the true metallicity gradient, correcting for seeing effects. We compare the observed metallicity gradient against global properties such as galaxy mass, size and SFR. From this we conclude the following:

- We find the average galaxy in our sample has a negative metallicity gradient. Nevertheless there is significant scatter and we classify 9 of the 94 galaxies as having positive metallicity gradients.
- We do not identify any significant correlation of the metallicity gradient with either total SFR or stellar mass. And we find no correlation whatsoever once the SFR is normalized relative to the main sequence.
- This lack of correlation in the latter runs contrary to previous studies. These studies, predominantly at higher redshifts ( $0.6 \lesssim z \lesssim 2.6$ ), cited such a correlation as being suggestive of sudden inflow or merger events that might trigger star-formation while simultaneously flattening/inverting the metallicity gradient. Our results, however, do not support this interpretation at the intermediate redshifts we study.
- The largest galaxies in our sample ( $r_d > 3$  kpc) are found to have almost exclusively negative metallicity gradients. On the contrary, the smaller galaxies ( $r_d < 3$  kpc) present a range of metallicity gradients. The small galaxies exhibit a larger intrinsic scatter in the metallicity gradient.
- We liken the large galaxies as similar to galaxies observed in the universe today, where galaxies present a common metallicity gradient. In addition we speculate that the size dichotomy may be related to a secular understanding of inside-out growth, where a common metallicity gradient is only established in large (well-evolved) systems.
- However, we advise caution on this last point. Intrinsically smaller galaxies are also more affected by seeing-induced resolution loss. Therefore for these small galaxies our inferred metallicity gradients (and their errors) are presumably more dependent on the accuracy of our modelling (see Section 3.3).

The MUSE GTO surveys are currently ongoing and in the future we will provide us with a larger sample of metallicity gradients. This data will allow us to separate potential selection effects and biases, which, in turn, will enable us to affirm our results.

In the future we will also study metallicity gradients in conjunction with gas kinematics of the galaxies. By also quantifying the local environments of our galaxies, we can study the impact of galaxy–galaxy interactions on the metallicity gradient, without relying on SFR as an indirect tracer.

## Acknowledgements

JB acknowledges support from FCT grant IF/01654/2014/CP1215/CT0003.

Additionally we wish to acknowledge both the PYTHON programming language and the Interactive Data Language (IDL) that were both used extensively throughout this work.

## Bibliography

- Abraham R. G., et al., 2007, *ApJ*, **669**, 184  
 Bacon R., et al., 2010, in *Ground-based and Airborne Instrumentation for Astronomy III*. p. 773508, doi:10.1117/12.856027  
 Bacon R., et al., 2015, *A&A*, **575**, A75  
 Baldry I. K., et al., 2014, *MNRAS*, **441**, 2440  
 Baldwin J. A., Phillips M. M., Terlevich R., 1981, *PASP*, **93**, 5  
 Bertin E., Arnouts S., 1996, *A&AS*, **117**, 393  
 Bresolin F., Kennicutt R. C., Ryan-Weber E., 2012, *ApJ*, **750**, 122  
 Brinchmann J., Charlot S., White S. D. M., Tremonti C., Kauffmann G., Heckman T., Brinkmann J., 2004, *MNRAS*, **351**, 1151  
 Brinchmann J., Charlot S., Kauffmann G., Heckman T., White S. D. M., Tremonti C., 2013, *MNRAS*, **432**, 2112  
 Bruzual G., Charlot S., 2003, *MNRAS*, **344**, 1000  
 Buchner J., et al., 2014, *A&A*, **564**, A125  
 Calzetti D., Armus L., Bohlin R. C., Kinney A. L., Koornneef J., Storchi-Bergmann T., 2000, *ApJ*, **533**, 682  
 Capak P., et al., 2007, *ApJS*, **172**, 99  
 Carton D., et al., 2015, *MNRAS*, **451**, 210  
 Carton D., et al., 2017, *MNRAS*, **468**, 2140  
 Casertano S., et al., 2000, *AJ*, **120**, 2747  
 Chabrier G., 2003, *PASP*, **115**, 763  
 Charlot S., Fall S. M., 2000, *ApJ*, **539**, 718  
 Contini T., et al., 2016, *A&A*, **591**, A49  
 Cresci G., Mannucci F., Maiolino R., Marconi A., Gnerucci A., Magrini L., 2010, *Nature*, **467**, 811  
 Danovich M., Dekel A., Hahn O., Ceverino D., Primack J., 2015, *MNRAS*, **449**, 2087  
 Dekel A., Birnboim Y., 2006, *MNRAS*, **368**, 2  
 Dekel A., et al., 2009, *Nature*, **457**, 451  
 Dopita M. A., Sutherland R. S., 2003, *Astrophysics of the diffuse universe*  
 Dopita M. A., Kewley L. J., Heisler C. A., Sutherland R. S., 2000, *ApJ*, **542**, 224  
 Dopita M. A., Sutherland R. S., Nicholls D. C., Kewley L. J., Vogt F. P. A., 2013, *ApJS*, **208**, 10

- Feroz F., Hobson M. P., 2008, *MNRAS*, 384, 449
- Feroz F., Hobson M. P., Bridges M., 2009, *MNRAS*, 398, 1601
- Feroz F., Hobson M. P., Cameron E., Pettitt A. N., 2013, preprint, ([arXiv:1306.2144](https://arxiv.org/abs/1306.2144))
- Few C. G., Gibson B. K., Courty S., Michel-Dansac L., Brook C. B., Stinson G. S., 2012, *A&A*, 547, A63
- Gibson B. K., Pilkington K., Brook C. B., Stinson G. S., Bailin J., 2013, *A&A*, 554, A47
- Guo Y., et al., 2013, *ApJS*, 207, 24
- Hao C.-N., Kennicutt R. C., Johnson B. D., Calzetti D., Dale D. A., Moustakas J., 2011, *ApJ*, 741, 124
- Ho I.-T., Kudritzki R.-P., Kewley L. J., Zahid H. J., Dopita M. A., Bresolin F., Rupke D. S. N., 2015, *MNRAS*, 448, 2030
- Jones T., Ellis R. S., Richard J., Jullo E., 2013, *ApJ*, 765, 48
- Jones T., et al., 2015, *AJ*, 149, 107
- Juneau S., et al., 2014, *ApJ*, 788, 88
- Kashino D., et al., 2017, *ApJ*, 835, 88
- Kauffmann G., et al., 2003, *MNRAS*, 346, 1055
- Kennicutt R. C., Evans N. J., 2012, *ARA&A*, 50, 531
- Kereš D., Katz N., Weinberg D. H., Davé R., 2005, *MNRAS*, 363, 2
- Kewley L. J., Ellison S. L., 2008, *ApJ*, 681, 1183
- Kewley L. J., Dopita M. A., Sutherland R. S., Heisler C. A., Trevena J., 2001, *ApJ*, 556, 121
- Knobel C., et al., 2012, *ApJ*, 753, 121
- Kriek M., van Dokkum P. G., Labbé I., Franx M., Illingworth G. D., Marchesini D., Quadri R. F., 2009, *ApJ*, 700, 221
- Larson R. B., 1976, *MNRAS*, 176, 31
- Leethochawalit N., Jones T. A., Ellis R. S., Stark D. P., Richard J., Zitrin A., Auger M., 2016, *ApJ*, 820, 84
- Luridiana V., Morisset C., Shaw R. A., 2015, *A&A*, 573, A42
- Marino R. A., et al., 2016, *A&A*, 585, A47
- Murphy E. J., et al., 2011, *ApJ*, 737, 67
- Onodera M., et al., 2016, *ApJ*, 822, 42
- Pilkington K., et al., 2012, *A&A*, 540, A56
- Portinari L., Chiosi C., 1999, *A&A*, 350, 827
- Prantzos N., Boissier S., 2000, *MNRAS*, 313, 338
- Queyrel J., et al., 2012, *A&A*, 539, A93
- Rafelski M., et al., 2015, *AJ*, 150, 31
- Rich J. A., Torrey P., Kewley L. J., Dopita M. A., Rupke D. S. N., 2012, *ApJ*, 753, 5
- Rosales-Ortega F. F., Díaz A. I., Kennicutt R. C., Sánchez S. F., 2011, *MNRAS*, 415, 2439
- Rupke D. S. N., Kewley L. J., Barnes J. E., 2010, *ApJ*, 710, L156
- Sánchez S. F., et al., 2014, *A&A*, 563, A49
- Sanders R. L., et al., 2016, *ApJ*, 816, 23
- Schönrich R., McMillan P. J., 2017, *MNRAS*,
- Shirazi M., Brinchmann J., Rahmati A., 2014, *ApJ*, 787, 120
- Soto K. T., Lilly S. J., Bacon R., Richard J., Conseil S., 2016, *MNRAS*, 458, 3210
- Steidel C. C., Strom A. L., Pettini M., Rudie G. C., Reddy N. A., Trainor R. F., 2016, *ApJ*, 826, 159
- Stewart K. R., Kaufmann T., Bullock J. S., Barton E. J., Maller A. H., Diemand J., Wadsley J., 2011, *ApJ*, 738, 39
- Stinson G. S., Bailin J., Couchman H., Wadsley J., Shen S., Nickerson S., Brook C., Quinn T., 2010, *MNRAS*, 408, 812

- Storey P. J., Hummer D. G., 1995, *MNRAS*, 272, 41
- Stott J. P., et al., 2014, *MNRAS*, 443, 2695
- Swinbank A. M., Sobral D., Smail I., Geach J. E., Best P. N., McCarthy I. G., Crain R. A., Theuns T., 2012, *MNRAS*, 426, 935
- Tacconi L. J., et al., 2013, *ApJ*, 768, 74
- Torrey P., Cox T. J., Kewley L., Hernquist L., 2012, *ApJ*, 746, 108
- Tremonti C. A., et al., 2004, *ApJ*, 613, 898
- Troncoso P., et al., 2014, *A&A*, 563, A58
- Vila-Costas M. B., Edmunds M. G., 1992, *MNRAS*, 259, 121
- Wang X., et al., 2017, *ApJ*, 837, 89
- Weilbacher P. M., Streicher O., Urrutia T., Jarno A., Pécontal-Rousset A., Bacon R., Böhm P., 2012, in *Software and Cyberinfrastructure for Astronomy II*. p. 84510B, doi:10.1117/12.925114
- Whitaker K. E., van Dokkum P. G., Brammer G., Franx M., 2012, *ApJ*, 754, L29
- Woods R. M., Wadsley J., Couchman H. M. P., Stinson G., Shen S., 2014, *MNRAS*, 442, 732
- Wuyts E., et al., 2016, *ApJ*, 827, 74
- York D. G., et al., 2000, *AJ*, 120, 1579
- Yuan T.-T., Kewley L. J., Swinbank A. M., Richard J., Livermore R. C., 2011, *ApJ*, 732, L14
- Yuan T.-T., Kewley L. J., Rich J., 2013, *ApJ*, 767, 106
- Zaritsky D., Kennicutt Jr. R. C., Huchra J. P., 1994, *ApJ*, 420, 87
- van de Voort F., Schaye J., Booth C. M., Dalla Vecchia C., 2011, *MNRAS*, 415, 2782
- van der Wel A., et al., 2012, *ApJS*, 203, 24
- van der Wel A., et al., 2014, *ApJ*, 788, 28

## Appendices

### A Additional figures

In Fig. 4.8 we provide an HST image atlas of our final galaxy sample. With each cutout image we indicate the inferred metallicity gradient.

In Figs. 4.9 & 4.10 we provide example plots for inspecting the quality of the model fit. Similar plots for all galaxies are available online (<https://doi.org/10.5281/zenodo.581221>).

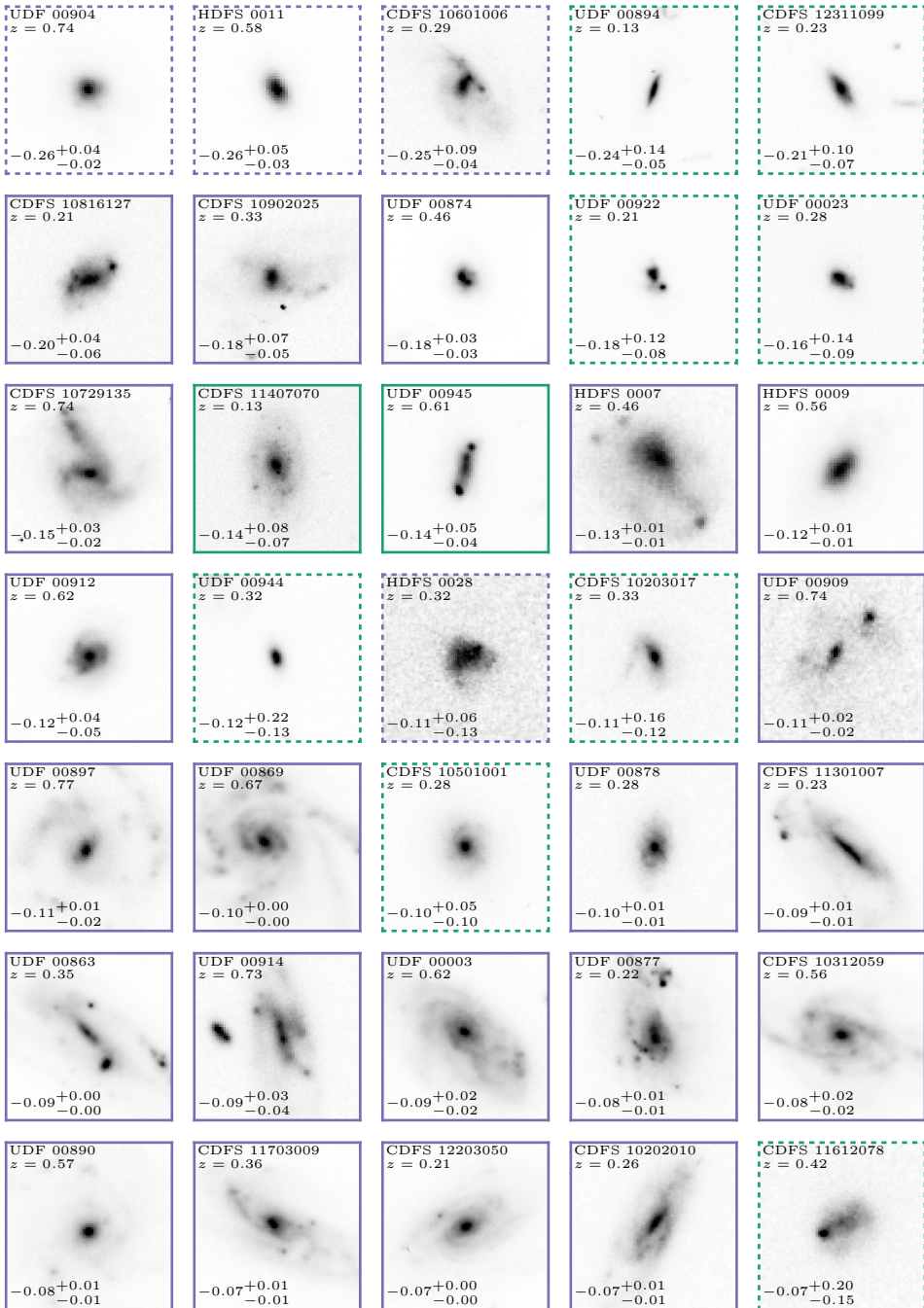


Figure 4.8: Image atlas showing cutouts of galaxies in our sample, shown in order of increasing metallicity gradient. Images are centred on the galaxy of interest, where North is up and East is left. The images are sized to be 16 kpc edge-to-edge. In the top-left corner of each panel we show the galaxy’s redshift. In the bottom-left corner we display the inferred metallicity gradient (units are dex/kpc). The border colour displays the metallicity gradient type: negative gradients (blue), positive gradients (orange), flat gradients (green). Galaxies flagged as unreliable have dashed borders.

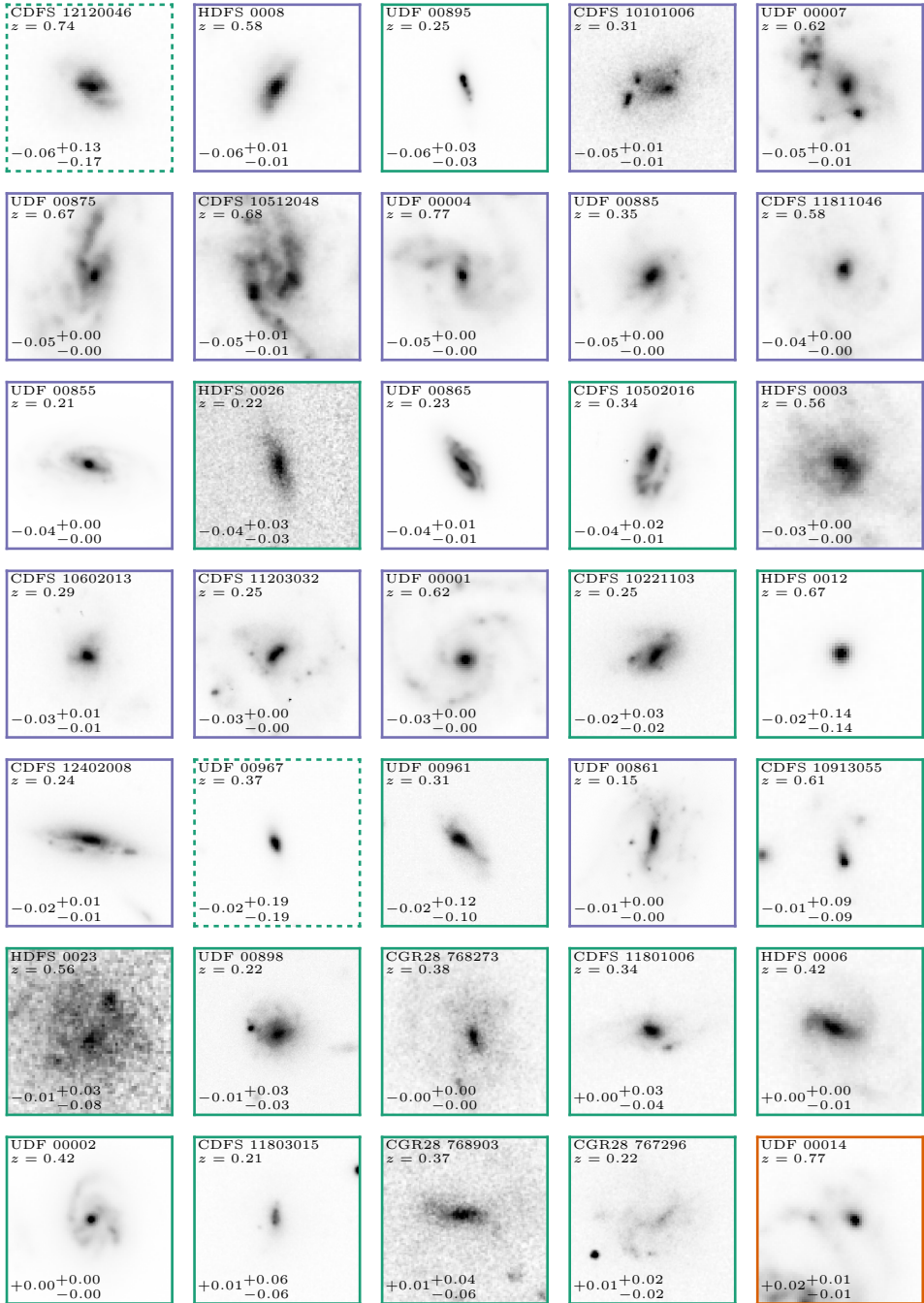


Figure 4.8 (cont.)

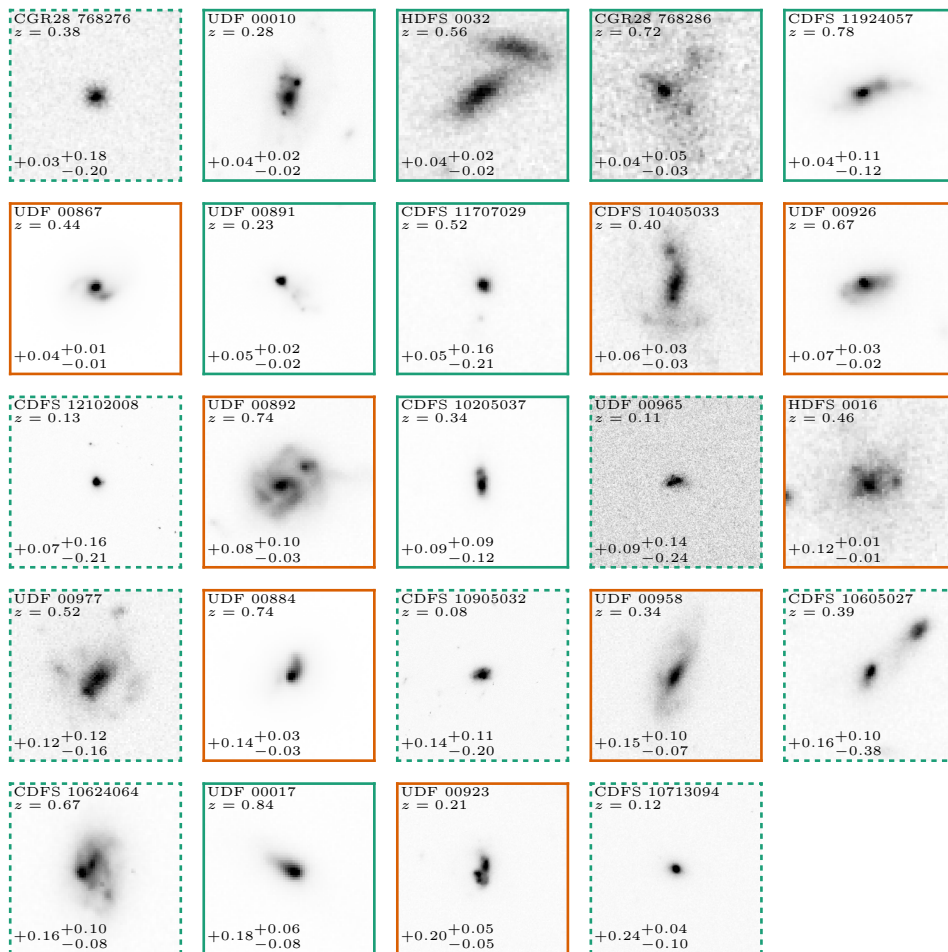


Figure 4.8 (cont.)

Figure 4.9: Visual quality assessment of model for galaxy HDFS-0003. This is an illustrative example and similar plots all galaxies can be found online. Top left: We show here the globally integrated MUSE spectrum. We also indicate the derived central metallicity,  $\log_{10} Z_0$  in dex, and derived metallicity gradient,  $\nabla_r(\log_{10} Z)$  in dex/kpc. Top right: We show the SFR map that was input into the modelling. A red cross indicate the galaxy centre. Left: We show the radial flux profiles for the modelled emission-lines. The name of the emission line is indicated in the top-right corner of each panel. An asterisk denotes lines that do not have observed fluxes in all spatial bins. Black data points indicate observed fluxes and their  $\pm 1\sigma$  errors. The red crosses show the median model solution. The size of the vertical bar indicates a  $\pm 2\sigma$  range in fluxes. Right: For each emission line we show three images. These are, respectively, the 2D binned images of the observed fluxes, model fluxes, and scaled residuals  $(\text{Observed} - \text{Model})/\text{Error}$  for each emission line. A black circle in the top-left corner represents the FWHM of the PSF. All images (including the SFR map) are shown on the same spatial scale. [For space, this plot has been truncated to show only  $\{[\text{O II}], \text{H}\delta, \text{H}\gamma, \text{H}\beta\}$ . The full plot showing all lines (including also  $\{[\text{O III}]4959, [\text{O III}]5007\}$ ) is available online.]

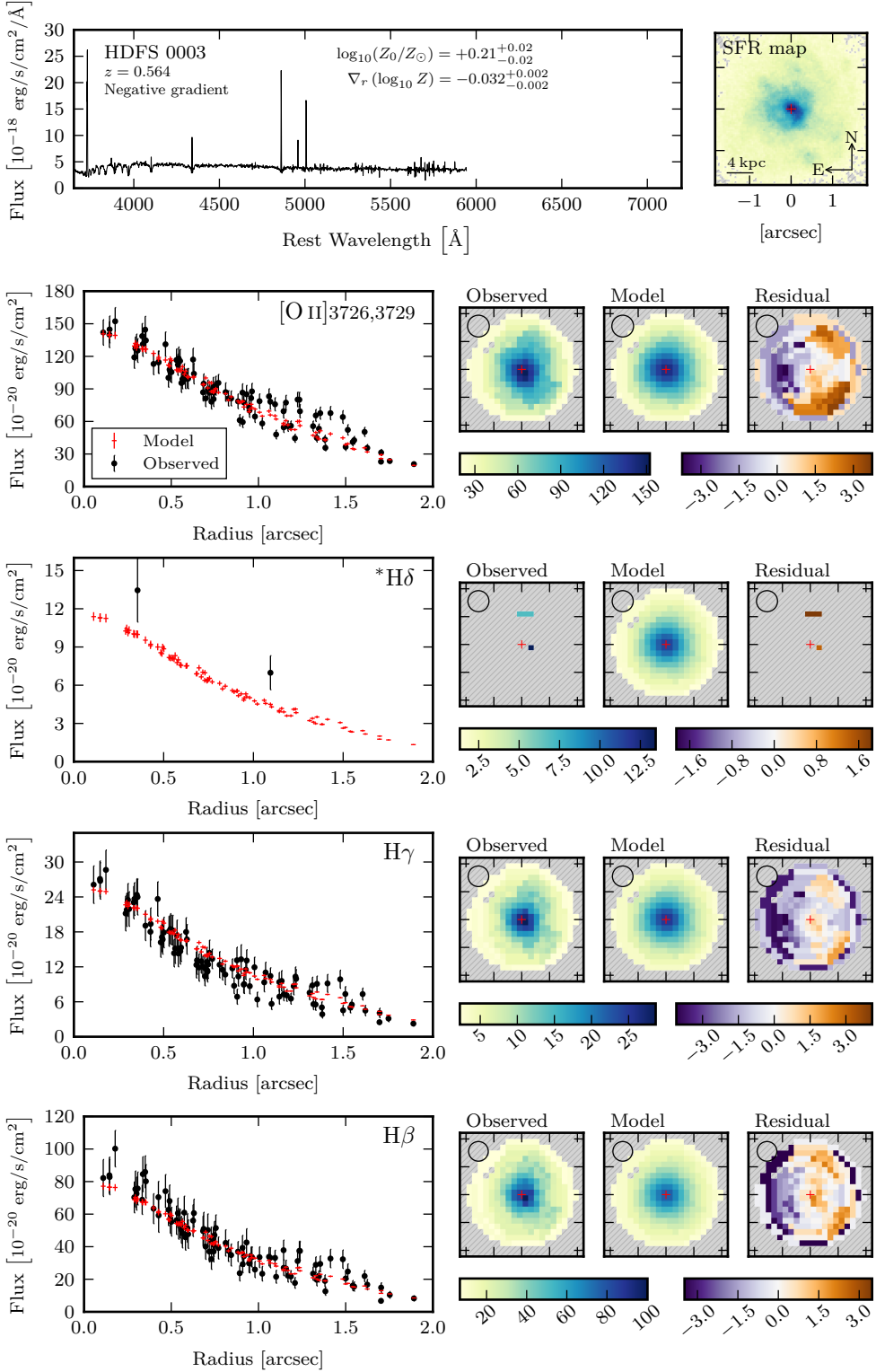


Figure 4.9 (caption is shown on preceding page)

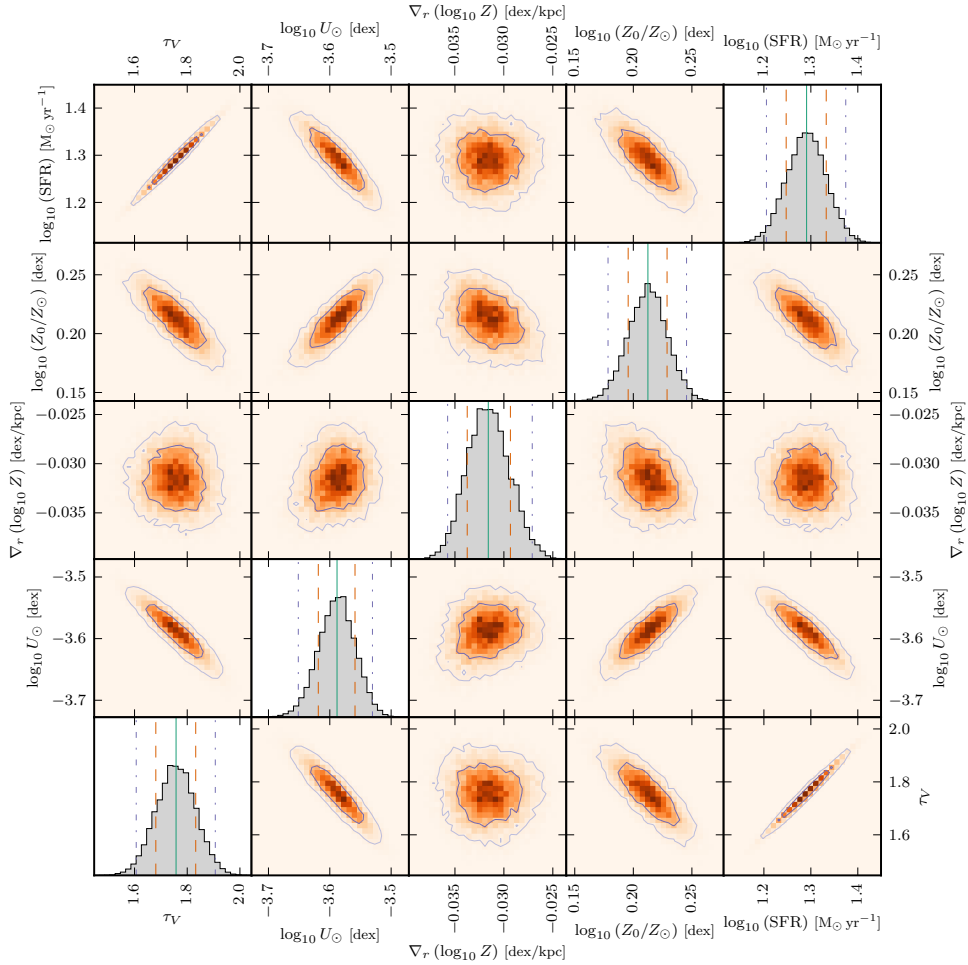


Figure 4.10: Plot showing derived model parameters for HDFS 0003. This is an illustrative example and similar plots all galaxies can be found online. We show both 1D and 2D marginalized histograms for all 5 parameters: the total star-formation rate,  $\log_{10}(\text{SFR})$ , central metallicity,  $\log_{10} Z_0$ , metallicity gradient,  $\nabla_r(\log_{10} Z)$ , ionization parameter at solar metallicity,  $\log_{10} U_{\odot}$ , and V-band optical depth,  $\tau_V$ . In each 1D histogram the vertical lines indicate the median (solid),  $\pm 1\sigma$  quantiles (dashed) and  $\pm 2\sigma$  quantiles (dash-dotted). In each 2D histogram we plot  $1\sigma$  and  $2\sigma$  contours. All axes span a  $[-4\sigma, 4\sigma]$  interval in their respective parameters.





# 5

---

## *A dependency between the mass-metallicity relation and the metallicity gradients of galaxies*

---

The relationship between a galaxy's stellar mass and its gas-phase metallicity results from the complex interplay between star formation and the inflow and outflow of gas. Since the gradient of metals in galaxies is also influenced by the same processes, it is therefore natural to contrast the metallicity gradient with the mass–metallicity relation. Here we study the interrelation of the stellar mass, central metallicity and metallicity gradient, using a sample of 72 galaxies spanning  $0.13 < z < 0.84$  with reliable metallicity gradient estimates. We find that typically the galaxies that fall below the mean mass–metallicity relation have flat or inverted metallicity gradients. We quantify their relationship taking full account of the covariance between the different variables and find that at fixed mass the central metallicity is anti-correlated with the metallicity gradient. We argue that this is consistent with a scenario that suppresses the central metallicity either through the inflow of metal poor gas or outflow of metal enriched gas.

David Carton, Jarle Brinchmann

## 1 Introduction

The existence of a correlation between the metallicity<sup>1</sup> and luminosity in galaxies has been known for a long time (Lequeux et al. 1979; Skillman et al. 1989), while more recently it has been argued that a more fundamental relation is between metallicity and galaxy mass (Garnett 2002; Tremonti et al. 2004; Foster et al. 2012). The existence of such a relationship is not particularly surprising from a theoretical point of view, with a variety of models predicting a correlation, e.g. leaky box models (Tremonti et al. 2004; Finlator & Davé 2008) and bathtub models (Bouché et al. 2010; Davé et al. 2012; Lilly et al. 2013).

Reducing the relationship between stellar mass and metallicity to a one-dimensional one is, however, over-simplified; there is significant scatter in the relationship and this scatter contains important physical information. As a result there have been a number of studies over the last decade trying to understand what physical properties cause the scatter. These include specific star-formation rates and sizes (e.g. Ellison et al. 2008), the star-formation rate (e.g. Lara-López et al. 2010; Mannucci et al. 2010) and gas content (e.g. Bothwell et al. 2013) to mention a few. There has been particular interest in identifying whether these relations are universal (redshift independent) and which of them is the most fundamental.

Chemical evolution models can be helpful for interpreting physics underlying these relations. For instance, the bathtub models typically assume the star-formation rate (SFR) in a galaxy is set by either the total amount of gas in the system, or the net rate at which gas is accreted to the system. In these models it is therefore the balance of inflows and outflows that governs the mass–metallicity relations.

But, to really grasp the nature of these inflow and outflow processes it is desirable to have spatially resolved the metallicity in galaxies. In other words, do the galaxies that fall below the bulk of galaxies on the mass–metallicity relation have spuriously low metallicities throughout their discs, or is the low metallicity gas concentrated in the central regions?

In this work we will study the mass – central metallicity relation for a modest sample of intermediate redshift galaxies ( $0.1 \lesssim z \lesssim 0.8$ ). We will also explore whether there is an additional dependency between central metallicity and the metallicity gradient of these galaxies.

In Section 2 we outline the data used. In Section 3 we explore dependencies of central metallicity on both mass and metallicity gradient. Finally we comment on and summarize our findings in Sections 4 & 5, respectively.

Throughout the paper we assume a  $\Lambda$ CDM cosmology with  $H_0 = 70 \text{ km s}^{-1} \text{ Mpc}^{-1}$ ,  $\Omega_m = 0.3$  and  $\Omega_\Lambda = 0.7$ .

## 2 Data

The galaxy sample and data that we use here were presented in Carton et al. (in prep.; herein Chapter 4). Therein we measured the metallicity profile for 94 galaxies observed with the Multi Unit Spectroscopic Explorer (MUSE; Bacon et al. (2010, and in prep.)). In this previous work we focused exclusively on the metallicity gradients in these galaxies, however, here we will also discuss the central metallicities of these galaxies.

In this paper we will only consider the 72 galaxies that were found to have reliable metallicity gradients in Chapter 4. These galaxies span a range of redshifts between  $0.13 < z < 0.84$ . We derive central metallicities,  $\log_{10} Z_0$ , and metallicity gradients,  $\nabla_r(\log_{10} Z)$ , using nebular emission-lines observed with MUSE. By applying a forward-modelling technique

---

<sup>1</sup>Throughout this work, unless otherwise noted, the gas-phase abundance of oxygen ( $12 + \log_{10}(\text{O}/\text{H})$ ) will simply be referred to as metallicity.

presented in Carton et al. (2017) we are able to correct for the resolution loss caused by atmospheric seeing. The stellar masses,  $\log_{10} M_*$ , of the galaxies are estimated from multi-band photometry, using FAST (Kriek et al. 2009).

In the model the metallicity is taken to be a linear function of the distance from the centre of the galaxy. The metallicity gradient is the slope of this function and the central metallicity the intercept at  $r = 0$ . As a result we expect these quantities to be anti-correlated, e.g. galaxies with steep negative metallicity gradients will have higher central metallicities. The degree to which  $\log_{10} Z_0$  and  $\nabla_r(\log_{10} Z)$  are correlated depends on both the spatial resolution and the signal-to-noise (S/N) of the data, and thus varies from galaxy to galaxy.

There is another reason why these two parameters are correlated. For galaxies above  $z \gtrsim 0.4$ , our metallicities are primarily constrained by the line ratios of [O II]<sub>3726,3729</sub>, H $\beta$  and [O III]<sub>5007</sub>. It is well known that metallicities defined from only these lines suffer from degeneracy between the metallicity and ionization-parameter (see Kewley & Dopita 2002). In our modelling we make the empirically motivated assumption that the ionization-parameter and metallicity are anti-correlated within a galaxy. Doing so mitigates against this degeneracy, but induces additional covariance between the central metallicity and the metallicity gradient of the galaxy.

Nevertheless, because our forward-modelling technique provides a joint posterior probability distribution of  $\log_{10} Z_0$  and  $\nabla_r(\log_{10} Z)$ , we are able to quantify the effects of both this and the slope/intercept degeneracy. For simplicity (and numerical stability/convergence) we approximate the joint posterior as a 2D normal distribution. Similarly for the stellar masses we also assume a 1D normal distribution, symmetrizing the  $\pm 1\sigma$  error quantiles about the median.

### 3 Results

In Fig. 5.1 we show mass-central metallicity relation ( $M_*-Z_0$ ) for our galaxies. Unsurprisingly, we recover the same positive trend that others find at lower redshift (e.g. Tremonti et al. 2004; Foster et al. 2012). However, we also observe a another dependence between the central metallicity and the metallicity gradient. It is clearly visible that at fixed mass galaxies with more positive metallicity gradients have lower central metallicities.

Our  $M_*-Z_0$  relation appears to show more scatter than the low redshift  $M_*-Z_0$  relationships in the literature. However, it is important to realise that our results are not necessarily directly comparable with these. The  $M_*-Z_0$  in the literature typically use metallicities integrated over some spatial region. For instance, the widely used SDSS results from Tremonti et al. (2004) are based on spectra of a region that contains on average 30% of the total light of the galaxy. Like other studies, Tremonti et al. (2004) make no attempt to infer the metallicity at the exact ( $r = 0$ ) centre of a galaxy. That said, if galaxies are exponential disks and have a common metallicity gradient when expressed in scale-lengths (e.g. Sánchez et al. 2014), the central and light-weighted integrated metallicity are related by a constant factor.

Nevertheless if we take our results at face value, the scatter in the  $M_*-Z_0$  relation is explained by the metallicity gradient. Given that low-redshift galaxies have a common metallicity gradient, one might naturally expect to see less scatter in the low-redshift  $M_*-Z_0$  relation.

It is interesting to note that we do not observe significant trends between the central metallicity and SFR (at fixed mass). We therefore do not recover a  $M_*-Z_0$ -SFR relation that we might have expected (Lara-López et al. 2010; Mannucci et al. 2010). We will discuss the potential implications of this in Section 4.1.

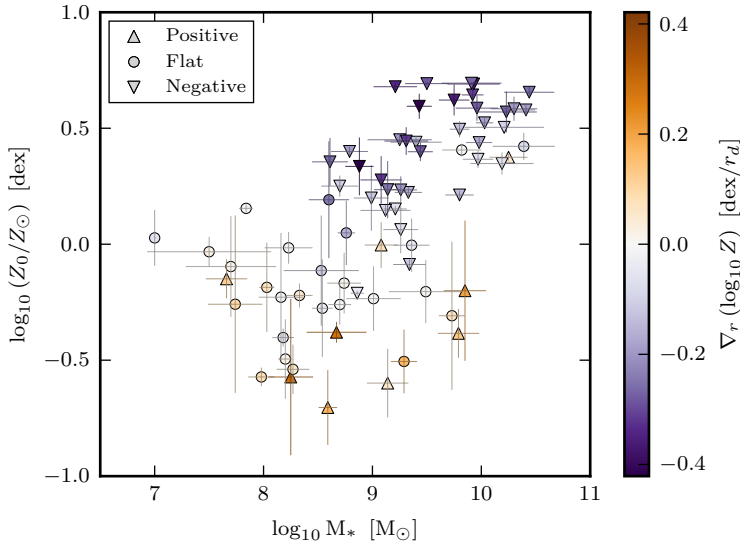


Figure 5.1: Datapoints indicate the central metallicities and metallicity gradients of our galaxy sample. The  $\pm 1\sigma$  errors are drawn for each galaxy. Colours indicate the galaxy’s metallicity gradient. Galaxies that have  $2\sigma$  significant positive/negative gradients are labelled as up/down pointing triangles. Galaxies which have metallicity gradients that are consistent with zero (i.e. flat) are drawn as circles. Here and throughout this work solar metallicity,  $Z_{\odot}$ , equates to an oxygen abundance of  $12 + \log_{10}(\text{O}/\text{H}) = 8.69$  (Grevesse et al. 2010).

### 3.1 Analysing a $M_{*}-Z_0-\nabla_r(\log_{10} Z)$ relation

We wish to fit an analytical function that describes the central metallicity of a galaxy as function of its stellar mass and its metallicity gradient. In addition, although we do not observe a strong redshift dependence, we will also permit some additional dependence of the central metallicity on redshift.

As noted in the Section 2, the uncertainties in the central metallicity and the metallicity gradient are correlated. Our model fit must account for this covariance, as well as the uncertainty the stellar mass. To achieve this we will use a hierarchical Bayesian approach that we shall now outline. We present a graphical representation of the hierarchical model in Fig. 5.2.

From visual inspection of Fig. 5.1 it appears appropriate to adopt a function with a constant  $M_{*}-Z_0$  slope that can be shifted vertically for different metallicity gradients. Therefore we will fit the following function for the central metallicity of the  $i^{\text{th}}$  galaxy

$$\log_{10} Z_{0,i} = \alpha + \beta (\log_{10} M_{*,i} - 9) + \gamma \nabla_r(\log_{10} Z)_i + \frac{\delta}{1 + z_i}, \quad (5.1)$$

where  $\alpha, \beta, \gamma$  and  $\delta$  are the regression coefficients that we are interested in. For each galaxy:  $\log_{10} M_{*,i}$  is the stellar mass,  $\nabla_r(\log_{10} Z)_i$  is the metallicity gradient, and  $z_i$  is the measured redshift. The variables  $\log_{10} M_{*,i}$  and  $\nabla_r(\log_{10} Z)_i$  are not observed directly, in the modelling terminology these are *latent* variables and we will use this term in the following. While we do not know the true stellar mass and true metallicity gradient, we do of course have constraints on their values. The latent variables and regression coefficients are sampled from uniform priors as shown in Fig. 5.2.

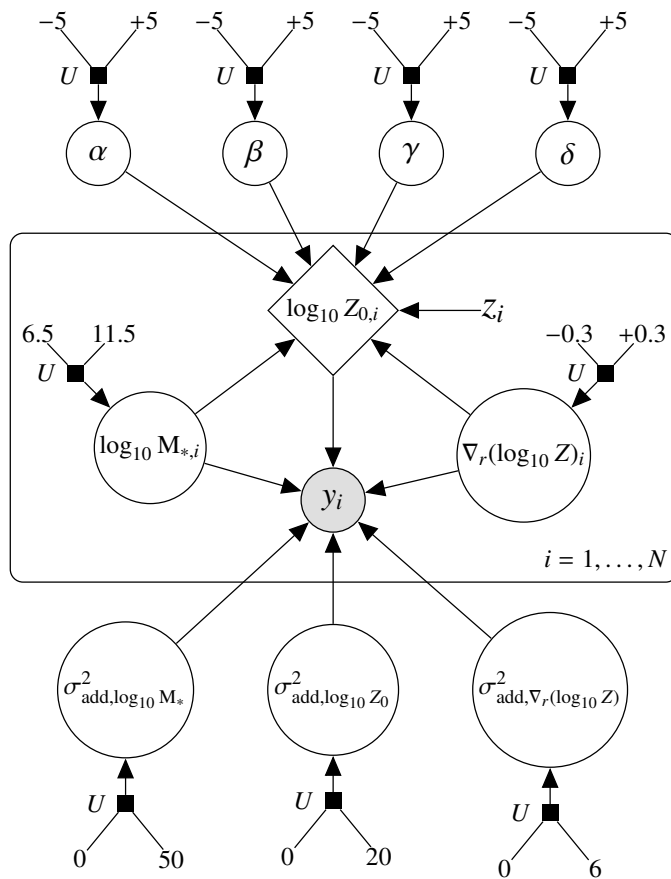


Figure 5.2: A directed factor graph representation of our hierarchical model. See text for a detailed model description. Unshaded circles represent latent (hidden) variables. The shaded circle represents the likelihood function. Diamonds indicate deterministic variables. Variables and numbers not enclosed in any shape are constants. Small black squares represent stochastic distributions. Here these distributions are all uniform,  $U$ , where their minima and maxima are indicated by their inputs.

We adopt a multinormal distribution for likelihood function of the observed mass, central metallicity and metallicity gradient

$$P\left(y_i | \log_{10} M_{*,i}, \log_{10} Z_{0,i}, \nabla_r(\log_{10} Z)_i\right) = \mathcal{N}(\mu_i, \Sigma_i), \quad (5.2)$$

where  $\mu_i$  is the mean vector

$$\mu_i = \left[ \log_{10} M_{*,i} \quad \log_{10} Z_{0,i} \quad \nabla_r(\log_{10} Z)_i \right], \quad (5.3)$$

and  $\Sigma_i$  the covariance matrix

$$\Sigma_i = \begin{bmatrix} \sigma_{i,M_*}^2 + \sigma_{\text{add},M_*}^2 & 0 & 0 \\ 0 & \sigma_{i,Z_0}^2 + \sigma_{\text{add},Z_0}^2 & \text{cov}_i(Z_0, \nabla_r Z) \\ 0 & \text{cov}_i(Z_0, \nabla_r Z) & \sigma_{i,\nabla_r Z}^2 + \sigma_{\text{add},\nabla_r Z}^2 \end{bmatrix}. \quad (5.4)$$

N.B. For clarity in the above matrix we have omitted the  $\log_{10}$  factors from the notation. The variances,  $\sigma_i^2$ , and the covariances,  $\text{cov}_i$ , are given by our fitting procedure for each galaxy. Acknowledging that our model might not capture all details of the galaxies and hence that these (co-)variances might be underestimated, we allow for an additional source of uncertainty. These  $\sigma_{\text{add}}^2$  parameters are treated as latent variables in the model and are sampled from uniformly distributed priors over the ranges indicated in Fig. 5.2. We are not interested in these parameters and marginalise over them.

### 3.1.1 Fitting results

The inferred mean values of  $\alpha$ ,  $\beta$ ,  $\gamma$  and  $\delta$  are

$$\alpha = -0.362, \quad \beta = 0.199, \quad \gamma = -1.57, \quad \delta = 0.455,$$

with covariances

$$\Sigma_{\alpha\beta\gamma\delta} = \begin{bmatrix} 0.0335 & -0.0020 & 0.0009 & -0.0461 \\ -0.0020 & 0.0012 & 0.0022 & 0.0027 \\ 0.0009 & 0.0022 & 0.0265 & 0.0016 \\ -0.0461 & 0.0027 & 0.0016 & 0.0651 \end{bmatrix}.$$

We compare the best fit model to the data in Figs. 5.3 & 5.4, which show two different projections of the parameter space. From both figures it can be seen that the model provides a reasonable description of the data. On the vertical axes we plot the central metallicity of a galaxy, extrapolated to  $z = 0$ . We do this to reduce the dimensionality of the data, making the plotting easier. Note that because the redshift dependence is relatively weak, and so, even though we span a modest range in redshift, the central metallicities of the galaxies are only revised by a small amount between +0.05 and +0.21 dex, depending on the galaxy's redshift.

Earlier (Section 2) we mentioned that we expect the errors of the metallicity gradient and central metallicity to be anti-correlated. Indeed we can observe the correlated errors in Fig. 5.3. However, it is worth noting that errorbars are typically much smaller than the spread of the data. Therefore there is a clearly real anti-correlation between metallicity gradient and central metallicity, i.e. beyond one that could have simply arisen from a degeneracy between the parameters.

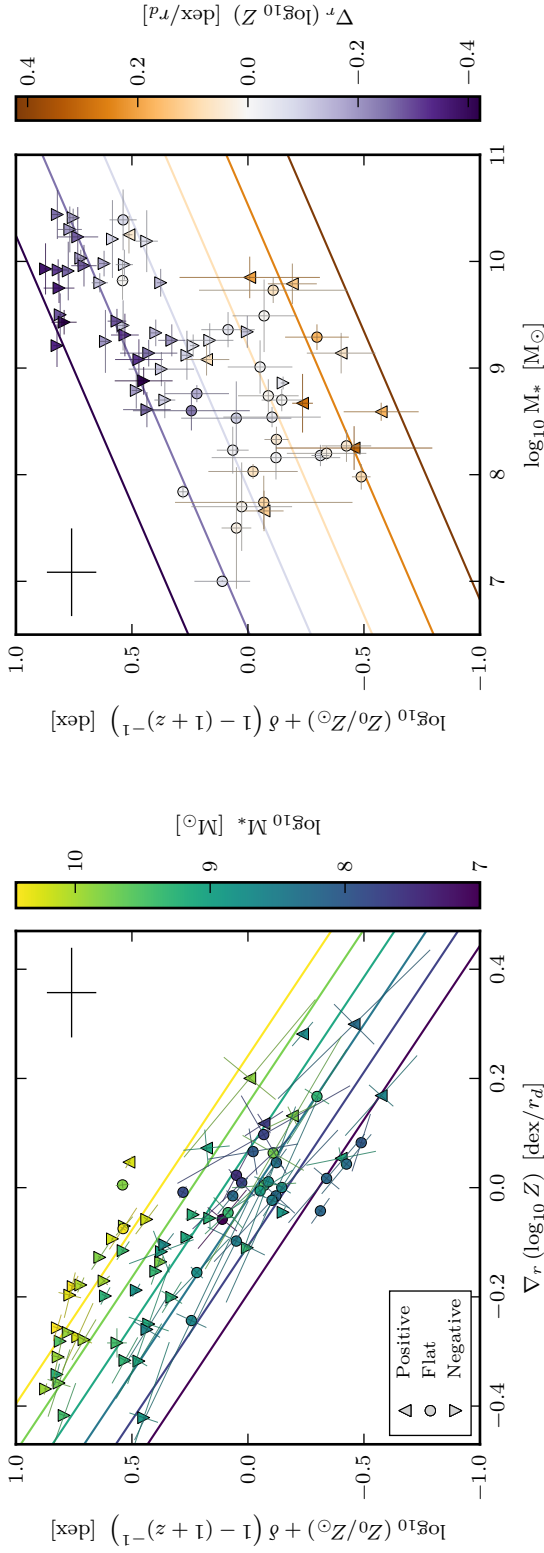


Figure 5.3: Comparison of model to data, showing metallicity gradient vs central metallicity (extrapolated to  $z = 0$ ). The redshift dependence is taken out by the  $\delta(1 + (1 + z)^{-1})$  term, where  $\delta = 0.455$  is best fit model value. The  $\pm 1\sigma$  errors are drawn for each galaxy datapoint. Colours indicate the galaxy’s total stellar mass. Symbol shape indicates the type of metallicity gradient: positive, flat, negative. Thick coloured lines indicate the best fit model to the data, as tracks of constant mass. The modelled additional uncertainty is plotted as a black error cross in the top-right corner of the panel.

Figure 5.4: Comparison of model to data, showing stellar mass vs central metallicity (extrapolated to  $z = 0$ ), coloured to indicate the galaxy’s metallicity gradient. Thick lines indicate the best fit model to the data, as tracks of constant metallicity gradient. For a full description of the plot, see caption of Fig. 5.3.

## 4 Discussion

In the previous section we identified that while our galaxy sample does not present a strong  $M_*-Z_0$  relation, this can be explained by the strong dependency between the central metallicity and the metallicity gradient.

It is not surprising that at fixed stellar mass we observe an anti-correlation between  $\log_{10} Z_0$  and  $\nabla_r(\log_{10} Z)$ . Consider the following reasoning. Our current understanding is that galaxies grow in a self-similar inside-out fashion. And as shown by [Portinari & Chiosi \(1999\)](#) and [Prantzos & Boissier \(2000\)](#) this inside-out growth produces galaxies with negative metallicity gradients. If deviations from this (i.e. flat and positive metallicity gradients) are then caused by suppressing the central metallicity, as opposed to raising the outer metallicity, then we would expect to observe an anti-correlation between  $\log_{10} Z_0$  and  $\nabla_r(\log_{10} Z)$ . Indeed the two common explanations of metallicity gradient inversion revolve around lowering the metallicity at the galaxy centre.

The first explanation is that the central metallicity is spuriously low because a significant amount of metal-poor gas has been deposited into the centre of the galaxy. This metal-poor gas could be acquired in a variety of ways. One mechanism invokes cold flows of metal-poor gas which originate from beyond the halo and are able to accrete directly onto the galaxy centre ([Cresci et al. 2010](#)). However, at late times ( $z < 1.8$ ) this mechanism is less favourable because cold-flows are expected to be less common ([Woods et al. 2014](#)). So, metal-poor gas in the outskirts of a galaxy's disc could provide an alternative source. Tidal encounters with other galaxies may trigger the infall of this gas through the disc ([Rupke et al. 2010](#); [Torrey et al. 2012](#)). That said, while galaxy-galaxy interactions can produce galaxies with flat metallicity gradients, it remains unclear whether such interactions can truly invert metallicity gradients.

A second explanation for the metal-poor galaxy centres invokes strong centrally-concentrated winds. These winds entrain metals in the outflows, stripping metals from the gas and thereby lowering the metallicity at the centre of the galaxy. While a wind that simply blows the metal enriched gas away from the galaxy might be inefficient ([Cresci et al. 2010](#)), the accretion of this metal enriched gas onto the outskirts of the galaxies would in fact make this process rather more efficient at inverting/flattening metallicity gradients ([Troncoso et al. 2014](#)). Note that there might be some delay between the time when the central starburst occurs in a galaxy and the time when we observe it with a raised outer metallicity.

In theory, by studying both the central metallicity and the metallicity gradients of galaxies, we may be able to distinguish the inflow and outflow mechanisms. Of course, in reality the two scenarios need not be mutually exclusive, the extra gas brought by inflows may trigger intense star-formation activity that subsequently launches the centrally-concentrated outflows.

In either case (inflows or outflows), we should expect to observe elevated SFRs in galaxies with spuriously low central metallicities. However, it was a key result of our previous work that we do not see a significant correlation between the SFR and the metallicity gradient of a galaxy (Chapter 4). Similarly and although not shown here, we do not observe a significant dependence of the  $M_*-Z_0$  relation with the total SFR. We shall discuss this further in the following section.

### 4.1 Implications for a $M_*-Z$ -SFR relation

Numerous studies have demonstrated that at fixed stellar mass there is an anti-correlation between SFR and metallicity (e.g. [Andrews & Martini 2013](#); [Salim et al. 2014](#)). Moreover some have even suggested that there exists a fundamental  $M_*-Z$ -SFR plane on which all galaxies lie, independent of redshift ([Lara-López et al. 2010](#); [Mannucci et al. 2010](#)). Although,

because many of these studies disagree on the strength of the dependency, the universality of such a relation remains difficult to verify.

To add to this confusion, our results suggest that there is no SFR dependency at  $0.1 \lesssim z \lesssim 0.8$ . However, as we shall now explain, our result may not actually be in strong contradiction with these results.

At low redshift much of the  $M_*$ - $Z$ -SFR work has been performed with multi-object fibre spectroscopy. Thus many studies observe metallicity and SFR within a small aperture at the centre of the galaxy. In contrast, we have measured the metallicity at the centre of our galaxies, but use the total SFR of the galaxy.

Had we been able to resolve a central SFR, we might have found a dependency of  $\log_{10} Z_0$  on SFR, at fixed stellar mass. Similarly, although not identically, we might have found a dependency of the globally averaged metallicity on the total SFR. Although seemingly subtle, the distinction between these two points should depend on whether the chemical evolution of galaxies is regulated on local scales within galaxies, or whether it is only regulated at the global scales.

Therefore we suggest that, while we see that the central metallicity depends on metallicity gradient, it is not so surprising that we do not see a similar correlation with the SFR. Additional, indirect support for this comes from recent work of [Bothwell et al. \(2016\)](#) who consider dependency with a fourth quantity, the molecular gas mass,  $M_{\text{H}_2}$ . With this they identify a  $M_*$ - $Z_0$ - $M_{\text{H}_2}$  relation that they claim to be more fundamental than a  $M_*$ - $Z_0$ -SFR relation. In other words, there is a more direct dependency between metallicity and molecular gas mass, than between metallicity and SFR. Combined with the above described aperture effects, this might explain our sensitivity to metallicity gradient, but not SFR.

## 5 Summary

We present the stellar masses, central metallicities and metallicity gradients for a sample of 72 galaxies between  $0.13 < z < 0.84$ . Our methodology accounts for the correlated uncertainties between the central metallicity and the metallicity gradient.

- Our key result is that, at fixed stellar mass, we find an anti-correlation between the metallicity gradient and central metallicity. This naturally would be expected if a process had recently lowered the central metallicity in the galaxies that fall below the  $M$ - $Z$  relation.
- Given the oft-reported relation between mass, metallicity and SFR relation, we might therefore expect to see a correlation between the SFR and the metallicity gradient. However, we do not find such a correlation. We reconcile this by suggesting that because we compare the *global* SFR to a *local* metallicity measurement, we may be largely insensitive to such trends. Therefore our results do not refute the existence of a mass – metallicity – SFR relation.

We must add caution that our results are based on a relatively small sample, and since we have a sample spanning a large range of masses and SFRs (with no simple selection criteria), the strength of our conclusions are limited.

Nevertheless, our results clearly motivate further studies with current integral field spectrographs, where one can study the spatially resolved masses, SFRs and metallicities of galaxies.

## Acknowledgements

JB acknowledges support from FCT grant IF/01654/2014/CP1215/CT0003.

Additionally we wish to acknowledge both the PYTHON programming language that was both used extensively throughout this work.

## Bibliography

- Andrews B. H., Martini P., 2013, *ApJ*, 765, 140
- Bacon R., et al., 2010, in *Ground-based and Airborne Instrumentation for Astronomy III*. p. 773508, doi:10.1117/12.856027
- Bothwell M. S., Maiolino R., Kennicutt R., Cresci G., Mannucci F., Marconi A., Cicone C., 2013, *MNRAS*, 433, 1425
- Bothwell M. S., Maiolino R., Cicone C., Peng Y., Wagg J., 2016, *A&A*, 595, A48
- Bouché N., et al., 2010, *ApJ*, 718, 1001
- Carton D., et al., 2017, *MNRAS*, 468, 2140
- Cresci G., Mannucci F., Maiolino R., Marconi A., Gnerucci A., Magrini L., 2010, *Nature*, 467, 811
- Davé R., Finlator K., Oppenheimer B. D., 2012, *MNRAS*, 421, 98
- Ellison S. L., Patton D. R., Simard L., McConnachie A. W., 2008, *ApJ*, 672, L107
- Finlator K., Davé R., 2008, *MNRAS*, 385, 2181
- Foster C., et al., 2012, *A&A*, 547, A79
- Garnett D. R., 2002, *ApJ*, 581, 1019
- Grevesse N., Asplund M., Sauval A. J., Scott P., 2010, *Ap&SS*, 328, 179
- Kewley L. J., Dopita M. A., 2002, *ApJS*, 142, 35
- Kriek M., van Dokkum P. G., Labbé I., Franx M., Illingworth G. D., Marchesini D., Quadri R. F., 2009, *ApJ*, 700, 221
- Lara-López M. A., et al., 2010, *A&A*, 521, L53
- Lequeux J., Peimbert M., Rayo J. F., Serrano A., Torres-Peimbert S., 1979, *A&A*, 80, 155
- Lilly S. J., Carollo C. M., Pipino A., Renzini A., Peng Y., 2013, *ApJ*, 772, 119
- Mannucci F., Cresci G., Maiolino R., Marconi A., Gnerucci A., 2010, *MNRAS*, 408, 2115
- Portinari L., Chiosi C., 1999, *A&A*, 350, 827
- Prantzos N., Boissier S., 2000, *MNRAS*, 313, 338
- Rupke D. S. N., Kewley L. J., Barnes J. E., 2010, *ApJ*, 710, L156
- Salim S., Lee J. C., Ly C., Brinchmann J., Davé R., Dickinson M., Salzer J. J., Charlot S., 2014, *ApJ*, 797, 126
- Sánchez S. F., et al., 2014, *A&A*, 563, A49
- Skillman E. D., Kennicutt R. C., Hodge P. W., 1989, *ApJ*, 347, 875
- Torrey P., Cox T. J., Kewley L., Hernquist L., 2012, *ApJ*, 746, 108
- Tremonti C. A., et al., 2004, *ApJ*, 613, 898
- Troncoso P., et al., 2014, *A&A*, 563, A58
- Woods R. M., Wadsley J., Couchman H. M. P., Stinson G., Shen S., 2014, *MNRAS*, 442, 732





## 1 Wat zijn metalen?

Kort na de Oerknal was het Universum heet en dicht genoeg om protonen en neutronen samen te brengen tot atoomkernen. Echter, omdat het Universum snel uitdijde en afkoelde was er alleen voldoende tijd voor het vormen van de lichtste elementen, en daardoor bestond het vroege Heelal bijna alleen maar uit waterstof en helium.

Onder invloed van zwaartekracht verenigde dit gas zich na een tijdje in gebieden met een hoge dichtheid waar later sterren zouden vormen. In de kern van de sterren waren the temperatuur en dichtheid weer hoog genoeg om waterstof en helium te fusering in zwaardere elementen. Deze “zware” elementen worden door astronomen *metalen* genoemd.

## 2 Waarom zijn metalen interessant?

Omdat metalen gevormd moeten zijn in sterren, geeft het bestuderen van de hoeveelheid metalen in sterrenstelsels informatie over de vroegere sterformatie in stelsels. Als we meer metalen waarnemen, moet er immers meer sterformatie hebben plaatsgevonden in het verleden.

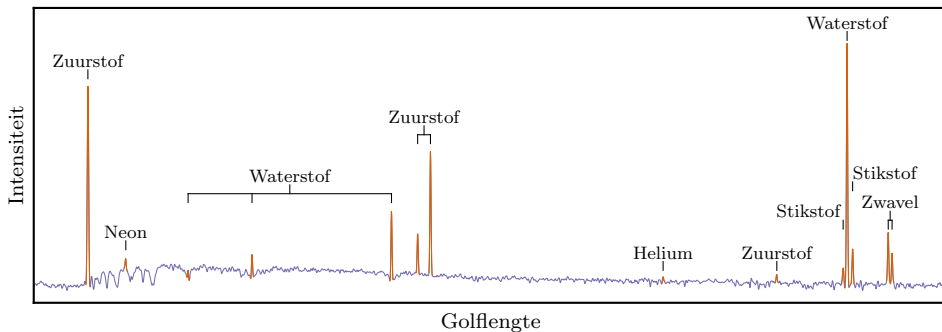
Als we echter de metalliciteit van sterrenstelsels berekenen (dit is the verhouding tussen metalen en waterstof in stelsels), vinden we over het algemeen minder metalen dan we zouden verwachten aan de hand van het aantal sterren dat we waarnemen. Dit verschil kan worden uitgelegd als stelsels tijdens hun leven gas van een hoge metalliciteit kunnen afstoten en/of metaalarm gas kunnen aantrekken.

Sterrenstelsels zijn niet geïsoleerd van hun omgeving. Het begrijpen van de stroom van gassen in of uit stelsels is fundamenteel om the evolutie van sterrenstelsel uit te leggen. Metalliciteit biedt een krachtig hulpmiddel voor het bestuderen van de brandstofvoorziening van sterrenstelsels.

## 3 Hoe meet men metalliciteit?

Er zijn twee soorten meetbare metalliciteit: de fractie van metalen in sterren zelf (de stermetalliciteit) en de fractie van metalen in het gas tussen sterren (the gasmetalliciteit). Hoewel de eerste soort een directere hoeveelheid is, is het moeilijker om te meten omdat hiervoor gedetailleerde waarnemingen van het licht van sterren nodig zijn. Het hete geïoniseerde gas waarmee jonge zware sterren worden omringd straalt juist licht uit op erg specifieke golflengten (de kleuren van het licht). Deze *emissielijnen* worden prominent weergegeven in de spectra van sterrenstelsels die actief nieuwe sterren vormen (zie Fig. 6.1).

De relatieve sterkte van de emissielijnen hangt af van de complexe balans tussen het ultraviolette licht dat wordt uitgezonden door jonge sterren (welke het gas opwarmen) en



Figuur 6.1: Een voorbeeldspectrum van een sterrenstelsels waarin nieuwe sterren worden gevormd. De heldere emissielijnen (gemarkeerd in oranje) zijn duidelijk zichtbaar in vergelijking tot het zwakkere sterlicht (weergegeven in blauw). We zien welk element verantwoordelijk is voor iedere emissielijn.

de snelheid waarmee het gas kan afkoelen. Omdat beide factoren gevoelig zijn voor de metalliciteit<sup>1</sup> kunnen we de metalliciteit van het gas bepalen aan de hand van de verhoudingen tussen de sterktes van bepaalde emissielijnen.

Om dit waar te nemen moet het licht gesplitst worden in zijn samengestelde golflengtes. Normaliter wordt dit gedaan door het licht van een klein gebied van de horizon, waargenomen met een telescoop (een *slit*), te verstrooien door middel van (bijvoorbeeld) een prisma. Het resultaat is een twee-dimensionale afbeelding met de ruimtelijke afstand langs de slit in één richting van de afbeelding, en het spectrum op iedere ruimtelijke positie hier loodrecht op.

### 3.1 De *Multi Unit Spectroscopic Explorer* (MUSE)

Een fundamentele beperking van deze traditionele op een slit gebaseerde spectrografen is dat we alleen een klein gedeelte van de hemel waar kunnen nemen. Dit is niet alleen verspilling van het kostbare licht dat de telescoop binnenvalt, maar het voorziet ons ook slechts van een klein venster op het Heelal.

Gelukkig hebben zich in de afgelopen decennia ontwikkelingen voorgedaan van zogenoemde *integral-field* spectrografen die, door een verscheidenheid aan technieken het mogelijk hebben gemaakt om spectra te verkrijgen over een twee-dimensionaal gebied aan de hemel. De meest vooruitstrevende van deze instrumenten is de *Multi Unit Spectroscopic Explorer* (MUSE), die sterk is geoptimaliseerd met het oog op het maken van lange observaties. Tot nu toe werden diepe spectroscopische waarnemen van ver gelegen sterrenstelsels uitgevoerd op geselecteerde sterrenstelsels. Echter, met de komst van MUSE is er nu de mogelijkheid om een niet-voorgeselecteerde spectroscopisch venster waar te nemen.

## 4 Deze thesis

In deze thesis focussen we niet alleen op het verkrijgen van de metalliciteit van sterrenstelsels, maar ook op hoe de metalliciteit verandert met de afstand tot het centrum van stelsels. Omdat er niet maar één waarde voor de metalliciteit is die het hele sterrenstelsel kan beschrijven, kunnen we een dieper inzicht verkrijgen als we deze variaties ruimtelijk in kaart brengen.

<sup>1</sup>Strikt gesproken hangt de eerste af van de stermetalliciteit en de tweede van de gasmetalliciteit

**Hoofdstuk 2** We bestuderen 50 relatief dichtbij gelegen sterrenstelsels (op ongeveer 350 miljoen lichtjaar bij ons vandaan), toen de leeftijd van het Heelal ongeveer 97% procent was van de huidige leeftijd<sup>2</sup> Deze sterrenstelsels zijn geselecteerd omdat de hoeveelheid gas die ze bevatten significant verschilt, hoewel ze in andere aspecten overeenkomstig zijn. We onderzoeken de suggesties uit vorige studies dat de metalliciteit van de buitenste regio's van de meeste gasrijke sterrenstelsels abnormaal laag is. Dit zou het geval zijn als sterrenstelsels recentelijk nieuw gas hadden aangetrokken in deze regio's, en tegelijkertijd zou dit hun lage globale metalliciteit en overmaat aan gas verklaren.

Onze resultaten ondersteunen dit idee echter niet. We vinden inderdaad sterrenstelsels met een extreem lage metalliciteit in de buitenste regio's, maar we vinden niet dat dit gerelateerd is aan de totale hoeveelheid gas in sterrenstelsels. In plaats daarvan vinden we dat, als men rekening houdt met de ruimtelijke verdeling van gas en sterren, de daling in metalliciteit in de buitenste regio's te verwachten is. Als we voldoende ver van het centrum zouden kunnen waarnemen, zouden we eigenlijk dalingen in alle stelsels verwachten.

**Hoofdstuk 3** Een van de meest significante beperkingen voor waarnemingen die met telescopen vanaf de aarde worden gedaan, is de versmering van het signaal dat door de turbulente aardatmosfeer wordt veroorzaakt (een effect dat *atmosferische seeing* wordt genoemd door astronomen). Hoewel dit ook een effect had op de sterrenstelsels die we bestudeerde in Hoofdstuk 2, kan dit effect voor verdere stelsels catastrofaal zijn als we de stelsels ruimtelijk op willen lossen. In de verre sterrenstelsels die we bestuderen in Hoofdstuk 4 & 5 zijn we niet in staat om de variaties in metalliciteit in detail te bestuderen. Het beste dat we kunnen hopen om te meten is de metalliciteit van het centrum van stelsels en de gemiddelde verandering metalliciteit naar de randen toe (i.e. de gradient van de metalliciteit).

Zelfs dan zal de atmosfeer het moeilijk maken om de gradient van de metalliciteit waar te nemen. Daarom moeten we corrigeren voor de atmosferische seeing als we de juiste gradient willen verkrijgen. Om dit te doen construeren we een modelsterrenstelsel, waarmee we onze waarnemingen kunnen simuleren. Door de metalliciteit in ons model aan te passen, zodat het overeen komt met die van onze waarnemingen, kunnen we de gradient van de metalliciteit vinden, en daarmee de ware gradient afleiden.

**Hoofdstuk 4** We passen de methode die beschreven is in Hoofdstuk 3 toe op een selectie van 84 sterrenstelsels die zijn waargenomen met MUSE. Deze sterrenstelsels staan op een afstand van tussen de 1 en 7 miljard lichtjaren, wat overeenkomt met een periode toen het Heelal tussen de 92% en 48% van haar huidige leeftijd was (de gradient in de metalliciteit is nooit eerder bestudeerd in dit tijdperk).

Over het algemeen vinden we een verscheidenheid aan gradienten in de metalliciteit in de sterrenstelsels; sommige stelsels hebben metaalrijke centra en metaalarme buitenste regio's, zoals de stelsels in het huidige Heelal. Andere hebben juist metaalarme centra en metaalrijke buitenste regio's, welke consistent zijn met wat is waargenomen in het verre Heelal. We vinden ook een voorlopig bewijs dat de gradient in de metalliciteit afhangt van de grootte van het stelsel, zodat de grootse stelsels over het algemeen lijken op de huidige ver geëvalueerde stelsels.

**Hoofdstuk 5** In Hoofdstuk 4 hebben we voorbeelden gevonden van sterrenstelsels met een negatieve gradient in de metalliciteit (stelsels waar de metalliciteit in het centrum hoger is dan die in de buitenste regio's) en voorbeelden van stelsels met een positieve gradient (waar de metalliciteit in de buitenste regio's hoger is dan in de centra). Een belangrijke vraag om te stellen is wat het mechanisme is achter deze eigenaardige stelsels met een positieve gradient.

---

<sup>2</sup>Omdat het tijd kost voor licht om te reizen, zijn we door het bestuderen van verre sterrenstelsels in staat om het Heelal in een eerder stadium te bekijken.

Zijn de buitenste regio's extreem rijk aan metalen, of zijn juist de centra ongebruikelijk arm aan metalen?

Na rekening te hebben gehouden met het aantal sterren in de stelsels, vinden we dat de sterrenstelsels met de meest positieve gradiënten in metalliciteit een lager dan verwachte centrale metalliciteit hebben. Ons resultaat sluit echter niet uit dat de metalliciteit in de buitenste regio's tegelijkertijd verhoogd is. Desalniettemin kan de methode die wij presenteren het mogelijk maken om (met een grotere selectie van sterrenstelsels) te bepalen in hoeverre stelsels gas van het centrum herverdelen naar hun buitenste regio's.





---

## Summary

---

### 1 What are metals?

In moments shortly after the Big Bang, the infant Universe was both sufficiently hot and dense to fuse protons and neutrons together to form atomic nuclei. However, because the Universe was rapidly expanding and cooling, there was sufficient time to only form the lightest elements, and consequently the early Universe was almost entirely composed of Hydrogen and Helium gas.

Over time this gas coalesced under gravity to create very dense regions of space that would become stars. At the centres of stars the temperatures and densities were once again high enough to fuse Hydrogen and Helium into heavier elements. These “heavy” elements are termed *metals* by astronomers.

### 2 Why study them?

Because metals must have been produced in stars, if we study the amount of metals in galaxies then we are able to trace the past star-formation activity of galaxies. The more metals we observe, the more star formation there must have been in the past.

However, it turns out that if we measure the metallicity of galaxies (the ratio between metals and Hydrogen in galaxies), we typically observe a lower metallicity than we would expect given the number of stars observed. This discrepancy can be reconciled if galaxies are able to expel metal-rich gas and/or acquire fresh metal-poor gas during their lives.

Galaxies are not isolated from their environment. Understanding the flow of gas into and out of galaxies is key to explaining the evolution of galaxies. Metallicity provides a powerful tool for studying the fuelling of galaxies.

### 3 How to measure metallicity?

There are two types of metallicity one can measure: the fraction metals in stars themselves (stellar metallicity) and the fraction of metals contained in the gas between stars (gas-phase metallicity). While the former is a more direct quantity to measure, it is more observationally challenging and requires detailed observations of the stellar light. While on the contrary the hot, ionized gas that surrounds massive young stars emits light at very specific wavelengths (colours of light). These *emission lines* show up prominently in the spectra of galaxies that are actively forming stars (see Fig. 7.1).

The relative strengths of the emission lines depends on the complex balance between the ultraviolet light produced by the young stars (which heats the gas) and the rate at which the gas

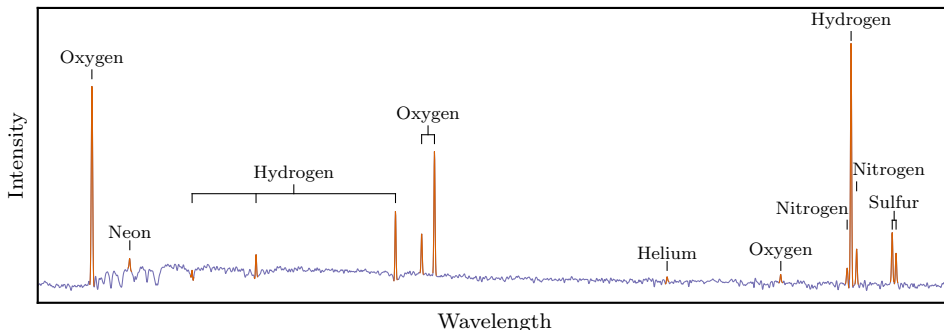


Figure 7.1: A typical spectrum of a star-forming galaxy. The bright emission lines (highlighted in orange) punctuate the comparatively faint stellar light (shown in blue). We label the elements that are responsible for each of the emission lines.

can cool. And because both these factors are sensitive to the metallicity<sup>1</sup> we are able to infer the metallicity of the gas from the ratio of emission-line strengths.

To make these observations one needs to split light into its constituent wavelengths. Traditionally this would be done by extracting a narrow portion of the sky observed by a telescope (a slit) and dispersing the light with (for example) a prism. The result of which is a two-dimensional image, with the spatial distance along the slit in one image direction, while the spectrum at each spatial position runs perpendicularly.

### 3.1 The Multi Unit Spectroscopic Explorer (MUSE)

A fundamental limitation of these traditional slit-based spectrographs is that we only observe a narrow patch of sky. Not only is this wasteful use of the precious little light that enters the telescope, but it also only provides a narrow window into the universe.

Fortunately, the past decades have seen the development of integral-field spectrographs that, through a variety of techniques, are able to obtain spectra over a two-dimensional patch of sky. At the current cutting edge of these instruments is The Multi Unit Spectroscopic Explorer (MUSE), which has been heavily optimized for the purpose of making long observations. Up until now, deep spectroscopic observations of distant galaxies were only performed on select galaxies. However, MUSE heralds the opportunity for an unbiased spectroscopic window into the distant universe, without such need for preselection.

## 4 This thesis

In this thesis we focus on not only determining the metallicity of galaxies, but also how metallicity varies with distance from the centre of galaxies. Since there is no one single value for the metallicity that can describe the whole of the galaxy, we can gain a much deeper insight if we resolve (map) these variations.

**Chapter 2** We study a sample of 50 relatively nearby galaxies (approx. 350 million light-years

<sup>1</sup>Strictly speaking the former depends on stellar metallicity, while the later depends on gas-phase metallicity.

away), at a time when the universe was roughly 97% of its present age<sup>2</sup>. These galaxies were chosen because, while similar in many respects, the amount of gas they contained was significantly varied. We followed up on previous suggestions that the outskirts of the most gas-rich galaxies were anomalously metal poor. This might be the case if galaxies had recently acquired fresh gas at their outskirts, simultaneously explaining the low metallicities and their excess gas.

However, our results do not support this. Indeed, while we do find galaxies with spuriously low outer metallicities, we do not find these occurrences to be associated with the total amount of gas in galaxies. Instead we find that if one accounts for the spatial distributions of gas and stars, then the outer drops in metallicity are to be expected. In fact if one could observe sufficiently far from the centre, we might expect to observe drops in all galaxies.

**Chapter 3** One of the most significant limitations for observations made from ground-based telescopes is the blurring caused by the Earth's turbulent atmosphere (an effect termed *atmospheric seeing* by astronomers). While there is a some impact on the galaxies we study in Chapter 2, for more distant galaxies the effect can be catastrophic if we want to spatially resolve galaxies. In the distant galaxies that we study in Chapters 4 & 5 we are unable to study the metallicity variations in detail. The best we can hope to measure is the metallicity the centre of galaxies and the average change in metallicity throughout the galaxy (i.e. the metallicity gradient).

Even then the atmosphere will partially wash out the metallicity gradient in galaxies, therefore, if we want to derive the true metallicity gradient we must correct for the atmospheric seeing. To do this we construct a model galaxy, from which we can simulate our observations. By adjusting the metallicity in our model we can find metallicity gradients that best matches our observed data, and thereby infer the true metallicity gradient.

**Chapter 4** We apply the method developed in Chapter 3 to a sample of 84 galaxies observed with MUSE. These galaxies are between 1 and 7 billion light-years away, corresponding to a period when the Universe was between 92% and 48% of its present age (a range not yet explored by other metallicity gradient studies).

In general we find galaxies with a range of metallicity gradients; some galaxies have metal-rich centres and metal-poor outskirts, like galaxies in the Universe today, and others have metal-poor centres and metal-rich outskirts, consistent with galaxies observed in the distant Universe. We also find tentative evidence that the metallicity gradient depends on the galaxy size, such that the largest galaxies are typically most like the well-evolved galaxies today.

**Chapter 5** In Chapter 4 we identified examples of galaxies with negative metallicity gradients (galaxies where the outskirts have a lower metallicity than at the centre) and cases of galaxies with positive metallicity gradients (galaxies where the outskirts have a higher metallicity than at the centre). An important question to ask is what drives these peculiar galaxies with positive metallicity gradients. Are the outskirts excessively metal rich, or are the centres unusually metal poor?

After accounting for the number of stars in the galaxies, we find that the galaxies with the most positive metallicity gradients have lower than expected central metallicities. Our results, however, do not preclude the possibility that outer metallicities are not simultaneously elevated. Nevertheless, the method we present could (with a larger sample of galaxies) allow one to constrain to what extent galaxies redistribute gas from the centre of galaxies to their outskirts.

---

<sup>2</sup>Because light does not travel instantaneously, by studying distant galaxies are able to see the Universe at an earlier stage.



---

# Publications

---

## Lead author

*Inferring gas-phase metallicity gradients of galaxies at the seeing limit: A forward modelling approach*

David Carton, Jarle Brinchmann, Maryam Shirazi, Thierry Contini, Benoît Epinat, Santiago Erroz-Ferrer, Raffaella A. Marino, Thomas P. K. Martinsson, Johan Richard, Vera Patrício

2017, [MNRAS](#), 468, 2140

*Gas-phase metallicity profiles of the Bluedisk galaxies: Is metallicity in a local star formation regulated equilibrium?*

David Carton, Jarle Brinchmann, Jing Wang, Frank Bigiel, Diane Cormier, Thijs van der Hulst, Gyula I. G. Józsa, Paolo Serra, Marc A. W. Verheijen

2015, [MNRAS](#), 451, 210

## Contributing author

*The Bluedisk Survey: molecular gas distribution and scaling relations in the context of galaxy evolution*

Diane Cormier et al.

2016, [MNRAS](#), 463, 1724

*A study of the kinematics of unusually HI-rich galaxies*

Milan den Heijer et al.

2015, [AN](#), 336, 284

*The MUSE 3D view of the Hubble Deep Field South*

Roland Bacon et al.

2015, [A&A](#), 575, 75



---

# Curriculum Vitae

---

At approximately MJD 48009.375 I was born in Winchester. Growing up nearby, it was clear to my primary school teachers that I harboured an affinity for science and the desire to ask questions. Thanks to my Father, this manifested itself in particular as an enthusiasm for astronomy. Such was my interest that, when time came, it was clear that there was only one thing I could choose to study when I went to university.

In 2008 CE I moved  $3^{\circ}47'$  North to Durham, where I began an undergraduate degree in Physics and Astronomy. Therein I found many like-minded friends, with whom I could share my passion for stargazing. I left after four years having acquired not only a degree, but also an unexpected passion for bell ringing.

Deciding that Durham (*Ding!*) was too small to stay there, I moved to the bright lights of Leiden and embarked on a PhD with Jarle Brinchmann. With my main requirements of doing a PhD with observational data, galaxies and spectra, a project with a new instrument called MUSE was right up my straat. And so, after a few years of pretending to know what I was doing, it was time to start writing up four thesis chapters, all of which can be found within these very pages!

In October 2016, not wanting to break with the pattern of moving to larger cities, I relocated to Lyon. At the present time I remain there, working as a “post” doctoral researcher, relying on the safety of continuing to work with MUSE.

The future? Who knows, perhaps I might even learn some French...



---

# Acknowledgements

---

Congratulations for reading the whole thesis up to this point. I'm sure you didn't just turn to this page to see if you got a mention.

First I would like to thank my officemates with whom I shared almost every day of my PhD ~~or~~ ~~deal~~ experience. Over the course of the many lunches and coffee breaks we discussed all topics, ranging from the key political issues of the day, to the finer points of Dutch cuisine. So, thank you Massimo for instilling us all with your inspirational and wholly optimistic postdoc spirit. And thank you to Jeroen for tolerating us while we openly debate many matters, including the person who is *zwart als roet*.

Fabian, thank you, not only for your continued encouragement and support, but also for simply being a truly great friend. You were there throughout many of the highlights during my time in Leiden and I will look back fondly at our nights spent in the Bonte Koe. And therein I should say thank you also too to Andrej, Clément, Emanuele and Ricardo for accompanying us on our quest to find the holy grail of elixirs, *Amstel and Water*.

Leah, ever since we first met for the interviews it has been a pleasure getting to know the awesome person that you are, whether it be over a good game of Pandemic, a glass of whisky or simply an afternoon cup of tea.

During the four years of my PhD I am pleased to have met so many fantastic people. To name a few: Aayush, 'Alex's (from all hemispheres), Ann-Sofie, Eleonora, Heather, Henriette, Jit, Laura, Marco, Marissa, Mattia, Tiffany, Tommaso, Vivianni and Wendy, thank you all for putting up with me. My time in Leiden would not have been so tolerable if it weren't for those I shared Levendaal 101c with; Andra, Michael and Luke you all made returning home in the evening a welcoming experience. Apologies to Edwin and Margot for insulting your Dutch ways, but thank you for enlightening me by showing the true meaning of being Dutch. Mieke, or perhaps I should call you *Frau Carton*, I have very much enjoyed your company over the past years, and I wish to thank you especially for the encouragement and motivation you have given me, as well as translating the summary of this thesis into Dutch. Finally, thank you Nikki, and although I only really got to know you towards the end of my time in Leiden, you were there when I needed it most.

As a persistent feature throughout the PhD, Big Dipper and your disciples (past, present and future), thank you for being that shining light at the end of the darkest weeks. Of course, Allison and Mason, we were indisputably the best (we even have backpacks to prove it). Plus I am happy to say that I am almost fully recovered from the experience, and I only slightly wince at the sight of ALDI.

Since the late delivery of this thesis will not have escaped the notice of many. I wish to also thank the many great people who welcomed me to Lyon and encouraged me to finish this book: Anna (×2), Alyssa, Benjamin, Floriane, Hanae, Joanne, Liz, Martin, Peter, Stephen, Vera, Wiki D and the rest of the Astro Gang.

And last but by no means least, thank you Jarle for your support, advice and extreme patience.

